UNIVERSITY OF BELGRADE
FACULTY OF PHYSICS

Stefan Stojku

PROPERTIES OF QUARK-GLUON PLASMA INFERRED FROM HIGH-$p_\perp$ DATA

Doctoral Dissertation

Belgrade, 2023

УНИВЕРЗИТЕТ У БЕОГРАДУ
ФИЗИЧКИ ФАКУЛТЕТ

Стефан Стојку

ОДРЕЂИВАЊЕ ОСОБИНА КВАРК-ГЛУОНСКЕ ПЛАЗМЕ ПОМОЋУ ВИСОКОЕНЕРГИЈСКИХ ЧЕСТИЦА

докторска дисертација

Београд, 2023. година

Thesis Defense Committee

Thesis advisor:

Dr. Magdalena Djordjević
Research Professor
Institute of Physics Belgrade
University of Belgrade

Committee member:

Dr. Bojana Ilić
Assistant Research Professor
Institute of Physics Belgrade
University of Belgrade

Committee member:

Prof. Dr. Maja Burić
Professor
Faculty of Physics
University of Belgrade

Committee member:

Prof. Dr. Voja Radovanović
Professor
Faculty of Physics
University of Belgrade

Acknowledgements

This thesis was completed under the mentorship of Dr. Magdalena Djordjević, Research Professor, at the Laboratory for High Energy and Nuclear Physics, at the Institute of Physics Belgrade, University of Belgrade. The presented research was supported by the European Research Council under the grant ERC-2016-COG: 725741 and by the Ministry of Science, Technological Development and Innovations of the Republic of Serbia.

I would like to express gratitude to my supervisor, Dr. Magdalena Djordjevic, for introducing me to the field and for competent guidance and support through my Ph.D. studies. Her intuition, knowledge, and perseverance are a continuing source of inspiration.

I thank Dr. Bojana Ilić for supervising the last part of my thesis. Her help and guidance were very useful for successfully completing this part of the project.

I want to thank the rest of our group, and especially Lidija Živković, Jussi Auvinen, Pasi Huovinen, Igor Salom and Marko Djordjević, whom I collaborated with during my Ph.D. studies. I am grateful to Dušan Žigić for valuable discussions.

Dušica, thank you for always being kind and helpful.

Many thanks to Bithika, Ana, Sanja, Veljko, and Dušan for a pleasant and productive work environment at the Institute of Physics Belgrade and all the amusing coffee breaks.

I am very grateful to my friends, who have made everything much more enjoyable. Aleksandra, thank you for your enduring friendship, all the travels, and adventures we've shared, and for being there whenever I needed it. Iva, thank you for always having the time, patience, and warm understanding for me. Ljubica, Filip, and Miljana, I am very grateful for all the joyful evenings we've spent together and for your help and support. Thank you, Miloš, Bojana, Jelena and Marta, for all the laughter and helpful conversations. Thank you, Barbara, Tijana, Tamara, Rade, for your love and friendship.

I am grateful to my family for being such a positive presence in my life. Finally, I thank my wonderful parents, Marinela and Dorel, for their unwavering support and devotion.

Abstract

Quark-gluon plasma (QGP) is a new form of matter created in the Little Bangs: collisions of heavy ions at ultrarelativistic energies at the Large Hadron Collider (LHC) and Relativistic Heavy Ion Collider (RHIC). It consists of deconfined quarks, antiquarks, and gluons. According to modern cosmology, quark-gluon plasma is believed to have existed shortly after the Big Bang. Thus, the study of quark-gluon plasma is of fundamental importance, giving us insight into this new form of matter governed by strong interaction while advancing our understanding of the early universe.

After the collision of two nuclei, most of the created particles ($\sim 99.9\%$), which constitute quark-gluon plasma, have low energy and form the thermalized medium. A small number ($\sim 0.1\%$) of particles are highly energetic – they are created early in the evolution of the medium, and traverse it while interacting with it through the strong force. In that way, these particles carry information on the properties of the medium. This fact is the central idea of the research presented in this thesis. The results will demonstrate how the theory, numerical calculations, and data related to the high-$p_\perp$ particles can be used with low-$p_\perp$ physics to extract essential properties of this new form of matter.

The results are organized into three main sections: the first one is related to the early stages of quark-gluon plasma formation, the second is related to the anisotropy of the quark-gluon plasma created in heavy-ion collisions, and finally, the third one will deal with the extension of the dynamical energy loss formalism to the case of multiple scattering centers.

The collective motion of low-$p_\perp$ particles, which form the medium created in heavy-ion collisions, is commonly described by applying relativistic hydrodynamics. However, the dynamics before the initial hydrodynamical evolution of quark-gluon plasma have yet to be established. We aim to use high-$p_\perp$ theory and data to explore the early stages of QGP formation before the onset of hydrodynamics. As a first step, we aim to determine the initial time of hydrodynamical transverse expansion (τ_0), an important parameter that has been only weakly constrained through low-$p_\perp$ physics. To this avail, we first focus on a simplified model with no pre-equilibrium transverse evolution and use high-$p_\perp$ numerical simulations and comparison with experimental data to constrain the value of this parameter. Since the model with no pre-equilibrium evolution is considered too simplified, we extend it to include more sophisticated pre-equilibrium evolution scenarios in the next step. Both approaches consistently show that the experimental data prefers the late onset of transverse expansion and energy loss in the medium.

Anisotropy of the quark-gluon plasma created in heavy-ion collisions (which can be thought of as the measure of the deviation of a droplet of quark-gluon plasma from the spherical shape)

is one of the fundamental properties of this medium. However, it is still impossible to infer this parameter's values directly from the experimental measurements despite its essential importance. Our research will demonstrate how this can be achieved using high-$p_\perp$ data. Namely, we first focus on a simplified model, where the medium expands only in the longitudinal direction. We then move on to the realistic hydrodynamical description of the model, with both longitudinal and transversal expansion, and explore whether its anisotropy can be related to the high-$p_\perp$ observables R_{AA} and v_2. According to our analysis, the anisotropy of the medium can be directly related to a modified ratio of these high-$p_\perp$ observables, $v_2/(1-R_{AA})$. Moreover, we propose a new observable – *jet-perceived anisotropy*, which is proportional to this ratio but can also be calculated directly from the hydrodynamical medium evolution. We argue that future hydrodynamical calculations should be tuned to reproduce the values of jet-perceived anisotropy obtained from the experimental data.

Finally, we will consider the problem of high-$p_\perp$ particles experiencing multiple scatterings (*opacity expansion*) within the medium. Namely, most of the existing radiative energy loss formalisms incorporate either the *optically thin* or the *optically thick* approximation. In the optically thin approximation, a jet encounters a single scattering center before radiating gluons. This approximation is used in the dynamical energy loss formalism, which describes the energy loss of high-$p_\perp$ partons in the medium. On the other hand, in the optically thick approximation, jets encounter infinite scattering centers before radiating gluons. Since the size of the medium created in Little Bangs is several fm, and the mean free path is $\lambda \approx 1$fm, it is clear that neither of these approximations is realistic. We thus derive the expressions for radiative energy loss within the dynamical energy loss formalism up to the 4^{th} order in opacity and implement them into our appropriately generalized numerical framework to generate the predictions for light and heavy probes. Our findings suggest that higher-order effects are negligible for RHIC and LHC and that the optically thin approximation is adequate for the dynamical energy loss formalism.

Keywords: quark-gluon plasma, high-$p_\perp$ data, early stages, anisotropy, opacity
Research field: Physics
Research subfield: High-energy and nuclear physics
UDC number:

Сажетак

Кварк-глуонска плазма је ново стање материје које настаје у експериментима који укључују сударе тешких јона убрзаних до ултрарелативистичких брзина у Великом сударачу хадрона (LHC) и у Релативистичком сударачу тешких јона (RHIC). Она се састоји од слободних кваркова, антикваркова и глуона. На основу модерне космологије, кварк-глуонска плазма је постојала убрзо након Великог праска, те је проучавање кварк-глуонске плазме од фундаменталне важности. Тиме стичемо увид у ново стање материје чије особине одређује јака интеракција, унапређујући разумевање раног универзума.

Након судара два језгра, већина насталих честица ($\sim 99.9\%$) које чине кварк-глуонску плазму има ниску енергију и формира термализован медијум. Мали број ($\sim 0.1\%$) честица има високу енергију - оне настају рано у еволуцији система, пролазе кроз медијум интерагујући са њим посредством јаке интеракције, и на тај начин носе информацију о његовим особинама. Ово је главна идеја истраживања које ће бити изложено у овој дисертацији. Резултати ће показати како теорија, нумерички прорачуни и подаци који су у вези са високоенергијским честицама могу бити коришћени заједно са физиком нискоенергијских честица како би се одредиле важне особине кварк-глуонске плазме.

Резултати су подељени у три одељка: први је везан за почетне стадијуме еволуције кварк-глуонске плазме, други за анизотропију кварк-глуонске плазме настале у сударима тешких јона, док се трећи бави проширењем динамичког формализма губитка енергије на случај вишеструких центара расејања у медијуму.

Уобичајено је да се колективно кретање нискоенергијских честица које чине медијум настао у сударима тешких јона описује применом релативистичке хидродинамике. Међутим, динамика пре почетног времена хидродинамичке еволуције кварк-глуонске плазме још увек није одређена. Наш циљ је да употребимо теорију и податке везане за високоенергијске честице како бисмо истражили ране фазе еволуције кварк-глуонске плазме, пре почетка ширења медијума у трансверзалној равни, које је добро описано релативистичком хидродинамиком. Желимо да одредимо почетно време хидродинамичке трансверзалне експанзије (τ_0), које је важан параметар, а до сада недовољно прецизно одређиван коришћењем физике нискоенергијских честица. Како бисмо ово остварили, прво разматрамо једноставан модел без еволуције медијума у трансверзалној равни пре остваривања равнотеже, и користимо нумеричке симулације високоенергијских честица и поређење са експерименталним подацима како бисмо одредили вредност овог параметра. Имајући у виду да се не сматра да је модел без еволуције медијума пре остваривања равнотеже реалистичан, у наредном кораку, проширујемо га укључивањем еволуције медијума пре τ_0. Оба ова приступа доследно показују да се поклапање са експерименталним подацима добија у случају каснијег почетка трансверзалне експанзије и губитка енергије високоенергијских

честица у медијуму.

Анизотропија кварк-глуонске плазме настале у сударима тешких јона – мера одступања насталог медијума од сферног облика – једна је од његових фундаменталних особина. Међутим, упркос важности ове опсервабле, још увек није могуће одредити њене вредности директно из експерименталних података. Наше истраживање показује како се ово може извести коришћењем високоенергијских података. Наиме, прво разматрамо поједностављен модел, где се медијум шири у лонгитудиналном правцу. Након тога, прелазимо на реалистичан, хидродинамички опис медијума, који се шири и у трансверзалној равни, и испитујемо да ли његова просторна анизотропија може бити повезана са високоенергијским опсерваблама R_{AA} и v_2. На основу наше анализе, анизотропија медијума се може директно повезати са модификованим односом ових високоенергијских опсервабли, $v_2/(1-R_{AA})$. На основу овога, предлажемо нову опсерваблу – *jet-perceived anisotropy* („температура коју виде џетови"), која је пропорционална овом модификованом односу, али која се може и директно израчунати из хидродинамичке еволуције медијума. Тврдимо да будући хидродинамички прорачуни треба да буду подешени да репродукују њене вредности добијене из експерименталних података.

Коначно, разматрамо проблем вишеструких центара расејања високоенергијских честица у медијуму. Наиме, већина постојећих формализама који описују губитке енергије високоенергијских честица укључује расејање на једном или на бесконачном броју центара расејања. На основу прве од ових апроксимација, џет наилази на један центар расејања пре него што израчи глуоне – она је коришћена у динамичком формализму губитка енергије високоенергијских честица. У другој апроксимацији, џетови наилазе на бесконачан број центара расејања пре него што израче глуоне. С обзиром на то да је величина медијума који настаје у сударима тешких јона величине неколико фемтометара, а да је средњи слободан пут партона у медијуму $\lambda \approx 1\text{fm}$, јасно је да ниједна од ових апроксимација није реалистична. Извели смо изразе за радијативне губитке енергије у оквиру динамичког формализма губитка енергије до четвртог реда у развоју по броју центара расејања, и имплементирали их у адекватно уопштен нумерички формализам како бисмо произвели предвиђања за лаке и тешке честице. Резултати сугеришу да су ефекти укључивања коначног броја центара расејања мали и да је коришћење једног центра расејања прикладна апроксимација за динамички формализам губитка енергије.

Кључне речи: кварк-глуонска плазма, високоенергијски подаци, рани стадијуми, анизотропија, вишеструки центри расејања
Научна област: Физика
Ужа научна област: Физика високих енергија и нуклеарна физика
УДК број:

Contents

List of figures

Chapter 1

Introduction

> After all, there are other thrills in other domains: the thrill of pure science is just as pleasurable as the pleasure of pure art. The main thing is to experience that tingle in any department of thought or emotion. We are liable to miss the best of life if we do not know how to tingle, if we do not learn to hoist ourselves just a little higher than we generally are in order to sample the rarest and ripest fruit of art which human thought has to offer.
>
> *Lectures on Literature*
> Vladimir Nabokov

This doctoral dissertation is devoted to the study of quark-gluon plasma. According to modern cosmology, quark-gluon plasma was present shortly after the Big Bang, and today, it is created in so-called Little Bangs — collisions of heavy ions at ultrarelativistic energies. The properties of this new form of matter are governed by the laws of quantum chromodynamics, the theory which describes the strong interaction between quarks and gluons. In order to introduce the reader to the phenomena discussed in the following Chapters, we here give an overview of quantum chromodynamics, quark-gluon plasma, and how it can be theoretically modeled, as well as of the heavy-ion experiments where it is created.

The results presented in this dissertation are based on the following publications [1, 2, 3, 4, 5]:

1. Stefan Stojku, Jussi Auvinen, Marko Djordjevic, Magdalena Djordjevic, Pasi Huovinen, *Initial Time τ_0 Constrained by High-$p_\perp$ Data*, Acta Phys. Pol. B Proc. Suppl. **16**, 1-A156 (2023)

2. Stefan Stojku, Jussi Auvinen, Marko Djordjevic, Pasi Huovinen, and Magdalena Djordjevic, *Early evolution constrained by high-$p_\perp$ quark-gluon plasma tomography*, Physical Review C **105**, L021901 (2022)

3. Magdalena Djordjevic, Stefan Stojku, Marko Djordjevic, and Pasi Huovinen, *Shape of the quark gluon plasma droplet reflected in the high- $p_\perp$ data*, Phys. Rev. C **100**, 031901(R) (2019)

4. Stefan Stojku, Jussi Auvinen, Lidija Zivkovic, Pasi Huovinen, Magdalena Djordjevic, *Jet-perceived anisotropy revealed through high-$p_\perp$ data*, Physics Letters B **835**, 137501 (2022)

5. Stefan Stojku, Bojana Ilic, Igor Salom, Magdalena Djordjevic, *Importance of higher orders in opacity in QGP tomography*, arXiv:2303.14527 [nucl-th] (under positive review in Physical Review C)

1.1 Quantum chromodynamics - the theory of the strong interaction

In the high-energy heavy-ion collisions, a deconfined phase of matter is created, which consists of interacting quarks, antiquarks, and gluons: quark-gluon plasma [6, 7, 8, 9]. This section will give a brief overview of quantum chromodynamics (QCD): the theory that describes the strong interaction that acts between quarks, mediated by gluons [10], and is central to all our descriptions of quark-gluon plasma. QCD is a non-abelian gauge theory with the symmetry group $SU(3)_c$ [10]. The index "c" comes from *color*. There are three charges in the theory (red, green, and blue), analogous to the three colors seen by the human eye. When compared to quantum electrodynamics (QED), the main complication in QCD arises since the gluons carry the color charges themselves and can therefore interact with each other. The theory has a rich phase diagram, and its non-abelian structure encodes important phenomena observed: confinement and asymptotic freedom, which we will discuss in more detail below.

1.1.1 The Eightfold Way

The middle of the twentieth century brought numerous advances in accelerator and detector technology, which enabled the discovery of many elementary particles [11, 12]. The list of strongly decaying mesons and baryons grew longer during these years – see Figure 1.1 for a brief timeline of particle discoveries. A theoretical framework was needed to make it possible to understand or at least classify the newly discovered particles.

In the late 1940s, there were ideas to organize the elementary particles inspired by the isospin formalism. A proposal made independently by Gell-Mann [13] (then at Caltech) and Ne'eman turned out to be successful: it was called *The Eightfold Way*, which takes its name from the Noble Eightfold Path of Buddhism. This classification scheme is based on the SU(3) symmetry group, and particles are classified into multiplets characterized by parity and spin numbers. Several experimental discoveries supported this new theory. First was the discovery of the η resonance in 1961, which fit perfectly into the octet of pions and kaons. The second was the discovery of Ω^- baryon in the Brookhaven Laboratory [14].

In 1964, Gell-Mann [13] and Zweig [15] independently proposed an interpretation of the Eightfold way, according to which hadrons were composed of smaller particles, which Gell-Mann named *quarks*, a word which appears in James Joyce's *Finnegans Wake*: "Three quarks for Muster Mark!" This proposal suggested that all hadrons are composite particles, made up of two or three quarks - this reduced hundreds of known hadronic particles to three fundamental constituents: these were called *up*, *down*, and *strange* quarks [12]. Quarks belong to the 3-dimensional representation of the $SU(3)_f$ (flavor) group. Mesons are $q\bar{q}$ states (therefore, they are baryons of spin 0 or 1) which belong to the 8-dimensional or singlet representations of

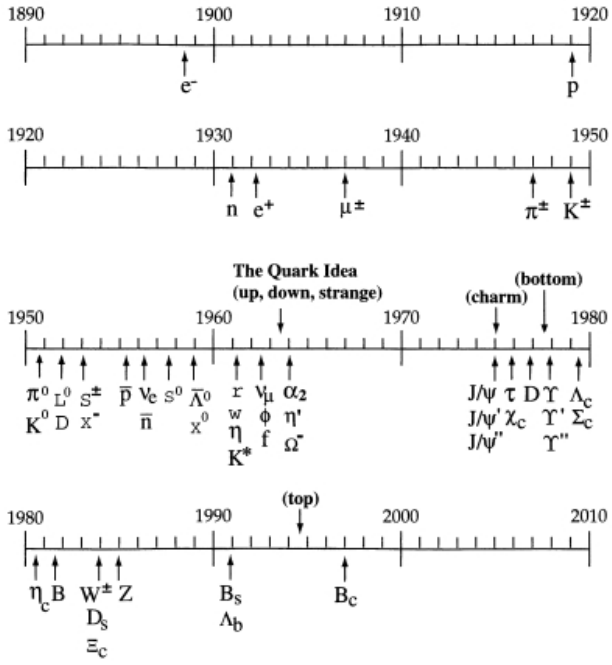

Figure 1.1: Timeline of particle discoveries during the twentieth century. Figure adapted from [11].

SU(3). Baryons are qqq bound states (and therefore fermions with spin 1/2 or 3/2), and they belong to 10-dimensional, 8-dimensional, and singlet representations of the SU(3) group.

The flavor symmetry group was expanded with the discovery of new quark flavors. After the discovery of the c (charm) quark by Richter and Ting, the symmetry group was expanded to SU(4), and after the discovery of t and b quarks, the flavor symmetry group was expanded to SU(6). Therefore, quarks come in six flavors, and we group them into three generations:

$$\begin{pmatrix} u \\ d \end{pmatrix}, \begin{pmatrix} c \\ s \end{pmatrix}, \begin{pmatrix} t \\ b \end{pmatrix}. \tag{1.1}$$

In addition to this, another degree of freedom was proposed: color [16, 17]. The following example shows why this new degree of freedom is required. Namely, the Δ^{++} baryon consists of three up quarks: uuu and has a spin of 3/2. Its spin wave function is symmetric in the $s_z = +3/2$ state. In the ground state, its orbital wave function is also symmetric. Therefore, its total wave function is symmetric, violating the Pauli principle. This issue can be solved by adding another degree of freedom (color) and requiring that the baryon wave function be antisymmetric with respect to this new quantum number. This new symmetry group is called $SU(3)_c$, and the quark wavefunction is a color triplet [10]:

$$\psi(x) = \begin{pmatrix} \psi_r(x) \\ \psi_b(x) \\ \psi_g(x) \end{pmatrix}. \tag{1.2}$$

Mesons always have the color-symmetric wave function:

$$\Psi_{c,mesons} = \frac{1}{\sqrt{3}}(R\bar{R} + G\bar{G} + B\bar{B}). \tag{1.3}$$

On the other hand, baryons have the color-antisymmetric wave function:

$$\Psi_{c,baryons} = \frac{1}{\sqrt{6}}(RGB - RBG + GBR - GRB + BRG - BGR). \tag{1.4}$$

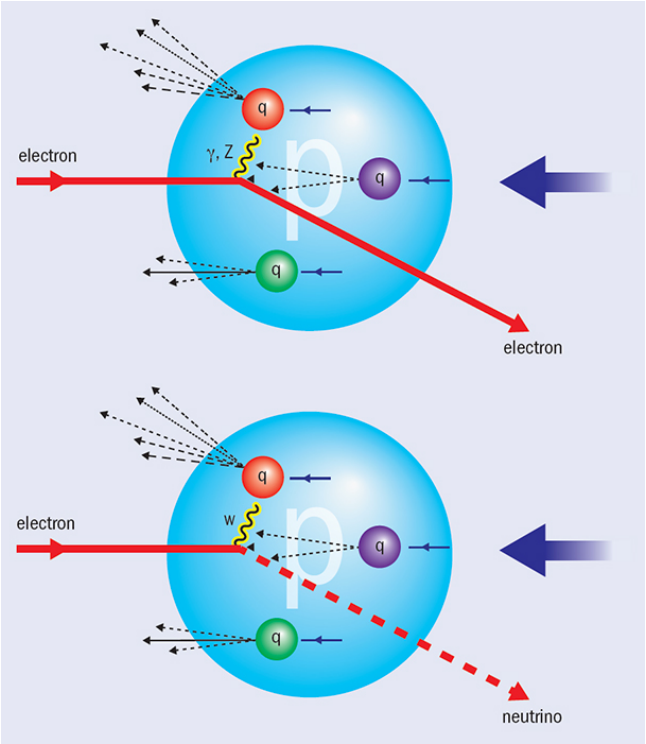

Figure 1.2: Deep inelastic scattering experiment. Figure adapted from DESY.

In the early days, quarks were deemed only a mathematical formality, and even Gell-Mann believed that they were only a mathematical convenience and not real objects that we could observe in experiments: "It is fun to speculate about the way quarks would behave if they were physical particles of finite mass (instead of purely mathematical entities as they would be in the limit of infinite mass). [...] A search for stable quarks of charge -1/3 or +2/3 and/or stable di-quarks of charge -2/3 or +1/3 or +4/3 at the highest energy accelerators would help to reassure us of the non-existence of real quarks." [13]

However, the experiments conducted in 1968 at Stanford Linear Accelerator Center (SLAC) – *deep inelastic scattering* [18, 19] – were the first that demonstrated that quarks indeed are real objects in nature, and not a mere mathematical convenience, see Figure 1.2. These experiments are analogous to Rutherford's experiment, which studied scattering patterns of alpha particles on atoms. Here, the inelastic scattering of electrons on liquid hydrogen (and later deuterium) targets was studied, and the results were strikingly similar to those obtained in Rutherford's experiment: most of the incident particles pass right through. At the same time, a small fraction of them experience large deflection. This result indicates that the proton's charge is not uniformly spread over its volume but instead concentrated in lumps, in the same way as Rutherford's experiment demonstrated that the atom's positive charge is concentrated in the nucleus. However, in the case of the proton, the scattering pattern indicated the existence of three lumps of charge [20] – compelling evidence supporting the existence of quarks.

1.1.2 Fundamental properties of QCD

The QCD Lagrangian. To describe the two fundamental properties of QCD relevant to understanding quark-gluon plasma, we will start with the QCD Lagrangian. It has the standard form of a Yang-Mills Lagrangian for a non-abelian gauge theory [21]:

$$\mathcal{L} = \sum_{k=1}^{n_q} \bar{\psi}_k (i\gamma^\mu D_\mu - m_k)\psi_k - \frac{1}{4} F^a_{\mu\nu} F^{\mu\nu a}. \tag{1.5}$$

The index a is summed over the generators of the symmetry group G of the theory, which is SU(3) in the case of QCD. The fermion multiplets ψ_k belong to the fundamental representation of SU(3). γ^μ are the Dirac gamma matrices, and the n_q quark flavors are summed over. The constants m_k represent the quark masses.

The covariant derivative is given by:

$$D_\mu \psi = (\partial_\mu - i g_s A^a_\mu \frac{\lambda^a}{2})\psi. \tag{1.6}$$

The second part of the Lagrangian is the kinetic term, where the field strength tensor is given by:

$$F^a_{\mu\nu} = \partial_\mu A^a_\nu - \partial_\nu A^a_\mu + g_s f^{abc} A^b_\mu A^c_\nu. \tag{1.7}$$

The coupling constant is given by $g_s = \sqrt{4\pi\alpha_s}$, with the value of α_s discussed below. The λ^a are Gell-Mann matrices ($a = 1 \ldots 8$ for SU(3)), and f^{abc} are the structure constants of the $\mathrm{su}(3)_c$ algebra. The potentials $A^{\mu a}$ belong to the adjoint representation of SU(3) and represent the gluons, the carriers of the strong interaction. From the form of the QCD Lagrangian (by substituting Eq. 1.7 in Eq. 1.5), we see that the interaction part of the Lagrangian gives rise to gluon self-interactions, i.e., 3- and 4-gluon vertices (Fig. 1.3). This feature was not present in quantum electrodynamics, where the mediators of the force (photons) do not carry charge.

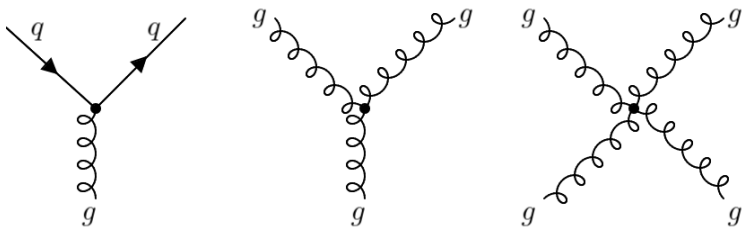

Figure 1.3: Interaction vertices in quantum chromodynamics. The first diagram shows the quark-gluon interaction, while the two diagrams on the right show the 3- and 4- gluon vertices.

Asymptotic Freedom. An important milestone in developing QCD theory was the discovery of *asymptotic freedom*. Namely, when we look at the renormalization-group running coupling for, e.g., massless $\lambda\phi^4$ theory or quantum electrodynamics, we see that the effective coupling is larger at high energy, equivalent to a short distance. Physically, we interpret this by the fact that a charge is screened by the production of virtual pairs in the vacuum, and as we approach the charge, we leave behind the screening cloud around it [22].

Until 1973, only the cases of theories with the positive β function were known. However, in 1973, Politzer [23], Gross [24], and Wilczek showed that non-abelian gauge theories allow for a negative β function, meaning that charge decreases at short distances in these theories.

For this discovery, Politzer, Gross, and Wilczek were jointly awarded the 2004 Nobel Prize in Physics [25].

Namely, the lowest-order renormalization-group β function for a non-abelian gauge theory is [22]:

$$\beta = -\frac{g_s^3}{48\pi^2}(11N_c - 2N_f). \tag{1.8}$$

Here, N_c refers to the number of colors, and N_f refers to the number of quark flavors. This expression is negative for $N_f < 5.5N_c$, which is fulfilled for SU(3) with six quark flavors, and thus, the running coupling g_s decreases with the increasing energy scale. Figure 1.4 summarizes the experimental confirmations of asymptotic freedom.

The leading-order behavior of the coupling in QCD is given by [23, 24, 26, 27]:

$$\alpha_s(Q^2) = \frac{\alpha_s(\mu^2)}{1 + \frac{\alpha_s(\mu^2)}{12\pi}(11N_c - 2N_f)\ln(\frac{Q^2}{\mu^2})}. \tag{1.9}$$

Here, Q^2 is the momentum transfer. The Equation 1.9 relates $\alpha_s(Q^2)$ with $\alpha_s(\mu^2)$ at a different scale – the parameter μ is called *the renormalization point* or *the subtraction point*. This equation explicitly shows the asymptotic freedom: the coupling approaches zero as $Q^2 \to \infty$. This fact signifies that perturbative QCD should work well at high Q^2 (small distances) but break down at small Q^2 (large distances), where the coupling increases.

It is common to introduce the *QCD scale parameter*, Λ_{QCD}, in the following way:

$$\Lambda_{QCD}^2 = \mu^2 \exp\left(-\frac{12\pi}{(11N_c - 2N_f)}\frac{1}{\alpha_s(\mu^2)}\right). \tag{1.10}$$

We can thus rewrite the expression for the running coupling:

$$\alpha_s(Q^2) = \frac{12\pi}{(11N_c - 2N_f)\ln(\frac{Q^2}{\Lambda_{QCD}^2})}. \tag{1.11}$$

This is the commonly used parametrization of $\alpha_s(Q^2)$ and Λ_{QCD} parameter is equal to the energy scale where $\alpha_s(Q^2)$ diverges, i.e. $\alpha_s(Q^2) \to \infty$ when $Q^2 \to \Lambda_{QCD}^2$ [28].

Confinement. While there is a wealth of experimental evidence for the existence of quarks, they have never been observed as free particles, despite many experimental attempts [29]. This fact is explained by the *color confinement*, a hypothesis that particles are always confined to color singlet states and that particles with non-zero color charge cannot propagate as free particles. While there is still no analytical proof of color confinement within any non-abelian gauge theory [30], it has been corroborated by the nonperturbative methods of lattice QCD [31, 32].

The likely origin of this phenomenon can also be understood qualitatively. Quarks interact by exchanging virtual gluons, which are themselves color-charged. When quarks are close to each other, the strong force between them is relatively weak. However, as they are pulled apart, the strong force becomes stronger, and the energy within the force field connecting them increases. At a certain point, the energy between the quarks becomes sufficient to create new quark-antiquark pairs from the vacuum. This phenomenon results in the creation of a flux tube between the quarks, often referred to as a QCD string or a color flux tube. We can think of

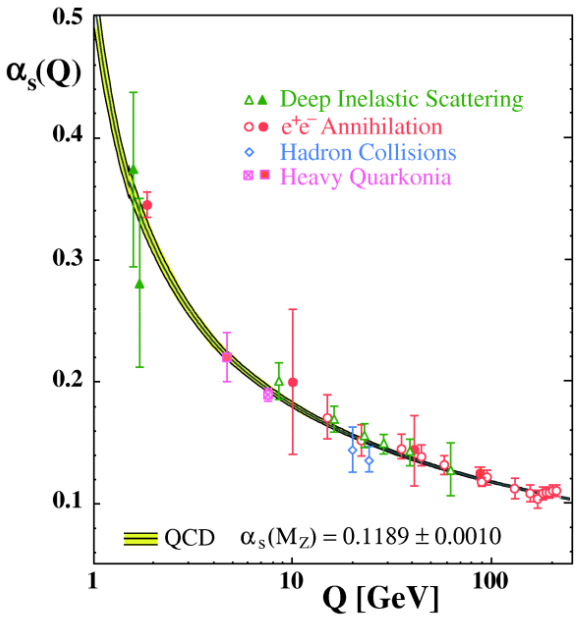

Figure 1.4: A summary of the measurements of the dependence of the running coupling $\alpha_s(Q)$ on the energy scale Q. The coupling is large at small Q (large distances) and goes to zero at large Q (small distances). Figure adapted from [28].

this flux tube as a stretchy rubber band that exerts a pulling force, attempting to bring the quarks back together. This force counteracts the separation force that's acting on the quarks. See Figure 1.5 for an illustration.

Consequently, quarks are permanently confined within color-neutral composite particles like mesons or baryons. When we attempt to isolate a single quark from a larger particle (hadron), the energy required to stretch the flux tube increases significantly. At a certain threshold, this energy becomes high enough to trigger the creation of new quark-antiquark pairs, effectively preventing the isolation of individual quarks. We can also see that from the form of the Equation 1.11 - it is divergent in the limit of small momentum transfers (large distances), i.e., it becomes energetically more favorable to create a new quark-antiquark pair than to isolate a quark from a hadron.

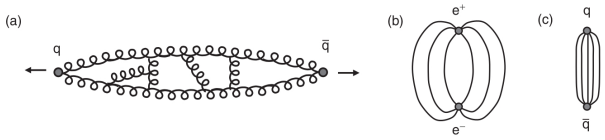

Figure 1.5: Left-hand side illustrates gluon-gluon interactions among gluons exchanged by two quarks. The right-hand side shows how the field lines between charges behave in the case of QED (b) and QCD (c). Figure adapted from [29].

The spectra of quarkonium states (a bound state of a heavy quark and its own antiquark [33]) can be modeled within non-relativistic models, where the potential has the following form (Cornell potential) [34, 35]:

$$V(r) = \sigma r - \frac{\alpha}{r}, \tag{1.12}$$

where σ represents the string tension, r is the distance between the quark and the antiquark, while α is the Coulomb-like constant.

Figure 1.6 shows a temperature dependence of the quark potential for a 3-flavor QCD. This plot shows that the obtained data agrees well with the Cornell potential in the low-temperature regime ($T < 0.5T_c$, where T_c is the QCD critical temperature). At higher temperature values, the deviation from the Cornell potential is more pronounced, thus suggesting the possibility of a different phase of (deconfined) matter.

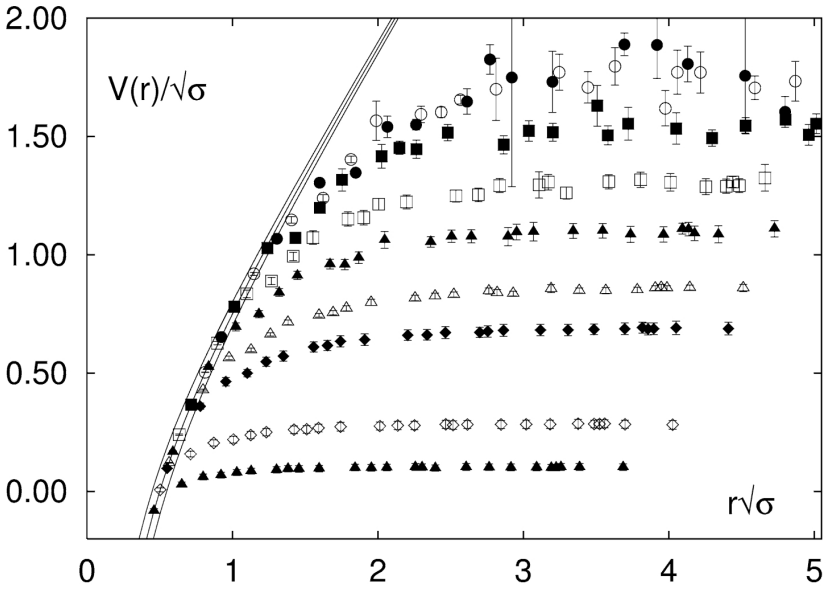

Figure 1.6: The heavy quark potential as a function of temperature. The band shows the Cornell potential in units of the square root of string tension, with $\alpha = 0.25 \pm 0.05$. The temperature varies from $T/T_c = 0.58$ (top) to $T/T_c = 1.15$ (bottom). Figure adapted from [35].

1.2 Heavy-ion collisions

In a typical heavy-ion experiment at the Large Hadron Collider or at the Relativistic Heavy Ion Collider, nuclei are accelerated to nearly the speed of light using powerful electromagnetic fields. These nuclei are stripped of their electrons, and Lorentz-contracted along the beam direction in the center-of-mass frame, resembling two thin discs. After a collision of two such nuclei, they pass through each other, depositing kinetic energy in a tiny volume and causing temperatures of the order $T \approx 300\,\mathrm{MeV}$ [7], (equal to $3 \cdot 10^{12}\,\mathrm{K}$). For the sake of comparison, we should note that this temperature is five orders of magnitude hotter than the center of the Sun (which is about $1.6 \cdot 10^7\,\mathrm{K}$ [36]). The produced hot and dense nuclear matter evolves through several stages, each characterized by different physical properties and exhibiting different phenomena. These stages are collectively called the "evolution of QCD matter" because they are governed by the strong nuclear force described by quantum chromodynamics (QCD). As we will see, the length and properties of specific stages can vary depending on factors such as the collision energy, the size of the system, and the type of colliding nuclei.

Figure 1.7 shows a space-time diagram of the main stages that QCD matter created in heavy-ion collisions goes through. These stages are:

- Initial state: The collision starts with the two colliding nuclei approaching each other at ultra-relativistic energies. Before the nuclear overlap and particle production, the

colliding nuclei are characterized by their nucleon distributions, typically described using models such as the Glauber model [37], which we will describe in more detail later.

- Pre-equilibrium: Immediately after the collision (i.e., at $\tau < \tau_0$, where τ_0 is the time of onset of the hydrodynamical description), the highly energetic and dense system of nucleons is in the pre-equilibrium phase. The dynamics before the initial time τ_0 are not yet properly understood, and the study of this stage is one of the aims of this doctoral dissertation.

- Quark-gluon plasma: Quarks and gluons are in a deconfined, albeit strongly interacting state. The QGP created in the collision expands collectively in a nearly perfect fluid-like manner [8]. This hydrodynamic expansion is driven by pressure gradients and is described well by the equations of relativistic viscous hydrodynamics. An overview of this approach will be given in more detail later.

- Hadronization: As the quark-gluon plasma expands and cools, it eventually reaches a point where the energy density is low enough for quarks and gluons to recombine and form color-neutral hadrons (e.g., mesons and baryons). This process is known as *hadronization*. It marks the end of the QGP phase. As the hadrons interact with each other through various scattering processes, their abundances can change. However, particle interactions become less frequent as the system cools and expands further. Eventually, the interactions become so sparse that the particle abundances are fixed. This stage is referred to as **the chemical freeze-out**.

  At chemical freeze-out, the relative abundances of different particle species are determined, and the particle ratios are no longer changing. The chemical freeze-out temperature and chemical potentials are crucial parameters that determine the hadron composition and relative particle yields at this stage.

- Kinetic freeze-out: After chemical freeze-out, where the particle ratios are fixed, and the particle species are no longer changing through inelastic interactions, the system continues to expand and cool. As the system cools down further, the particle interactions become less frequent, and the mean free paths between particle collisions become larger.

  At **kinetic freeze-out**, the particle scattering cross sections become small enough that the particles essentially stop interacting, allowing them to move freely without further rescattering. This stage marks the end of the particle interactions and the time when the particle momenta are frozen.

  Kinetic freeze-out is essential for understanding the final-state distributions of particles measured in heavy-ion collision experiments. The particle momentum distributions at kinetic freeze-out carry valuable information about the system's properties during the earlier stages, such as the temperature, collective flow, and other transport properties [37].

- Detection and Measurement: The final stage of the evolution is detecting and measuring the produced particles in particle detectors. Experimental observables, such as particle yields, momentum distributions, and correlations, provide crucial information about the properties of the evolving QCD matter.

1.2.1 Important concepts and physical quantities: an overview

The following section gives an overview of the most important theoretical concepts and observables related to the study of heavy-ion collisions. Familiarity with these is necessary to

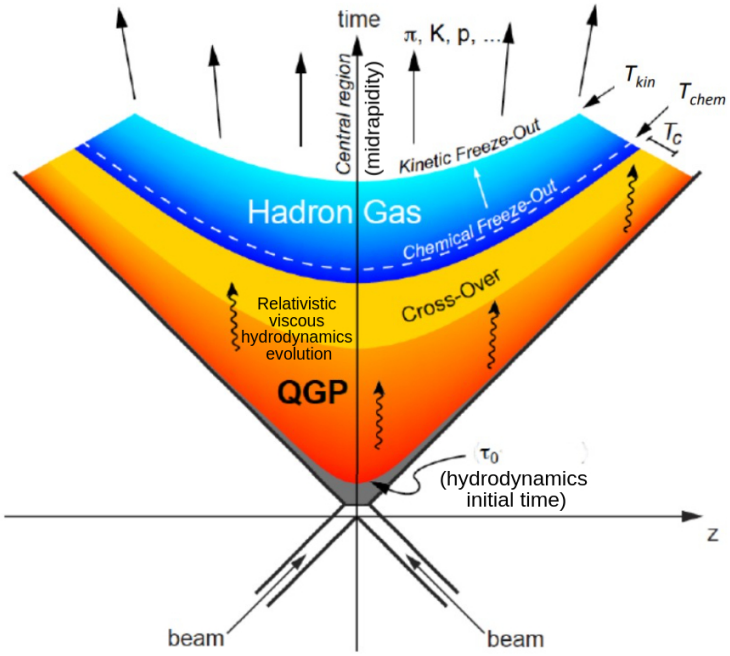

Figure 1.7: Space-time diagram of the different stages of evolution of QCD matter created in heavy-ion collisions. The beam axis is denoted by z, and t is time. The Lorentz-invariant proper time ($\tau = \sqrt{t^2 - z^2}$) is constant along the hyperbolic curves that separate different stages. Figure adapted from [38].

understand the results presented in this thesis. We will also show examples of related experimental data.

Participants and spectators. When considering two colliding nuclei, one assumes that nucleons travel along parallel trajectories, and one can separate *participants* from *spectators* [37]. Nucleons that do not encounter other nucleons on their paths are called *spectators*, and those that interact with each other are called *participants*. The participants that suffered at least one inelastic collision are called *wounded nucleons*. These two terms are often used interchangeably since, at very high energies, inelastic processes dominate the collisions [39].

Impact vector and the reaction plane. An important concept is the *impact vector* $\vec{\mathbf{b}}$ [37] - the vector that connects the centers of the colliding nuclei in the plane perpendicular to the trajectory of the nuclei. Its length is called *the impact parameter*. It is not measurable, but it influences the geometry and future evolution of the system. [39] It is common to introduce a coordinate system whose z-axis is along the beam trajectory, and the x-axis is along the direction of the impact vector. The plane spanned by this coordinate system's x and z axes is called *the reaction plane*. Figure 1.8 illustrates this.

Rapidity y is used as a measure of relativistic velocity, and it is defined in the following way [37]:

$$y = \frac{1}{2} \ln \frac{E + p_\parallel}{E - p_\parallel}. \tag{1.13}$$

Here, $E = \sqrt{\vec{\mathbf{p}}^2 + m^2}$ is the energy of the particle with mass m and 3-momentum $\vec{\mathbf{p}}$, while $p_\parallel$ is the magnitude of its longitudinal momentum. Rapidity is additive with respect to Lorentz boosts along the z-axis, which is its main advantage when compared with standard velocity.

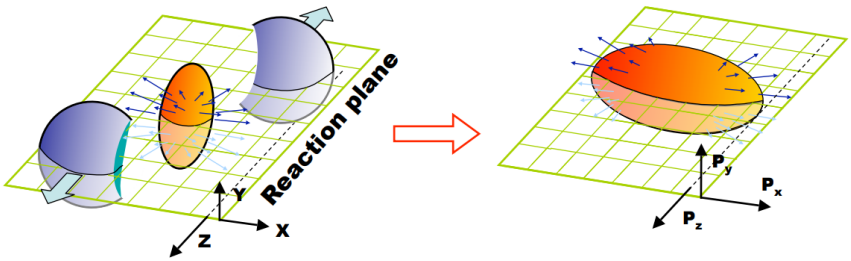

Figure 1.8: Illustration of QGP created in a heavy ion collision. The usual setup of the coordinate system is shown: the z-axis is along the beam trajectory, and the x-axis is along the direction of the impact vector. The plane spanned by this coordinate system's x and z axes is called *the reaction plane*. The initial spatial anisotropy (ϵ) is converted to the momentum anisotropy (v_2). Figure adapted from [40].

One similarly defines pseudorapidity [37]:

$$\eta = \frac{1}{2} \ln \frac{|\vec{\mathbf{p}}| + p_{\parallel}}{|\vec{\mathbf{p}}| - p_{\parallel}} = -\ln\left(\tan\left(\frac{\theta}{2}\right)\right). \tag{1.14}$$

Here, θ is the angle between the particle 3-momentum ($\vec{\mathbf{p}}$) and the positive direction of the z-axis.

In the massless limit, pseudorapidity and rapidity become the same, while in the case of finite mass, their relations are more complicated. The $y = 0$ region is called *the mid-rapidity region* and is particularly interesting. The particles in this region are either new particles created during the collision or already present in the beams but underwent several rescatterings, significantly altering their initial completely longitudinal momenta [37].

The relation between pseudorapidity and rapidity distributions in the midrapidity region is straightforward – they are related through the particle transverse velocity:

$$\left.\frac{dN}{d\eta d^2p_{\perp}}\right|_{\eta=0} = \frac{p_{\perp}}{m_{\perp}} \left.\frac{dN}{dyd^2p_{\perp}}\right|_{y=0}. \tag{1.15}$$

Here, $m_{\perp}$ is called the particle's *transverse mass*, and it is given by $m_{\perp} = \sqrt{m^2 + \mathbf{p}_{\perp}^2}$, where $\mathbf{p}_{\perp}$ is the transverse component of the particle's momentum.

Particle multiplicity [41] – an essential quantity that characterizes the collision event – refers to the number of particles produced in a specific collision. When two nuclei collide at high energies, many new particles are created due to the collision. These particles can be various types of hadrons (such as pions, kaons, protons, and others) and other particles like photons, electrons, and muons [37]. Naturally, the number and types of particles produced depend on factors such as the collision energy, participant number, and the nature of the colliding nuclei.

As already explained, particle multiplicity is typically measured within a specific region, such as the midrapidity region, which is of particular interest. The multiplicity distribution refers to the statistical distribution of the number of particles produced in many similar collision events.

Figure 1.9 shows the experimentally measured charged multiplicities at midrapidity, $dN_{ch}/d\eta|_{\eta=0}/(\langle N_{part}\rangle/2)$ as a function of the participant number, $\langle N_{part}\rangle$ from [41]. The charged multiplicity is scaled by the number of participant pairs, $\langle N_{part}/2\rangle$. The results from ATLAS (A Toroidal LHC ApparatuS), CMS (Compact Muon Solenoid), ALICE (A Large Ion

Collider Experiment) collaborations are compared with the RHIC data. A moderate increase of $dN_{ch}/d\eta|_{\eta=0}/(\langle N_{part}\rangle/2)$ is observed, from about 4.6 (in the peripheral collisions, equivalent to a smaller number of participants) to 8.8 (in the central collisions, equivalent to a larger number of participants).

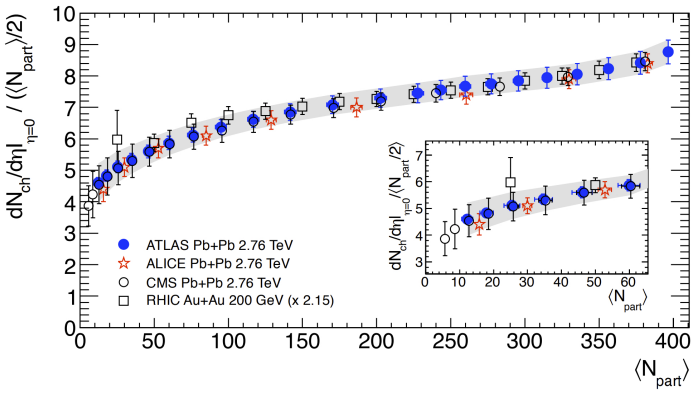

Figure 1.9: Experimentally measured charged particles multiplicities at midrapidity scaled with the number of participant pairs as a function of $\langle N_{part}\rangle$. The results from LHC are for the Pb+Pb collision system at $\sqrt{s_{\mathrm{NN}}} = 2.76\,\mathrm{TeV}$ (ATLAS – blue circles, ALICE – red stars, CMS – open circles), while the RHIC results (multiplied with 2.15 to facilitate comparison) are for Au+Au at $\sqrt{s_{\mathrm{NN}}} = 200\,\mathrm{GeV}$ (open squares). Figure adapted from [41].

Boost invariance was initially introduced in a seminal paper by Richard Feynman [42]. In the context of heavy-ion collisions, it pertains to a significant concept that governs the behavior of specific quantities in the collisions when observed from different reference frames related through Lorentz boosts. This concept becomes relevant in scenarios where particular quantities associated with a particle collision remain unchanged under Lorentz boosts along the beam axis. For instance, the thermodynamic properties like temperature, pressure, and energy density employed in the hydrodynamic description of heavy-ion collisions are considered Lorentz scalars [37]. Consequently, they solely depend on transverse coordinates and the proper time $\tau = \sqrt{t^2 - z^2}$. It is generally considered that boost invariance is a good approximation for the central region in very high-energy heavy-ion collisions.

The principle of boost invariance is notably evident in the (pseudo)rapidity distribution of generated particles. This phenomenon leads to a plateau-like configuration within the pseudorapidity distribution around the midrapidity region (around $\eta = 0$). Figure 1.10 shows the results from the ALICE collaboration [43] of the charged-particle pseudorapidity density ($dN_{ch}/d\eta$) as a function of pseudorapidity for different centrality classes in Pb+Pb collisions at $\sqrt{s_{NN}} = 5.02$ TeV. The plot shows a characteristic plateau-like structure around $\eta = 0$, a consequence of the boost invariance.

Transverse energy (often denoted as E_T) is an important observable used to characterize the energy the produced particles carry in the transverse direction to the beam axis. It can be calculated in several ways, but the definition used in practice is [44]:

$$E_T = \sum_{j=1}^{M} E_j \sin(\theta_j), \tag{1.16}$$

where E_j is the energy measured by the j-th tower of the calorimeter, while θ_j is its polar angle. The sum runs over all the towers of the calorimeter. E_T can also be defined so that the

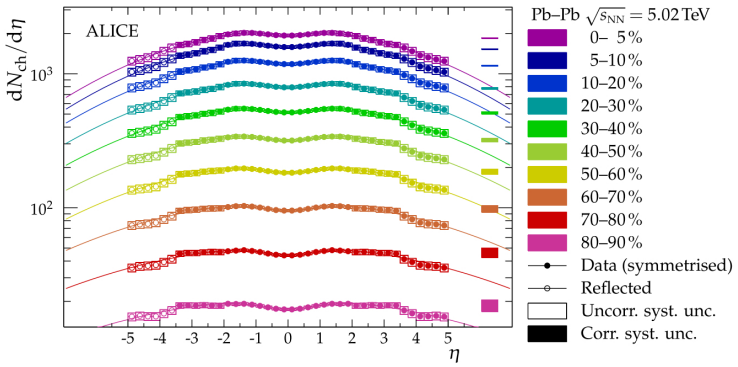

Figure 1.10: Charged-particle pseudorapidity density $dN_{ch}/d\eta$ as a function of pseudorapidity measured by the ALICE collaboration for different centrality classes in Pb+Pb collisions at $\sqrt{s_{\mathrm{NN}}} = 5.02$ TeV. Figure adapted from [43].

sum goes over single-particle paths, but in order to match the calorimeter-related definition, E_js have to be replaced by single-particle energies [44].

Figure 1.11 shows the summary of some experimental measurements of $\langle E_T/d\eta\rangle/\langle dN_{ch}/d\eta\rangle$, which is a measure of the average transverse energy per particle, as a function of the participant number $\langle N_{part}\rangle$. We observe that $\langle E_T/d\eta\rangle/\langle dN_{ch}/d\eta\rangle$ increases about 1.25 times when going from $\sqrt{s_{\mathrm{NN}}} = 200$ GeV to $\sqrt{s_{\mathrm{NN}}} = 2.76$ TeV.

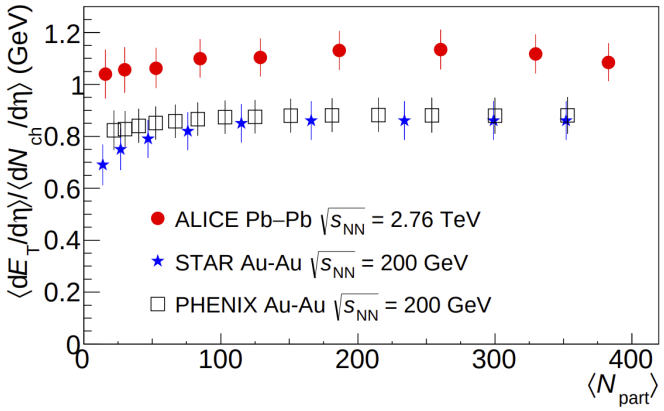

Figure 1.11: $\langle E_T/d\eta\rangle/\langle dN_{ch}/d\eta\rangle$ versus $\langle N_{part}\rangle$ for two collision systems at different center-of-mass energies. It shows the results from ALICE (red circles) for Pb+Pb at $\sqrt{s_{NN}} = 2.76$ TeV [44], STAR [45] (blue stars) and PHENIX [46, 47] (open squares) for Au+Au at $\sqrt{s_{NN}} = 200$ GeV. Figure adapted from [44].

Centrality [37] refers to a measure of how head-on or central the collision is between the two colliding nuclei – it is an essential concept as it helps categorize different types of collisions based on the degree of overlap and interaction between the colliding nuclei.

During a heavy-ion collision, the nuclei pass through each other, and the extent of overlap or interaction between them varies depending on the impact parameter defined above. Intuitively, a collision with a small impact parameter indicates a more central collision with a higher degree of overlap. In contrast, a large impact parameter indicates a peripheral collision with less overlap.

Centrality is usually defined as a percentage of the total nuclear cross section [48], and the collisions are divided into centrality classes or bins. These classes represent different impact

parameter ranges, with the most central collisions falling into the lowest centrality bins (e.g., 0-5% centrality) and the most peripheral collisions assigned to the highest centrality bins (e.g., 90-100% centrality). The centrality percentile c of a A+A collision can be expressed as [49]:

$$c = \frac{\int_0^b \frac{d\sigma}{db'} db'}{\int_0^\infty \frac{d\sigma}{db'} db'} = \frac{1}{\sigma_{AA}} \int_0^b \frac{d\sigma}{db'} db', \tag{1.17}$$

where σ_{AA} is the total inelastic nucleus-nucleus cross section, b is the impact parameter and $d\sigma/db'$ is the impact parameter distribution.

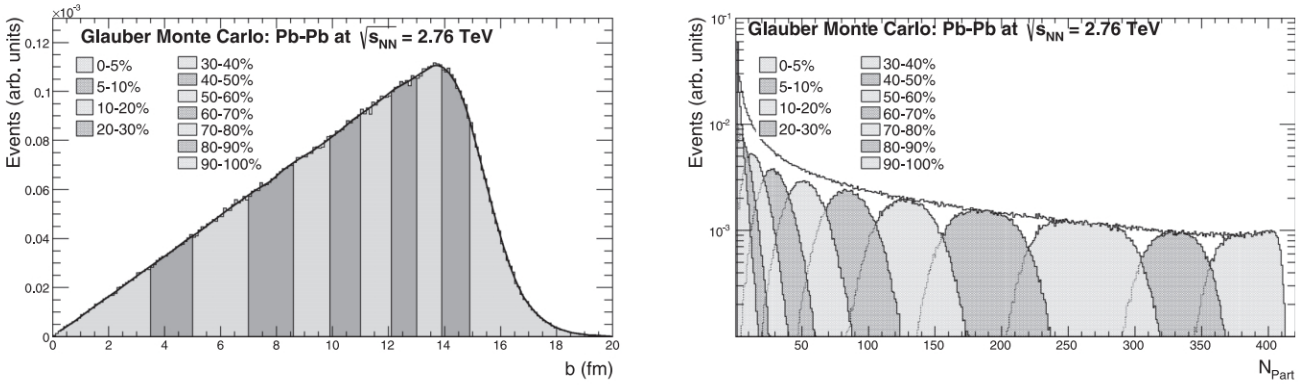

Figure 1.12: An illustration of classifying events into different centrality classes. The figures represent results obtained within the Monte Carlo Glauber model for Pb+Pb collisions at $\sqrt{s_{NN}}$ = 2.76TeV. The plot on the left shows the impact parameter distribution of events – the larger the impact parameter b, the higher the centrality class. The plot on the right shows the number of participants distribution – the larger the number of participants, the lower the centrality class. Different centrality classes are marked on the plots. Figure adapted from [49].

Figure 1.12 shows an example of how Pb+Pb at $\sqrt{s_{\mathrm{NN}}}$ = 2.76 TeV collision events are generated theoretically within the Monte Carlo Glauber model [49] (described in more detail in Section 1.3) are sorted into centrality classes.

Nuclear modification factor. The observable which is commonly used to quantitatively describe the energy loss of high-$p_\perp$ particles is the nuclear modification factor R_{AA}. If we consider a case with no medium effects, the yields of high-$p_\perp$ particles would grow with the number of partonic interactions, which is proportional to the number of nucleon-nucleon collisions. If we look at single-inclusive hadronic spectra at midrapidity, we could write [50]:

$$\frac{\mathrm{d}N^{AA\to h}}{\mathrm{d}^2p_\perp \mathrm{d}y} = \langle N_{coll}^{AA} \rangle \frac{\mathrm{d}N^{pp\to h}}{\mathrm{d}^2p_\perp \mathrm{d}y}. \tag{1.18}$$

Here, $\langle N_{coll}^{AA} \rangle$ is the average number of nucleon-nucleon collisions. The nucleon-nucleon spectrum is obtained experimentally in p+p collisions. To characterize deviations from this scenario, we introduce the nuclear modification factor. In other words, to obtain information on the thermodynamic and transport properties of the QCD medium produced in nucleus-nucleus (A+A) collisions, we need to compare the results for a given observable with the results in proton-proton collisions ("QCD vacuum") [51]. Schematically:

$$R_{AA} = \frac{Yield(\mathrm{A+A})}{Yield(\mathrm{p+p})} = \frac{"hot/dense\ QCD\ medium"}{"QCD\ vacuum"}. \tag{1.19}$$

More concretely, we can define the nuclear modification factor in the following way [37]:

$$R_{AA}(p_T, \phi) = \frac{1}{N_{coll}} \frac{\frac{\mathrm{d}N_{AA}}{\mathrm{d}p_\perp \mathrm{d}\phi}}{\frac{\mathrm{d}N_{pp}}{\mathrm{d}p_\perp \mathrm{d}\phi}}, \tag{1.20}$$

where $\mathrm{d}N_{AA}/\mathrm{d}p_\perp \mathrm{d}\phi$ is the spectrum of a particular kind of particles in $A + A$ collisions, $\mathrm{d}N_{pp}/\mathrm{d}p_\perp \mathrm{d}\phi$ is the spectrum in $p + p$ collisions, ϕ is the angle in transversal (orthogonal to the beam direction) plane, and N_{coll} is the number of binary collisions. The angular-averaged version is given as:

$$R_{AA}(p_\perp) = \frac{1}{2\pi} \int_0^{2\pi} R_{AA}(p_\perp, \phi)\mathrm{d}\phi. \tag{1.21}$$

Intuitively, if a collision between two nuclei were a simple superposition of $p+p$ collisions, the value of R_{AA} would be 1. It is between 0 and 1 if the medium suppresses the production of hard particles. Therefore, R_{AA} reflects the suppression of high-$p_\perp$ particles due to the energy loss in the medium formed in heavy-ion collisions (i.e., larger suppression corresponds to the smaller value of R_{AA}). See Figure 1.13 for an illustration of hot versus cold nuclear matter effects, which compares A+A collisions with p+A collisions. The creation of quark-gluon plasma in p+A collisions is still an open question [52, 53].

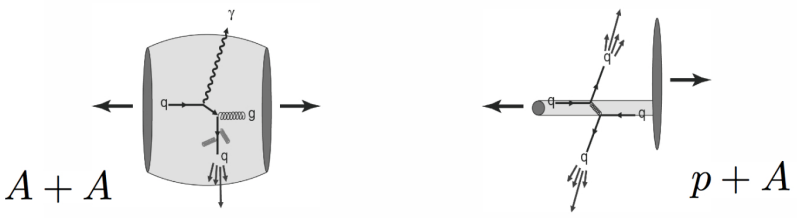

Figure 1.13: Hot versus cold nuclear matter effects: an illustration of a nucleus-nucleus (A+A) collision versus a proton-nucleus (p+A) collision. The gray-shaded area on the illustration on the left shows the QGP medium formed in the collision. The hard partons are suppressed as they traverse the medium. Whether QGP is created in p+A collisions is still an open question (see e.g. [52]). Figure adapted from [53].

Collective flow. Important information about the quark-gluon plasma can be obtained if we consider the differences in particle production in different directions. Namely, the momentum distribution of the particles produced in a nucleus-nucleus collision can be represented in the following way [54, 55]:

$$\frac{\mathrm{d}N}{\mathrm{d}y\mathrm{d}^2p_\perp} = \frac{\mathrm{d}N}{2\pi \mathrm{d}y p_\perp \mathrm{d}p_\perp} \left[1 + \sum_n 2v_n \cos(n(\phi - \psi_{RP}))\right]. \tag{1.22}$$

Here, ψ_{RP} is the angle that defines the reaction plane. The reflection symmetry with respect to the reaction plane causes the sine terms from this expansion to vanish [56]. The coefficients in this expansion are, in general, dependent on transverse momentum and rapidity and are given by:

$$v_n(p_\perp, y) = \langle \cos[n(\phi - \psi_{RP}]\rangle. \tag{1.23}$$

The average runs over the particles, summed over all the events, for a particular $(p_\perp, y)$ bin. For individual events, all v_n are non-vanishing. [39] In particular, v_1 is called *the directed flow*, v_2 is *the elliptic flow* and v_3 is *the triangular flow*. Using the word 'flow' for these coefficients reflects that they quantify the phenomena that arise due to the collective motion of particles, the hydrodynamics-like expansion of matter created in heavy-ion collisions.

An approximate way to calculate v_2 of high-$p_\perp$ particles is given by [57]:

$$v_2 \approx \frac{1}{2}\frac{R^{in}_{\mathrm{AA}} - R^{out}_{\mathrm{AA}}}{R^{in}_{\mathrm{AA}} + R^{out}_{\mathrm{AA}}}. \tag{1.24}$$

Here, R^{in}_{AA} is related to the suppression of particles in the in-plane ($\phi = 0$) direction, and R^{out}_{AA} is related to the particles in the out-of-plane ($\phi = \pi/2$) direction. See Figure 1.8 for an illustration: the x-axis corresponds to the in-plane direction, while the y-axis corresponds to the out-of-plane direction. Intuitively said, the v_2 coefficient of high-$p_\perp$ particles reflects the spatial anisotropy of the medium: particles traversing the medium in the in-plane and out-of-plane directions traverse different path lengths and consequently have different suppressions.

1.2.2 The QCD phase diagram

The phase diagram of QCD matter is often depicted with temperature (T) on the vertical axis and baryon chemical potential (μ_B) on the horizontal axis [58], see Figure 1.14. However, since the exact behavior of QCD matter at various values of (μ_B, T) is still an active area of research, the phase diagram is subject to ongoing refinement and exploration. Different regions of the phase diagram represent distinct phases or crossovers between them.

Hadronic phase: Nuclear matter exists in the hadronic phase at low temperatures and densities. In this phase, quarks and gluons are confined within composite particles – hadrons, such as protons and neutrons.

Quark-gluon plasma (QGP) phase: As the temperature and density increase, the phase diagram predicts a transition to the quark-gluon plasma phase. In this phase, the energy density is high enough so that quarks and gluons are deconfined, resulting in a plasma of almost free quarks and gluons. The QGP phase is believed to have existed shortly after the Big Bang and can be created artificially in high-energy heavy-ion collision experiments. Figure 1.14 shows different areas of the phase diagram accessible by different experimental facilities.

Crossover region: At low baryon chemical potentials, the transition from the hadronic phase to the QGP phase is expected to be smooth. There is no clear boundary between the two phases in this region, and the system's properties change gradually. Lattice gauge theories generally predict that the cross-over occurs at $T_c(\mu_B = 0) = 154 \pm 9\,\mathrm{MeV}$ and $\epsilon_c = 0.18 - 0.5\,\mathrm{GeV/fm^3}$ [59].

First-order phase transition: The transition may become a first-order phase transition at higher baryon chemical potentials, such as those encountered in the core of neutron stars. In this case, a distinct boundary exists between the hadronic and the QGP phases, with a jump in thermodynamic quantities like energy density or pressure at the transition point.

Exotic phases: The phase diagram also suggests the existence of other exotic phases under extreme conditions, such as the color superconductor phase [60]: at extremely high densities, quark matter may undergo a color superconducting phase transition. In this phase, matter exists as a degenerate Fermi gas of quarks where Cooper pairs are formed.

1.2.3 Experimental observations and empirical evidence for the existence of quark-gluon plasma

Experimental measurements relevant to the study of QCD matter at extreme conditions are conducted in particle accelerators, which are sophisticated and complex research facilities. The two most relevant accelerators for studying the physics of quark-gluon plasma are RHIC and LHC.

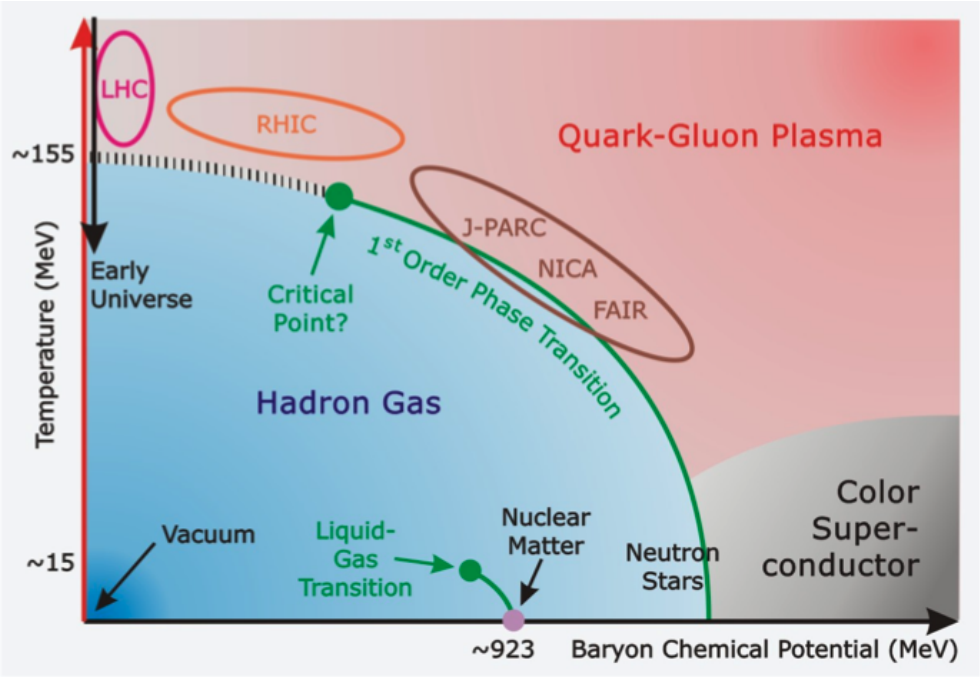

Figure 1.14: A sketch of the phase diagram of QCD matter. Values of (μ_B, T) accessible by different experiments are also shown on the plot. Figure adapted from GSI [61].

The Relativistic Heavy Ion Collider (RHIC) is a particle accelerator facility located at Brookhaven National Laboratory in Upton, New York, USA. It is one of the world's most powerful and versatile heavy-ion colliders designed to study nuclear matter under extreme conditions. It is a crucial facility for exploring the quark-gluon plasma. It is a circular accelerator that spans approximately 3.8 kilometers in circumference [34]. It can accelerate various types of ions, including gold (Au), copper (Cu), and others, as well as protons. The primary purpose of RHIC is to collide heavy ions at extremely high energies, up to 200 GeV per nucleon pair. RHIC has had several large and sophisticated experimental detectors, including the STAR (Solenoidal Tracker at RHIC) and PHENIX (Pioneering High Energy Nuclear Interaction eXperiment), BRAHMS (Broad Range Hadron Magnetic Spectrometers) and PHOBOS (PHOton and heavy IOn Spectrometer).

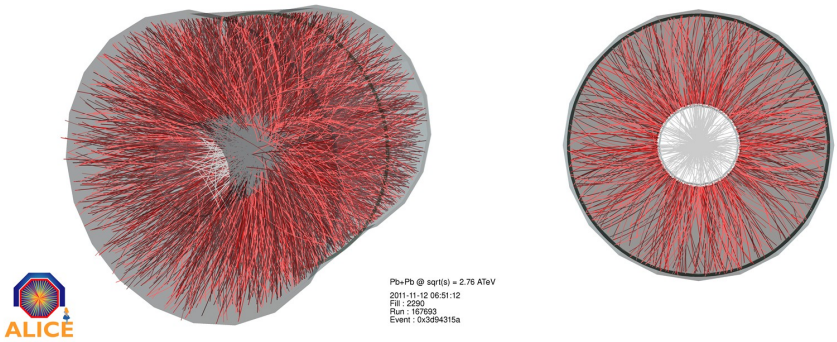

Figure 1.15: A depiction of a Pb+Pb collision at the ALICE experiment [62], one of the three major experiments at CERN in Geneva, Switzerland.

The Large Hadron Collider (LHC) is currently the world's largest and most powerful particle accelerator. It is located at CERN (European Organization for Nuclear Research) near

Geneva, Switzerland. The LHC is a circular accelerator spanning a circumference of about 27 kilometers. The primary purpose of the LHC is to accelerate protons and heavy ions (e.g., lead) to nearly the speed of light and collide them at extremely high energies. The highest collision energies for lead-lead (Pb + Pb) and xenon-xenon (Xe + Xe) systems are 5.02 TeV and 5.44 TeV, respectively. The LHC has four primary particle detectors - ATLAS (A Toroidal LHC ApparatuS), CMS (Compact Muon Solenoid), ALICE (A Large Ion Collider Experiment), and LHCb (Large Hadron Collider beauty). These detectors capture the results of proton-proton and heavy-ion collisions, providing valuable data for analysis. Of these, ALICE [63] is dedicated solely to the study of heavy-ion collisions. A depiction of a heavy-on collision in the ALICE detector with particles flying out of the collision point towards the detectors is shown in Figure 1.15.

In this section, we will briefly overview the breakthrough results indicating that quark-gluon plasma is formed in a heavy-ion collision.

In the Au+Au collisions at $\sqrt{s_{NN}} = 130$GeV, it was reported by the PHENIX collaboration at RHIC [64] that the spectra from central collisions were significantly suppressed with respect to proton-proton spectra scaled with the number of binary collisions. This is deemed [53] the most important discovery of RHIC physics. In order to confirm that the observed effect is due to the creation of hot nuclear matter in Au+Au collisions and not an effect of cold nuclear matter, measurements in deuteron-gold (d+Au) collisions were performed at RHIC in 2003, and the obtained findings were so definitive that the results from all four RHIC experiments were featured on the cover of Physical Review Letters that year (the cover is shown on the left-hand side of the Figure 1.16).

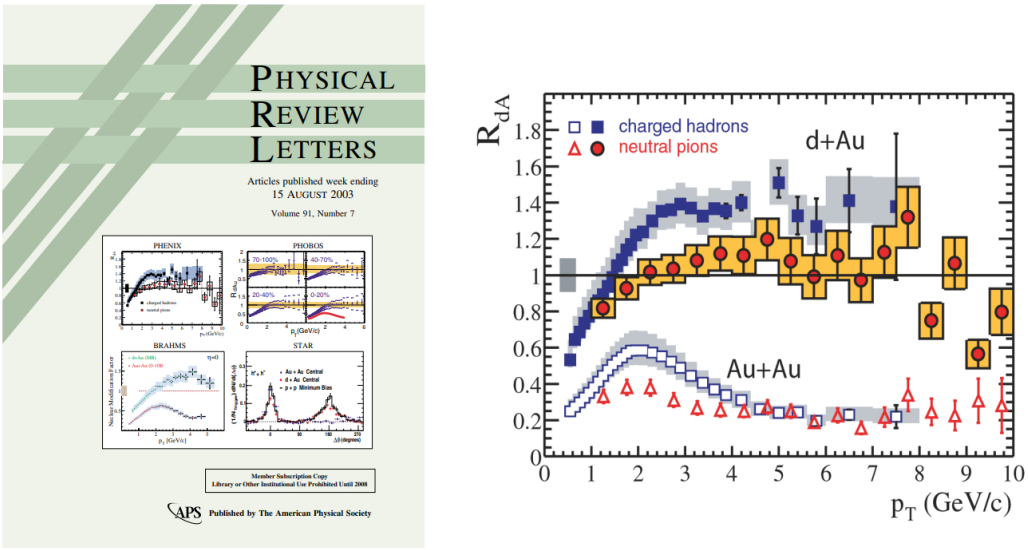

Figure 1.16: The image on the left shows the cover of Physical Review Letters (Volume 91, Number 7, August 2003), with all four RHIC experiments showing definitive signs of quark-gluon plasma creation. The plot on the right shows the R_{AA} of charged hadrons ($h^{\pm}$) and neutral pions (π^0) in the d+Au and Au+Au collisions systems at $\sqrt{s_{NN}} = 200$GeV from the PHENIX collaboration from that volume [65]. Figure adapted from [53].

The right-hand side of Figure 1.16 shows the nuclear modification factor R_{AA} as a function of transverse momentum $p_{\perp}$ for non-identified charged hadrons ($h^{\pm}$) and neutral π-mesons (π^0) in Au+Au and d+Au collisions at $\sqrt{s_{NN}} = 200$GeV [65]. We can draw several conclusions from this plot. Namely, the suppression of both $h^{\pm}$ and π^0 is observed in the Au+Au collision system but not in d+Au. This demonstrates that the suppression is due to the effects of a hot nuclear

medium formed in Au+Au collisions. Moreover, $h^{\pm}$ and π^0 show different suppression patterns in both collision systems – therefore, particle identification is important in these measurements, as different particle species behave differently.

Another important signal of the creation of quark-gluon plasma is the collective flow of particles created in the collision, quantified by the first several coefficients in the Fourier expansion of the azimuthal angle distribution (see Eq. 1.22). Figure 1.17 shows a summary of the anisotropy parameter (v_2) measurements for various hadron species (π, K, p, Λ) from STAR [66, 67, 68, 69] and PHENIX [70] experiments at RHIC. The non-zero value of v_2 in these experiments represents conclusive evidence of strong collective behavior of matter produced in Au+Au collisions.

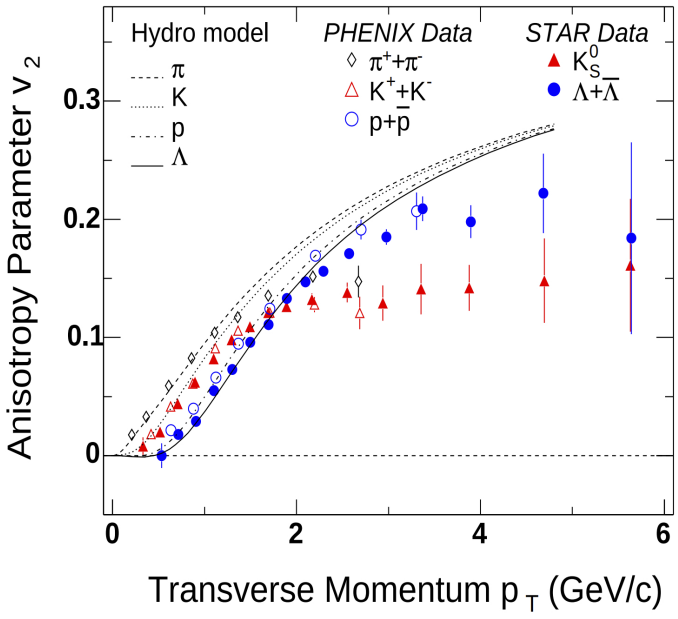

Figure 1.17: A summary of measurements of the anisotropy parameter (v_2) at RHIC. The plot shows STAR [66, 67, 68, 69] (solid symbols) and PHENIX [70] (open symbols) measurements for various hadron species (π, K, p, Λ) in Au+Au collisions at $\sqrt{s_{NN}} = 200$GeV. Figure adapted from [7].

1.3 The initial state

The initial state refers to the state of the colliding nuclei before they interact and form quark-gluon plasma (see Fig. 1.7). An abundance of theoretical models have been developed to describe the initial state in heavy-ion collisions – they aim to understand the distribution of relevant quantities, such as the energy density and temperature that set the stage for the subsequent evolution of the system. In this Section, we will give an overview of some of the different models of the initial state in heavy-ion collisions that have been utilized to produce the results presented in this thesis.

1.3.1 Glauber Model: the basics

We here give a short overview of the Glauber Model, since it is one of the initial-state models used to generate the results in this thesis. The Glauber model is a theoretical model which

is used to calculate the geometric quantities pertaining to the heavy-ion collision, such as the impact parameter (b) and the number of participants (N_{part}) [71]. The aim of employing Monte Carlo implementations of the Glauber model (Monte Carlo Glauber) is to *i)* stochastically calculate the positions of nucleons in each nucleus and then *ii)* simulate their collision process event-by-event by assuming nucleons travel in straight lines along the beam axis. The nucleons are marked as either participants or spectators and geometric properties are calculated by conducting numerous nucleus-nucleus collision simulations. These calculated properties are then used to determine the average values for different centrality classes, which classify the events in a manner that was explained earlier, in the Section 1.2. See Figure 1.12 for an example.

To begin with, in the Glauber model of nuclear collisions, the Woods-Saxon nuclear density distribution is commonly used to describe the spatial distribution of nucleons (protons and neutrons) within the colliding nuclei. [72]

The formula gives the modified Woods-Saxon nuclear density distribution:

$$\rho(r) = \rho_0 \frac{1 + w(\frac{r}{R})^2}{1 + \exp(\frac{r-R}{a})}. \tag{1.25}$$

The values of the parameters are given in [73]. Here, ρ_0 is the nuclear density in the center of the nucleus, R is the radius of the nucleus ($R = (6.62 \pm 0.06)$ fm for the ^{208}Pb nucleus [49], while for ^{136}Xe it is $R = (4.7964 \pm 0.0047)$ fm [74]), a is the parameter which dictates how fast does the nuclear density fall off near the edge of the nucleus ($a = (0.546 \pm 0.010)$ fm), and w is the parameter which describes the deviations from the spherical shape ($w = 0$ for the ^{208}Pb nucleus).

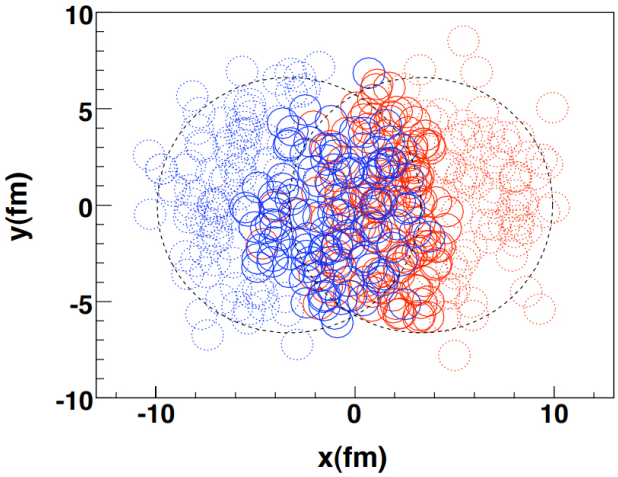

Figure 1.18: A typical Glauber Monte Carlo-generated event of a Pb+Pb collision at the LHC energy. Solid circles represent wounded nucleons, while dotted circles represent the spectators. Figure adapted from [75].

The other input required for the calculations within the Glauber Model is the nucleon-nucleon inelastic cross section (σ_{inel}^{NN}), which depends on the collision energy [75]. It is estimated to have the value of $\sigma_{NN}^{inel} = 42$ mb at the RHIC energy of $\sqrt{s_{NN}} = 200$GeV, while at the LHC, it is estimated to be around $\sigma_{NN}^{inel} = (64 \pm 5)$ mb at $\sqrt{s_{\mathrm{NN}}} = 2.76$ TeV [49].

After having assembled the nuclei according to the nuclear density distribution, Glauber Monte Carlo proceeds by drawing the value of the impact parameter from a distribution $dN/db \propto b$ [48]. In a nucleus-nucleus collision, it is commonly assumed that the collision can be broken down into a series of independent binary nucleon-nucleon interactions.

In the simplest variant of the Monte Carlo approach, a nucleon-nucleon collision is considered to occur when the distance (d) between the nucleons in the plane perpendicular to the beam axis satisfies [48]:

$$d \leq \sqrt{\frac{\sigma_{NN}^{inel}}{\pi}}, \tag{1.26}$$

with σ_{NN}^{inel} being the total inelastic nucleon-nucleon cross section.

Nucleons are not confined to specific spatial coordinates in the optical approximation (Optical Glauber Model) [48, 76]. Instead, this model suggests that at sufficiently high energies, nucleons possess enough momentum, leading to minimal deflection as nuclei pass through one another. This theory also assumes that nucleons move independently within the nucleus, and the nucleus's size greatly surpasses the range of the nucleon-nucleon force. By presuming independent linear trajectories for nucleons, it becomes possible to derive simple analytical expressions for the cross-section of nucleus-nucleus interactions. Moreover, these expressions aid in determining the count of interacting nucleons and nucleon-nucleon collisions. These calculations are established in relation to the fundamental nucleon-nucleon cross-section.

Figure 1.19 shows results produced within the Monte Carlo Glauber and Optical Glauber models. The plot on the left shows the total cross section for a $A + B$ collision (which is the integral of $d\sigma/db$ distributions) as a function of the nucleon-nucleon inelastic cross section σ_{NN}. As the nucleon-nucleon cross section becomes more point-like, the two results obtained from these approaches converge [48]. The plot on the right shows the results for simple geometric quantities: the number of participants N_{part} and the number of binary nucleon-nucleon collisions N_{coll} as functions of the impact parameter b. The two approaches give results that almost completely overlap.

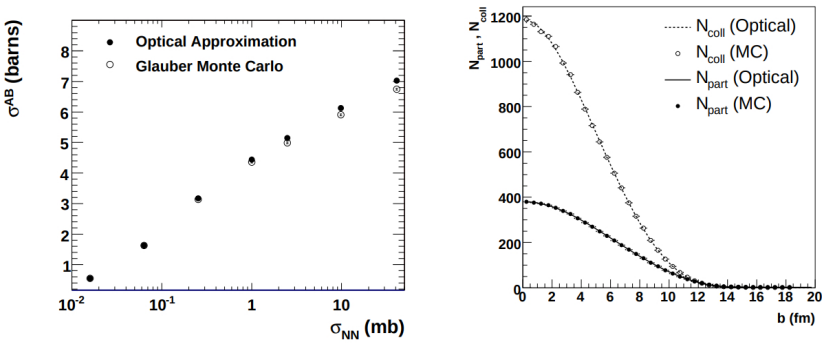

Figure 1.19: An example of results obtained within the Glauber Monte Carlo and the Optical Glauber models. The plot on the left shows the total cross-section as a function of the nucleon-nucleon inelastic cross-section. The plot on the right shows the number of participants and binary nucleon-nucleon collisions as a function of the impact parameter b, obtained within the optical approximation (lines) and Glauber Monte Carlo (symbols). Figure adapted from [48].

1.3.2 Color glass condensate

IP-Glasma [77, 78] (**i**mpact **p**arameter glasma) is a model based on *color glass condensate* [79]: a new form of hadronic matter, hypothesized to exist at very high energies. The development of this model was motivated by the experimental results from HERA.

Earlier in this Chapter, in Section 1.1, deep inelastic scattering experiments were described. In these experiments, an electron emits a virtual photon which then scatters off a quark in a hadron. We can introduce the Bjorken x variable in a frame-independent way:

$$x = \frac{Q^2}{2p \cdot Q}. \tag{1.27}$$

Here, p is the momentum of the hadronic target, and Q is the virtual photon momentum transferred to the hadron in the rest frame [79].

HERA (*Hadron Elektron Ring Anlage*, or *Hadron Electron Ring Accelerator*) was a particle accelerator located at the DESY laboratory in Germany, which collided electrons or positrons with protons to study the structure of protons: one of the key contributions of HERA was to provide precise measurements of parton distribution functions (PDFs). In this context, quarks and gluons are collectively reffered to as partons. Namely, at very small values of Bjorken-x, the measurements at HERA indicated that the gluon density in the proton becomes very high [80, 81]. This is relevant because, at high energies and densities, the gluon density in a hadron can become so large that saturation effects become important. Moreover, HERA data indicated that at small Bjorken-x, the gluon distribution function increases much more rapidly than expected. This was seen as evidence of high parton densities and the possibility of a saturated gluon state. See the left plot of Figure 1.20 for the gluon distribution function measured by the ZEUS collaboration at HERA.

Thus, these findings led to the idea of *color glass condensate*. The term *color* in its name originates from the fact that gluons possess color charge. The term *glass* is used because the associated fields exhibit gradual changes over natural time scales, analogous to glass which appears solid on short time scales despite being liquid or disordered on longer time scales. The term *condensate* is applied due to the dense accumulation of massless gluons. This density saturates at $1/\alpha_s >> 1$, akin to a Bose-Einstein condensate.

As we can see on Figure 1.20, the gluon density $xG(x, Q^2)$ rises with decreasing x (or increasing resolution Q^2). Note that at a fixed Q^2, decreasing x corresponds to the higher interaction energy. In other words, the density of gluons per unit area per unit rapidity of a hadron increases as x decreases. [8] These low-x gluons are densely packed in the transverse directons, however – the interaction strength must be weak, $\alpha_s \ll 1$. This dense but weakly coupled system is called a *color glass condensate*. Moreover, on the central and right plots in Figure 1.20, we see that MSTW2008 next-to-leading order results for parton distribution functions [81] corroborate that gluons dominate the dynamics in the small-x region.

The IP-Glasma initial state model [77, 78] is based on color glass condensate [82, 83, 84, 85]. It calculates the initial state as a collision of two color glass condensates and evolves the generated fluctuating gluon fields by solving classical Yang-Mills equations [77, 78].

As for the other models used in this thesis, the Eskola-Kajantie-Ruuskanen-Tuominen (EKRT) model [86, 87, 88] is based on the NLO perturbative QCD computation of the transverse energy and a gluon saturation conjecture. The Reduced Thickness Event-by-event Nuclear Topology model (T$_\mathrm{R}$ENTo) [89] is a phenomenological model capable of interpolating between wounded nucleon and binary collision scaling, and with a proper parameter value, of mimick-

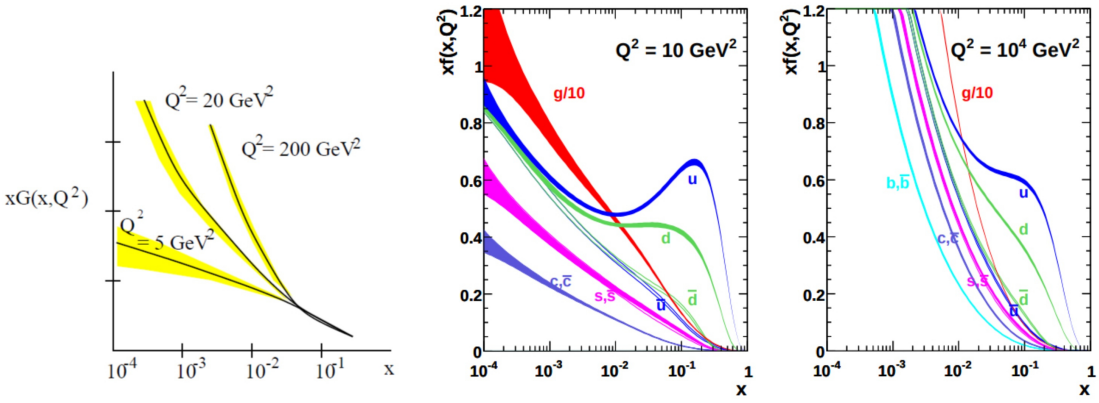

Figure 1.20: The Figure on the left shows the ZEUS gluon distribution functions. The figures in the center and on the right show MSTW2008 next-to-leading order (NLO) parton distribution functions (PDFs) at scale $Q^2 = 10$ GeV and $Q^2 = 10^4$GeV for the LHC. Figure adapted from [79, 80, 81].

ing the EKRT and IP-Glasma initial states. The Monte Carlo Kharzeev-Levin-Nardi model (MC-KLN) is an initial state model based on the color glass condensate [90].

1.4 Hydrodynamical description of a heavy-ion collision

At first, due to the effects such as asymptotic freedom and color screening, quark-gluon plasma created in heavy-ion collisions at ultrarelativistic energies was expected to behave as a weakly interacting gas [91]. However, the early success of calculations based on relativistic hydrodynamics in explaining the experimental data has motivated its extensive application to describe this medium, and it has become the standard approach in the field. This section briefly overviews the hydrodynamical description of QGP formed in ultrarelativistic heavy ion collisions.

Within the hydrodynamical description, in a heavy-ion collision [37, 92], a large kinetic energy of colliding nuclei causes the creation of a large number of particles in a small volume. These particles then collide with each other very often to reach a state of local thermal equilibrium. After reaching thermal equilibrium, various quantities can be attributed to the system, such as the field of temperature $T(x)$, chemical potentials $\mu_i(x)$, and flow velocity $u^\mu(x)$. The subsequent evolution of the system can be described by applying hydrodynamical equations of motion until the particles become so dilute that local thermal equilibrium is no longer a viable assumption, and they continue to move as free particles.

A hydrodynamic description of the system offers numerous advantages [92]:

1. We can characterize the system using various thermodynamic variables.
2. Utilizing familiar quantities such as temperature and pressure, we can develop an intuitive understanding of the evolving QCD medium created in heavy-ion collisions.
3. The models are relatively straightforward.
4. With knowledge of the initial state and the equation of state of nuclear matter, we can determine system dynamics without delving into microscopic interactions.

1.4.1 The Bjorken model

A straightforward hydrodynamical model without transverse expansion is the Bjorken model [93, 94]. This model is based on the assumption that the rapidity distribution of charged particles, dN_{ch}/dy, remains constant within the mid-rapidity region (see Fig. 1.10 and the corresponding discussion). This holds in a narrow rapidity range near $y = 0$. Consequently, the central region remains invariant under Lorentz boosts along the beam axis, as discussed earlier in this Chapter, in Section 1.2. Since it does not depend on transverse coordinates, this one-dimensional model lends itself to simple analytical treatment. The Bjorken model has been employed to derive certain results presented in this thesis, which will be elaborated upon in the subsequent Chapters. See Figure 1.21 for a schematic depiction of Bjorken evolution.

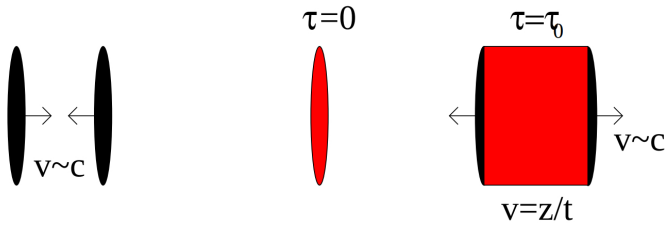

Figure 1.21: The schematic depiction of Bjorken evolution. Two Lorentz-contracted nuclei collide, leading to the creation of highly excited in the region between them. This medium thermalizes after τ_0, and the subsequent longitudinal expansion is hydrodynamical. Figure adapted from [95].

We define the proper time:

$$\tau = \sqrt{t^2 - z^2}. \tag{1.28}$$

If we assume boost invariance, the result should be independent of rapidity. In this case, initial conditions are given as [94]:

$$p(\tau);\ \epsilon(\tau);\ u^\mu = \gamma(1, 0, 0, z/t). \tag{1.29}$$

Here, p is the pressure, ϵ is the energy density and u^μ is the four-velocity of a fluid element, z is its longitudinal coordinate, and γ is the Lorentz factor.

The hydrodynamic equations read:

$$\frac{d\epsilon}{d\tau} + \frac{\epsilon + p}{\tau} = 0. \tag{1.30}$$

By using the ideal equation of state, $\epsilon = 3p$, we get the following solutions for the energy density and the temperature:

$$\epsilon(\tau) = \frac{\epsilon_0}{\tau^{4/3}}, \tag{1.31}$$

$$T(\tau) = \frac{T_0}{\tau^{1/3}}. \tag{1.32}$$

Hence, within the Bjorken model, we observe a straightforward analytical relationship between temperature and proper time.

1.4.2 Equations of motion

Hydrodynamical equations of motion are essentially conservation laws. In the ideal (non-viscous) case, the local conservation laws can be written as [96]:

$$\partial_\mu T^{\mu\nu}_{id} = 0, \tag{1.33}$$

$$\partial_\mu j^\mu_B = 0, \tag{1.34}$$

where $T^{\mu\nu}_{id}$ is the energy-momentum tensor, and j^μ_B are the net baryon four-currents. The energy-momentum tensor and net baryon currents can be expressed as:

$$T^{\mu\nu}_{id} = (\epsilon + P)u^\mu u^\nu - Pg^{\mu\nu}, \tag{1.35}$$

$$J^\mu_B = \rho_B u^\mu. \tag{1.36}$$

Here, ϵ is the energy density, P is the pressure, ρ_B is the baryon density, and u^μ is the flow four-vector. Dissipative effects like viscosity or heat conductivity are neglected here, and the fluid is assumed to always be in perfect local equilibrium. [92] In order to close this system of equations, one also needs to add an equation of state (EoS) as a local restraint on the variables:

$$p = p(\epsilon, \rho_B). \tag{1.37}$$

A quantity that is very important in hydrodynamics [50] is the speed of sound squared, c_s^2, and it is extracted from the equation of state:

$$c_s^2 = \frac{\partial p}{\partial \epsilon}. \tag{1.38}$$

If we take the ideal equation of state ($\epsilon = 3p$), we get $c_s^2 = 1/3$. Equations of state with the speed of sound approaching this value are called *hard*. In contrast, a *soft* equation of state predicts a speed of sound that is smaller than in the ideal case. This indicates that the medium being described by the EoS has more complex interactions between its constituents and that an increase in energy density does not translate as efficiently into a change of pressure.

Ideal hydrodynamics, which includes no dissipative effects, was first used to describe heavy-ion collisions, and it described the experimental data surprisingly well, as shown in Figure 1.22.

In order to improve these results and to learn more about the properties of matter created in heavy-ion collisions, viscous hydrodynamics was introduced. Naturally, it reduces to the case of ideal hydrodynamics in the vanishing limit of the dissipative transport coefficients (e.g., shear viscosity, bulk viscosity, heat conductivity). It can be implemented in the first order through the Navier-Stokes formalism [96], which is simple but introduces unphysical signal propagation at infinite speed. The second-order formalism is called the Israel-Stewart formalism [96], which solves this problem. Figure 1.23 shows an example of results obtained within a state-of-the-art viscous hydrodynamical calculation. It shows root-mean-squared $\langle v_n^2 \rangle^{1/2}$ as a function of transverse momentum $p_\perp$, calculated by using MUSIC viscous hydrodynamical model, with IP-Glasma as the initial state model [97]. We observe remarkable agreement with experimental data from ATLAS.

A significant quantity in the viscous hydrodynamical description is the shear viscosity, η. In everyday life, we have the notion of viscosity as a fluid's resistance to flow. Microscopically, it measures the strength of interactions between the particles that make up a fluid. The lower

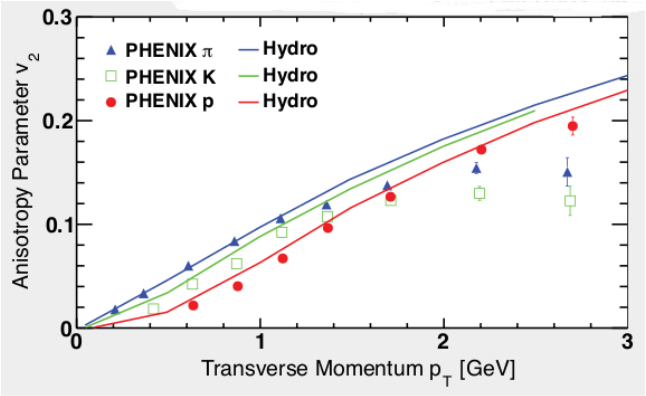

Figure 1.22: Early success of ideal (non-viscous) hydrodynamics. The anisotropy parameter v_2 is a function of the transverse momentum $p_\perp$. The theoretical (hydrodynamical) predictions (represented by lines) are compared with the experimental data from the PHENIX collaboration at RHIC (represented by symbols) for different hadron species (π, K, p). The collision system is Au+Au at $\sqrt{s_{\mathrm{NN}}} = 130\,\mathrm{GeV}$. Figure adapted from [96].

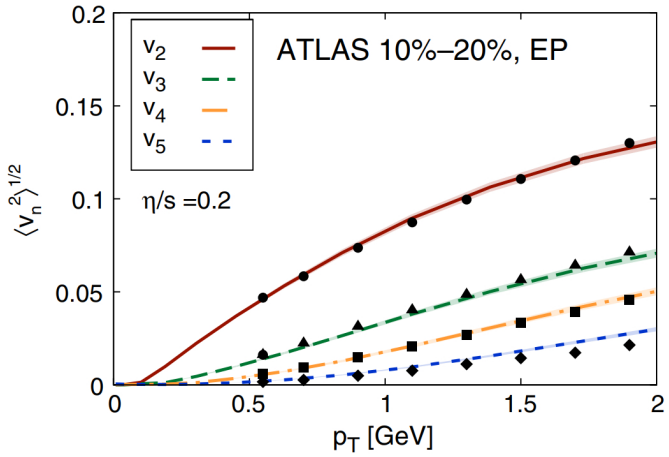

Figure 1.23: An example of state-of-the-art viscous hydrodynamical calculations. The figure shows root-mean-square anisotropic flow coefficients $\langle v_n^2 \rangle^{1/2}$ as a function of transverse momentum $p_\perp$. The value of shear viscosity over entropy is constant, $\eta/s = 0.2$. The theoretical results obtained within the IP-Glasma + MUSIC model (represented by lines) are compared with experimental data from ATLAS (represented by symbols) and show excellent agreement. Figure adapted from [97].

value of the shear viscosity means that fluid flows more easily, i.e., disturbances of a part of a fluid are more readily transmitted to adjacent parts. In the opposite limit – ideal gas, which has no interactions among its constituents – the shear viscosity is infinite [91]. It is common to consider the ratio between shear viscosity and the entropy density, η/s, as this facilitates comparison of the strength of interaction per constituent among vastly different systems on different energy scales. By using AdS/CFT correspondence, a universal lower limit for the value of η/s was posited, which is expected to hold for a wide class of quantum field theories [98]:

$$\frac{\eta}{s} = \frac{\hbar}{4\pi k_B} \approx 6.08 \cdot 10^{-13}\,\mathrm{Ks}. \tag{1.39}$$

It is common to cite this value in natural units, i.e., as $1/(4\pi)$.

Figure 1.24 shows η/s as a function of temperature for substances that can be found in nature [99]. We see that water, a ubiquitous substance, as well as others that are produced in specially prepared conditions, such as liquid helium and an ultracold Fermi gas, have the values of η/s that are well above the lower boundary from Equation 1.39. On the other hand, the values of η/s for quark-gluon plasma are not far from the lower boundary [99, 100, 101, 102, 103]. Because of this fascinating property, quark-gluon plasma is sometimes referred to as *the perfect fluid*.

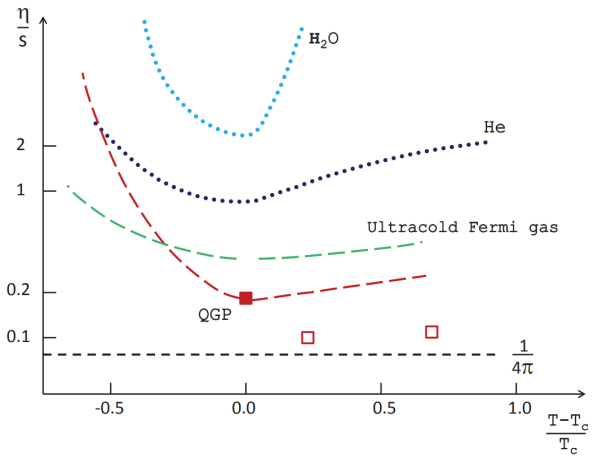

Figure 1.24: Shear viscosity over entropy density ratio for various fluids in nature. T_c denotes the various critical temperatures: for water and helium, it is the temperature at the critical endpoint of liquid-gas phase transition; for ultracold Fermi gases – the temperature of superfluid transition; for QCD – the deconfinement temperature. The theoretical curves for QGP are from [100, 101]. The solid red square is the upper boundary for $(\eta/s)_{QGP}$ from [102]. The open red squares represent a lattice result of the upper boundary for $(\eta/s)_{QGP}$ from [103]. The dashed line denotes the lower limit from AdS/CFT $(1/(4\pi))$. Figure adapted from [99].

Figure 1.25 shows a realistic QGP temperature profile obtained by using a 3+1-dimensional viscous hydrodynamical model described in detail in [104]. The energy-momentum tensor is decomposed into densities, flow velocity and dissipative currents, while the relativistic fluid-dynamical equations are the usual local conservation of energy-momentum and net-charge currents [104]. These equations are closed by adding an equation of state, together with the equations that describe the evolution of dissipative quantities [104]. The temperature profile obtained through this model is one of the profiles utilized to generate the results in this thesis, with temperature given as a function of spatial coordinates in the mid-rapidity plane. With increasing proper time τ, we can observe that the system cools, and the initial spatial anisotropy dilutes.

1.5 Outline of this thesis

The results shown in this thesis will demonstrate how high-$p_\perp$ theory and data can be used in conjunction with low-$p_\perp$ (i.e., viscous hydrodynamical calculations) physics in order to extract important properties of the new form of matter described in this Chapter: the quark-gluon plasma.

The thesis follows this outline: **Chapter 2** provides a concise overview of the employed research methodology. It introduces the state-of-the-art dynamical energy loss formalism, uti-

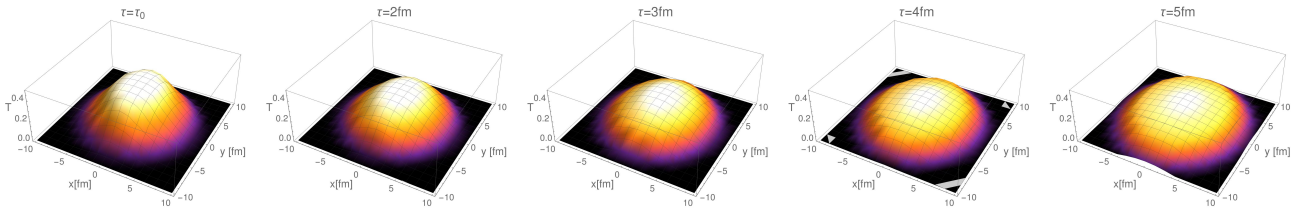

Figure 1.25: A depiction of the QGP evolution: the temperature is given in MeV. The initial state is calculated within the Glauber model, while the subsequent evolution is hydrodynamical. The initial time is $\tau_0 = 1$fm, the collision system is Pb+Pb at $\sqrt{s_{NN}} = 5.02$TeV. This is one of the profiles generated as input for high-$p_\perp$ calculations to obtain some results in this thesis, which will be presented in the subsequent chapters.

lized for studying the energy loss of rare high-$p_\perp$ probes traversing the quark-gluon plasma. This formalism is integrated into the DREENA framework, serving as the primary tool for calculating the necessary observables required for subsequent analyses.

In **Chapter 3**, the results pertaining to the study of the early stages of quark-gluon plasma formation will be shown. In particular, our primary goal is to constrain the value of the initial time of the medium's hydrodynamical (transverse) expansion. To achieve this, we first focus on the hydrodynamical temperature profiles which were generated with no pre-equilibrium evolution in the transverse direction, and we constrain the value of the initial time of hydrodynamical (transverse) expansion through high-$p_\perp$ simulations and comparison with data. However, since this is not believed to be a realistic model of the evolution of quark-gluon plasma created in heavy-ion collisions, we then explore how this picture changes once we include pre-equilibrium evolution in our hydrodynamical model.

Chapter 4 contains the results related to the study of the anisotropy of quark-gluon plasma created in heavy-ion collisions and how it can be constrained by using high-$p_\perp$ data. We first explore a simplified picture: a 1D Bjorken evolution of the medium with no transverse expansion and whether we can relate high-$p_\perp$ observables to the anisotropy of this medium. Afterward, in order to ensure the universality of our findings, we proceed to the full-fledged medium evolution and explore the relationship between high-$p_\perp$ data and the anisotropy of the medium in a diverse variety of cases, which include different collision systems, collision energies, initial states, and subsequent hydrodynamical evolution models.

Chapter 5 will address the importance of higher orders in opacity in the energy loss of high-$p_\perp$ probes. Namely, the radiative energy loss formalism embedded in the original DREENA framework considers the medium as *optically thin*: a jet encounters a single scattering center before radiating gluons. This is opposed to the *optically thick* approximation, where jets encounter infinite scattering centers. However, since the size of the medium created in heavy-ion collisions is several fm, it is reasonable to expect both approximations to be unrealistic. Thus, we implement a finite number of scattering centers into radiative energy loss within the DREENA framework and show how this affects the high-$p_\perp$ observables.

Chapter 6 will summarize the main findings of this thesis.

The Appendices contain supplementary results that could create clutter in the main body of the text.

Chapter 2

Methodology

The main idea behind the research presented in this thesis is to use rare high-$p_\perp$ particles to study the properties of quark-gluon plasma created in relativistic heavy-ion collisions - *QGP tomography*. It has already been established that high-$p_\perp$ particles are excellent tools for studying the properties of quark-gluon plasma for several important reasons: *i)* they are created in the early stages of QGP formation and thus carry information on the entire evolution of the system; *ii)* they significantly interact with the medium; *iii)* they can be studied by applying perturbative QCD techniques. However, to use high-$p_\perp$ particles for QGP tomography, a reliable and comprehensive description of their energy loss in the QCD medium is required. The dynamical energy loss formalism [105, 106] has been developed and embedded within DREENA numerical framework [107, 108, 109], with state-of-the-art features outlined in this Chapter. Within this proper description of their interaction with the medium, high-$p_\perp$ particles become excellent tomography tools, i.e., *high-$p_\perp$ probes*. This framework has been utilized to generate predictions for high-$p_\perp$ observables, which were subsequently employed in theoretical analyses within this thesis. Furthermore, in Chapter 5, we will generalize this formalism to a finite number of scattering centers in the medium.

2.1 The dynamical energy loss formalism

Historically, Gyulassy, Levai and Vitev, the creators of the GLV model [110, 111, 112, 113, 114], addressed the energy loss of an energetic (massless) parton traversing a finite quark-gluon plasma, which was also generalized to all orders in opacity (i.e., number of scattering centers that a jet experiences in the medium), using the reaction-operator approach [112]. Djordjevic and Gyulassy further expanded the GLV model by introducing the heavy quark mass M in the radiative energy loss in static finite-size quark-gluon plasma, thus creating the DGLV model [115]. Remarkably, they discovered that the general result is obtained by shifting all frequencies in the GLV series by $(m_g^2 + x^2M^2)/(2xE)$, where m_g is the effective gluon mass, x is the fraction of the energy carried by the radiated gluon, while E is the initial energy of the jet [115]. Moreover, in the massless limit, DGLV recovers GLV results.

However, the DGLV model assumes that the QGP medium consists of randomly distributed static scattering centers, where collisional energy loss is equal to zero [115]. Some studies [116] have suggested that radiative energy loss alone is not sufficient to explain the heavy flavor R_{AA}

results from RHIC.

Thus, to address this issue, the dynamical energy loss was developed, which is our most sophisticated model. It has the following features:

- Radiative energy loss [105], applicable to both light and heavy flavor;
- Collisional energy loss, calculated under the same theoretical framework, applicable to both light and heavy flavor [106];
- The formalism considers QCD medium of *finite* size (L) and temperature (T), which consists of dynamical (i.e., moving) partons, in a distinction to models with widely used static approximation and vacuum-like propagators [117, 118, 110, 119];
- Calculations are based on generalized Hard-Thermal-Loop approach [22, 120], with naturally regulated infrared divergences [105, 121, 122].
- The formalism is generalized to finite magnetic mass [123] and running coupling [124];
- Recently, soft-gluon approximation has been relaxed, expanding the applicability region of this formalism [125].

It was previously shown [126] that all the model ingredients noted above affect the high-$p_\perp$ data and thus should be included to explain it accurately.

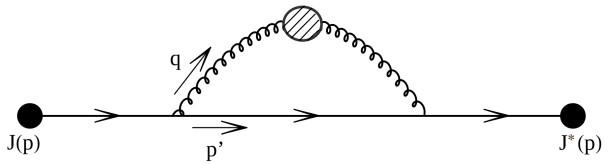

Figure 2.1: One hard thermal loop diagram, which gives the 0^{th} order collisional and radiative rates. Figure adapted from [106].

Figure 2.1 shows the one hard thermal loop (HTL) diagram from which we can obtain the 0^{th} order radiative and collisional diagrams. The contribution to the collisional energy loss is obtained by "cutting" (putting on shell) the parton propagators. On the other hand, the radiative contribution is obtained by cutting through parton and gluon propagators. [106]

Collisional energy loss within the dynamical energy loss formalism has been developed by M. Djordjevic in [106]. It refers to the processes with the same number of incoming and outgoing particles. It is computed in the finite-temperature QCD medium from the diagram shown on Figure 2.2.

The effective gluon propagator shown in Figure 2.2 has both transverse and longitudinal contributions. In Coulomb gauge the gluon propagator has the following form [106]:

$$D^{\mu\nu}(\omega, \vec{\mathbf{q}}) = -P^{\mu\nu}\Delta_T(\omega, \vec{\mathbf{q}}) - Q^{\mu\nu}\Delta_L(\omega, \vec{\mathbf{q}}), \tag{2.1}$$

where $q = (\omega, \vec{\mathbf{q}})$ is the 4-momentum of the gluon, while Δ_T and Δ_L are effective transverse and longitudinal gluon propagators given by [106, 108]:

$$\Delta_T^{-1} = \omega^2 - \vec{\mathbf{q}}^2 - \frac{\mu_E(T)^2}{2} - \frac{(\omega^2 - \vec{\mathbf{q}}^2)\mu_E(T)^2}{2\vec{\mathbf{q}}^2}(1 + \frac{\omega}{2|\vec{\mathbf{q}}|}\ln|\frac{\omega - |\vec{\mathbf{q}}|}{\omega + |\vec{\mathbf{q}}|}|), \tag{2.2}$$

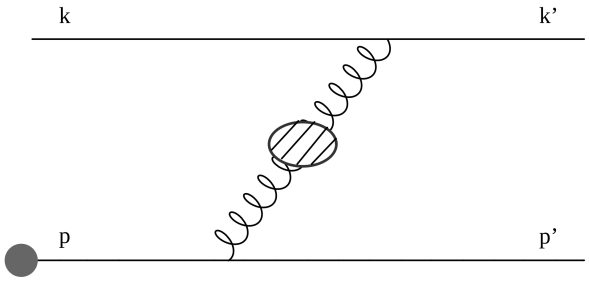

Figure 2.2: Feynman diagram represents the collisional energy loss in the finite temperature QCD medium. The dashed circle denotes the effective gluon propagator. Figure adapted from [106].

$$\Delta_L^{-1} = \vec{\mathbf{q}}^2 + \mu_E(T)^2(1 + \frac{\omega}{2|\vec{\mathbf{q}}|}\ln|\frac{\omega - |\vec{\mathbf{q}}|}{\omega + |\vec{\mathbf{q}}|}|), \tag{2.3}$$

where $\mu_E(T)$ is the electric screening (the Debye mass) [108].

The only nonzero terms in transverse ($P_{\mu\nu}$) and longitudinal ($Q_{\mu\nu}$) projectors are the following [106]:

$$P^{ij} = \delta^{ij} - \frac{q^i q^j}{|\vec{\mathbf{q}}|^2}, \tag{2.4}$$

$$Q^{00} = 1. \tag{2.5}$$

The analytical expression for collisional energy loss per unit length is given by the following expression [106]:

$$\begin{aligned}\frac{dE_{coll}}{d\tau} &= \frac{2C_R}{\pi v^2}\alpha_s(ET)\alpha_s(\mu_E^2(T))\int_0^\infty n_{eq}(|\vec{\mathbf{k}}|,T)d|\vec{\mathbf{k}}| \\ &\times\Big[\int_0^{|\vec{\mathbf{k}}|/(1+v)} d|\vec{\mathbf{q}}|\int_{-v|\vec{\mathbf{q}}|}^{v|\vec{\mathbf{q}}|}\omega d\omega + \int_{|\vec{\mathbf{k}}|/(1+v)}^{|\vec{\mathbf{q}}|_{max}} d|\vec{\mathbf{q}}|\int_{|\vec{\mathbf{q}}|-2|\vec{\mathbf{k}}|}^{v|\vec{\mathbf{q}}|}\omega d\omega\Big] \\ &\times\Big[|\Delta_L(q,T)|^2\frac{(2|\vec{\mathbf{k}}|+\omega)^2 - |\vec{\mathbf{q}}|^2}{2} + |\Delta_T(q,T)|^2\frac{(|\vec{\mathbf{q}}|^2-\omega^2)((2|\vec{\mathbf{k}}|+\omega)^2+|\vec{\mathbf{q}}|^2)}{4|\vec{\mathbf{q}}|^4}(v^2|\vec{\mathbf{q}}|^2-\omega^2)\Big],\end{aligned} \tag{2.6}$$

where $n_{eq}(|\vec{\mathbf{k}}|,T) = \frac{N_c}{e^{|\vec{\mathbf{k}}|/T}-1} + \frac{N_f}{e^{|\vec{\mathbf{k}}|/T}+1}$ is the equilibrium momentum distribution [127] including gluons, quarks and antiquarks, where N_c is the number of colors and N_f is the number of flavors. Temperature is denoted by T, $\mu_E(T)$ is the electric (Debye) screening mass, while the running coupling is given by α_s^2, which can be factorized as $\alpha_s(\mu_E^2)\alpha_s(ET)$ [128], where E is the energy of the jet. $C_R = 4/3$ ($C_R = 3$) for the quark (gluon) jet, k is the 4-momentum of the incoming medium parton, v is velocity of the initial jet and $q = (\omega, \vec{\mathbf{q}})$ is the 4-momentum of the exchanged gluon. $|\vec{\mathbf{q}}|_{max}$ is provided in Ref. [106], while $\Delta_T(q,T)$ and $\Delta_L(q,T)$ are effective transverse and longitudinal gluon propagators, given by Equations 2.2 and 2.3.

Radiative energy loss within the dynamical energy loss formalism has been developed by M. Djordjevic in [105]. It originates from processes in which there are more outgoing than incoming particles. In the original numerical framework, it is calculated up to the 1^{st} order in opacity (see Figure 2.3). In Chapter 5, we will expand this approach and include higher orders in opacity in the radiative energy loss.

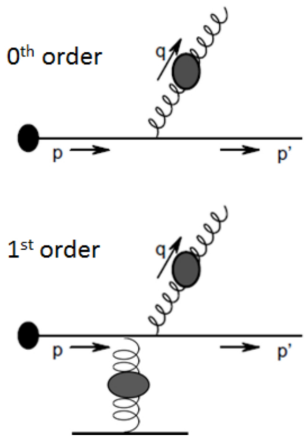

Figure 2.3: The diagrams represent radiative energy loss contributions that come from 1HTL (upper diagram) and 2HTL (lower diagram) gluon propagator. Figure adapted from [106].

The general form of the 1^{st} order in opacity term for gluon radiation spectrum in a finite-size medium with dynamical constituents is given by (see Chapter 5 and Appendix B for more details):

$$\left(\frac{dN_g^{(1)}}{dx}\right) = \frac{4C_R}{\pi x}\int_0^L dz_1 \int \frac{d^2\mathbf{k}}{\pi}\int \frac{d^2\mathbf{q}_1}{\pi}\,\alpha_s(Q_k^2)\frac{1}{\lambda_{dyn}}\frac{\mu_E^2-\mu_M^2}{(\mathbf{q}_1^2+\mu_E^2)(\mathbf{q}_1^2+\mu_M^2)} \frac{\chi^2(\mathbf{q}_1\cdot(\mathbf{q}_1-\mathbf{k}))+(\mathbf{q}_1\cdot\mathbf{k})(\mathbf{k}-\mathbf{q}_1)^2}{(\chi^2+\mathbf{k}^2)(\chi^2+(\mathbf{k}-\mathbf{q}_1)^2)^2}\sin^2\left(\frac{\chi^2+(\mathbf{k}^2-\mathbf{q}_1)^2}{4xE}z_1\right). \tag{2.7}$$

Here, $\mathbf{k}$ is the 2D momentum of the radiated gluon, while $\mathbf{q}$ is the 2D momentum of the exchanged gluon [105]. $\mu_E(T)$ is the electric screening [108], while $\mu_M(T)$ is the magnetic screening [108]. λ_{dyn} is the dynamical mean free path, given by $\lambda_{dyn}^{-1} = 3\alpha_s(Q_v^2)T$, with $Q_v^2 = ET$ [105]. Running coupling $\alpha_s(Q_v^2)$ corresponds to the interaction between the jet and the virtual (exchanged) gluon, while E is the jet's energy [124]. Q_k^2 which appears in $\alpha_s(Q_k^2)$ is the off-shellness of the jet prior to the gluon radiation and is equal to $Q_k^2 = \frac{\mathbf{k}^2+M^2x^2+m_g^2}{x}$ [124], where M is the jet mass, x is the longitudinal momentum fraction of the jet carried away by the emitted gluon, while $m_g(T) = \mu_E(T)/\sqrt{2}$ is the effective mass for gluons in finite-temperature QCD medium [108]. L is the size of the medium, while χ^2 is given by $\chi^2 = M^2x^2 + m_g^2$.

2.2 The numerical framework

The dynamical energy loss formalism is embedded in the DREENA framework, a fully optimized computational procedure that generates predictions for high-$p_\perp$ observables for various collision systems, collision energies, centralities, and probes.

By the scheme presented in Figure 2.4, the suppressed spectrum of light and heavy particles can be expressed within the DREENA framework as a generic pQCD convolution:

$$\frac{E_f d^3\sigma}{dp_f^3} = \frac{E_i d^3\sigma(Q)}{dp_i^3} \otimes P(E_i \to E_f) \otimes D(Q \to H_Q). \tag{2.8}$$

Here, indices i and f stand for 'initial' and 'final', respectively, while Q denotes initial light or heavy high-energy parton (light or heavy quarks or gluons). $E_i d^3\sigma(Q)/dp_i^3$ is the initial momentum spectrum for the given particle, which is calculated according to [129] (step 1 on the scheme), $P(E_i \to E_f)$ represents the energy loss probability for the given particle which was calculated within the dynamical energy loss formalism (step 2 on the scheme), which includes multi-gluon [130] fluctuations, referring to the probability of jet radiating a number of gluons (0, 1, 2...). In the approximation that the fluctuations of gluon numbers are uncorrelated, the probabilty that the jet radiates a particular number of gluons can be modeled by the Poisson distribution [130].

$D(Q \to H_Q)$ represents the fragmentation function of light and heavy partons into hadrons (step 3 on the scheme), where for light hadrons, D and B mesons, we use Daniel de F.-Sassot-Stratmann (DSS) [131], Braaten-Cheung-Fleming-Yuan (BCFY) [132], Kartvelishvili-Likhoded-Petrov (KLP) [133] fragmentation functions, respectively.

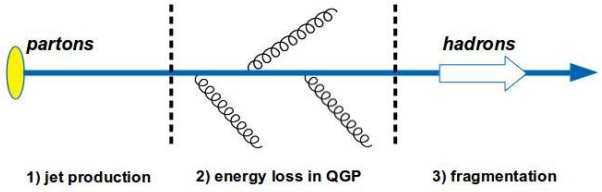

Figure 2.4: Schematic representation of the QCD convolution upon which the DREENA framework is based. Figure adapted from [134].

Various versions of the DREENA framework have been developed, but the three versions relevant to this thesis are DREENA-C, DREENA-B, and DREENA-A.

DREENA-C (C – *constant*) is fully described in [107]. It is the simplest version of the DREENA framework, as in it, the QGP medium is modeled in the simplest possible way: as a constant (average) temperature medium. The average temperature is determined by $T = c\left(\frac{\frac{dN_{ch}}{dy}}{A_\perp \bar{L}}\right)$ [107]. Here, $A_\perp$ is the overlap area, $\bar{L}$ is the average size of the medium for a particular centrality region [107]. $\frac{dN_{ch}}{dy}$ is the experimentally measured charged particle multiplicity [107], measured for 5.02 TeV Pb+Pb collisions at the LHC across different centralities [135], while c is a constant, which can be fixed through ALICE measurement of effective temperature for 0-20% centrality at 2.76 TeV Pb+Pb collisions at LHC [136]. Path-length fluctuations are included in the framework [137], with an additional hard-sphere restriction in the Woods-Saxon nuclear density distribution to regulate the path lengths in the peripheral collisions [107]. DREENA-C does not have any free parameters. It keeps all the dynamical energy loss formalism ingredients, and is thus appropriate for studying the jet-medium interactions. It was previously used by the author of this thesis to extract the temperature dependence of high-$p_\perp$ particles' energy loss in the medium. [138] Within this thesis, DREENA-C was used as a basis for the implementation of higher orders in opacity in the radiative energy loss, and the associated findings will be presented in Chapter 5.

DREENA-B (B – *Bjorken*), described in detail in [108], was developed as the intermediate step towards DREENA with realistic, hydrodynamical medium evolution. It models the medium as a simple 1D Bjorken evolution (described in Section 1.4), where the medium expands in the longitudinal direction but not in the transverse direction. We used DREENA-B as a simple model to explore whether high-$p_\perp$ observables can be related to the anisotropy of quark-gluon plasma formed in heavy-ion collisions, as described in Chapter 4.

DREENA-A (A – *adaptive*), the details of which can be found in [109], is the most advanced version of the DREENA framework. It can be used to calculate high-$p_\perp$ observables R_{AA} and v_2 on an arbitrary smooth hydrodynamical background while retaining all the sophisticated details of the jet-medium interactions pertaining to the dynamical energy loss formalism described earlier. Moreover, it was recently extended and is able to utilize arbitrary event-by-event fluctuating temperature profiles [139] and calculate predictions for higher harmonics (v_3 and higher). In order to produce predictions for high-$p_\perp$ observables within DREENA-A, the only required input is a temperature profile that describes the space-time evolution of the quark-gluon plasma. The framework is fully optimized and parallelized, allowing it to use modern multicore workstations. It was used to study the early stages of quark-gluon plasma evolution (the results of which were presented in Chapter 3), as well as to explore the connection between the anisotropy of quark-gluon plasma created in heavy-ion collisions and high-$p_\perp$ data (Chapter 4).

Chapter 3

Early Stages of Quark-Gluon Plasma Evolution Explored through High-$p_\perp$ Data

In this Chapter, based on [1, 2], we present results related to examining the initial phases in the evolution of quark-gluon plasma. As the Introduction outlines, following the collision of two nuclei in a heavy-ion experiment, the created medium evolves through various stages (refer to Figure 1.7). We will employ high-$p_\perp$ theory and data to constrain the value of the initial time τ_0, which signifies the onset of the hydrodynamical evolution of the quark-gluon plasma.

Our analysis (presented in [1, 2]) reveals that high-$p_\perp$ $R_{\rm AA}$ and v_2 exhibit greater sensitivity to the QGP initial time, τ_0, in comparison to the distributions of low-$p_\perp$ particles. The high-$p_\perp$ observables indicate a preference for a relatively later onset of hydrodynamical expansion, around $\tau_0 \sim 1$ fm/c. Notably, the elliptic flow parameter v_2 displays more pronounced sensitivity to τ_0 than $R_{\rm AA}$, attributed to the differences in the evolution of temperature profiles in the in-plane and out-of-plane directions.

Additionally, we incorporate pre-equilibrium evolution within our model and demonstrate that high-$p_\perp$ $R_{\rm AA}$ and v_2 are responsive to the initial dynamics of expansion. The high-$p_\perp$ observables consistently prefer a delayed initiation of energy loss and transverse hydrodynamical expansion.

3.1 Determination of quark-gluon plasma initial time

3.1.1 Introduction

In this section, we analyze how high-$p_\perp$ $R_{\rm AA}$ and v_2 depend on the QGP initial time τ_0, i.e., the onset time of fluid-dynamical expansion. The dynamics before the initial time τ_0 and applicability of hydrodynamics and, therefore, the associated energy loss phenomena are not established yet. Some simple scenarios for mapping the pre-equilibrium energy loss were discussed in Ref. [140]. To avoid speculation and provide a baseline calculation for further studies, in this section, we assume free streaming of high-$p_\perp$ particles before the initial time τ_0, neglecting the medium's pre-equilibrium evolution. After the initial time τ_0, the QCD medium is described as a relativistic viscous fluid, and high-$p_\perp$ probes start to lose energy through interactions with

this medium. Consequently, the initial time τ_0 is an important parameter, affecting both the system's evolution and interactions of the high-$p_\perp$ particles with the medium.

The conventional approach to fix the initial time is to carry out hydrodynamical simulations with various values of τ_0, calculate the distributions of low-$p_\perp$ particles, compare them to data, and keep varying τ_0 until the best possible fit to the data is achieved. However, an analysis employing sophisticated Bayesian statistics has shown that low-$p_\perp$ data provides only weak limits to the initial time, $\tau_0 = 0.59 \pm 0.41$ fm/c with 90% credibility [141], and further constraints would be instrumental.

When calculating how the high-$p_\perp$ observables depend on τ_0, one has to ensure that the QGP medium evolution is compatible with the observed distributions of low-$p_\perp$ particles. We describe the medium evolution using the 3+1-dimensional viscous hydrodynamical model from Ref. [104]. For simplicity, we ignore pre-equilibrium evolution in the transverse plane, i.e. $v_r(x, y, \tau_0) = 0$, choose a constant shear viscosity to entropy density ratio $\eta/s = 0.12$, and base the initial transverse energy density profile e_T on the binary collision density n_{BC} from the optical Glauber model:

$$\begin{aligned} e_T(\tau_0, x, y, b) &= C_e(\tau_0)\ f_{BC}, \\ f_{BC} &= n_{BC} + c_1 n_{BC}^2 + c_2 n_{BC}^3. \end{aligned} \tag{3.1}$$

The parameters C_e, c_1, and c_2 are tuned separately for each τ_0 value to approximately describe the observed charged particle multiplicities and $v_2\{4\}$ in Pb+Pb collisions at $\sqrt{s_{NN}} = 5.02$ TeV. $v_n\{4\}$ (four-particle cumulant v_n) is defined as $v_n\{4\}^4 = -c_n\{4\}$, where diagonal cumulants $c_n\{4\}$ are measurable quantities [142]. The initial (i.e. hydro initialization) time τ_0 has been varied from 0.2 fm to 1.2 fm. For the longitudinal profile, we keep the parametrization used for $\sqrt{s_{NN}} = 2.76$ Pb+Pb collisions in Ref. [104]. Likewise, the decoupling temperature $T_{\rm dec} = 100$ MeV, and the equation of state $s95p$-PCE-v1 [143] is the same as in that article.

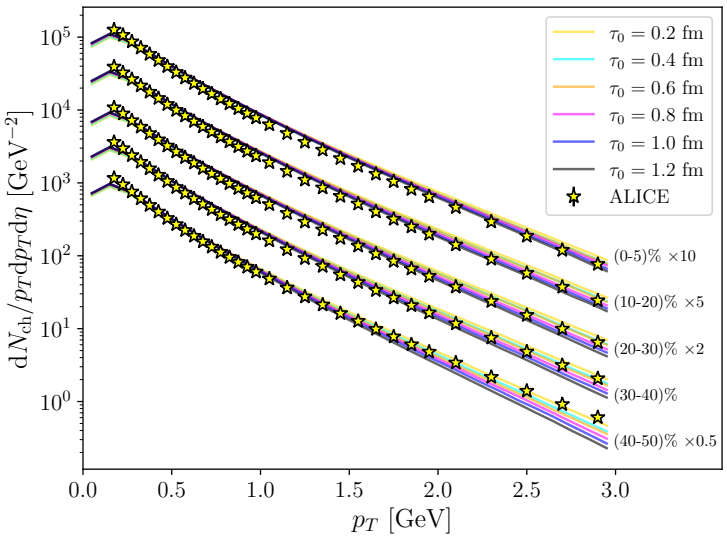

Figure 3.1: The agreement of low-$p_\perp$ data for all the temperature profiles with various values of the initial time τ_0. The figure shows the transverse momentum spectrum of charged particles in five centrality classes in Pb+Pb collisions at $\sqrt{s_{NN}} = 5.02$TeV, with the initial time τ_0 varied from 0.2 fm to 1.2 fm. ALICE data is taken from [144].

The transverse momentum distributions of charged particles are shown in Fig. 3.1, and $p_\perp$-differential elliptic flow parameter $v_2(p_\perp)$ in the low momentum part ($p_\perp < 2$ GeV) of the lower panels of Fig. 3.2 (note that the scale on the $v_2(p_\perp)$ plots is logarithmic). The overall

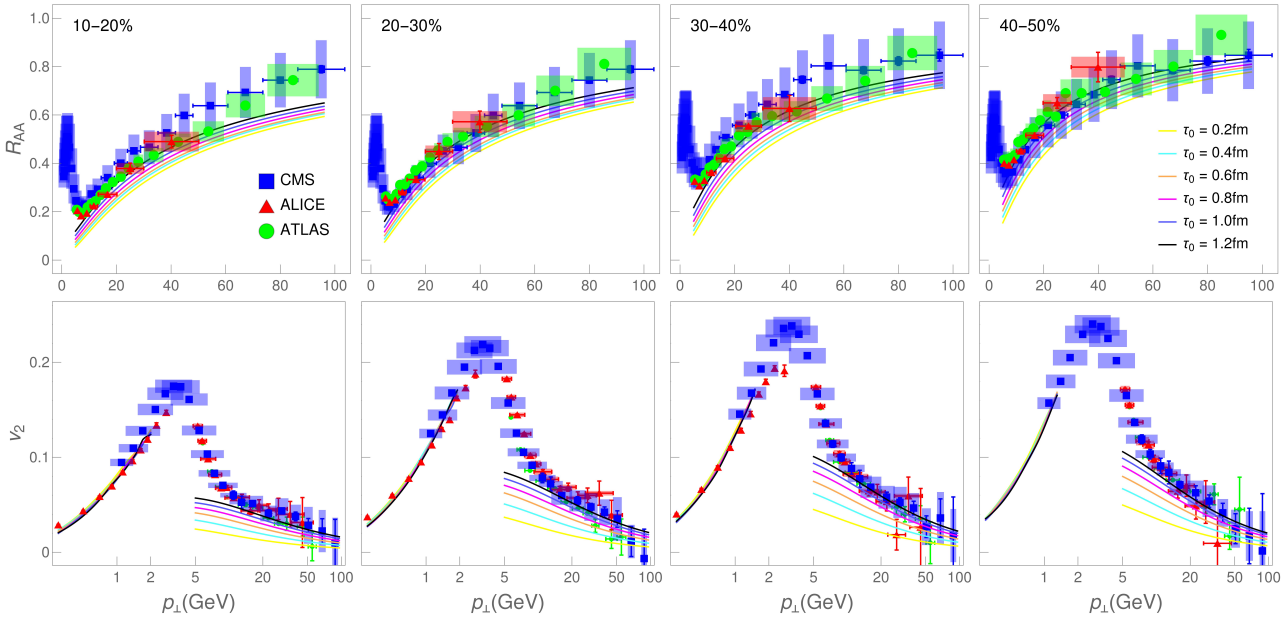

Figure 3.2: Charged hadron DREENA-A R_{AA} (upper panels) and v_2 (lower panels) predictions, generated for six different τ_0 (indicated on the legend), are compared with ALICE [144, 145], CMS [146, 147] and ATLAS [148, 149] data. Four columns, from left to right, correspond to 10–20%, 20–30%, 30–40% and 40–50% centralities at $\sqrt{s_{NN}} = 5.02$ Pb+Pb collisions at the LHC. At low $p_\perp$ ($p_\perp < 2$ GeV) v_2 is 4-cumulant $v_2\{4\}$, whereas at high $p_\perp$ ($p_\perp > 5$ GeV) we evaluate v_2 as $v_2 = (1/2)\,(R_{\rm AA}^{\rm in} - R_{\rm AA}^{\rm out})/(R_{\rm AA}^{\rm in} + R_{\rm AA}^{\rm out})$. Note that the $p_\perp$ scale in the upper (R_{AA}) row is regular, while in the lower (v_2), it is logarithmic.

agreement with the data is acceptable, and consistently with Ref. [141], we observe only a weak dependence on τ_0—especially $v_2(p_\perp)$ is almost independent of τ_0.

3.1.2 High-$p_\perp$ $R_{\rm AA}$ and v_2 results

The next step in our study is to generate the high-$p_\perp$ predictions for the six temperature profiles (with different values of τ_0) and to compare them with the experimental data. To achieve this, we use the DREENA-A framework described in Chapter 2.

In particular, collisional and radiative energy losses are computed by using Equations 2.6 and 2.7, we use $\Lambda_{QCD} = 0.2$ GeV and effective light quark flavors $n_f = 3$. For light quark mass, we assume to be dominated by the thermal mass $M = \mu_E/\sqrt{6}$, and for the gluon mass, we take $m_g = \mu_E/\sqrt{2}$ [122]. The temperature-dependent Debye mass μ_E is obtained by applying procedure from [150], which leads to results compatible with the lattice QCD [151]. The charm (bottom) mass is $M = 1.2$ GeV ($M = 4.75$ GeV). Magnetic to electric mass ratio is $0.4 < \mu_M/\mu_E < 0.6$ [152, 153, 154, 155], but for simplicity, we take $\mu_M/\mu_E = 0.5$, leading to the uncertainty of up to 10% for both R_{AA} and v_2 results.

The resulting DREENA-A predictions for charged hadron R_{AA} in four different centrality classes, and τ_0 in the range of 0.2–1.2 fm, are shown in the upper panel of Fig. 3.2, and compared with experimental data. In the lower panel of Fig. 3.2, we show a similar comparison of predicted high-$p_\perp$ v_2 to data (note that the scale is logarithmic). In distinction to the low-$p_\perp$ distributions, we see that high-$p_\perp$ predictions can be resolved against experimental data and that the later onset of hydrodynamical expansion is preferred by both R_{AA} and v_2. This

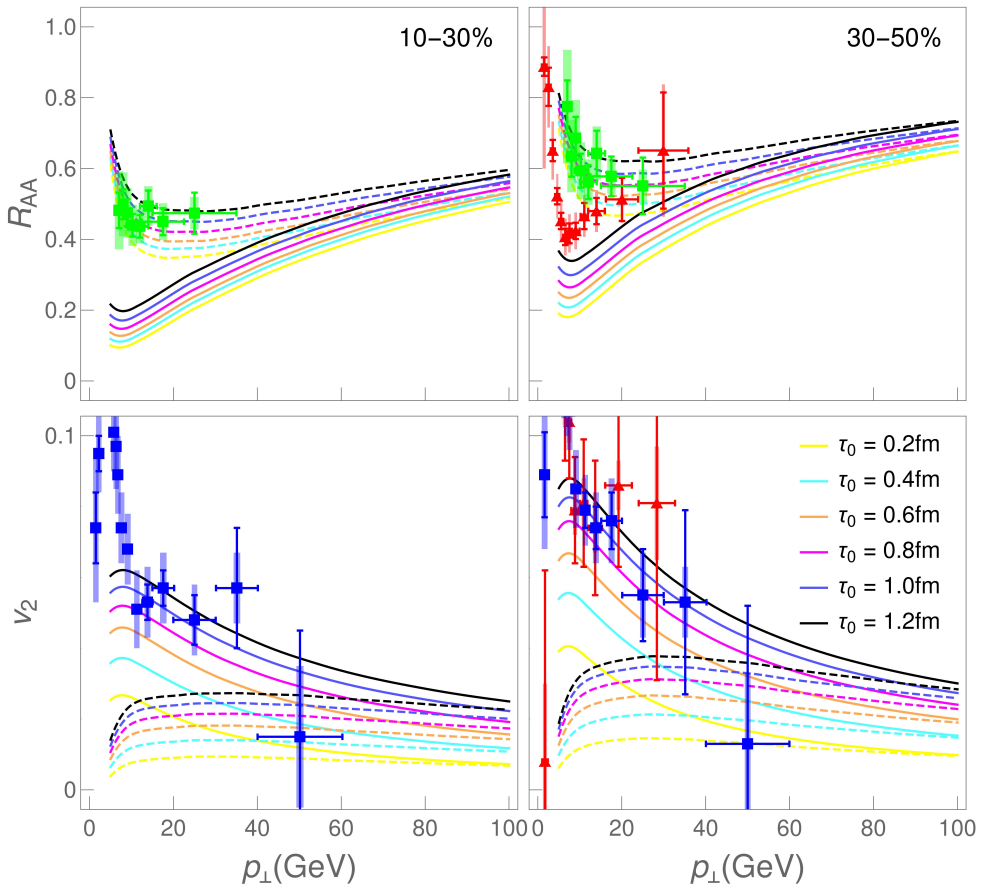

Figure 3.3: This figure shows the predictions for high-$p_\perp$ observables obtained within DREENA-A for heavy flavor with different values of the initial time τ_0. Predicted D (full curves) and B meson (dashed curves) R_{AA} (upper panels) and v_2 (lower panels) in Pb+Pb collisions at $\sqrt{s_{NN}} = 5.02$ TeV. The predictions for D mesons are compared with ALICE [156, 157] (red triangles) and CMS [158] (blue squares) D meson data, while predictions for B mesons are compared with CMS [159] (green circles) non-prompt J/Ψ data. The predictions are generated on each panel for six different τ_0 (indicated in the legend).

resolution is apparent for v_2 predictions, which approach the high-$p_\perp$ tail of the data, as τ_0 is increased. One can also observe that this resolution (i.e., difference between the adjacent predicted curves) increases for higher centralities, which we will analyze below.

Furthermore, we obtain that heavy quarks (charm and bottom) are even more sensitive to τ_0, as shown in Fig. 3.3. The data are mainly unavailable for bottom probes, which makes these true predictions, to be tested against upcoming high luminosity LHC Run 3 data. The available experimental data for charm probes are much more sparse (with larger error bars) than the charged hadron data. However, where available, a comparison of our predictions with the data suggests the same tendency as for charged hadrons, i.e., a preference towards later onset of hydrodynamical expansion. These results are significant for studying the properties of QGP, as consistency between light and heavy flavor is crucial and highly non-trivial, as confirmed by the well-known heavy flavor puzzle: unexpected similar suppression of light and heavy probes observed at RHIC [160].

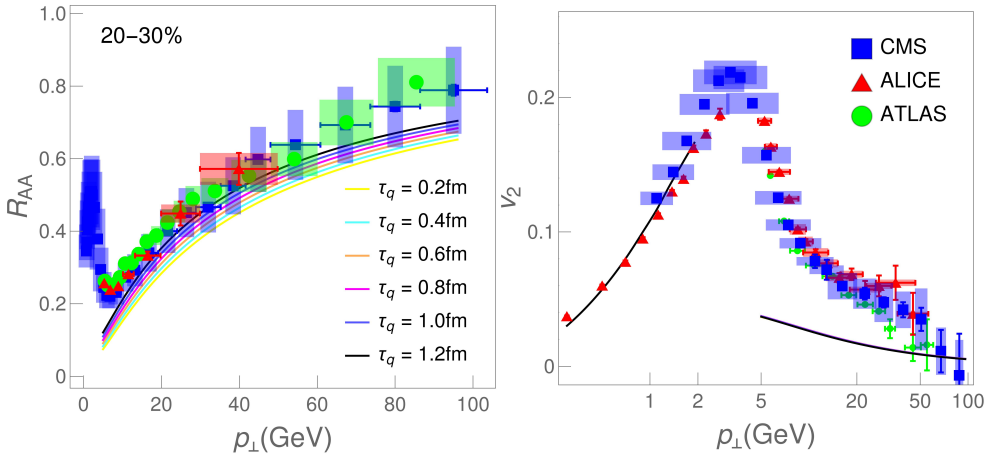

Figure 3.4: Exploring whether later quenching time can explain the observed sensitivity of high-$p_\perp$ predictions on τ_0. The panel shows DREENA-A predictions for charged hadron R_{AA} (left) and v_2 (right) in 20–30% centrality class of $\sqrt{s_{NN}} = 5.02$ TeV Pb+Pb collisions at the LHC, generated for $\tau_0 = 0.2$ fm and six different τ_q (indicated on the legend). The predictions are compared with ALICE [144, 145], ATLAS [148, 149] and CMS [146, 147] data.

3.1.3 Can later quenching time explain the observed sensitivity of high-$p_\perp$ observables to τ_0?

Ref. [161] proposed that jet quenching may start later than the bulk QCD medium's thermalization and subsequent fluid dynamical evolution. To test this scenario, we follow that work and introduce a separate quenching start time $\tau_q \geq \tau_0$. In Fig. 3.4 we show the high-$p_\perp$ $R_{\rm AA}$ and v_2 in 20-30% centrality for $\tau_0 = 0.2$fm, and τ_q values in the range of 0.2–1.2 fm. The sensitivity to τ_q is similar in other centralities, for larger τ_0, and heavy flavor. $R_{\rm AA}$ shows similar sensitivity to τ_q as to τ_0; compare Figs. 3.4 and 3.2. The v_2 is surprisingly insensitive to τ_q and way below the data, consequently not supporting the idea that quenching can start later than hydrodynamical evolution.

To investigate the origin of the sensitivity of $R_{\rm AA}$ and v_2 to τ_0 and τ_q, we evaluate the temperature along the paths of jets traveling in-plane ($\phi = 0$) and out-of-plane ($\phi = \pi/2$) directions, and average over all sampled jet paths. To explain the sensitivity of v_2, in Fig. 3.5 we show the resulting temperature evolution in 10–20% and 30-40% central collisions for $\tau_0 = 0.2$ and 1.2 fm. As τ_0 is increased, the differences between in-plane and out-of-plane temperature profiles also increase. Since v_2 is proportional to the difference in suppression along in-plane and out-of-plane directions, a larger difference along these directions leads to larger v_2. It causes the observed dependency on τ_0. As well, for fixed τ_0, increasing τ_q hardly changes v_2 since at early times the average temperature in- and out-of-plane directions is almost identical, and no v_2 is built up at that time in any case. Furthermore, the more peripheral the collision, the larger the difference in average temperatures, which leads to higher sensitivity of v_2 to τ_0 as seen in the lower panels of Fig. 3.2.

The change in τ_0 affects the average temperature along the jet path in two ways. First, smaller τ_0 means more significant initial gradients, faster flow build-up, and faster initial spatial anisotropy dilution. Second, since the initial jet production is azimuthally symmetric, and jets travel along eikonal trajectories, at early times, both in- and out-of-plane jets probe the temperature of the medium almost the same way. The average temperature of both is almost

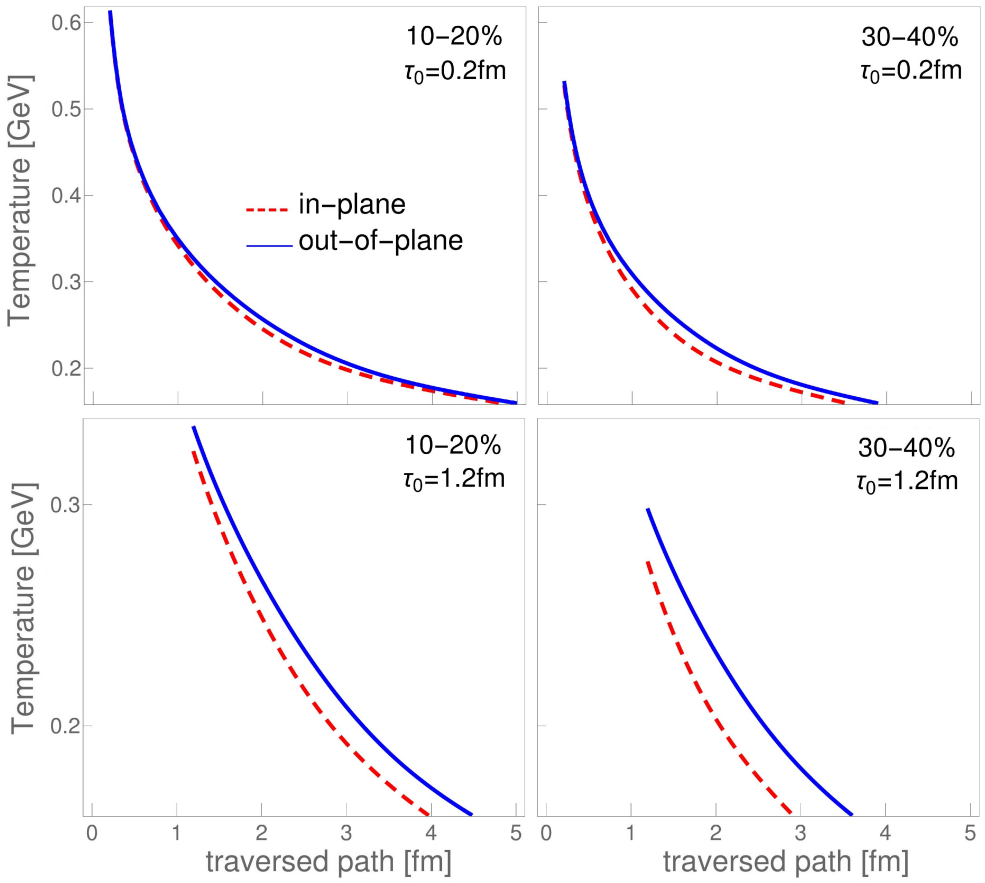

Figure 3.5: Average temperature along the jet path traversing the system in out-of-plane (full curve) and in-plane (dashed curve) directions. The average is over all sampled jet paths, and the path ends at the critical temperature, $T_C \approx 160$ MeV [162]. The centrality of the collision and τ_0 is indicated on the legend of each panel.

identical at $\tau_0 = 0.2$ fm. Only over time will the spatial distribution of in- and out-of-plane jets differ, and the average temperature along their paths begins to reflect the anisotropies of the fluid temperature. The qualitative understanding above is essential, as it shows that the obtained conclusions are largely model-independent, even though we arrived at them through our DREENA-A framework.

From Fig. 3.5, we can also understand the increase in R_{AA} with larger τ_0 and τ_q as seen in Figs. 3.2 and 3.4. Larger τ_0 or τ_q cuts away the large temperature part of the profile, decreasing the average temperature and thus increasing the angular averaged R_{AA}.

As mentioned above, here we do not include any pre-equilibrium evolution along the lines of, e.g., Refs. [163, 164, 165, 166]. We do not expect pre-equilibrium evolution to destroy the sensitivity of high-$p_\perp$ observables to τ_0 [140], but it may affect the favored value of τ_0. Reproduction of high-$p_\perp$ v_2 requires that the spatial anisotropy is not smeared away too fast. Since pre-equilibrium evolution is expected to reduce the anisotropy [164, 167], it is possible that when it is included, the favored τ_0 is even larger than seen here. In order to test these assumptions, in the following section of this Chapter, we will explore different scenarios, which include pre-equilibrium evolution.

To summarize Section 3.1, we presented an example of using high-$p_\perp$ theory and data to constrain a weakly sensitive parameter to bulk QGP evolution – the initial time of fluid-dynamical expansion, τ_0. Specifically, we used high-$p_\perp$ R_{AA} and v_2 to infer that experimental data prefer late onset of hydrodynamical expansion. The heavy flavor shows considerable

sensitivity to τ_0, so the upcoming high luminosity measurements will further test our conclusion. v_2 shows a higher sensitivity to τ_0 than R_{AA}, and we showed that v_2 is affected by τ_0 because of differences in the in- and out-of-plane temperature profiles.

3.2 Constraining the early stages of quark-gluon plasma formation through high-$p_\perp$ data

In this Section, we will take an approach to studying the early stages of quark-gluon plasma formation, which is complementary to the one described in the first part of this Chapter. Namely, we here introduce the pre-equilibrium evolution of the medium.

3.2.1 Introduction: pre-equilibrium evolution

During the last few years, our understanding of the very early evolution of QGP has evolved a lot. In particular, the discovery of the attractor solutions of the evolution of non-equilibrated systems [168, 169, 170], and models based on effective kinetic theory [171, 172] have been significant milestones. However, the exact dynamics of early evolution and hydrodynamization of the medium– -i.e., the approach to the state where the system can be described using fluid dynamics– -are still being settled.

Furthermore, to our knowledge, there are no reliable methods to calculate jet energy loss in a medium out of equilibrium. Instead of microscopic calculation of the early-time dynamics, we take a complementary approach. We calculate the high-$p_\perp$ $R_{\rm AA}$ and v_2 in a few straightforward scenarios and show whether the comparison to high-$p_\perp$ data could constrain the early evolution.

In the attractor solutions, the final evolution is fluid dynamical even if the initial state is quite far from equilibrium. This fact allows us to entertain the notion that even if the early state is not in local equilibrium, we could use fluid dynamics to describe its evolution from very early times [173], say from $\tau_0 = 0.2$ fm, where τ_0 is the initial time of fluid dynamical evolution. Correspondingly, we may argue that the temperature entering fluid dynamical evolution also controls the jet energy loss, and we may start the jet energy loss at the same time, $\tau_q = 0.2$ fm, which is our first scenario. On the other hand, we studied the pre-equilibrium energy loss in various scenarios [140], and see that even if the data could not properly distinguish these scenarios, Bjorken-type temperature evolution at very early times tended to push $R_{\rm AA}$ too low. This finding may suggest that applying the equilibrium jet-medium interactions to the pre-equilibrium stage (even if close enough to fluid dynamical) overestimates the energy loss. Due to this, we here, for simplicity, assume an opposite limit, where we start the energy loss later than the fluid dynamical evolution: $\tau_q = 1.0$ fm and $\tau_0 = 0.2$ fm, which is our second scenario (a similar scenario was proposed in [161]).

Frequently used toy model to study the effects of early non-equilibrium evolution is the free streaming approach [174, 164], where (fictional) particles are allowed to stream freely until the initial time of fluid dynamical evolution τ_0. As our third scenario, we allow free streaming until $\tau_0 = 1.0$ fm. Consistently with the assumed absence of interactions in the bulk medium, we assume no jet-medium interactions during the out-of-equilibrium stage so that $\tau_0 = \tau_q = 1.0$ fm. For comparison's sake, as the fourth scenario, we also explore the "old-fashioned" scenario where "nothing" happens before the fluid dynamical initial time $\tau_0 = \tau_q = 1.0$ fm, i.e. we start the fluid-dynamical evolution at $\tau = 1.0$ fm with zero transverse flow velocity.

In the same manner as in the previous section, when calculating how the high-$p_\perp$ observables depend on our different scenarios, we must ensure that the QGP medium evolution is compatible with the observed distributions of low-$p_\perp$ particles. We describe the medium evolution using the 3+1-dimensional viscous hydrodynamical model [104]. For simplicity, we choose a constant shear viscosity to entropy density ratio $\eta/s = 0.12$ for the cases without pre-hydro transverse flow, and $\eta/s = 0.16$ for the free-streaming initialization. In all the cases, the initial energy density profile in the transverse plane is given by the binary collision density n_{BC} from the optical Glauber model (see Equation 3.1).

The parameters C_e, c_1 and c_2 are tuned separately for each scenario, to approximately describe the observed charged particle multiplicities and $v_2\{4\}$ in Pb+Pb collisions at $\sqrt{s_{NN}} = 5.02$ TeV. For the longitudinal profile, we keep the parametrization used for $\sqrt{s_{NN}} = 2.76$ Pb+Pb collisions [104]. The equation of state is $s95p$-PCE-v1 [143]. We use freeze-out temperatures $T_{\rm chem} = 150$ MeV and $T_{\rm dec} = 100$ MeV for cases without pre-hydro flow but with free streaming, we use $T_{\rm chem} = 175$ MeV [175] to mimic bulk viscosity around the critical temperature T_c required to fit the p_T distributions, and $T_{\rm dec} = 140$ MeV.

In the free-streaming initialization massless particles stream freely from $\tau = 0.2$ fm to $\tau_0 = 1.0$ fm, where the energy-momentum tensor based on the distributions of these particles is evaluated. The energy-momentum tensor is decomposed into densities, flow velocity, and dissipative currents, which are used as the initial state of the subsequent fluid-dynamical evolution. The switch from massless non-interacting particles to strongly interacting constituents of QGP causes large positive bulk pressure at τ_0. In our calculations, the bulk viscosity coefficient is always zero, and the initial bulk pressure will approach zero according to Israel-Stewart equations [104].

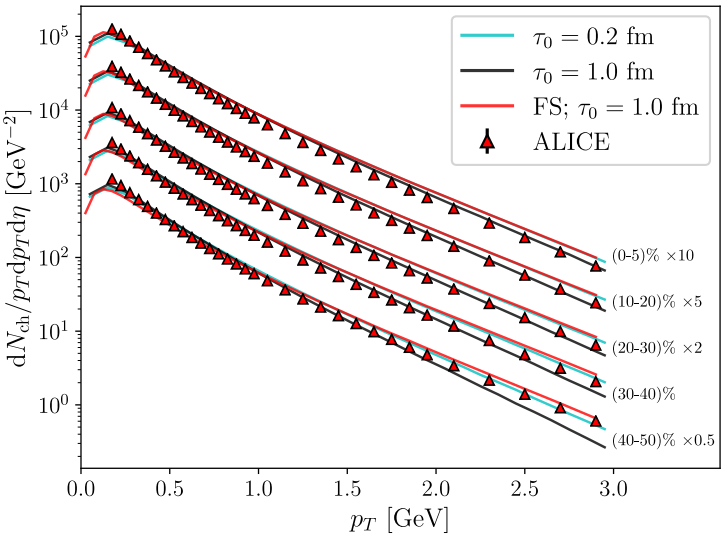

Figure 3.6: Agreement with low-$p_\perp$ data for all the temperature profiles that we explore. The figure shows the transverse momentum spectrum of charged particles in five centrality classes in Pb+Pb collisions at $\sqrt{s_{NN}} = 5.02$TeV, with two initial times $\tau_0 = 0.2$ and $\tau_0 = 1.0$fm, and free streaming initialization (FS). ALICE data is taken from [144].

The transverse momentum distributions of charged particles are shown in Fig. 3.6, and $p_\perp$-differential elliptic flow parameter $v_2\{4\}(p_\perp)$ in the low momentum part ($p_\perp < 2$ GeV) of the lower panels of Fig. 3.7. As seen, the overall agreement with the data is acceptable.

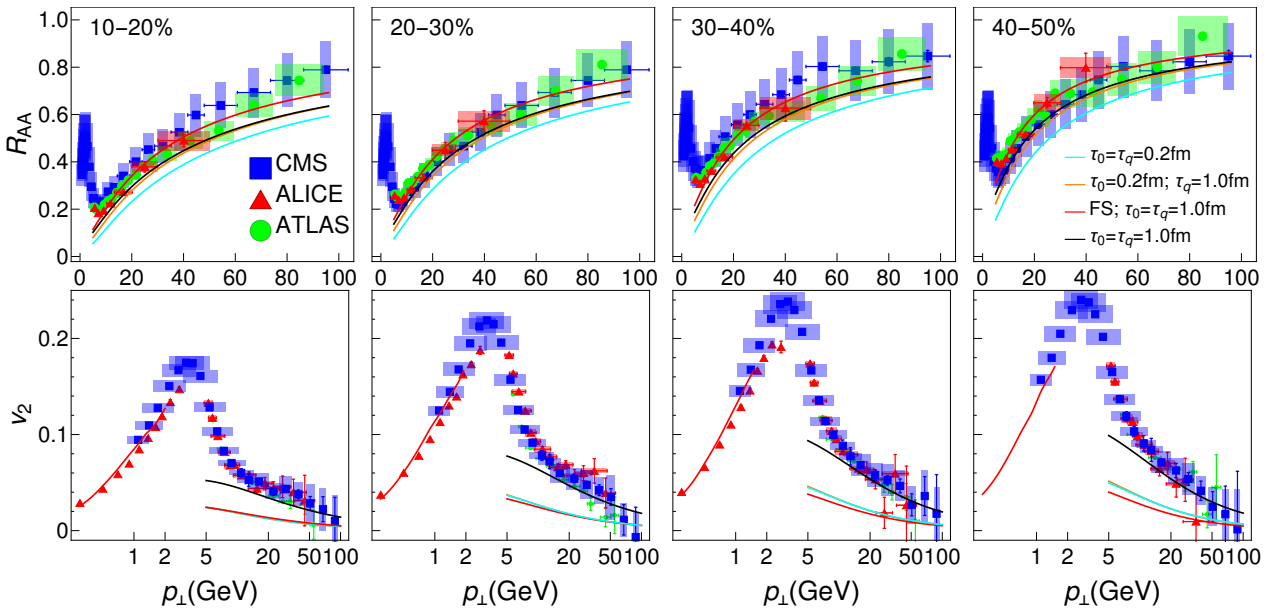

Figure 3.7: Charged hadron DREENA-A R_{AA} (upper panels) and v_2 (lower panels) predictions, generated for different τ_0, τ_q, and initialization (see the legend, FS stands for free streaming), are compared with ALICE [144, 145], CMS [146, 147] and ATLAS [148, 149] data. Four columns, from left to right, correspond to 10–20%, 20–30%, 30–40% and 40–50% centralities at $\sqrt{s_{NN}} = 5.02$ Pb+Pb collisions at the LHC. At low $p_\perp$ ($p_\perp < 2$ GeV) v_2 is 4-cumulant $v_2\{4\}$, whereas at high $p_\perp$ ($p_\perp > 5$ GeV) we evaluate v_2 as $v_2 = (1/2)\,(R_{\rm AA}^{\rm in} - R_{\rm AA}^{\rm out})/(R_{\rm AA}^{\rm in} + R_{\rm AA}^{\rm out})$. Note that the $p_\perp$ scale in the upper (R_{AA}) row is regular, while in the lower (v_2), it is logarithmic.

3.2.2 High-$p_\perp$ $R_{\rm AA}$ and v_2 results

We then use DREENA-A to generate high-$p_\perp$ predictions for the four described scenarios of early evolution and compare them with the experimental data. We use the same parameter set as already described in this Chapter (Subsection 3.1.2).

The resulting DREENA-A predictions for charged hadron R_{AA} and v_2 in four different centrality classes, and four scenarios of early evolution, are shown in Fig. 3.7 and compared with experimental data. We here focus on these four limiting cases, while the results for more sophisticated initializations can be found in Appendix A. As one can expect, the later the energy loss begins, the higher the $R_{\rm AA}$, and evaluating the energy loss as in thermalized medium already at $\tau_q = 0.2$ fm is slightly disfavored. Furthermore, early free-streaming evolution leads to larger $R_{\rm AA}$ than fluid-dynamical evolution. On the other hand, the behavior of v_2 is different. First, if the early expansion is fluid dynamical, we see that delaying the onset of energy loss barely changes the value of v_2. Second, early free-streaming evolution does not lead to better data reproduction, but in peripheral collisions, the fit is even worse. The only case when our v_2 predictions approach the data is when *both* the jet energy loss *and* the transverse expansion are delayed to $\tau = 1$ fm.

As shown in Fig. 3.8, heavy quarks are even more sensitive to early evolution. The data are mainly unavailable for bottom probes, making these true predictions. The available experimental data for charm probes are much more sparse (with larger error bars) than the charged hadron data. However, where available, a comparison of our predictions with the data suggests the same preference towards delayed energy loss and transverse expansion as charged hadrons. As mentioned, these results are significant, as consistency between light and heavy flavor is

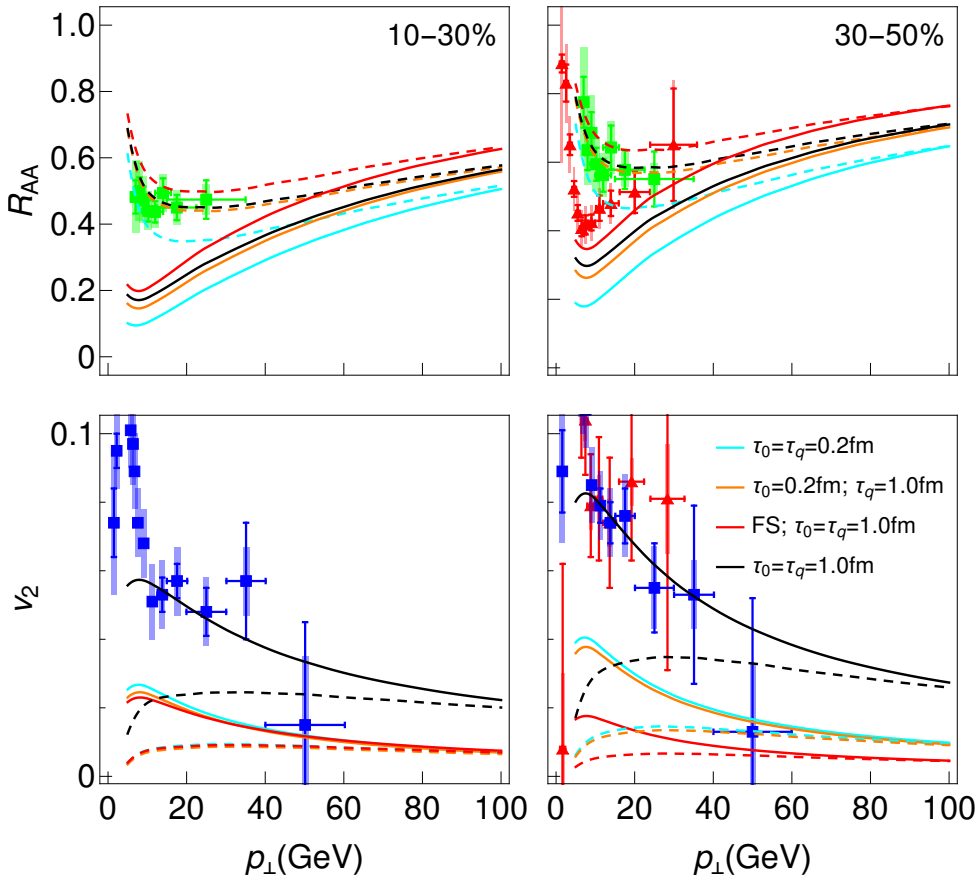

Figure 3.8: Heavy flavor predictions for the four explored scenarios of early evolution. Predicted D (full curves) and B meson (dashed curves) R_{AA} (upper panels) and v_2 (lower panels) in Pb+Pb collisions at $\sqrt{s_{NN}}$ = 5.02 TeV. The predictions for D mesons are compared with ALICE [156, 157] (red triangles) and CMS [158] (blue squares) D meson data, while predictions for B mesons are compared with CMS [159] (green circles) non-prompt J/Ψ data.

crucial (though highly non-trivial, as implied by the well-known heavy flavor puzzle [160]) for studying the QGP properties.

3.2.3 Explaining the observed sensitivity

To investigate the origin of the sensitivity of $R_{\rm AA}$ and v_2 to the early evolution, we evaluate the temperature along the paths of jets traveling in-plane ($\phi = 0$) and out-of-plane ($\phi = \pi/2$) directions, and average over all sampled jet paths. In Fig. 3.9 we show the time evolution of the average temperatures in in- and out-of-plane directions, and their difference in 10–20% and 30-40% central collisions for $\tau_0 = 0.2$ and 1.0 fm, and the free streaming initialization.

The behavior of $R_{\rm AA}$ is now easy to understand in terms of average temperature: Larger τ_q, i.e., a delay in the onset of energy loss cuts away the large temperature part of the profile, decreasing the average temperature, and thus increasing the R_{AA}. Similarly, for the late start of the transverse expansion, i.e., $\tau_0 = 1.0$ fm, the temperature is first slightly larger and later lower than for $\tau_0 = 0.2$ fm, and thus the $R_{\rm AA}$ in $\tau_0 = \tau_q = 1.0$ fm and $\tau_0 = 0.2$ with $\tau_q = 1.0$ cases is almost identical. On the other hand, due to the rapid expansion of the edges of the system, free streaming initialization leads to lower average temperature than any other scenario, and thus to the largest $R_{\rm AA}$.

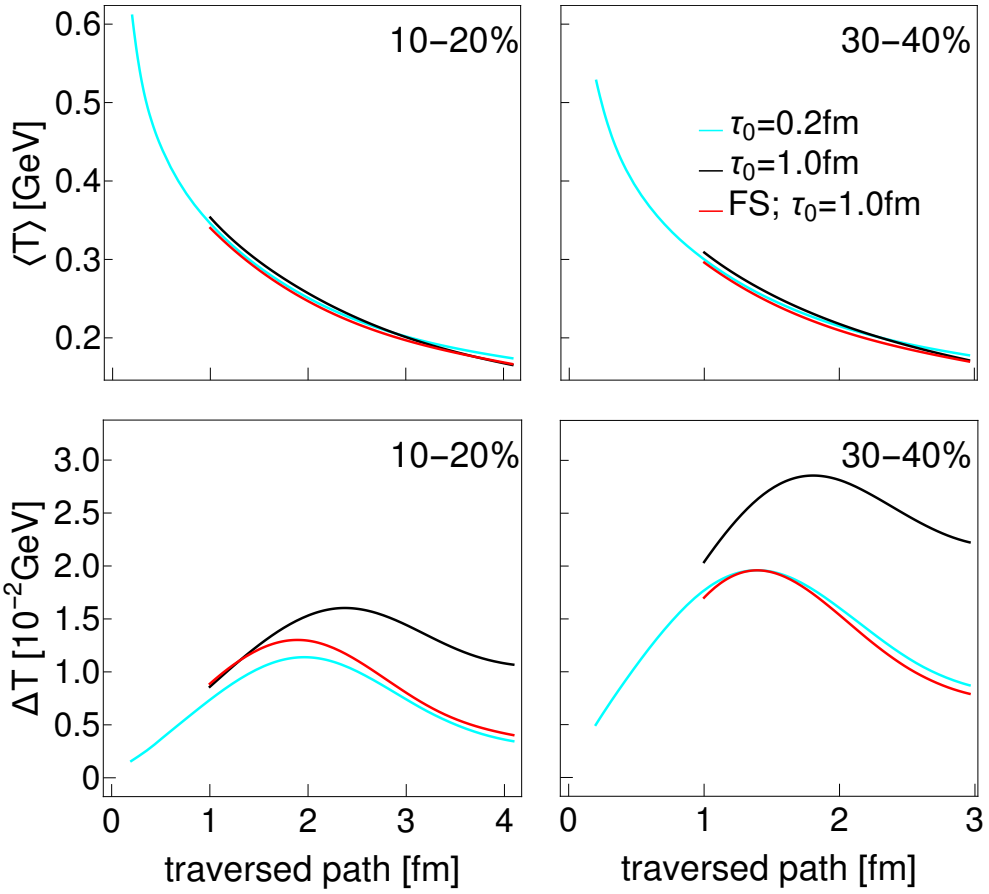

Figure 3.9: Average temperature along the jet path traversing the system (upper panel) and the difference of average temperatures in out-of-plane and in-plane directions (lower panel) for $\tau_0 = 0.2$ and 1.0 fm and free-streaming initialization at 10-20% and 30-40% centrality classes. The average is over all sampled jet paths, and the path ends at the critical temperature, $T_C \approx 160$ MeV [162].

High-$p_\perp$ v_2, on the other hand, is proportional to the difference in temperature along in-plane and out-of-plane directions and to a lesser extent, to the average temperature. Delaying the onset of transverse expansion to $\tau_0 = 1.0$ fm leads to a larger difference than early fluid-dynamical or free streaming expansion; thus, v_2 is the largest. As well as delaying the onset of energy loss by increasing τ_q hardly changes v_2, since at early times the temperatures that are seen by jets in in- and out-of-plane directions are almost identical, and no v_2 is built up at that time. Early free streaming and early fluid-dynamical expansion lead to similar differences in temperatures. The slightly larger difference in the 10-20% centrality class is counteracted by slightly lower temperature, and thus final v_2 is practically identical in both cases. The temperature differences are almost identical in the more peripheral 30-40% class, but the lower average temperature leads to lower v_2 for free streaming.

The delay in transverse expansion affects the average temperature along the jet in two ways. First, smaller τ_0 means more significant initial gradients, faster flow build-up, and faster initial spatial anisotropy dilution. Similarly, free-streaming leads to an even faster flow build-up and dilution of spatial anisotropies than early fluid-dynamical expansion. Second, since the initial jet production is azimuthally symmetric, and jets travel along eikonal trajectories, at early times, both in- and out-of-plane jets probe the temperature of the medium almost the same way. Only over time will the spatial distribution of in- and out-of-plane jets differ, and the average temperature along their paths begins to reflect the anisotropies of the fluid

temperature. This qualitative understanding indicates that the obtained conclusions are largely model-independent.

The idea of using high-$p_\perp$ theory and data to explore QGP is not new; see e.g. Refs. [176, 177, 178, 179, 180, 181, 182, 183, 184, 185, 186]. While some of these approaches can achieve a reasonable agreement with the data (see e.g. [180, 187, 188]), this agreement relies on adjusting fitting parameter(s) in the energy loss model, which prevents them from constraining the bulk medium properties. These models thus largely concentrate on investigating the nature of parton interactions (e.g., a new phenomenon of magnetic monopoles is systematically introduced in [180]) rather than exploring which dynamical evolution better explains the data. In contrast, the goal of our approach is to constrain the bulk QGP behavior. The major advantage of our framework is that it does not use fitting parameters in the energy loss model, enabling us to explore the effects of different bulk medium evolutions. We can even use R_{AA} to make conclusions about the bulk properties of the system, where our R_{AA} results imply that the energy loss during the very early evolution is weaker than energy loss in a fully thermal system.

Furthermore, our study shows that not only is early energy loss suppressed [177, 179], but the early build-up of transverse expansion must be delayed as well. It is insufficient to delay cooling, as suggested in Ref. [177]. However, the initial anisotropy must be diluted much slower than given by free streaming or fluid dynamics. We do not expect current more sophisticated approaches to pre-equilibrium dynamics, like KøMPøST (a stylized acronym formed from the names of its authors: Kurkela, Mazeliauskas, Paquet, Schlichting, Teaney) based on effective kinetic theory [171, 172], to resolve this issue. This approach uses nonequilibrium Green's functions to propagate the initial energy-momentum tensor to the phase where hydrodynamics is applicable [171]. As seen in Ref. [166], except in most peripheral collisions, both KøMPøSTing and free streaming lead to very similar final distributions. Thus we may expect that at the time of switching to fluid dynamics, they both have led to very similar flow and temperature profiles (and thus anisotropies).

Alternatively, the initial spatial anisotropies could be way larger than considered here. It is known that both IP-Glasma and EKRT approaches lead to larger eccentricities than Glauber, but we have tested that they both lead to too low high-$p_\perp$ v_2 if the fluid dynamical evolution begins as usually assumed in calculations utilizing IP-Glasma or EKRT initializations (refer to Appendix A for these results). Event-by-event fluctuations may enhance spatial anisotropies as well, and by generating shorter-scale structures, they may enhance the sensitivity of high-$p_\perp$ v_2 to spatial anisotropies. However, for these additional structures to enhance the high-$p_\perp$ v_2, they should be correlated with the event plane[1] [189, 139], which is not necessarily the case.

In summary, in this Chapter, we presented (to our knowledge) the first example of using high-$p_\perp$ theory and data to provide constraints to bulk QGP evolution. Specifically, we inferred that experimental data suggest that the system's energy loss and transverse expansion at early times should be significantly weaker than in conventional models. We emphasize that the assumption that no energy loss nor transverse expansion takes place before $\tau_0 = 1.0$ fm is unrealistic. We are not advocating such a scenario, but note that the only way to test our hypothesis that the early energy loss and expansion should be suppressed was to take the limit of no energy loss nor transverse expansion. This approach significantly improves the agreement with the data, thus supporting our hypothesis. While our finding of delayed onset of energy loss and transverse expansion has yet to be physically understood, there have been several anomalies in the history of heavy-ion physics, and this result is one more of them.

[1] The event plane is defined by the azimuthal angle Ψ_n – it is the plane which maximizes anisotropy v_n [189]. One can define a normalized low-$p_\perp$ flow vector for the n-th harmonic as $Q_n = |v_n|e^{in\Psi_n}$, with the event plane angle given as $\Psi_n = \arctan\left(\frac{\mathrm{Im}Q_n}{\mathrm{Re}Q_n}\right)/n$ [139]. One can define similar quantities for high-$p_\perp$ flow coefficients [139].

Furthermore, heavy flavor observables show significant sensitivity to the details of early evolution, so the upcoming high-luminosity measurements will further test our conclusion. Our results demonstrate inherent interconnections between low- and high-$p_\perp$ physics, strongly supporting the utility of our QGP tomography approach, where bulk QGP properties are *jointly* constrained by low- and high-$p_\perp$ data.

Chapter 4

The Anisotropy of Quark-Gluon Plasma Constrained through High-$p_\perp$ Data

This Chapter is based on [3, 4]. We show, through analytic arguments, numerical calculations, and comparison with experimental data, that the ratio of the high-$p_\perp$ observables $v_2/(1-R_{\rm AA})$ reaches a well-defined saturation value at high $p_\perp$, and that this ratio depends only on the spatial anisotropy of the quark-gluon plasma (QGP) formed in ultrarelativistic heavy-ion collisions. To this end, we use our state-of-the-art dynamical energy loss formalism embedded in the DREENA framework. In the first step, the medium is modeled as a simple 1+1D Bjorken expansion and later by full hydrodynamical simulations. We show that the ratio of high-$p_\perp$ v_2 and $(1-R_{AA})$ predictions directly reflects the time-averaged anisotropy of the evolving QGP, as seen by the jets and introduce a new observable (*jet-perceived anisotropy*) to quantify this effect.

4.1 In the Bjorken-expanding medium

4.1.1 Introduction

The quark-gluon plasma, created at the LHC and RHIC experiments by colliding heavy ions at ultra-relativistic energies, can be of different sizes, densities, and shapes, depending on the colliding nuclei's size and the collision's energy and centrality. In non-central collisions, the overlap region of the colliding nuclei has an ellipsoidal shape. Thus in the standard experimental setup, in which the colliding nuclei and collision energy are fixed (e.g. in Pb+Pb collisions at $\sqrt{s_{\rm NN}} = 5.02$TeV collision energy at the LHC), the centrality of collision defines both the size and shape of the created QGP fireball.

The eccentric shape of the collision system leads to corresponding anisotropy in the azimuthal distribution of final particles (so-called elliptic and triangular flows), where the elliptic flow parameter v_2 is the second Fourier coefficient of the azimuthal distribution of produced particles (see Equation 1.22 in Chapter 1).

The mechanism of how the initial spatial anisotropy is converted to final momentum anisotropy is different for low- and high-$p_\perp$ particles:

- For low-$p_\perp$ particles, the eccentric shape leads to different pressure gradients in different directions affecting the strength of collective motion in different directions, and thus to azimuthal variation in the particle emission.
- For high $p_\perp$ particles, eccentricity leads to different paths and consequently different energy losses of high-$p_\perp$ jets when they traverse the medium in the in-plane and out-of-plane directions.

While the observed anisotropies of final state particles have an essential role in studying the properties of the QCD matter, to extract, say, the shear viscosity coefficient over entropy density ratio η/s from the final state distributions, one must know the initial state anisotropy as well.

However, despite its essential importance, it still needs to be possible to infer the initial anisotropy from experimental measurements directly. It is possible to measure the anisotropy at the last point of interaction, i.e., at freeze-out, using Hanbury-Brown interferometry [190]. Alternatively, one can measure event-by-event fluctuations of the anisotropy by measuring fluctuations of elliptic and triangular flows [191]. However, it is not possible to measure the average initial state anisotropy.

Several theoretical studies [192, 193, 194, 90] have provided different methods for calculating the initial density distribution of the matter produced in heavy-ion collisions and, thus, the initial anisotropy. These approaches, however, lead to notably different predictions. Since an accurate estimate of anisotropy is a major limiting factor for precision QGP tomography, it is evident that alternative approaches for inferring anisotropy are necessary. Optimally, these approaches should complement the existing predictions and rely on a method that is not based on models of early stages of QCD matter.

With this goal in mind, we propose a novel approach where the anisotropy of the droplet of quark-gluon plasma can be inferred from the already available high-$p_\perp$ measurements. Namely, the energy loss of rare high-momentum partons traversing this matter is known to be an excellent probe of its properties [107, 108, 109]. Different observables probe the medium differently, such as the nuclear modification factor $R_{\rm AA}$ and the elliptic flow parameter v_2 of high-$p_\perp$ particles. However, they all depend not only on the properties of the medium but also on the density, size, and shape of the QGP droplet created in a heavy-ion collision. Thus drawing firm conclusions about the material properties of QGP is very time-consuming and requires a simultaneous description of several observables. It would therefore be instrumental if there were an observable, or combination of observables, which would be sensitive to only one or just a few of all the parameters describing the system.

For high-$p_\perp$ particles, spatial asymmetry leads to different paths, and consequently to different energy losses. Consequently, v_2 (angular differential suppression) carries information on both the spatial anisotropy and material properties that affect energy loss along a given path. On the other hand, $R_{\rm AA}$ (angular average suppression) carries information only on material properties affecting the energy loss [107, 108, 195, 196], so one might expect to extract information on the system anisotropy by taking a ratio of expressions which depend on v_2 and $R_{\rm AA}$. Of course, it is far from trivial whether such intuitive expectations hold, and what combination of v_2 and $R_{\rm AA}$ one should take to extract the spatial anisotropy. To address this, we here use both analytical and numerical analysis to show that the ratio of v_2 and $1-R_{\rm AA}$ at high $p_\perp$ depends only on the spatial anisotropy of the system. This approach provides a complementary method for evaluating the anisotropy of the QGP fireball, and advances the applicability of high-$p_\perp$ data to a new level as, up to now, these data were mainly used to study the jet-medium interactions rather than inferring bulk QGP parameters.

4.1.2 Anisotropy and high-$p_\perp$ observables

In [108, 197], it was shown that at very large values of transverse momentum $p_\perp$, the fractional energy loss $\Delta E/E$ (which is otherwise very complex, both analytically and numerically, due to inclusion of multiple effects; see Chapter 2 for more details) shows asymptotic scaling behavior

$$\Delta E/E \approx \chi(p_\perp)\langle T\rangle^a \langle L\rangle^b, \tag{4.1}$$

where $\langle L\rangle$ is the average path length traversed by the jet, $\langle T\rangle$ is the average temperature along the path of the jet, χ is a proportionality factor (which depends on initial jet $p_\perp$), and a and b are proportionality factors which determine the temperature and path-length dependence of the energy loss. Based on Refs. [117, 118, 110, 119], we might expect values like $a = 3$ and $b = 1$ or 2, but a fit to a full-fledged calculation yields the following values [138, 197, 198]:

$$a \approx 1.2,$$
$$b \approx 1.4.$$

Thus the temperature dependence of the energy loss is close to linear, while the length dependence is between linear and quadratic. To evaluate the path length, we follow Ref. [137]:

$$L(x, y, \phi) = \frac{\int_0^\infty \mathrm{d}\lambda\, \lambda\, \rho(x + \lambda\cos(\phi), y + \lambda\sin(\phi))}{\int_0^\infty \mathrm{d}\lambda\, \rho(x + \lambda\cos(\phi), y + \lambda\sin(\phi))}, \tag{4.2}$$

which gives the path length of a jet produced at point (x, y) heading to direction ϕ, and where $\rho(x, y)$ is the initial density distribution of the QGP droplet. To evaluate the average path length we take average over all directions and production points.

If $\Delta E/E$ is small (i.e., for high $p_\perp$ and in peripheral collisions), we obtain [130, 107, 108, 197]

$$R_{\mathrm{AA}} \approx 1 - \xi\langle T\rangle^a \langle L\rangle^b, \tag{4.3}$$

where:

$$\xi = \frac{(n-2)}{2}\chi, \tag{4.4}$$

where χ is a proportionality factor [107] and n is the steepness of a power-law fit to the initial transverse momentum distribution:

$$\frac{\mathrm{d}N}{\mathrm{d}p_\perp} \propto \frac{1}{p_\perp^n}. \tag{4.5}$$

Thus $1 - R_{\mathrm{AA}}$ is proportional to the average size and temperature of the medium. To evaluate the anisotropy, we define the average path lengths in the in-plane and out-of-plane directions,

$$\begin{aligned} \langle L_{in}\rangle &= \frac{1}{\Delta\phi}\int_{-\Delta\phi/2}^{\Delta\phi/2} \mathrm{d}\phi\, \langle L(\phi)\rangle, \\ \langle L_{out}\rangle &= \frac{1}{\Delta\phi}\int_{\pi/2-\Delta\phi/2}^{\pi/2+\Delta\phi/2} \mathrm{d}\phi\, \langle L(\phi)\rangle, \end{aligned} \tag{4.6}$$

where $\Delta\phi = \pi/6$ [199] is the acceptance angle with respect to the event plane (in-plane) or orthogonal to it (out-of-plane), and $\langle L(\phi)\rangle$ the average path length in ϕ direction. Note that the obtained calculations are robust with respect to the precise value of the small angle $\pm\Delta\phi/2$, but we still keep a small cone ($\pm\pi/12$) for R_{AA}^{in} and R_{AA}^{out} calculations to have the same numerical setup as in our Ref. [108]. Now we can write:

$$\langle L\rangle = \frac{\langle L_{out}\rangle + \langle L_{in}\rangle}{2}, \tag{4.7}$$

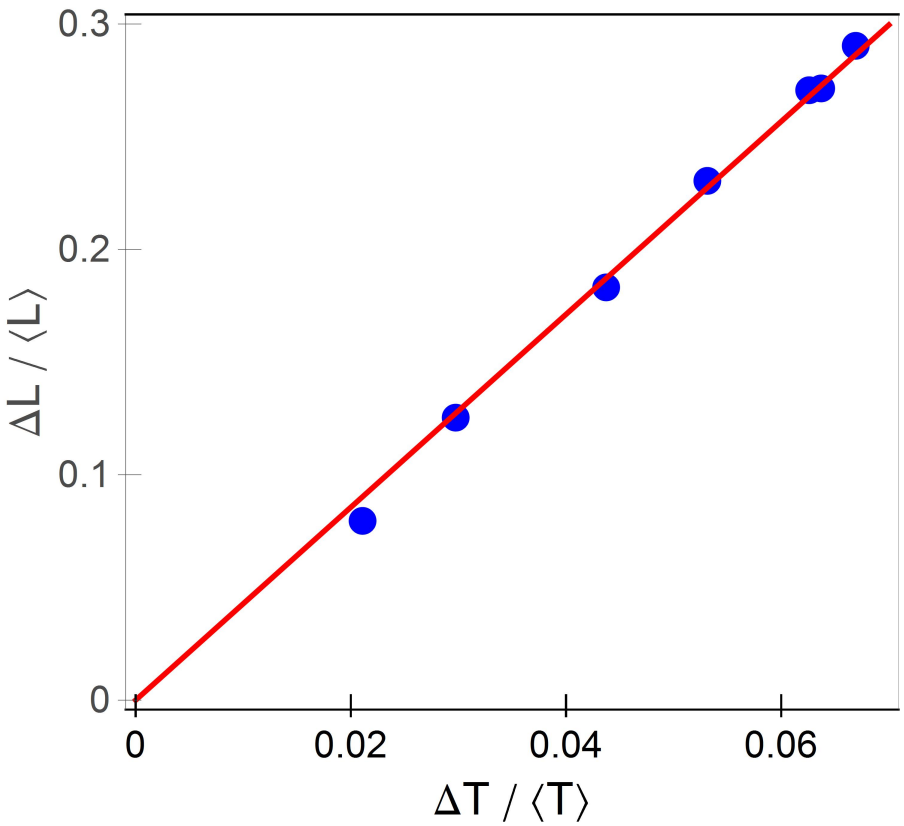

Figure 4.1: The anisotropy expressed through temperature ($\Delta T/\langle T\rangle$) versus the anisotropy expressed through path-lengths ($\Delta L/\langle L\rangle$) in Pb+Pb collisions at $\sqrt{s_{\rm NN}} = 5.02$ TeV collision energy at various centralities (5-10%, 10-20%, 20-30%, 30-40%, 40-50%, 50-60%, 60-70%) [107, 108]. The more peripheral the collision, the larger the values. The red solid line depicts a linear fit to the values.

and

$$\Delta L = \frac{\langle L_{out}\rangle - \langle L_{in}\rangle}{2}. \tag{4.8}$$

Similarly, the average temperature along the path length can be split to average temperatures along paths in in- and out-of-plane directions:

$$\langle T_{in}\rangle = \langle T\rangle + \Delta T, \tag{4.9}$$

and

$$\langle T_{out}\rangle = \langle T\rangle - \Delta T. \tag{4.10}$$

When applied to an approximate way to calculate v_2 of high-$p_\perp$ particles (refer to the definition of v_2 in Chapter 1), we obtain

$$\begin{aligned} v_2 &\approx \frac{1}{2}\frac{R^{in}_{\rm AA} - R^{out}_{\rm AA}}{R^{in}_{\rm AA} + R^{out}_{\rm AA}} \approx \frac{\xi\langle T_{out}\rangle^a\langle L_{out}\rangle^b - \xi\langle T_{in}\rangle^a\langle L_{in}\rangle^b}{4} \\ &\approx \xi\langle T\rangle^a\langle L\rangle^b\left(\frac{b}{2}\frac{\Delta L}{\langle L\rangle} - \frac{a}{2}\frac{\Delta T}{\langle T\rangle}\right), \end{aligned} \tag{4.11}$$

where we have assumed that $\xi\langle T\rangle^a\langle L\rangle^b \ll 1$, and that $\Delta L/\langle L\rangle$ and $\Delta T/\langle T\rangle$ are small as well. Note that the first approximate equality in Eq. (4.11) can be shown to be exact if the higher harmonics v_4, v_6, etc., are zero, and the opening angle where $R^{in}_{\rm AA}$ and $R^{out}_{\rm AA}$ are evaluated is zero (cf. definitions of $\langle L_{out}\rangle$ and $\langle L_{in}\rangle$, Eq. (4.6)).

By combining Eqs. (4.3) and (4.11), we obtain:

$$\frac{v_2}{1-R_{\rm AA}} \approx \left(\frac{b}{2}\frac{\Delta L}{\langle L\rangle} - \frac{a}{2}\frac{\Delta T}{\langle T\rangle}\right). \tag{4.12}$$

This ratio carries information on the anisotropy of the system, but through both spatial ($\Delta L/\langle L\rangle$) and temperature ($\Delta T/\langle T\rangle$) variables. From Eq. (4.12), we see the usefulness of the (approximate) analytical derivations, since the term $(1-R_{\rm AA})$ in the denominator could hardly have been deduced intuitively or pinpointed by numerical trial and error. Figure 4.1 shows a linear dependence:

$$\frac{\Delta L}{\langle L\rangle} \approx c\frac{\Delta T}{\langle T\rangle}, \tag{4.13}$$

where $c \approx 4.3$, with the temperature evolution given by one-dimensional Bjorken expansion, as sufficient to describe the early evolution of the system. Eq. (4.12) can thus be simplified to

$$\begin{aligned} \frac{v_2}{1-R_{\rm AA}} &\approx \frac{1}{2}\left(b-\frac{a}{c}\right)\frac{\langle L_{out}\rangle - \langle L_{in}\rangle}{\langle L_{out}\rangle + \langle L_{in}\rangle} \approx 0.57\varsigma, \\ \text{where}\quad \varsigma &= \frac{\langle L_{out}\rangle - \langle L_{in}\rangle}{\langle L_{out}\rangle + \langle L_{in}\rangle} \quad \text{and} \quad \frac{1}{2}(b-\frac{a}{c}) \approx 0.57, \end{aligned} \tag{4.14}$$

when $a \approx 1.2$ and $b \approx 1.4$. Consequently, the asymptotic behavior of observables $R_{\rm AA}$ and v_2 is such that, at high $p_\perp$, their ratio is dictated solely by the geometry of the fireball. Therefore, the anisotropy parameter ς can be extracted from the high-$p_\perp$ experimental data.

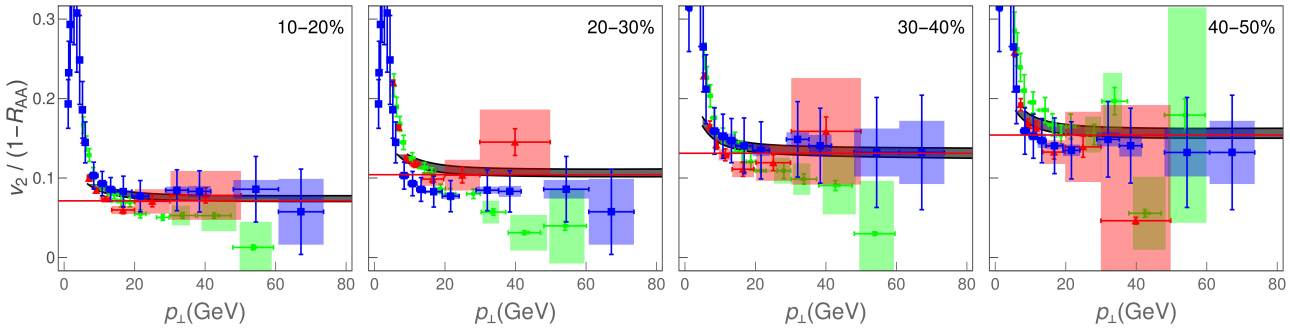

Figure 4.2: Theoretical predictions for $v_2/(1-R_{AA})$ ratio of charged hadrons as a function of transverse momentum $p_\perp$ compared with 5.02 TeV $Pb+Pb$ ALICE [144, 145] (red triangles), CMS [146, 147] (blue squares) and ATLAS [148, 149] (green circles) data. Panels correspond to 10-20%, 20-30%, 30-40%, and 40-50% centrality bins. The gray band corresponds to the uncertainty in the magnetic to electric mass ratio μ_M/μ_E. The upper (lower) boundary of the band corresponds to $\mu_M/\mu_E = 0.4$ (0.6) [152, 153]. In each panel, the red line corresponds to the limit 0.57ς from Eq. (4.14).

Regarding the parametrization used to derive Eq. (4.14) (constants a, b and c), we note that a and b are well established within our dynamical energy loss formalism and follow from $R_{\rm AA}$ predictions that are extensively tested on experimental data [197, 198] and do not depend on the details of the medium evolution. Regarding c, it may (to some extent) depend on the type of the implemented medium evolution, but this will not affect the obtained scaling, only (to some extent) the overall prefactor in Eq. (4.14).

4.1.3 Numerical results

To assess the applicability of the analytically derived scaling in Eq. (4.14), we calculate $v_2/(1-R_{\rm AA})$ using our full-fledged numerical procedure for calculating the fractional energy loss described in Chapter 2.

The formalism was further embedded into DREENA-B framework [108], which includes all the ingredients of the dynamical energy loss formalism, and models the medium as a 1+1D Bjorken expansion (see Chapters 1 and 2 for more details).

The framework was recently used to obtain joint R_{AA} and v_2 predictions for 5.02 TeV Pb+Pb collisions at the LHC [108], showing a good agreement with the experimental data.

It was previously shown [126] that all the model ingredients affect the high-$p_\perp$ data and thus should be included to explain it accurately. In that respect, DREENA-B differs from many other approaches, which use a sophisticated medium evolution, but an (over)simplified energy loss model. However, it was shown that, for explaining the high-$p_\perp$ data, an accurate description of high-$p_\perp$ parton-medium interactions is at least as important as an advanced medium evolution model. For example, the dynamical energy loss formalism, embedded in 1D Bjorken expansion, explains well the v_2 puzzle [108], i.e., the inability of other models to jointly explain R_{AA} and v_2 measurements.

Our results for the longitudinally expanding system (1D Bjorken) and the corresponding data are shown in Fig. 4.2. The gray band shows our full DREENA-B result (see above) with the band resulting from the uncertainty in the magnetic to electric mass ratio μ_M/μ_E [152, 153]. The red line corresponds to the 0.57ς limit from Eq. (4.14), where ς is the anisotropy of the path lengths used in the DREENA-B calculations [108, 107]. Significantly, for each centrality, the asymptotic regime – where the $v_2/(1-R_{\rm AA})$ ratio does not depend on $p_\perp$ but is determined by the geometry of the system – is already reached from $p_\perp \sim$ 20–30 GeV; the asymptote corresponds to the analytically derived Eq. (4.14), within $\pm 5\%$ accuracy. It is also worth noting that our asymptotic behavior prediction was based on approximations that are not necessarily valid in these calculations. However, the asymptotic regime is nevertheless reached, meaning those assumptions were sufficient to capture the dominant features. If, as we suspect, the high-$p_\perp$ parton-medium interactions are more important than the medium evolution model in explaining the high-$p_\perp$ data, this behavior reflects this importance, and the analytical derivations based on a static medium may capture the dominant features seen in Fig. 4.2.

Furthermore, to check if the experimental data support the derived scaling relation, we compare our results to the ALICE [144, 145], CMS [146, 147] and ATLAS [148, 149] data for $\sqrt{s_{\rm NN}} = 5.02$ TeV $Pb+Pb$ collisions. The experimental data for all three experiments show the same tendency, i.e., the independence on the $p_\perp$ and consistency with our predictions, though the error bars are still considerable. Therefore, from Fig. 4.2, we see that at each centrality, both the numerically predicted and experimentally observed $v_2/(1-R_{\rm AA})$ approach the same high-$p_\perp$ limit. This robust, straight-line, asymptotic value carries information about the system's anisotropy, which is, in principle, simple to infer from the experimental data.

Ideally, the experimental data (here from ALICE, CMS, and ATLAS) would overlap and have small error bars. In such a case, the data could directly extract the anisotropy parameter ς by fitting a straight line to the high-$p_\perp$ part of the $v_2/(1-R_{\rm AA})$ ratio. While such direct anisotropy extraction would be highly desirable, the available experimental data are unfortunately still not near the precision level needed to implement this. However, we expect this to change in the upcoming high-luminosity 3$^{\rm rd}$ run at the LHC, where the error bars are expected to be significantly reduced so that this procedure can be directly applied to experimental data.

4.1.4 The anisotropy parameter

It is worth remembering that the anisotropy parameter ς, which can be extracted from the high-$p_\perp$ data, is not the commonly used anisotropy parameter ϵ_2 [200],

$$\epsilon_2 = \frac{\langle y^2 - x^2 \rangle}{\langle y^2 + x^2 \rangle} = \frac{\int \mathrm{d}x\, \mathrm{d}y\, (y^2 - x^2)\, \rho(x,y)}{\int \mathrm{d}x\, \mathrm{d}y\, (y^2 + x^2)\, \rho(x,y)}, \tag{4.15}$$

where $\rho(x,y)$ is the initial density distribution of the QGP droplet. We may also expect that once the transverse expansion is included in the description of the evolution, the path-length anisotropy ς reflects the time-averaged anisotropy of the system (and indeed, we will see that this is the case in the upcoming section), and therefore is not directly related to the initial-state anisotropy ϵ_2. Nevertheless, it is instructive to check how the path-length anisotropy in our simple model relates to conventional ϵ_2 values in the literature. For this purpose, we construct a variable [3]:

$$\epsilon_{2L} = \frac{\langle L_{out} \rangle^2 - \langle L_{in} \rangle^2}{\langle L_{out} \rangle^2 + \langle L_{in} \rangle^2} = \frac{2\varsigma}{1 + \varsigma^2}. \tag{4.16}$$

We have checked that ϵ_2 and ϵ_{2L} agree within $\sim$10% accuracy for different density distributions.

We have extracted the parameters ς from the DREENA-B results shown in Fig. 4.2; the corresponding ϵ_{2L} results are shown as a function of centrality in Fig. 4.3 and compared to ϵ_2 evaluated using various initial-state models in the literature [192, 193, 194, 90]. Note that conventional (EKRT [193], IP-Glasma [194]) ϵ_2 values trivially agree with our *initial* ϵ_2 (not shown in the Figure), i.e., the initial ϵ_2 characterize the anisotropy of the path lengths used as an input to DREENA-B, which we had chosen to agree with the conventional models [1]. It is, however, much less trivial that, through this procedure, in which we calculate the ratio of v_2 and $1 - R_{AA}$ through complete DREENA framework, our *extracted* ϵ_{2L} almost exactly recovers our initial ϵ_2. Note that ϵ_2 is *indirectly* introduced in R_{AA} and v_2 calculations through path-length distributions, while our calculations are performed using full-fledged numerical procedure, not just Eq. (4.1). Consequently, such direct extraction of ϵ_{2L} and its agreement with our initial (and consequently also conventional) ϵ_2 is highly non-trivial and gives us a good deal of confidence that $v_2/(1 - R_{\mathrm{AA}})$ is related to the anisotropy of the system only, and not its material properties.

High-$p_\perp$ theory and data are traditionally used to explore interactions of traversing high-$p_\perp$ probes with QGP, while bulk properties of QGP are obtained through low-$p_\perp$ data and the corresponding models. On the other hand, high-$p_\perp$ probes are also powerful tomography tools since they are sensitive to global QGP properties. We demonstrated this in the spatial anisotropy of the QCD matter formed in ultrarelativistic heavy-ion collisions. We used our dynamical energy loss formalism and DREENA-B framework to show that a (modified) ratio of two main high-$p_\perp$ observables, R_{AA} and v_2, approaches an asymptotic limit at experimentally accessible transverse momenta and that this asymptotic value depends only on the shape of the system, not on its material properties. However, how exactly this asymptotic value reflects the shape and anisotropy of the system requires further study employing full three-dimensional expansion, the results of which will be shown in the upcoming section of this Chapter.

The experimental accuracy still needs to allow the extraction of the anisotropy from the data using our scheme. However, once the accuracy improves in the upcoming LHC runs, we expect the anisotropy of the QGP formed in heavy-ion collisions can be inferred directly from the data. Such an experimentally obtained anisotropy parameter would provide an essential

[1] Binary collision scaling calculated using optical Glauber model with additional cut-off in the tails of Woods-Saxon potentials, to be exact.

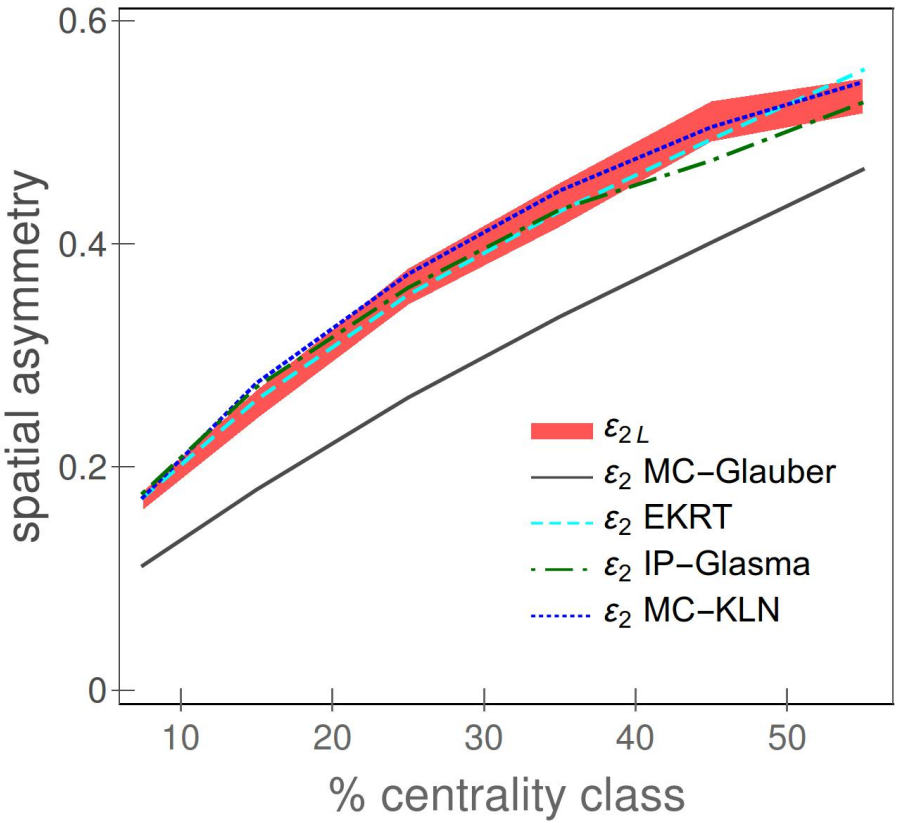

Figure 4.3: Comparison of ϵ_{2L} (red band) obtained from our method, with ϵ_2 calculated using Monte Carlo (MC) Glauber [192] (gray band), EKRT [193] (the purple band), IP-Glasma [194] (green dot-dashed curve), and MC-KLN [90] (blue dotted curve) approaches. MC-Glauber and EKRT results correspond to 5.02 TeV, while IP-Glasma and MC-KLN correspond to 2.76 TeV $Pb + Pb$ collisions at the LHC.

constraint to models describing the early stages of heavy-ion collision and QGP evolution and demonstrate the synergy of high-$p_\perp$ theory and data with more common approaches for inferring QGP properties.

4.2 Exploring the anisotropy of the fully evolving medium through high-$p_\perp$ data

We previously argued that, at large enough values of transverse momentum (high-$p_\perp$), the ratio of the elliptic flow v_2 and $1-R_{\rm AA}$, where $R_{\rm AA}$ is the nuclear suppression factor, saturates and reflects the initial geometry of the system. However, this argument was based on analytic considerations and a simple 1-dimensional expansion [93, 108], where the geometry does not depend on time. To see how the evolving shape of the collision system affects the high-$p_\perp$ observables and, subsequently, the $v_2/(1-R_{\rm AA})$ ratio, we here study the behavior of this ratio in a system that expands both in longitudinal and transverse directions.

Furthermore, there is experimental evidence for such saturation. As shown in Fig. 4.4, at high values of transverse momentum, v_2 and $1-R_{\rm AA}$ are directly proportional, which is equivalent to a $p_\perp$-independent ratio of v_2 and $1-R_{\rm AA}$. We here explore whether state-of-the-art fluid-dynamical calculations tuned to reproduce the low-$p_\perp$ data can reproduce such proportionality and whether we can relate this proportionality to a physical property of the system, namely to the anisotropy of its shape.

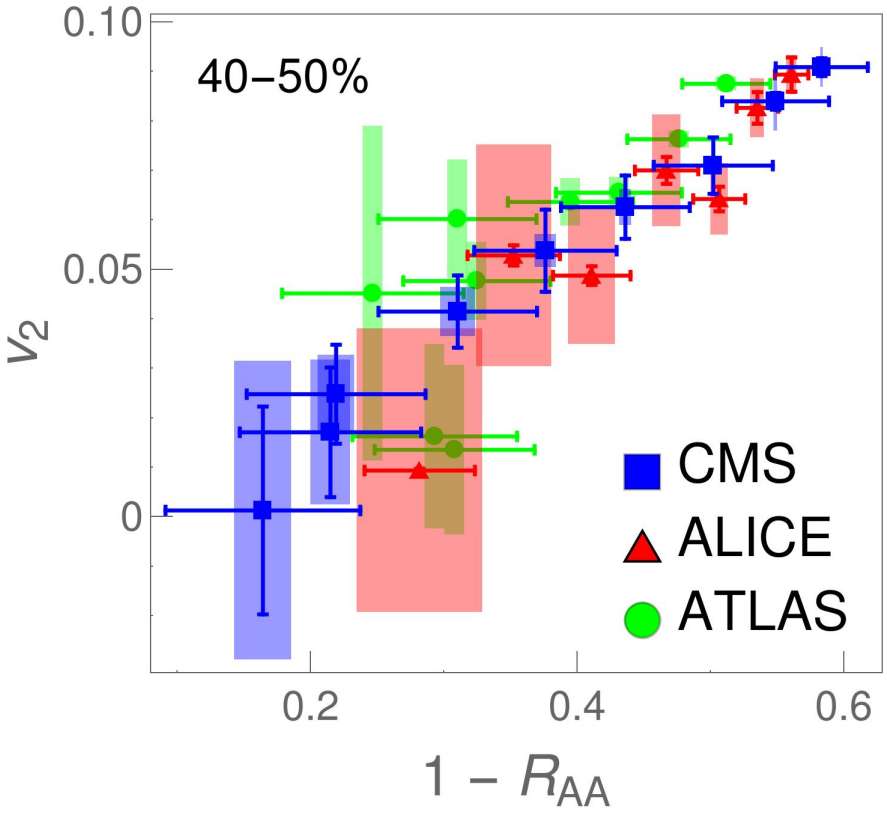

Figure 4.4: Direct proportionality of high-$p_\perp$ v_2 and $1-R_{AA}$, which suggests that their ratio is $p_\perp$-independent. The figure shows v_2 vs $1-R_{\rm AA}$ for $p_\perp > 10$ GeV data for charged hadrons from 5.02 TeV Pb+Pb ALICE [144, 145] (red triangles), CMS [146, 147] (blue squares) and ATLAS [148, 149] (green circles) experiments. The data is shown for the 40-50% centrality bin, while similar relation is obtained for other centralities (see Fig. B.1 in Appendix B). Each collaboration's datapoints correspond to different values of $p_\perp$, with both v_2 and $1-R_{\rm AA}$ decreasing with increasing $p_\perp$.

In line with the standard approach in the study of ultrarelativistic heavy-ion collisions, we assume the collision system behaves as a locally thermalized dissipative fluid. The transverse

expansion of such a system largely depends on the initial gradients of the system, i.e., the initial state, and also on the equation of state (EoS) and dissipative properties of the fluid. Thus, to provide more general conclusions about the asymptotic behavior of $v_2/(1-R_{\rm AA})$, it is necessary to explore not only one but several different fluid-dynamical evolution scenarios. On the other hand, it is known that at low-$p_\perp$, the elliptic flow parameter v_2 is proportional to the initial anisotropy of the system $\epsilon_{2,2}$ [201]. However, the proportionality constant depends on the calculation parameters, say the freeze-out temperature. To avoid similar ambiguity, we prefer not to vary the initialization model's parameters randomly but constrain the calculation to reproduce the low-$p_\perp$ data and explore the universality of our results using several different initialization models, collision energies, and systems. In particular, to initialize Pb+Pb collisions at $\sqrt{s_{\rm NN}} = 5.02$ TeV collision energy, we employ optical Glauber [48], T$_{\rm R}$ENTo [89], IP-Glasma [77, 78], and EKRT [86, 87, 88] initializations. In addition, we explore the sensitivity to collision energy and colliding nuclei by using optical Glauber initialization for Pb+Pb collisions at $\sqrt{s_{\rm NN}} = 2.76$ TeV and Xe+Xe collisions at $\sqrt{s_{\rm NN}} = 5.44$ TeV.

We will see that the temperature evolution in different evolution scenarios is different enough to lead to observable differences in high-$p_\perp$ v_2 and $1-R_{\rm AA}$, and the ratio of these observables is directly related to a suitably defined measure of the system anisotropy. The differences in high-$p_\perp$ v_2 and $1-R_{\rm AA}$ mean that constraining the calculation to reproduce the low-$p_\perp$ data does not guarantee to reproduce the high-$p_\perp$ data. Simultaneous reproduction of both is not an aim of this study but is left for future work.

4.2.1 Medium evolution

Our starting point and reference for all collision energies and systems is a simple optical Glauber model-based initialization. In Pb+Pb collisions at full LHC energy ($\sqrt{s_{\rm NN}} = 5.02$ TeV) we used initial times $\tau_0 = 0.2$, 0.4, 0.6, 0.8, and 1.0 fm, whereas the lower energy ($\sqrt{s_{\rm NN}} = 2.76$ TeV) Pb+Pb and Xe+Xe ($\sqrt{s_{\rm NN}} = 5.44$ TeV) calculations were carried out for $\tau_0 = 0.2$, 0.6, and 1.0 fm. The initialization and code used to solve viscous fluid-dynamical equations in 3+1 dimensions are described in detail in Ref. [104], and parameters to describe Pb+Pb collisions at $\sqrt{s_{\rm NN}} = 5.02$ TeV are the same as in the previous Chapter. In particular, we use a constant shear viscosity to entropy density ratio $\eta/s = 0.12$ (Pb+Pb) or $\eta/s = 0.10$ (Xe+Xe), and the EoS parametrization $s95p$-PCE-v1 [143].

Different initial state models lead to slightly different shapes of the initial state. To find if our findings are a feature of the Glauber model or have broader significance, we did the Pb+Pb calculations at the full LHC energy using several different initial state models. The first option in this extended set, Glauber + Free streaming, is to use the Glauber model to provide the initial distribution of (marker) particles, allow the particles to stream freely from $\tau = 0.2$ to 1.0 fm, evaluate the energy-momentum tensor of these particles, and use it as the initial state of the fluid. We evolve the fluid using the same code as in the case of pure Glauber initialization. The EoS is $s95p$-PCE175, i.e., a parametrisation with $T_{\rm chem} = 175$ MeV [175], and temperature-independent $\eta/s = 0.16$. For further details, see the second part of the previous Chapter.

As more sophisticated initializations, we employ EKRT, IP-Glasma, and T$_{\rm R}$ENTo.

- The EKRT model [86, 87, 88] is based on the NLO perturbative QCD computation of the transverse energy and a gluon saturation conjecture. We employ the same setup as used in Ref. [202] (see also [175]), compute an ensemble of event-by-event fluctuating initial density distributions, average them, and use this average as the initial state of the

fluid dynamical evolution. We again use the code of Molnar et al., [104] but restricted to boost-invariant expansion. The shear viscosity over entropy density ratio is temperature dependent with favored parameter values from the Bayesian analysis of Ref. [202]. Initial time is $\tau_0 = 0.2$ fm, and the EoS is the $s83s_{18}$ parametrisation from Ref. [202].

- IP-Glasma model [77, 78] is based on Color Glass Condensate [82, 83, 84, 85]. It calculates the initial state as a collision of two color glass condensates and evolves the generated fluctuating gluon fields by solving classical Yang-Mills equations. The calculated event-by-event fluctuating initial states [203] were further evolved [204] using the MUSIC code [205, 206, 207] constrained to boost-invariant expansion. We subsequently averaged the evaluated temperature profiles to obtain one average profile per centrality class. In these calculations, the switch from Yang-Mills to fluid-dynamical evolution took place at $\tau_{\text{switch}} = 0.4$ fm, shear viscosity over entropy density ratio was constant $\eta/s = 0.12$, and the temperature-dependent bulk viscosity coefficient over entropy density ratio had its maximum value $\zeta/s = 0.13$. The equation of state was based on the HotQCD lattice results [208] as presented in Ref. [209].

- T$_\text{R}$ENTo [89] is a phenomenological model capable of interpolating between wounded nucleon and binary collision scaling, and with a proper parameter value, of mimicking the EKRT and IP-Glasma initial states. As with the EKRT initialization, we create an ensemble of event-by-event fluctuating initial states, sort them into centrality classes, average, and evolve these average initial states. Unlike in other cases, we employ the version of the VISH2+1 code [210] described in Refs. [211, 212]. We run the code using the favored values of the Bayesian analysis of Ref. [212]; in particular, allow free streaming until $\tau = 1.16$ fm, the minimum value of the temperature-dependent η/s is 0.081, and the maximum value of the bulk viscosity coefficient ζ/s is 0.052. The EoS is the same HotQCD lattice results [208] based parametrization used in Refs. [211, 212].

It is worth noticing that the initial nuclear configuration in all these cases is similar Woods-Saxon parametrization of nuclear matter density, which is either assumed to be continuous (optical Glauber) or Monte-Carlo sampled to create ensembles of nucleons (EKRT, IP-Glasma, T$_\text{R}$ENTo). The differences in the fluid-dynamical initial state depend on the initial particle production and subsequent evolution before the fluid-dynamical stage (none, Yang-Mills, free streaming).

All these calculations were tuned to reproduce, in minimum, the centrality dependence of charged particle multiplicity, $p_\perp$ distributions and $v_2(p_\perp)$ in Pb+Pb collisions at both collision energies, and the centrality dependence of charged particle multiplicity and $v_2\{4\}$ in Xe+Xe collisions.

4.2.2 Numerical and experimental results

To calculate high-$p_\perp$ R_{AA} and v_2, we used the DREENA-A framework [109], described in more detail in Chapter 2.

We succinctly note that the framework does not have free parameters in the energy loss, i.e., all the parameters are fixed to standard literature values. Consequently, it can fully utilize different temperature profiles as the only input in DREENA-A. R_{AA} and v_2 predictions, generated under the same formalism and parameter set (and calculated in a conventional way, see [109]), can thus be systematically compared to experimental data to map out the bulk properties of QGP.

In the context of the results presented in this Chapter, it is worth noting that while the model has several unique features in describing parton-medium interactions, it could still be improved by including, e.g., the flow velocity of the bulk medium and transverse gradients of temperature and density (see, e.g., [213, 214, 215, 216]). However, such improvements are in their infancy in any framework, and implementing them into the dynamical energy loss model while keeping all existing ingredients is challenging. Nevertheless, such improvements might somewhat influence the quantitative results presented in this Chapter, and quantifying such effects is an important future goal.

We compared our predictions with data from the Pb+Pb collisions at $\sqrt{s_{\rm NN}} = 2.76$ and 5.02 TeV analysed by the LHC experiments ALICE [144, 145, 217, 218], CMS [146, 147, 219, 220], and ATLAS [148, 149, 221, 222]. We used v_2 measurement obtained with the scalar product method (defined in [149]). Since we are interested in the high $p_\perp$ region, we considered data with $p_\perp > 10$ GeV. The $p_\perp$ bins are chosen as in the v_2 measurements, and the R_{AA} distributions are interpolated to the chosen binning. Since the CMS experiment used coarser granularity in centrality for R_{AA} measurements, i.e., 10-30% and 30-50%, we assigned the values obtained from 10-30% (30-50%) to both 10-20% and 20-30% (30-40% and 40-50%). Finally, combined uncertainties on the $v_2/(1 - R_{AA})$ are calculated assuming that v_2 and R_{AA} are correlated.

To gain an intuitive insight into how different initializations influence high-$p_\perp$ predictions, we show in Fig. 4.5 temperatures encountered by partons in $\sqrt{s_{\rm NN}} = 5.02$ TeV Pb+Pb collisions as a function of traversed distance using four different temperature profiles. These plots are produced by generating initial high-$p_\perp$ partons' positions according to binary collision densities. Then these partons traverse the medium in the in-plane (red) or out-of-plane (blue) directions, and the temperature they experience is plotted as a function of their path until they leave QGP. The larger the temperature that partons experience while traversing the QGP, the larger the suppression in high-$p_\perp$ observables. Similarly, a larger difference between in-plane or out-of-plane temperatures is related to a larger high-$p_\perp$ v_2.

From Fig. 4.5, we observe that partons traveling in the in-plane and out-of-plane directions experience different temperatures in different scenarios, leading to the different behavior of high-$p_\perp$ particles. For example, based on the maximum temperature encountered, we expect the largest suppression (i.e., the smallest R_{AA}) for 'EKRT'. In contrast, 'Glauber + FS' is expected to lead to the largest R_{AA}. On the other hand, from the difference in in-plane and out-of-plane temperatures, we expect the largest v_2 for 'Glauber, $\tau_0 = 1$ fm', followed by 'IP-Glasma', while v_2 for 'EKRT' should be notably smaller. The ordering of $R_{\rm AA}$ and v_2 is thus different for different evolution scenarios, and therefore it is a priori unclear what the ordering of $v_2/(1 - R_{AA})$ might be.

In this section, we aim to address the following questions:

- Is the saturation in $v_2/(1 - R_{AA})$ at high-$p_\perp$ still observed for these different profiles, as expected from our previous analytical arguments and simple 1D Bjorken expansion?
- If yes, does this saturation carry information about the anisotropy of the system?
- What kind of anisotropy measure corresponds to the high-$p_\perp$ data?

To start addressing these questions, we show in Fig. 4.6 how $v_2/(1-R_{\rm AA})$ depends on $p_\perp$ in Pb+Pb collisions at $\sqrt{s_{\rm NN}} = 2.76$ and 5.02 TeV using different temperature profiles. To avoid cluttering the Figure, at $\sqrt{s_{\rm NN}} = 5.02$ TeV, we concentrate on the same four profiles as shown in Fig. 4.5. The ratio is almost independent of $p_\perp$ above $p_\perp \approx 30$ GeV, although IP-Glasma shows

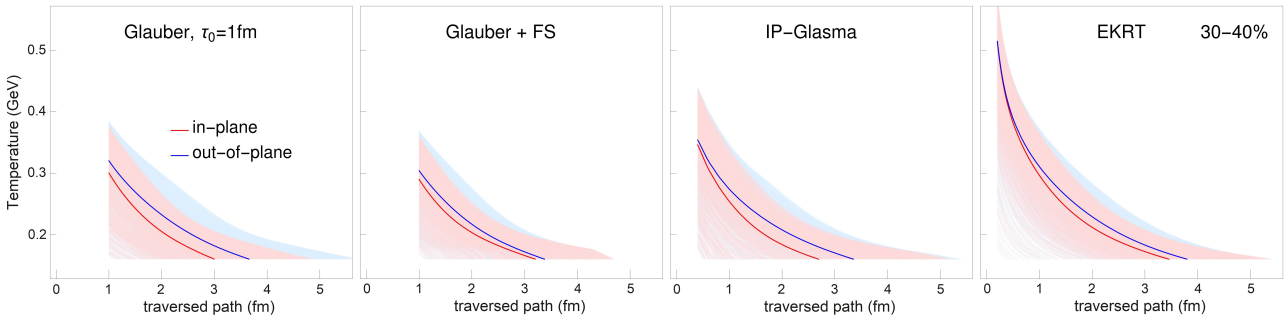

Figure 4.5: Light red (light blue) shaded areas represent the temperatures along the paths of high-$p_\perp$ partons when traversing the medium in the in-plane (out-of-plane) direction. For every scenario, we show 1250 in-plane and out-of-plane trajectories. The temperature profiles are from fluid-dynamical calculations of $\sqrt{s_{\rm NN}} = 5.02$ TeV Pb+Pb collisions in the 30-40% centrality class, utilizing the Glauber model (with $\tau_0 = 1.0$ fm), Glauber + free streaming (FS), IP-Glasma, and EKRT initializations. Dark red (dark blue) curves represent the average temperature experienced by the particles in the in-plane (out-of-plane) directions.

some $p_\perp$ dependence even above this limit. We also confirmed that the saturation is obtained for other hydrodynamic calculations outlined in the Medium evolution subsection (not shown). Thus, we confirm that the phenomenon of $v_2/(1-R_{\rm AA})$ saturation is indeed robust, i.e., holds for a variety of different transversely expanding systems.

We also observe that some profiles lead to better agreement with the data than others. The general trend is that the later the transverse expansion begins (fluid dynamical or otherwise), the better the fit to the data. We have discussed some implications of this finding in Chapter 3. However, here, we explore how the differences in the medium evolution are reflected through high-$p_\perp$ data and leave further comparisons between predictions and the data to later studies.

To find out whether the saturation values of $v_2/(1-R_{\rm AA})$ are correlated with the system geometry, we evaluate the average path length of partons, $\langle L\rangle$, and its anisotropy

$$\frac{\Delta L}{\langle L\rangle} = \frac{\langle L_{out}\rangle - \langle L_{in}\rangle}{\langle L_{out}\rangle + \langle L_{in}\rangle}, \tag{4.17}$$

where $\langle L_{in}\rangle$ and $\langle L_{out}\rangle$ refer to the average path-length of high-$p_\perp$ particles in the in-plane and out-of-plane directions. For every temperature profile, $\langle L_{in}\rangle$ and $\langle L_{out}\rangle$ is calculated using the Monte Carlo method to generate an initial hard parton position in the XY plane according to the binary collision densities. The parton then traverses the medium in the $\phi = 0$ (or $\phi = \pi/2$) direction until the temperature at the parton's current position drops below critical temperature T_c. We use T_c=160 MeV, which is within the uncertainty of the lattice QCD critical temperature of 154 ± 9 MeV [162]. We then obtain $\langle L_{in}\rangle$ and $\langle L_{out}\rangle$ by averaging the in-plane and out-of-plane path lengths over many different partons.

In Fig. 4.7 we have plotted the values of $v_2/(1-R_{AA})$ evaluated at 100 GeV for different initializations, collision energies, and systems vs. the corresponding path-length anisotropies $\Delta L/\langle L\rangle$. Except for IP-Glasma, each case is presented with four points corresponding to the centrality classes 10-20%, 20-30%, 30-40%, and 40-50%. We have omitted the 40-50% class of IP-Glasma since the average profile for this centrality class was not smooth enough to produce reliable v_2 and R_{AA} results.

Figure 4.7 shows a surprisingly simple relation between $v_2/(1-R_{\rm AA})$ and $\Delta L/\langle L\rangle$, independently on the collision system and energy, where the dependence is linear with a slope of

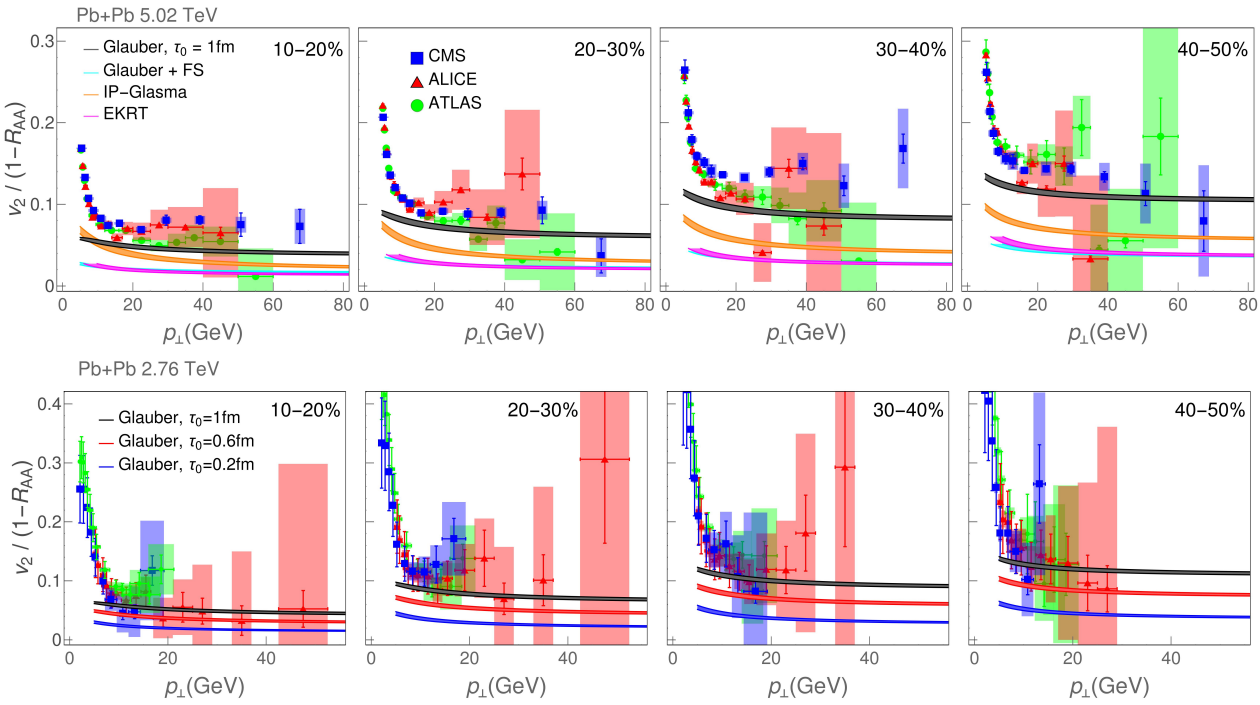

Figure 4.6: Calculated and experimentally observed $v_2/(1-R_{AA})$ ratio for charged hadrons as a function of transverse momentum $p_\perp$ in $\sqrt{s_{\rm NN}} = 5.02$ (upper) and 2.76 (lower) TeV Pb+Pb collisions. The calculations within DREENA-A framework were carried out using four different temperature profiles (Glauber with $\tau_0 = 1.0$ fm, Glauber + free streaming (FS), IP-Glasma, and EKRT) at $\sqrt{s_{\rm NN}} = 5.02$ TeV, and three at $\sqrt{s_{\rm NN}} = 2.76$TeV (Glauber with initial times $\tau_0 = 0.2$, 0.6 and 1.0 fm). The data are by ALICE [144, 145, 217, 218] (red triangles),CMS [146, 147, 219, 220] (blue squares) and ATLAS [148, 149, 221, 222] (green circles) collaborations. Each panel corresponds to a different centrality (10-20%, 20-30%,30-40%, 40-50%). The bands correspond to the uncertainty in the magnetic-to-electric mass ratio. Each band's upper (lower) boundary corresponds to $\mu_M/\mu_E = 0.4$ (0.6).

almost 1. Therefore, the system's geometry dominates the saturation value, although, at small values of $\Delta L/\langle L\rangle$, there is a deviation from the linear proportionality. It is worth noticing that here the values of $\Delta L/\langle L\rangle$ are much smaller than in our earlier 1D study, presented in Section 4.1. Also, even if the values of $\Delta L/\langle L\rangle$ are very different for different initializations; the initial anisotropies, $\epsilon_{2,2}$, are not so different. The general trend is that the earlier the transverse expansion begins (fluid dynamical or otherwise), the smaller the $\Delta L/\langle L\rangle$ in the same centrality class. The time it takes the parton to reach the system's edge is almost independent of τ_0. However, small τ_0 means that the system has evolved longer by the time the parton reaches the edge, and the initial anisotropy has been diluted more. Thus, the earlier the expansion begins, the lower is the ΔL and $\Delta L/\langle L\rangle$ depicts the mentioned sensitivity to the time when expansion begins.

4.2.3 Are these results robust?

Different collision system. In order to confirm that the saturation of $v_2/(1-R_{AA})$ is observed in other collision systems, we show this ratio (obtained within DREENA-A) as a function of $p_\perp$ for Xe+Xe collisions at $\sqrt{s_{\rm NN}} = 5.44$ TeV on Figure 4.8. We observe that $v_2/(1-R_{AA})$ saturates at high values of transverse momentum, which justifies our usage of data related to

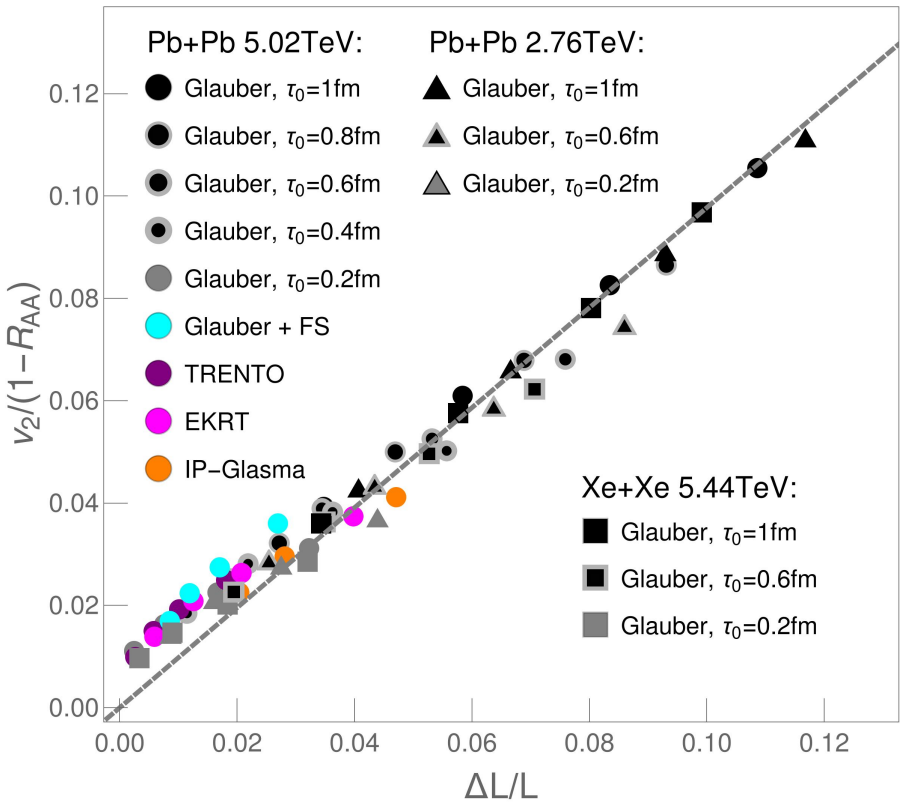

Figure 4.7: Charged hadron $v_2/(1-R_{AA})$ as a function of path-length anisotropies $\Delta L/L$, for different collision systems and energies (Pb+Pb at $\sqrt{s_{\rm NN}}$ = 2.76 and 5.02 TeV and Xe+Xe at $\sqrt{s_{\rm NN}}$ = 5.44 TeV), various centrality classes and temperature profiles, as indicated on the legend. For every profile, the point with the lowest $\Delta L/L$ corresponds to the 10-20% centrality class, the next one corresponds to 20-30%, and so on, up to 40-50% (except IP-Glasma, where the highest centrality is 30-40%). The value of transverse momentum is fixed at $p_\perp = 100$ GeV, and the linear fit yields a slope of ≈ 1.

this collision system in further analyses.

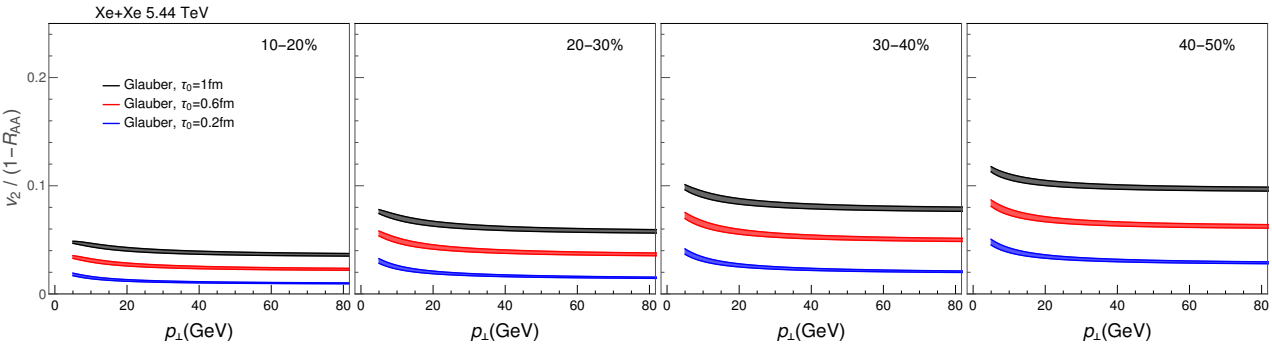

Figure 4.8: $v_2/(1-R_{AA})$ ratio for charged hadrons as a function of transverse momentum $p_\perp$ in $\sqrt{s_{\rm NN}}$ = 5.44 TeV Xe+Xe collisions. The calculations within the DREENA-A framework were carried out using three different temperature profiles (Glauber with initial times τ_0 = 0.2, 0.6 and 1.0 fm). Each panel corresponds to a different centrality (10-20%, 20-30%,30-40%, 40-50%). The bands correspond to the uncertainty in the magnetic-to-electric mass ratio. Each band's upper (lower) boundary corresponds to $\mu_M/\mu_E = 0.4$ (0.6).

Different energy loss model. Furthermore, we explore if we can reproduce the same results if we switch to a different energy loss model. In particular, we investigate if the saturation of $v_2/(1-R_{\mathrm{AA}})$ is still present at high $p_\perp$ and whether we can correlate its values to the anisotropy of path lengths $\Delta L/L$. As explained in Chapter 2, the formalism embedded in the DREENA-A procedure includes radiative and collisional energy loss mechanisms. To test the behavior of $v_2/(1-R_{\mathrm{AA}})$ for different energy loss models, we use DREENA-A but modified so that it calculates high-$p_\perp$ R_{AA} and v_2 taking into account **only radiative** (or **only collisional**) energy loss mechanisms.

Figure 4.9 shows $v_2/(1-R_{\mathrm{AA}})$ calculated within the DREENA-A framework, but focusing exclusively on radiative energy loss (with collisional energy loss artificially set to zero). We observe that the obtained $v_2/(1-R_{\mathrm{AA}})$ ratio saturates at high values of $p_\perp$, confirming the robustness of this phenomenon with respect to the change in the energy loss model.

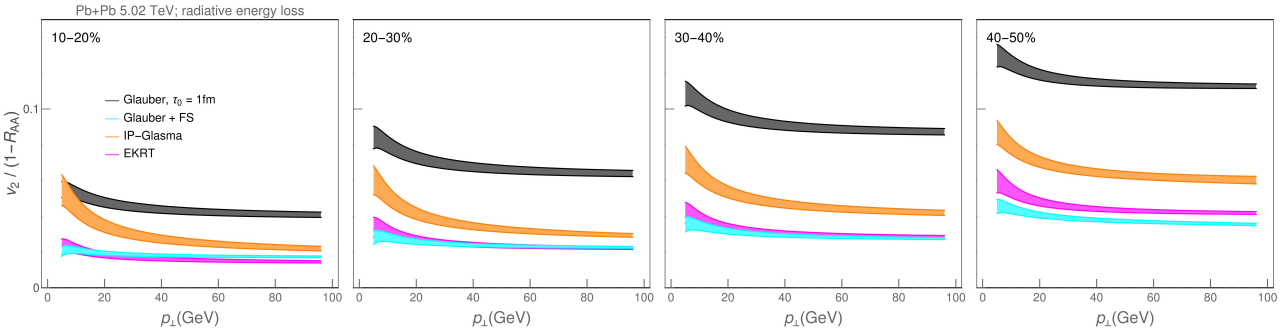

Figure 4.9: Calculated observed $v_2/(1-R_{AA})$ ratio for charged hadrons as a function of transverse momentum $p_\perp$ in $\sqrt{s_{\mathrm{NN}}} = 5.02$ Pb+Pb collisions, considering only radiative energy loss. The calculations within the DREENA-A framework were carried out using four different temperature profiles (Glauber with $\tau_0 = 1.0$ fm, Glauber + free streaming (FS), IP-Glasma, and EKRT) at $\sqrt{s_{\mathrm{NN}}} = 5.02$ TeV. Each panel corresponds to a different centrality (10-20%, 20-30%, 30-40%, 40-50%). The bands correspond to the uncertainty in the magnetic-to-electric mass ratio. Each band's upper (lower) boundary corresponds to $\mu_M/\mu_E = 0.4$ (0.6).

Moreover, we conduct a similar analysis as beforehand, i.e., we plot the values of $v_2/(1-R_{\mathrm{AA}})$ (obtained taking into account only radiative energy loss) at 100 GeV as a function of the anisotropy of path lengths $\Delta L/L$, refer to Figure 4.10, and we again observe linear dependence with a slope that is close to 1.

Now we conduct the equivalent analysis but take into account only collisional energy loss (with radiative energy loss artificially set to zero), and the results are shown in Figures 4.11 and 4.12. We again observe that $v_2/(1-R_{AA})$ saturates at high transverse momentum, and we observe a linear dependence between $v_2/(1-R_{\mathrm{AA}})$ and $\Delta L/L$. However, the slope value is different than 1, but this is to be expected since neither radiative or collisional energy loss alone is sufficient to explain the experimental data adequately.

From these results, we conclude that the phenomenon of $v_2/(1-R_{AA})$ saturation and its relation to the anisotropy of the system is indeed robust and energy loss model-independent.

4.2.4 Jet-perceived anisotropy

$\Delta L/\langle L\rangle$ depends on the shape of the system, and how the shape evolves, but it is not easy to see how the evolution affects it. To change the point of view from individual jets and their

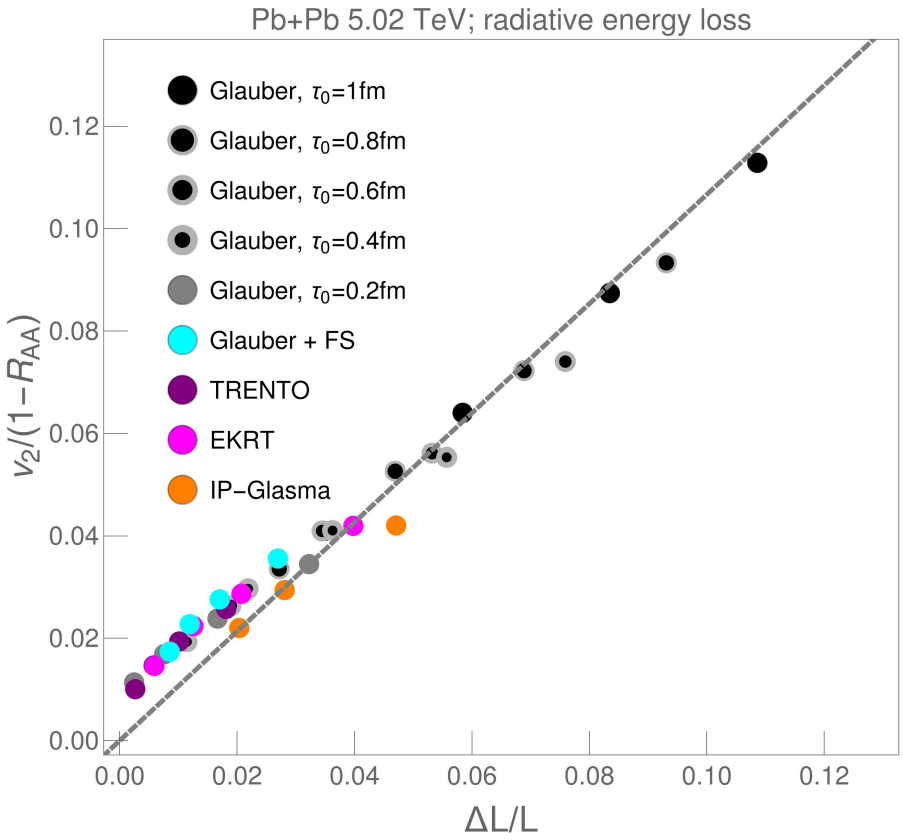

Figure 4.10: Charged hadron $v_2/(1-R_{AA})$ (calculated by taking into account only radiative energy loss) as a function of path-length anisotropies $\Delta L/L$, for Pb+Pb at $\sqrt{s_{\rm NN}} = 5.02$ TeV, various centrality classes and temperature profiles, as indicated on the legend. For every profile, the point with the lowest $\Delta L/L$ corresponds to the 10-20% centrality class, the next one corresponds to 20-30%, and so on, up to 40-50% (except IP-Glasma, where the highest centrality is 30-40%). The value of transverse momentum is fixed at $p_\perp = 100$ GeV, and the linear fit yields a slope of ≈ 1.

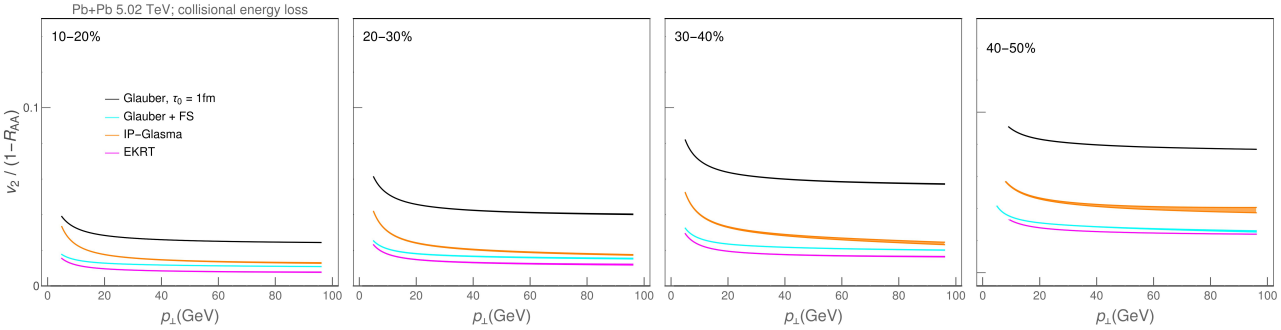

Figure 4.11: Calculated observed $v_2/(1-R_{AA})$ ratio for charged hadrons as a function of transverse momentum $p_\perp$ in $\sqrt{s_{\rm NN}} = 5.02$ Pb+Pb collisions, taking into account only collisional energy loss. The calculations within the DREENA-A framework were carried out using four different temperature profiles (Glauber with $\tau_0 = 1.0$ fm, Glauber + free streaming (FS), IP-Glasma, and EKRT) at $\sqrt{s_{\rm NN}} = 5.02$ TeV. Each panel corresponds to a different centrality (10-20%, 20-30%,30-40%, 40-50%).

paths to the shape of the bulk medium and its evolution, we devised a measure similar to

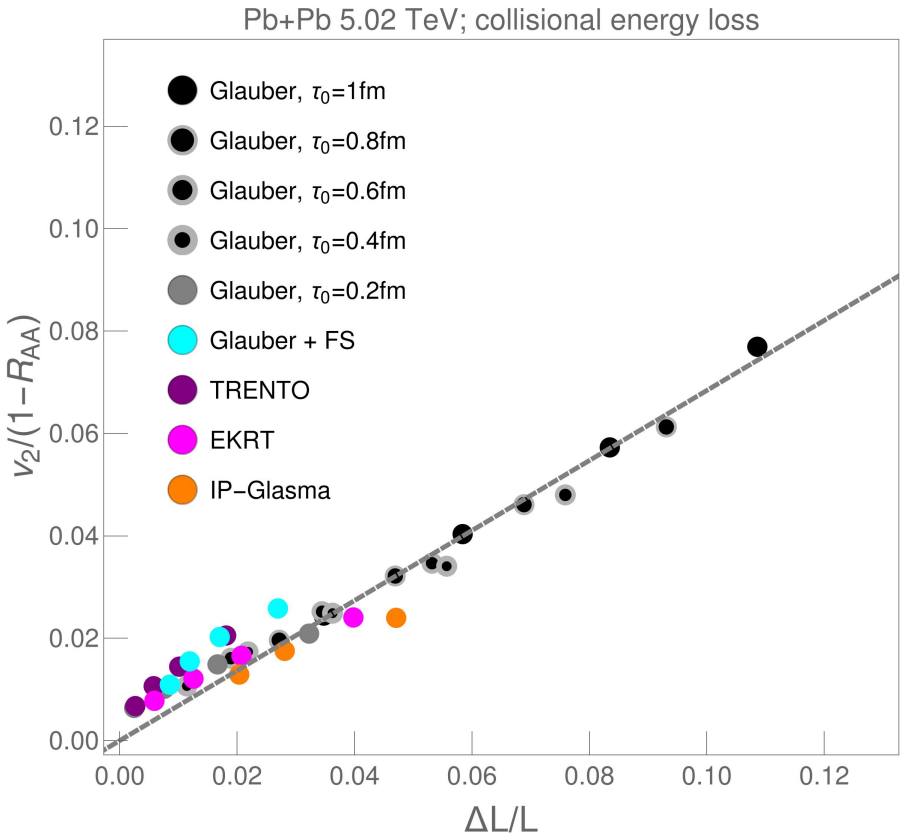

Figure 4.12: Charged hadron $v_2/(1-R_{AA})$ (calculated by taking into account only collisional energy loss) as a function of path-length anisotropies $\Delta L/L$, for Pb+Pb at $\sqrt{s_{\rm NN}} = 5.02$ TeV, various centrality classes and temperature profiles, as indicated on the legend. For every profile, the point with the lowest $\Delta L/L$ corresponds to the 10-20% centrality class, the next one corresponds to 20-30%, and so on, up to 40-50% (except IP-Glasma, where the highest centrality is 30-40%). The value of transverse momentum is fixed at $p_\perp = 100$ GeV, and the linear fit yields a slope of ≈ 0.7.

the conventional measure of the spatial anisotropy (e.g. ϵ_2 defined in Equation 4.15, or higher eccentricity coefficients given in, e.g., [200]): We evaluate the average of temperature cubed encountered by partons propagating with angle ϕ with respect to the reaction plane [4]:

$$jT(\tau,\phi) \equiv \frac{\int \mathrm{d}x\mathrm{d}y\, T^3(x+\tau\cos\phi, y+\tau\sin\phi,\tau)\, n_0(x,y)}{\int \mathrm{d}x\mathrm{d}y\, n_0(x,y)}, \tag{4.18}$$

where $n_0(x,y)$ is the density of the jets produced in the primary collisions, i.e., the density of the binary collisions. This distribution is not azimuthally symmetric, and we may evaluate its second Fourier coefficient:

$$jT_2(\tau) = \frac{\int \mathrm{d}x\mathrm{d}y\, n_0(x,y) \int \mathrm{d}\phi \cos 2\phi\, T^3(x+\tau\cos\phi, y+\tau\sin\phi,\tau)}{\int \mathrm{d}x\mathrm{d}y\, n_0(x,y) \int \mathrm{d}\phi\, T^3(x+\tau\cos\phi, y+\tau\sin\phi,\tau)}. \tag{4.19}$$

Moreover, a simple time-average of jT_2,

$$\langle jT_2 \rangle = \frac{\int_{\tau_0}^{\tau_{\rm cut}} \mathrm{d}\tau\, jT_2(\tau)}{\tau_{\rm cut} - \tau_0}, \tag{4.20}$$

where $\tau_{\rm cut}$ is defined as the time when the center of the fireball has cooled down to critical temperature T_c, is directly proportional to the ratio $v_2/(1-R_{\rm AA})$ as shown in Fig. 4.13 (without an off-shift observed for low values of $v_2/(1-R_{\rm AA})$ in Fig. 4.7).

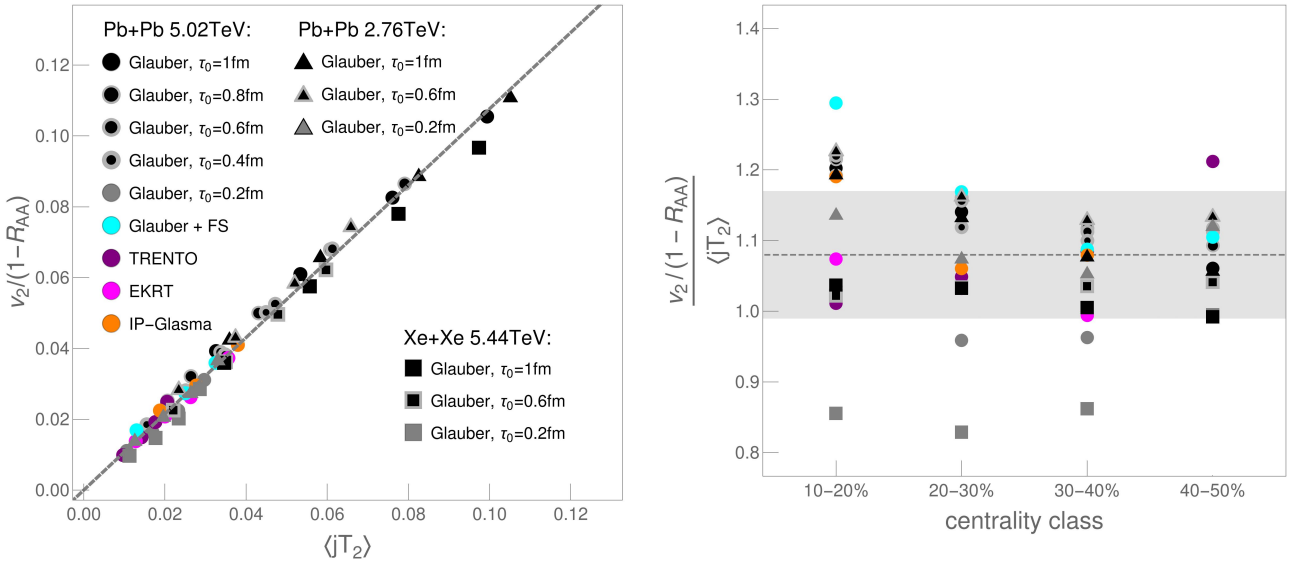

Figure 4.13: The plot on the left shows the values of $v_2/(1-R_{AA})$ of charged hadrons as a function of the average jet-perceived anisotropy $\langle jT_2\rangle$ for different collision systems and energies (Pb+Pb at $\sqrt{s_{\rm NN}} = 2.76$ and 5.02 TeV and Xe+Xe at $\sqrt{s_{\rm NN}} = 5.44$ TeV), various centrality classes and temperature profiles, as indicated on the legend. For every profile, the point with the lowest $\langle jT_2\rangle$ corresponds to the 10-20% centrality class, the next one corresponds to 20-30%, and so on, up to 40-50% (except IP-Glasma, where the highest centrality is 30-40%). The value of transverse momentum is fixed at $p_\perp = 100$ GeV, and the linear fit yields a slope of ≈ 1. The plot on the right shows $v_2/(1-R_{\rm AA})$ and $\langle jT_2\rangle$ the ratio for every point from the plot on the left as a function of the centrality class.

We call this measure the average jet-perceived anisotropy of the system. We evaluate the ratio of $v_2/(1-R_{\rm AA})$ and $\langle jT_2\rangle$ in the $p_\perp$ range where the $v_2/(1-R_{\rm AA})$ ratio has saturated for all models ($p_\perp > 80$ GeV), and average over all the cases shown in Fig. 4.13 to obtain

$$\frac{v_2/(1-R_{\rm AA})}{\langle jT_2\rangle} = 1.08 \pm 0.09. \tag{4.21}$$

As shown in the right panel of Fig. 4.13, deviations from this behavior are modest and random. This indicates that $\langle jT_2\rangle$ describes the leading term in the process creating high-$p_\perp$ $v_2/(1-R_{\rm AA})$, and therefore this ratio carries direct information on the system geometry and its anisotropy. Since unity is within one standard deviation from the average for practical purposes we can use an approximation $v_2/(1-R_{\rm AA}) = \langle jT_2\rangle$.

The above analysis was performed on $h^\pm$. However, if $v_2/(1-R_{\rm AA})$ indeed reflects the anisotropy $\langle jT_2\rangle$, then the Eq. (4.21) should be independent of flavor. Due to large mass, R_{AA} and v_2 of heavy flavor particles depend on $p_\perp$ differently from charged hadrons' R_{AA} and v_2. To test whether the $v_2/(1-R_{\rm AA})$ ratio of heavy flavor particles also saturates at high $p_\perp$, and whether Eq. (4.21) is valid for them, we performed the same analysis on R_{AA} and v_2 of D and B mesons. We obtained that $v_2/(1-R_{\rm AA})$ indeed saturates at $p_\perp > 20$ GeV for B mesons and at $p_\perp > 80$ GeV for D mesons, and that, after saturation, the Eq. (4.21) is robust for all types of flavor (results not shown). This further supports that $v_2/(1-R_{\rm AA})$ at high-$p_\perp$ directly carries information on the medium property, as revealed through this extensive analysis.

Finally, we evaluated the favored $\langle jT_2\rangle$ range from the experimentally measured $R_{\rm AA}(p_\perp)$ and $v_2(p_\perp)$ for $h^\pm$ at different centralities. The $\langle jT_2\rangle$ values are obtained by fitting $v_2(p_\perp)/(1-$

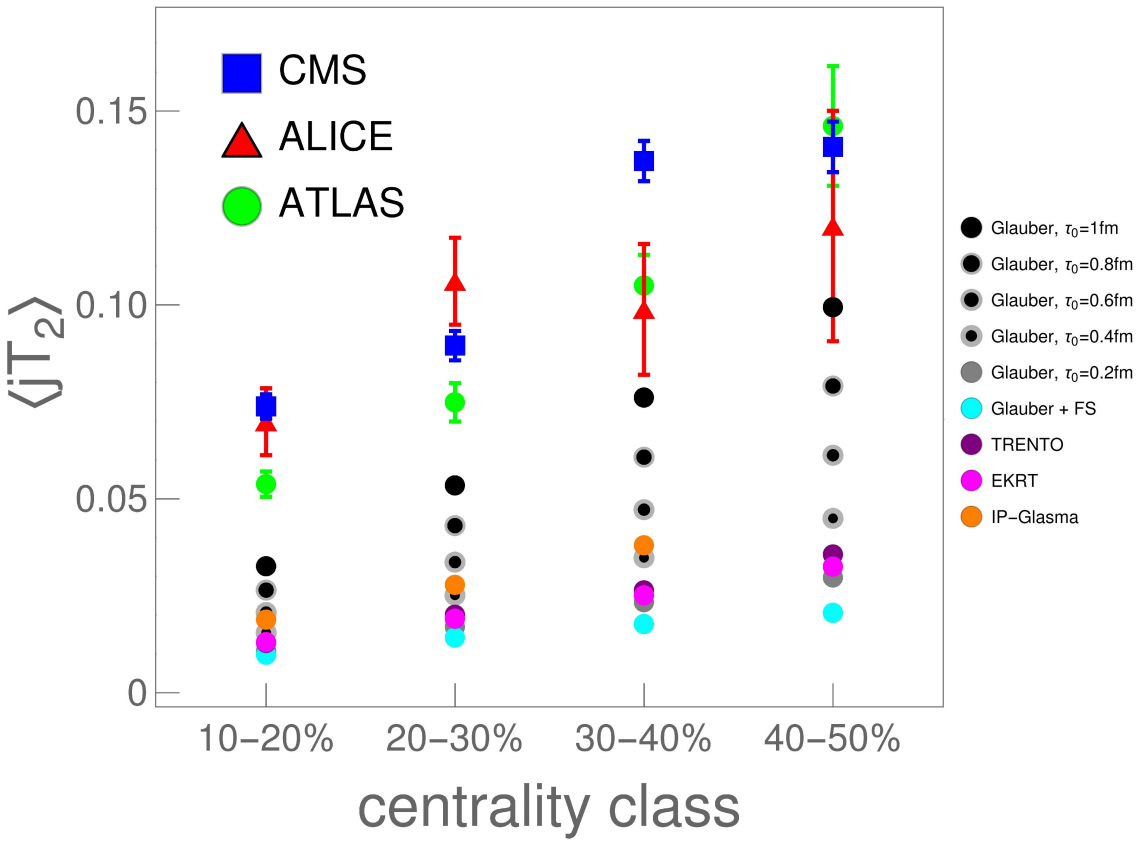

Figure 4.14: Constraints to jet-perceived anisotropy ($\langle jT_2 \rangle$, shown on y-axis) evaluated from high-$p_\perp > 20$ GeV R_{AA} and v_2 experimental data using $\langle jT_2 \rangle = v_2/(1 - R_{\rm AA})$ (see Eq. 4.21), for four different centrality regions (shown on the x-axis): 10-20%, 20-30%, 30-40%, 40-50%. 5.02 TeV Pb+Pb ALICE [144, 145] (red triangles), CMS [146, 147] (blue squares) and ATLAS [148, 149] (green circles) data are used. For each centrality, the experimental constraints are compared with the average jet-perceived anisotropy $\langle jT_2 \rangle$ for various evolution scenarios indicated in the legend.

$R_{\rm AA}(p_\perp)$) data shown in Fig. 4.6 with a constant function for $p_\perp > 20$ GeV using MINUIT [223] package within ROOT [224] code, taking uncertainties into account. The fitted ratio was then converted to $\langle jT_2 \rangle$ by assuming their equality. As shown in Fig. 4.14, all three experiments lead to similar values of $\langle jT_2 \rangle$, though the uncertainty is still large.

We also note that $\langle jT_2 \rangle$ is a bulk-medium property, which can be directly evaluated from bulk-medium simulations through Eqs. (2)–(4), independently of high-$p_\perp$ data. Thus, experimental data can be used to restrict the value of this quantity. In Fig. 4.14, we see that none of the evolution scenarios tested in this manuscript is in good agreement with the data (despite the above-mentioned large uncertainty), i.e., lead to smaller jet-perceived anisotropy than experimentally favored. We thus show that jet-perceived anisotropy provides an important constraint on bulk-medium simulations and those future bulk-medium calculations should be tuned to reproduce the experimentally constrained $\langle jT_2 \rangle$ as well. Moreover, in the high-luminosity 3^{rd} run at the LHC, the error bars for $R_{\rm AA}(p_\perp)$ and $v_2(p_\perp)$ are expected to be significantly reduced, which will subsequently lead to a notably better experimental constraint of $\langle jT_2 \rangle$, also enabling better constraint on bulk-medium simulations.

4.2.5 Summary

In this study, we used the recently developed DREENA-A framework to explore how the temperature evolution of the QGP droplet influences high-$p_\perp$ $v_2/(1-R_{AA})$ predictions. The framework does not use any free parameter within the energy loss model and consequently allows us to fully explore these profiles as the only input in the model. We showed that saturation in $v_2/(1-R_{AA})$, clearly seen in the experimental data is robustly obtained for the comprehensive set of fluid-dynamical calculations covered in this study, as well as different types of flavor, collision energies, and collision systems, supporting the generality of our findings. Also, by folding spatial coordinates and temperature, we further revealed that this saturation value corresponds to a property of the system we defined as average jet-perceived anisotropy $\langle jT_2 \rangle$. We also showed how to relate $\langle jT_2 \rangle$ to experimental data, providing a new important constraint on bulk-medium simulations. None of the evolution scenarios that we tested here were in good agreement with experimentally inferred $\langle jT_2 \rangle$ values, which argues that it is important to tune the bulk-medium simulations accordingly, particularly with the high-luminosity 3^{rd} run at the LHC. Our approach demonstrates the utility of QGP tomography, i.e., the potential for extracting the bulk QGP properties jointly from low and high-$p_\perp$ data.

Chapter 5

Importance of Higher Orders in Opacity in QGP Tomography

This Chapter is based on [5]. It considers the problem of including a finite number of scattering centers in dynamical energy loss and classical DGLV formalism. Previously, one or an infinite number of scattering centers were considered in radiative energy loss calculations, while efforts to relax such approximations require a more conclusive and complete treatment. In reality, however, the number of scattering centers is generally estimated to be 4-5 at RHIC and the LHC, making the above approximations (a priori) inadequate and this theoretical problem significant for QGP tomography.

We derived explicit analytical expressions for dynamical energy loss and DGLV up to the 4^{th} order in opacity, resulting in complex - highly oscillatory - mathematical expressions. These expressions were then implemented into an appropriately generalized DREENA framework to calculate the effects of higher orders in opacity on a wide range of high-$p_\perp$ light and heavy flavor predictions. Results of extensive numerical analysis and interpretations of nonintuitive results are presented here. We demonstrate that, for both RHIC and the LHC, higher-order effects on high-$p_\perp$ observables are minor, and the approximation of a single scattering center is adequate for dynamical energy loss and DGLV formalisms.

5.1 Introduction

Hard probes are one of the main tools for understanding and characterizing the QGP properties [7], where hard processes dominate interactions of these probes with QGP constituents. These interactions are dominantly described by energy loss, where radiative is one of the most important mechanisms at high transverse momentum ($p_\perp$) [105]. The radiative energy loss can be analytically computed through pQCD approaches, typically under the assumption of the optically thick or optically thin medium (e.g., Baier-Dokshitzer-Mueller-Peigne-Schiff-Zakharov (BDMPS-Z) [117, 225], Armesto-Salgado-Wiedemann (ASW) [118], (D)GLV [110, 115], Higher-Twist (HT) and Higher-Twist Majumder (HT-M) [119, 226], Arnold-Moore-Yaffe (AMY) [227], dynamical energy loss [105, 121] and different applications/extensions of these methods) and tested against the experimental data.

Optically thick medium corresponds to the approximation of a jet experiencing infinite scatterings with medium constituents. While such an approximation would be adequate for QGP created in the early universe (Big Bang), Little Bangs are characterized by short, finite-size droplets of QCD matter. Another widely used approximation is an optically thin medium, assuming one scattering center. However, the medium created in Little Bangs is typically several fm in size (with mean free path $\lambda \approx 1$ fm), so considering several scattering centers in radiative energy loss calculations is needed. Thus, it is evident that both approaches represent two extreme limits to the realistic situations considered in RHIC and LHC experiments, and relaxing these approximations to the case of a finite number of scattering centers is necessary (see Figure 5.1 for an illustration). Thus, relaxing such approximation is a highly nontrivial problem, first addressed in [110], with recently renewed interest [228, 229, 230, 231, 232, 233, 234]. Some of these approaches are analytically quite advanced, e.g., providing full expressions for a gluon radiation spectrum (or splitting functions) with relaxed soft-gluon approximation in DGLV formalism [232, 233] or derivation of gluon emission spectrum with full resummation of multiple scatterings within the BDMPS-Z framework [228, 230, 231]. However, in our view, this issue requires a more conclusive and complete treatment. Namely, the importance of including higher orders in opacity effects on experimental observables is still not addressed. In relaxing this approximation, it is not only needed to estimate these effects on, e.g., the energy loss and gluon radiation spectrum, but also to implement these corrections in the numerical frameworks needed to generate predictions for high-$p_\perp$ observables measured at RHIC and the LHC experiments. Furthermore, most of these studies were done in massless quarks and gluons limit and/or use the assumption of an uncorrelated medium. Since we, *a priori*, do not know the magnitude of the effects of the inclusion of multiple scattering centers, nor how the mentioned approximations can influence this magnitude, we find it questionable to discuss higher order corrections while ignoring the effects which might potentially overshadow or alter the final effects. For example, due to a finite temperature medium, light quarks and gluons gain mass in QGP, which can significantly numerically modify the importance of these effects on experimental observables.

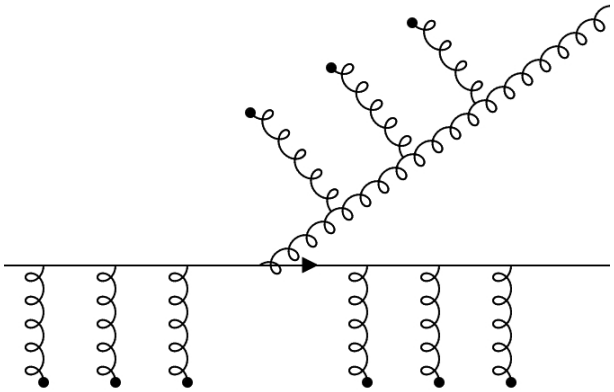

Figure 5.1: A parton in the medium experiences several scatterings before radiating a gluon.

In this study, we start from our dynamical energy loss formalism [105, 121], computed under the approximation of an optically thin QCD medium, i.e., one scattering center. We use general expressions from [234] to relax this approximation to the case of a finite number of scattering centers, where explicit analytical expressions up to the 4^{th} order in opacity (scattering centers) are presented. These expressions are implemented in the (appropriately modified) DREENA-C [107] framework (which assumes a constant temperature medium – refer to Chapter 2), enabling us to more straightforwardly estimate the effects of higher orders in opacity on high-

$p_\perp$ R_{AA} and v_2 observables. Based on these results, we also provide estimates for the fully evolving medium, while a rigorous study in this direction is left for future work.

While the initial expressions taken from [234] were, strictly speaking, derived in the approximation of static scattering centers, we apply them here in the context of a dynamic QCD medium. Namely, by careful calculation, we have shown in [121] that – at least in the first order in opacity – the generalization from the static to dynamic medium eventually amounts to a mere appropriate replacement of the mean free path and effective potential in the final expressions. Following general arguments given in [110] and the expectations expressed in [234], we assume that the same prescription for progressing from static to dynamic medium remains valid in higher orders of opacity.

The outline of this Chapter is as follows: Sections 5.2 and 5.3 present the outline of theoretical and numerical frameworks used in this study, with more detailed analytical results presented in the Appendices. In the Results section, we will numerically analyze the effects of higher orders in opacity on the gluon radiation spectrum and high-$p_\perp$ R_{AA} and v_2 predictions. Intuitive explanations behind obtained results will be presented. This section will also analyze a particular case of static QCD medium (extension of (D)GLV [110, 115] to the finite number of scattering centers). The main results will be summarized in the last section.

5.2 Theoretical framework

In this study, we use our dynamical radiative energy loss [105, 121] formalism described in Chapter 2.

However, as the Introduction notes, this radiative energy loss is developed up to the first order in opacity. Thus, to improve the applicability of this formalism for QGP tomography, it is necessary to relax this approximation. To generalize the dynamical energy loss to finite number in scattering centers, we start from a closed-form expression - Eq. (46) from [234] and Eq. (20) from [115] - derived for static QCD medium (i.e., (D)GLV case [110, 115]) but applicable for a generalized form of effective potential $v(\mathbf{q_i})$ ($\mathbf{q_i}$ are the momenta of the exchanged gluons), and mean free path λ [234].

$$x\frac{dN^{(n)}}{dx\,d^2\mathbf{k}} = \int_0^L dz_1 \cdots \int_{z_{n-1}}^L dz_n \int \prod_{i=1}^{n} \left(d^2\mathbf{q}_i \, \frac{v^2(\mathbf{q}_i) - \delta^2(\mathbf{q}_i)}{\lambda(z)} \right) \times \frac{C_R \alpha_s(Q_k^2)}{\pi^2} \left(-2\,\mathbf{C}_{(1\cdots n)} \cdot \mathbf{B}_n \left[\cos \sum_{k=2}^{n} \omega_{(k\cdots n)} \Delta z_k - \cos \sum_{k=1}^{n} \omega_{(k\cdots n)} \Delta z_k \right] \right), \quad (5.1)$$

here $|v_i(\mathbf{q}_i)|^2$ is defined as the normalized distribution of momentum transfers from the i^{th} scattering center (i.e., "effective potential"), $\lambda(i)$ is the mean free path of the emitted gluon, C_R is the color Casimir of the jet ($C_R = 4/3$ ($C_R = 3$) for the quark (gluon) jet), Δz_i are distances between scattering centers. Note that we denote transverse 2D vectors as bold $\mathbf{p}$ for consistency with our previous work.

The running coupling is defined as in [124]:

$$\alpha_s(Q^2) = \frac{4\pi}{(11 - \frac{2}{3}n_f)\ln(\frac{Q^2}{\Lambda_{QCD}})}, \quad (5.2)$$

here $Q_k^2 = \frac{\mathbf{k}^2 + M^2x^2 + m_g^2}{x}$, appearing in Eq. (5.1) above is the off-shellness of the jet before gluon radiation [124], where x is the longitudinal momentum fraction of the quark jet carried away

by the emitted gluon, M is the mass of the quark, $m_g = \mu_E/\sqrt{2}$ is the effective mass for gluons with hard momenta [122], and $\mathbf{k}$ is the momentum of the radiated gluon.

$\omega_{(m\ldots n)}$ is the inverse of the formation time or the (longitudinal) momentum

$$\omega_{(m\ldots n)} = \frac{\chi^2 + (\mathbf{k} - \mathbf{q}_m - \ldots \mathbf{q}_n)^2}{2xE}, \tag{5.3}$$

where n is the final scatter, while m varies from the first to the final scatter. $\chi^2 \equiv M^2x^2 + m_g^2$, where $\mathbf{k}$ is the momentum of the radiated gluon, $\mathbf{q_i}$ are the momenta of the exchanged gluons, x is the longitudinal momentum fraction of the quark jet carried away by the emitted gluon, M is the mass of the quark, $m_g = \mu_E/\sqrt{2}$ is the effective mass for gluons with hard momenta [122], and μ_E is the Debye mass (i.e., electric screening).

'Cascade' terms represent the shifting of the momentum of the radiated gluon due to momentum kicks from the medium:

$$\mathbf{C}_{(i_1 i_2 \ldots i_m)} = \frac{(\mathbf{k} - \mathbf{q}_{i_1} - \mathbf{q}_{i_2} - \ldots - \mathbf{q}_{i_m})}{\chi^2 + (\mathbf{k} - \mathbf{q}_{i_1} - \mathbf{q}_{i_2} - \ldots - \mathbf{q}_{i_m})^2}. \tag{5.4}$$

A special case of $\mathbf{C}$ without any momentum shifts is defined as the 'Hard' term:

$$\mathbf{H} = \frac{\mathbf{k}}{\chi^2 + \mathbf{k}^2}, \text{ and } \mathbf{B}_i = \mathbf{H} - \mathbf{C}_i. \tag{5.5}$$

In [105, 121, 123], we showed that, despite much more involved analytical calculations, the radiative energy loss in a dynamical medium has the same form as in the static medium, except for two straightforward substitutions in mean free path and effective potential:

$$\lambda_{\text{stat}} \to \lambda_{\text{dyn}}, \tag{5.6}$$

where:

$$\lambda_{\text{stat}}^{-1} = 6\frac{1.202}{\pi^2}\frac{1 + n_f/4}{1 + n_f/6}\lambda_{\text{dyn}}^{-1}, \tag{5.7}$$

while the 'dynamical mean free path' is given by [105, 121]:

$$\lambda_{dyn}^{-1} = 3\alpha_s(Q_v^2)T, \tag{5.8}$$

with $Q_v^2 = ET$ [124]. Running coupling $\alpha_s(Q_v^2)$ corresponds to the interaction between the jet and the virtual (exchanged) gluon, while E is the jet's energy.

$$\left[\frac{\mu_E^2}{\pi(\mathbf{q}^2+\mu_E^2)^2}\right]_{\text{stat}} \to \left[\frac{\mu_E^2 - \mu_M^2}{\pi(\mathbf{q}^2+\mu_E^2)(\mathbf{q}^2+\mu_M^2)}\right]_{\text{dyn}}, \tag{5.9}$$

here μ_M is magnetic screening. Thus, we assume that the Eq. (5.1) can also be used in our case, with the above modification of effective potential and mean free path. In the Appendix C, we use this general expression to derive an explicit expression for the gluon radiation spectrum for 1st, 2nd, 3rd and 4th order in opacity ($\frac{dN_g^{(1)}}{dx}$, $\frac{dN_g^{(2)}}{dx}$, $\frac{dN_g^{(3)}}{dx}$, $\frac{dN_g^{(4)}}{dx}$, respectively).

5.3 Numerical framework

To generate the results presented in this work, we used the (appropriately generalized, see below) DREENA-C framework, described in more detail in Chapter 2.

We use the following parameters in the numerical procedure: $\Lambda_{QCD} = 0.2$ GeV and $n_f = 3$. Temperature-dependent Debye chromoelectric mass $\mu_E(T)$ has been extracted from [150]. For the mass of light quarks, we take the thermal mass $M \approx \mu_E/\sqrt{6}$, and for the gluon mass, we use $m_g = \mu_E/\sqrt{2}$ [122]. The mass of the charm (bottom) quark is $M = 1.2$ GeV ($M = 4.75$ GeV). The magnetic and electric mass ratio is $0.4 < \mu_M/\mu_E < 0.6$ [152, 153]. All the results presented in this Chapter are generated for the Pb+Pb collision system at $\sqrt{s_{NN}} = 5.02$ TeV.

As DREENA-C (see Chapter 2 and [107]) does not include suppression from multiple scattering centers in the medium, we now upgrade this framework to include the 2^{nd} and 3^{rd} order in opacity contributions. We integrate the expressions obtained from (5.1) analytically for z_i (i.e., distance at which i-th scattering occurs, see Appendices C.1 and C.2), and then numerically for momenta $\mathbf{k}$ and $\mathbf{q}_i$ using the quasi-Monte Carlo method to obtain $\frac{dN_g}{dx}$ up to 3^{rd} order in opacity. Also, to test the importance of multiple scattering centers on radiative energy loss, we exclude the collisional contributions from the DREENA-C framework and only generate predictions for radiative energy loss. At the same time, we show the results for full (radiative and collisional) energy loss in Appendices E, and F. Appendix C also includes expressions for the 4^{th} order in opacity. We implemented 4^{th} order into DREENA-C, but as the resulting integrals are highly oscillatory, we could not reach convergence for this order using our available computational resources. Notably, this numerical complexity is significantly higher, estimated to be ~ 2 orders of magnitude larger than for the 3^{rd} order (e.g., for the 1^{st} order, we needed ~ 25 CPUh; for the 2^{nd} order ~ 2500 CPUh; for the 3^{rd} order ~ 70000 CPUh). Nevertheless, we found the 4^{th} order contribution negligible at specific points where we reached a convergence, as expected from the results presented in the next section.

5.4 Numerical results

In Fig. 5.2, the effect of higher orders in opacity on $\frac{dN_g}{dx}$ as a function of x is shown for typical medium length $L = 5$fm. In each plot, we use double axes for clarity: the lower axis corresponds to magnetic to electric mass ratio μ_M/μ_E=0.6 (and the curves with the peak on the left side), while the upper axis corresponds to μ_M/μ_E=0.4 (and the curves with the peak on the right side) - note that, in each case, maximum is reached for low values of x.

The importance of higher orders in opacity decreases with increased jet energy and mass. They also decrease with decreasing the medium size, as shown in Appendix D (equivalent figures for $L = 3$fm and $L = 1$fm). For bottom quarks, higher-order effects are negligible independently of the jet momentum. In contrast, these effects are moderate for charm and light quarks and can influence the jet observables, as discussed below. Note that, due to color triviality, the results for light quarks show the (scaled) result for gluons, too. This holds up to the fact that, due to the indistinguishability of the radiated gluon from the gluon in the jet, the limits for subsequent integration of dN_g/dx with respect to x is performed from $x_{lower} = 0$ to $x_{upper} = 1/2$ (as opposed to $x_{upper} = 1$ for light quarks).

Before employing the full-fledged procedure to obtain high-$p_\perp$ observables, we first calculated the fractional energy loss in the medium ($\Delta E/E$), which is shown in Figure 5.3 as a function of transverse momentum $p_\perp$ for various quark flavors (bottom, charm, and light quarks), as well as

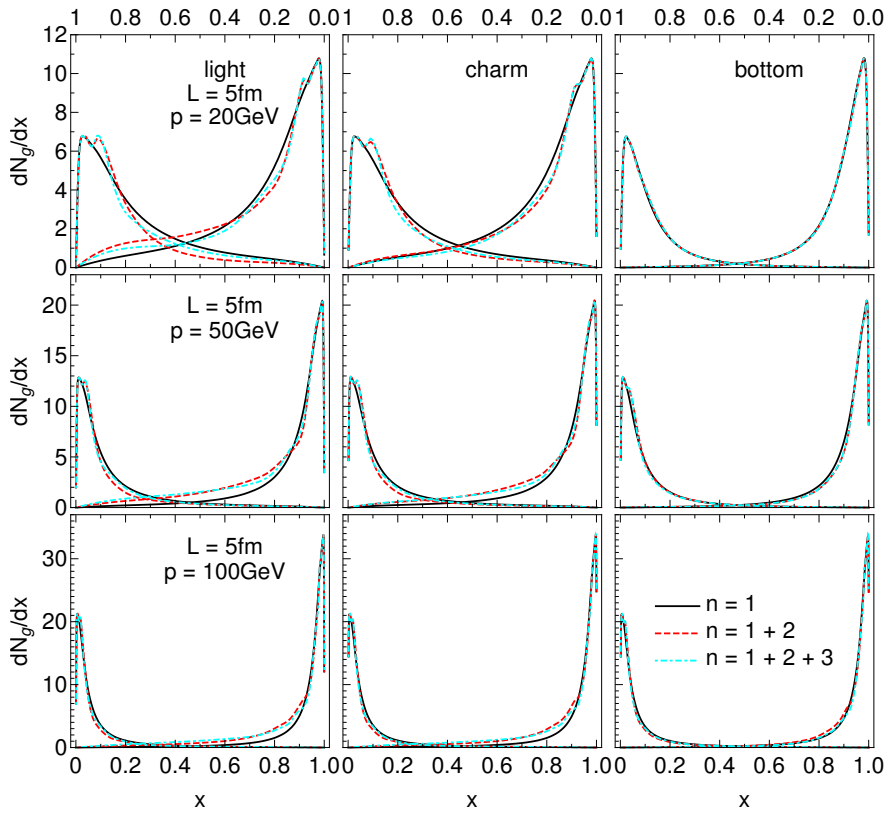

Figure 5.2: Gluon radiation spectrum dN_g/dx as a function of x, for the typical medium length of $L = 5fm$ and various jet momenta. Different columns correspond to light, charm, and bottom quarks. Solid black curves show the 1st order in opacity results, red dashed curves show the results up to the 2nd order, while cyan dot-dashed curves up to the 3rd order in opacity. Curves with the peaks on the left (right) side of each of the plots correspond to the $\mu_M/\mu_E = 0.6$ ($\mu_M/\mu_E = 0.4$) case, and the numerical values should be read off on the lower (upper) x-axis.

for gluons. The path-length is fixed to $L = 3$fm, and we show the results for $\mu_M/\mu_E = 0.4$ and $\mu_M/\mu_E = 0.6$. Fractional energy loss can be used as a proxy observable to estimate the behavior of R_{AA} — the larger the fractional energy loss, the smaller the expected R_{AA}. From this panel, we again observe that the effect of including higher orders of opacity is more pronounced with the decreasing parton mass (lowest for bottom quarks and highest for gluons). We also observe that the effect of including higher orders in opacity is more pronounced in the $\mu_M/\mu_E = 0.4$ case than in the $\mu_M/\mu_E = 0.6$ case. Moreover, we see that the effect has a different sign in these two cases (inclusion of higher orders in opacity increases the fractional energy loss in the $\mu_M/\mu_E = 0.4$, and decreases it in the $\mu_M/\mu_E = 0.6$ case). Its behavior is consistent with the behavior of radiative R_{AA} (shown in Figure 5.4).

In Fig. 5.4, we show the effect of higher orders in opacity on radiative R_{AA} observable. Our computations show that the effect on v_2 is similar to that on R_{AA} (see Appendix E for v_2 results). Thus, we concentrate only on R_{AA} to avoid redundancy.

We first observe that the effect on R_{AA} is smaller for more peripheral collisions. This is expected, as the medium is shorter on average, so including multiple scattering centers becomes less important.

Furthermore, we find that higher orders in opacity are negligible for B mesons, while these effects increase with decreasing mass, as expected from Fig. 5.2 and Fig. 5.3. The reason behind this is the decrease in the gluon formation time with increasing jet mass. When the gluon

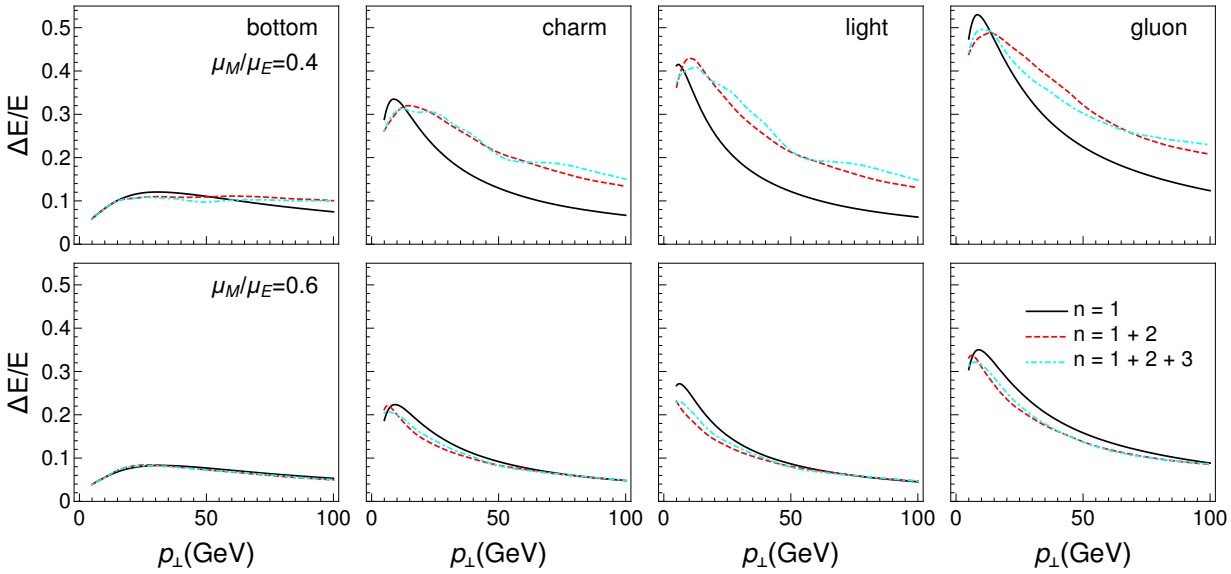

Figure 5.3: Fractional radiative energy loss ($\Delta E/E$) as a function of transverse momentum – the effects of different orders in opacity. The results are generated for the Pb+Pb collision system at $\sqrt{s_{NN}} = 5.02$ TeV. The path length is fixed to $L = 3$fm. Different columns correspond to the bottom quark, charm quark, light quark, and gluons. The upper (lower) row corresponds to the $\mu_M/\mu_E = 0.4$ ($\mu_M/\mu_E = 0.6$) case. Solid black curves show the 1$^{\text{st}}$ order in opacity results, red dashed curves show the results up to the 2$^{\text{nd}}$ order, while cyan dot-dashed curves up to the 3$^{\text{rd}}$ order in opacity.

formation time is short, the energy loss approaches the incoherent limit, where it was previously shown that the effects of higher orders in opacity are negligible [115]. Thus, our results are consistent with the previous findings. On the other hand, for large gluon formation time (massless quark and gluon limit), the higher orders in opacity effects become significant, also in general agreement with the previous findings [228]. In finite temperature QGP (considered in this study), light quarks and gluons gain mass due to Debye screening, reducing the effects of higher orders in opacity on the energy loss, consistently with Fig. 5.4.

Unexpectedly, we also observe that, in accordance with Fig. 5.3, for different magnetic mass limiting cases, these effects on R_{AA} are opposite in sign: for μ_M/μ_E=0.6, the inclusion of higher orders in opacity reduces energy loss (and, consequently, suppression). In contrast, for μ_M/μ_E=0.4, the effect is both opposite in sign and more significant in magnitude. What is the reason behind these unexpected results?

To answer this question, we go back to the effective potential [123] $v(\mathbf{q})$ in dynamical QCD medium, which can be written in the following form

$$v(\mathbf{q}) \;=\; v_L(\mathbf{q}) - v_T(\mathbf{q})\,, \tag{5.10}$$

here $v_L(\mathbf{q})$ is longitudinal (electric), and $v_T(\mathbf{q})$ is transverse (magnetic), contribution to the effective potential. The general expressions for the transverse and longitudinal contributions to the effective potentials are [123]:

$$v_L(\mathbf{q}) \;=\; \frac{1}{\pi}\left(\frac{1}{(\mathbf{q}^2+\mu_{pl}^2)} - \frac{1}{(\mathbf{q}^2+\mu_E^2)}\right), \quad v_T(\mathbf{q}) = \frac{1}{\pi}\left(\frac{1}{(\mathbf{q}^2+\mu_{pl}^2)} - \frac{1}{(\mathbf{q}^2+\mu_M^2)}\right), \tag{5.11}$$

here μ_E, μ_M and $\mu_{pl} = \mu_E/\sqrt{3}$ are electric, magnetic and plasmon masses, respectively. As seen from Eq. (5.10), this potential has two contributions - electric and magnetic, where the electric

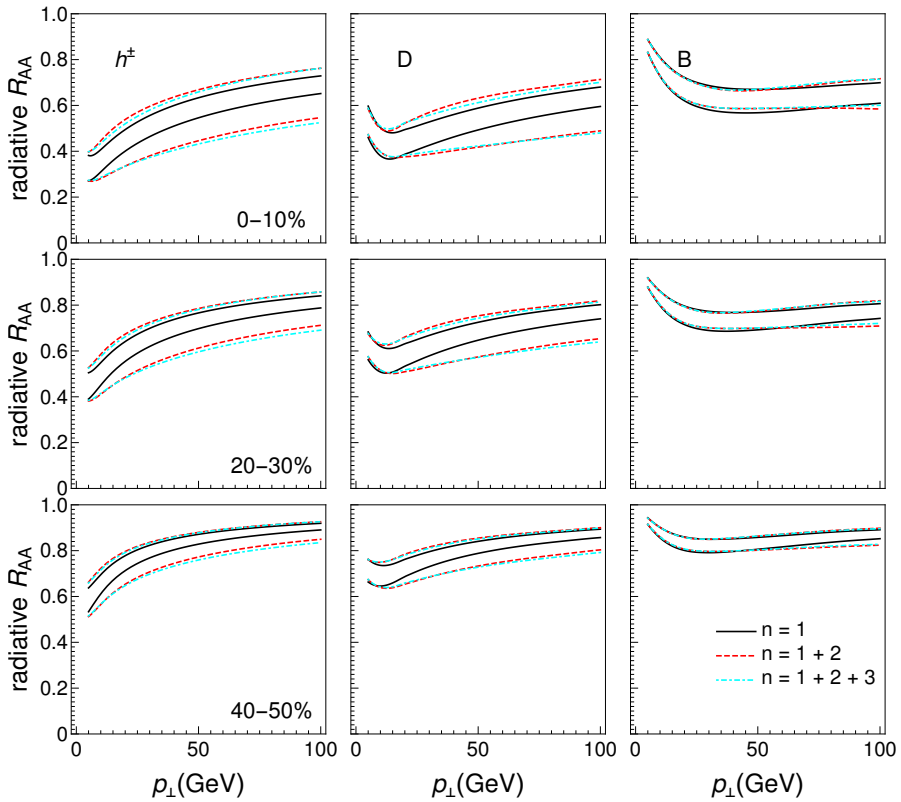

Figure 5.4: Radiative R_{AA} results obtained within DREENA-C – the effects of different orders in opacity. The results are generated for the Pb+Pb collision system at $\sqrt{s_{NN}} = 5.02$ TeV, and all the other figures in the manuscript show the results for the same collision system and energy. Different columns correspond to charged hadrons, D, and B mesons, while different rows show different centrality classes. Solid black curves show the 1$^{\text{st}}$ order in opacity results, red dashed curves show the results up to the 2$^{\text{nd}}$ order, while cyan dot-dashed curves up to the 3$^{\text{rd}}$ order in opacity. The upper (lower) boundary of each band corresponds to the $\mu_M/\mu_E = 0.6$ ($\mu_M/\mu_E = 0.4$) case.

contribution is always positive due to $\mu_{pl} < \mu_E$. On the other hand, magnetic contribution depends non-trivially on the value of magnetic mass. That is, for $\mu_M > \mu_{pl}$, we see that magnetic contribution decreases the energy loss. In contrast, for $\mu_M < \mu_{pl}$, it increases the energy loss and consequently suppression, as shown in Fig. 5.4, which may intuitively explain the observed energy loss and R_{AA} behavior.

Furthermore, the Debye mass μ_E is well defined from lattice QCD, where the perturbative calculations are consistent [150]. Thus, the electric potential is well defined in dynamical energy loss, and we can separately test the effect of higher orders in opacity on this contribution (by replacing $v(\mathbf{q})$ by $v_L(\mathbf{q})$ in the DREENA framework). Surprisingly, we find it negligible, as shown in Fig. 5.5. Thus, higher orders in opacity essentially do not influence the electric contribution in a dynamical QCD medium, which is an interesting and intuitively unexpected result. That is, the higher orders mainly influence the magnetic contribution to energy loss (keeping the electric contribution unaffected), where the sign of the effect depends on the magnetic mass value. For example, as μ_M/μ_E=0.4 is notably smaller than $\mu_{pl}/\mu_E = 1/\sqrt{3}$, the higher orders in opacity are significant for this limit and increase the suppression, in agreement with Fig. 5.4. On the other hand, μ_M/μ_E=0.6 is close to (but slightly larger than) μ_{pl}/μ_E, so higher orders in opacity are small for this magnetic mass limit and reduce the suppression, also in agreement with Fig. 5.4. Additionally, note that the most recent 2+1 flavor lattice QCD results with physical quark masses further constrain the magnetic screening to $0.58 < \mu_M/\mu_E <$

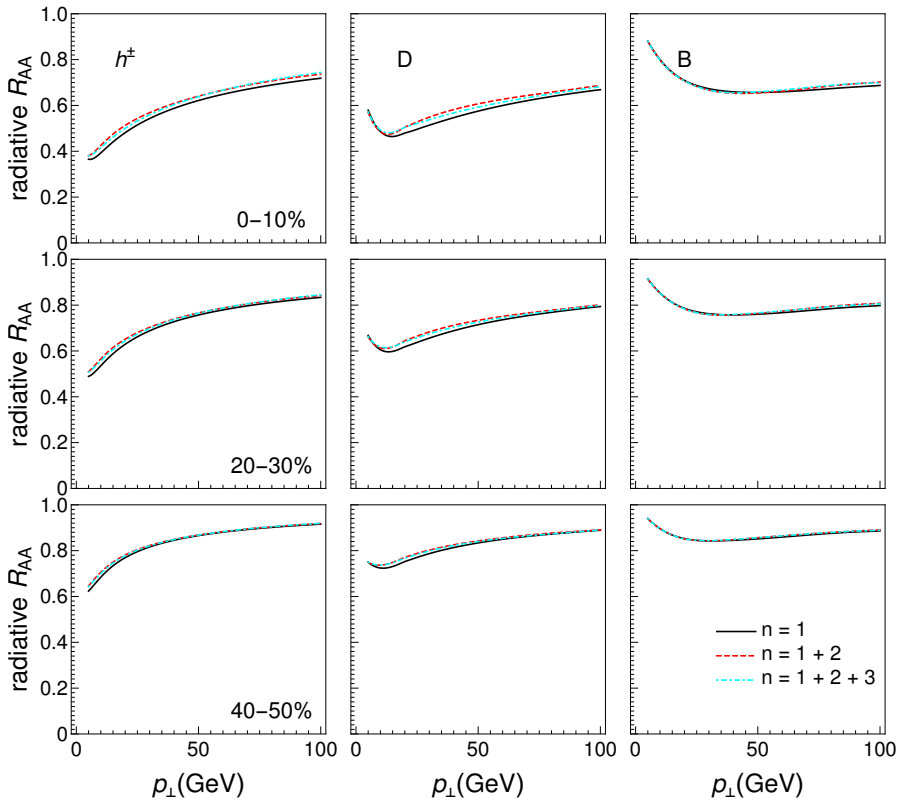

Figure 5.5: R_{AA} results, obtained within DREENA-C when only electric contribution ($v_L(\mathbf{q})$) to radiative energy loss is considered. Different columns correspond to charged hadrons, D, and B mesons, while different rows show different centrality classes. Solid black curves show the 1$^{\text{st}}$ order in opacity results, red dashed curves show the results up to the 2$^{\text{nd}}$ order, while cyan dot-dashed curves up to the 3$^{\text{rd}}$ order in opacity.

0.64 [235]. Thus, for this range of magnetic screening, we conclude that the effects of higher orders in opacity are minor in a dynamical QCD medium and can be safely neglected.

Furthermore, Fig. 5.5 raises another important question: as it is well known, only electric contribution exists in *static* QCD medium approximation [22, 120] (though it has a different functional form compared to the electric contribution in dynamical QCD medium). That is, the magnetic contribution is inherently connected with the dynamic nature of the QCD medium. As most existing energy loss calculations assume (simplified) static QCD medium approximation, does this mean higher orders in opacity can be neglected under such approximation?

We first note that this does not necessarily have to be the case because the effective potential for electric contribution is significantly different in static compared to the dynamical medium. However, to address this question, we repeat the same analyses as above, this time assuming the static medium effective potential (left-hand side of Eq. (5.9)) and mean free path (λ_{stat}). Fig. 5.6 shows the effects of higher orders in opacity in static medium approximation (DGLV case). While larger than those in Fig. 5.5, these effects are still minor (i.e., less than 6%). Thus, for optically thin medium models with static approximation, we show that including multiple scattering centers has a negligible effect on the numerical results, i.e., these effects can also be neglected.

Finally, we ask how the inclusion of evolving medium would modify these results. Including higher-order effects in the evolving medium is very demanding and out of the scope of this manuscript. However, it can be partially addressed by studying how higher-order effects depend on the temperature, which changes in the evolving medium. To address this, in Fig. 5.7, we

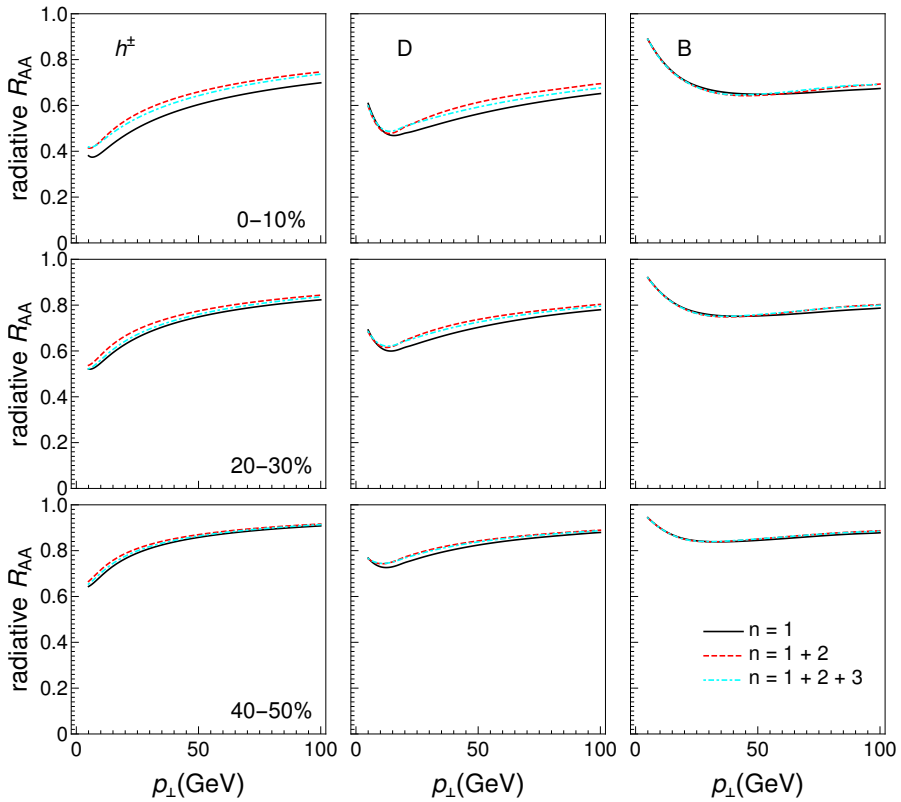

Figure 5.6: Radiative R_{AA} results obtained within DREENA-C under the *static* medium approximation. Different columns correspond to charged hadrons, D, and B mesons, while different rows show different centrality classes. Solid black curves show the 1st order in opacity results, red dashed curves show the results up to the 2nd order, while cyan dot-dashed curves up to the 3rd order in opacity.

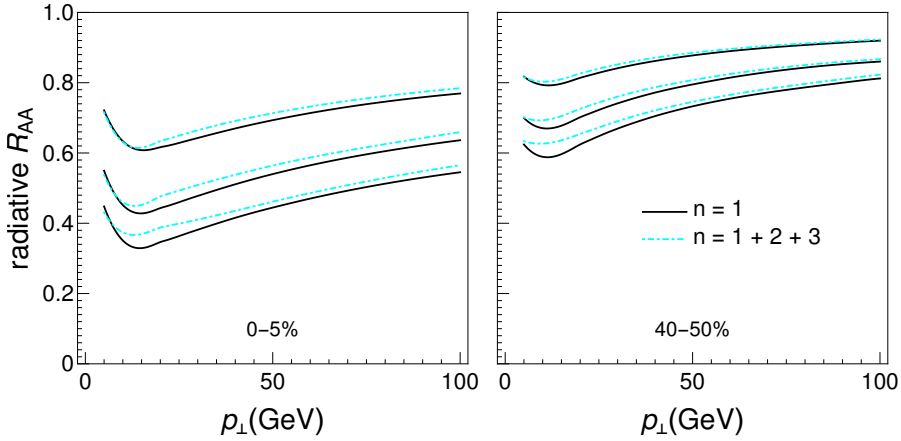

Figure 5.7: D meson radiative R_{AA} results obtained within DREENA-C for different temperature values. The left panel corresponds to 0-5% centrality, while the right panel corresponds to 40-50% centrality. The values of temperature are $T = 200$ MeV (the uppermost curves), 400 MeV (the middle curves), and 600 MeV (the lowest curves). The solid black curves show the 1^{st} order in opacity results, while cyan dot-dashed curves show the results up to the 3^{rd} order in opacity. The chromomagnetic and chromoelectric mass ratio is fixed to $\mu_M/\mu_E = 0.6$.

focus on D meson R_{AA}, $\mu_M/\mu_E = 0.6$ (per agreement with [235]) and study the effects of higher orders in opacity for three different temperature values $T = 200, 400, 600$ MeV (which

broadly covers the range of temperatures accessible at RHIC and the LHC). See Appendix G for the entire panel, which also includes the results up to the 2^{nd} order in opacity. We find that the higher-order effects are largely independent of these values. Thus, we do not expect that including medium evolution will significantly influence the results presented in this study, i.e., expect the effect of multiple scattering centers to remain small.

5.5 Summary

In this Chapter, we generalized our dynamical energy loss and DGLV formalisms towards finite orders in opacity. For bottom quarks, we find that higher orders in opacity are insignificant due to short gluon formation time, i.e., the incoherent limit. For charm and light quarks, including 2^{nd} order in opacity is sufficient, i.e., the 3^{rd} order numerical results almost overlap with the 2^{nd}. Surprisingly, we also find that for limits of magnetic screening, $\mu_M/\mu_E = 0.4$ and $\mu_M/\mu_E = 0.6$, the effects on the R_{AA} are opposite in sign. For $\mu_M/\mu_E = 0.6$ ($\mu_M/\mu_E = 0.4$), higher orders in opacity decrease (increase) the energy loss and subsequently suppression. The intuitive reason behind such behavior is the magnetic contribution to the dynamical energy loss. That is, while electric contribution remains almost insensitive to increases in the order of opacity, magnetic screening larger (smaller) than plasmon mass value decreases (increases) the energy loss and suppression, in agreement with the theoretical expectations. We also show that in the static QCD medium approximation, in which (per definition) only electric contribution remains, the effects of higher orders in opacity on high-$p_\perp$ observables are minor and can be safely neglected. Thus, for static QCD medium, the first order in opacity is an adequate approximation for finite-size QCD medium created in the RHIC and the LHC. For dynamical energy loss, both the effect's sign and size depend on the magnetic screening, as outlined above. However, for most of the current estimates of magnetic screening [235], these effects remain less than 5%, so they can also be safely neglected.

The analyses presented here are obtained for a constant temperature medium (and adequately generalized DREENA-C framework). However, we also tested how the effects of including multiple scatterers depend upon temperature and found this influence to be also small (affecting the radiative R_{AA} for less than 5%). Thus, we expect that including higher orders in opacity in the evolving medium will not change the qualitative results obtained here, but this remains to be rigorously tested.

Chapter 6

Conclusions

Quark-gluon plasma is a new form of matter created in heavy-ion collisions at ultrarelativistic energies, consisting of deconfined quarks, antiquarks, and gluons. Most particles created after such a collision form the thermalized medium, while a tiny fraction is the high-energy/high-$p_\perp$ particles. In this thesis, we utilized high-$p_\perp$ theory and data to infer properties of quark-gluon plasma. Namely, with a proper description of the energy loss of rare high-energy particles, it becomes evident that they become excellent tools for quark-gluon plasma tomography. To this avail, we used the state-of-the-art dynamical energy loss formalism, which can accurately describe the interaction of the high-$p_\perp$ particles with the medium. This Chapter will summarize the most important research results presented in this thesis.

In Chapter 3, we demonstrated how high-$p_\perp$ theory and data can be used to constrain τ_0 — the initial time, i.e., the time of onset of hydrodynamical evolution of quark-gluon plasma — a parameter that has previously been only weakly constrained through low-$p_\perp$ data. First, we explored a simplified scenario with no pre-equilibrium medium evolution. We determined high-$p_\perp$ observables on a set of temperature profiles with various initial times (in the range 0.2fm $\leq \tau_0 \leq$ 1.2fm), which all give good agreement with low-$p_\perp$ spectra, and the obtained predictions were compared with high-$p_\perp$ R_{AA} and v_2 experimental results. We observed that high-$p_\perp$ predictions show sensitivity to τ_0 and that they can be resolved against the experimental data. Moreover, the data prefers later thermalization time ($\tau_0 \sim$ 1fm). In order to try to explain these findings, we entertained the notion that jet quenching may start later than the thermalization of the medium. We tested this scenario by introducing quenching time $\tau_q \geq \tau_0$. However, while R_{AA} shows sensitivity to τ_q, we find that v_2 is entirely insensitive to τ_q (for a given temperature profile with a particular τ_0), thus refuting the idea that jet quenching can start later than the medium thermalization. Finally, we show that the obtained sensitivity of high-$p_\perp$ R_{AA} and v_2 to τ_0 is due to the differences in temperatures that jets see while traversing the medium in the in-plane and out-of-plane directions. Larger τ_0 cuts away the large-temperature part of the profile (decreasing its average temperature), which explains the behavior of R_{AA}; furthermore, profiles with larger τ_0 show a more significant difference between in-plane and out-of-plane temperatures, which explains the behavior of v_2.

In the second part of Chapter 3, we introduce pre-equilibrium evolution into our calculations. Namely, we consider four limiting scenarios, i.e., four temperature profiles with various values of hydrodynamics initial time (τ_0) and quenching time (τ_q): *i*) no pre-equilibrium transverse expansion until $\tau_0 = \tau_q =$ 0.2fm; *ii*) no pre-equilibrium transverse expansion until $\tau_0 =$ 0.2fm

and $\tau_q = 1$fm; *iii*) free streaming from $\tau = 0.2$fm until $\tau_0 = \tau_q = 1$fm; *iv*) no pre-equilibrium transverse expansion until $\tau_0 = \tau_q = 1$fm. All these four profiles give good agreement with low-$p_\perp$ spectra and low-$p_\perp$ v_2. High-$p_\perp$ R_{AA} and v_2 have been calculated on these profiles and compared with the experimental data. As expected, the later the energy loss begins, the higher the R_{AA} and starting the energy loss already at $\tau_q = 0.2$fm is disfavored. On the other hand, if the early expansion is fluid-dynamical, delaying the onset of energy loss barely changes the value of v_2. Moreover, the free streaming case leads to an even worse fit for the data. The only case in which v_2 predictions approach the data is when *both* the energy loss and transverse expansion are delayed to $\tau = 1$fm. We also generated heavy-flavor R_{AA} and v_2, which show even stronger sensitivity to the early evolution. To investigate the origin of this sensitivity of R_{AA} and v_2 to the early evolution, we again evaluate the average temperature along the paths of jets traversing the medium in the in-plane and out-of-plane directions, as well as their difference. From this, we find that delaying the onset of transverse expansion to $\tau_0 = 1.0$fm leads to a larger difference in temperatures than either early fluid-dynamical or free-streaming expansion, which allows enough v_2 to be built up in that case.

Chapter 4 presents the results of the study of the anisotropy of quark-gluon plasma created in heavy-ion collisions. We propose a novel approach where this vital bulk parameter is extracted from the already available experimental data. To begin with, we considered a simple 1+1D longitudinally-expanding Bjorken model. Even though this model does not include transverse expansion (and is therefore not realistic), simple scaling arguments related to the dynamical energy loss model can be applied within it. By using these scaling arguments, we deduce that, at high $p_\perp$, the ratio of v_2 and $1 - R_{AA}$ is expected to depend only on the anisotropy of the system, through the anisotropy of path lengths, $\Delta L/L$. In order to test this, we employ the full-fledged DREENA-B framework to calculate $v_2/(1 - R_{AA})$ as a function of the transverse momentum. We obtain that it indeed saturates at $p_\perp > 20$GeV, and its value at high $p_\perp$ is equal to the value predicted by the scaling arguments. Finally, we construct a proxy variable from $\Delta L/L$, which closely resembles ϵ_2 (the parameter usually used to quantify the spatial anisotropy of QGP), and calculate its values by using our full-fledged $v_2/(1-R_{AA})$ predictions. In this way, we can recover the ϵ_2 from conventional initial state models — a highly non-trivial result which confirms that $v_2/(1 - R_{AA})$ indeed carries information on the anisotropy of the system.

In the second part of this Chapter, we explore the relation between high-$p_\perp$ data and anisotropy in a fully evolving medium. In order to check the universality of our findings, we study a large set of temperature profiles generated by using various initial state models (Glauber, Glauber + free streaming, EKRT, IP-Glasma, T$_R$ENTo), subsequent hydrodynamical evolutions (3+1D hydrodynamical model, MUSIC, VISHNU) for different collision systems and energies: Pb + Pb at 5.02TeV and 2.76TeV and Xe + Xe at 5.44TeV. We calculate $v_2/(1-R_{AA})$ within DREENA-A, and obtain that $v_2/(1 - R_{AA})$ saturates at high $p_\perp$ for all the examined temperature profiles. Moreover, we find a simple linear dependence between the values of $v_2/(1-R_{AA})$ at high-$p_\perp$ and the anisotropy of path lengths, $\Delta L/L$. However, in order to relate the anisotropy inferred from high-$p_\perp$ predictions more directly to the properties of the evolving medium, we introduce a new observable, *jet-temperature anisotropy* $\langle jT_2 \rangle$, which explicitly depends on the medium evolution. We find that it is directly proportional to $v_2/(1 - R_{AA})$, with a slope close to unity. We estimate jet-perceived anisotropy from hydrodynamical evolutions and compare the values with the values obtained from the v_2 and R_{AA} experimental measurements. None of the tested evolutions reproduce the experimentally obtained jet-temperature anisotropy. However, since jet-perceived anisotropy is a medium property, we argue that future hydrodynamical calculations should be tuned to reproduce the experimentally obtained $\langle jT_2 \rangle$.

Finally, in Chapter 5, we study the effects of including a finite number of scattering centers

in radiative energy loss within the dynamical energy loss formalism. Contrary to most energy loss models, usually based on optically thick or optically thin approximation, we derive the analytical expressions up to the 4^{th} order in opacity within the dynamical energy loss formalism. We implement them into the DREENA-C framework and calculate radiative R_{AA} and v_2 (we observe similar behavior in these two observables). The effects of higher orders in opacity on R_{AA} are minor for more peripheral collisions, as expected. Furthermore, we find that higher orders in opacity are negligible for B mesons, while these effects increase with decreasing mass. Unexpectedly, we observe that the effects are opposite in sign for different magnetic mass limiting cases: for $\mu_M/\mu_E = 0.6$, the inclusion of higher orders in opacity reduces the energy loss, while for $\mu_M/\mu_E = 0.4$ the effect has the opposite sign and a much larger magnitude. The intuitive reason behind such behavior is the magnetic contribution to the dynamical energy loss. While the electric contribution is almost insensitive to the higher orders in opacity, the magnetic screening larger (smaller) than plasmon mass decreases (increases) the energy loss, thus explaining the observed behavior. We also explored the static QCD medium approximation (which has only the electric contribution). In this case, we found that the first order in opacity is an adequate approximation for a finite-size QCD medium created in heavy-ion collisions. In the dynamical medium, both the magnitude and the sign of the effects depend on the magnetic screening. However, for the most current estimates of its value, we conclude that the effects remain less than 5% and can be safely neglected.

All these results demonstrate the usefulness of high-energy particles for studying the properties of quark-gluon plasma. Our results advance the applicability of high-$p_\perp$ data and show the interconnections between the low- and high-$p_\perp$ sector, which can be jointly used to constrain the properties of this new form of matter.

Appendix A

High-$p_\perp$ R_{AA} and v_2 for various pre-equilibrium evolution scenarios

In the second part of Chapter 3, we showed high-$p_\perp$ R_{AA} and v_2 results for four limiting scenarios (see Figure 3.7). In order to confirm the universality of our findings, we here include an expanded panel with three additional temperature profiles with more sophisticated initializations: EKRT, IP-Glasma, and T$_R$ENTo.

- In the case of EKRT initialization [86, 87, 88], we employ the same setup as used in Ref. [202] (see also [175]), compute an ensemble of event-by-event fluctuating initial density distributions, average them, and use this average as the initial state of the fluid dynamical evolution. We use the code of Molnar et al., [104] but restricted to boost-invariant expansion. The shear viscosity over entropy density ratio is temperature dependent with favored parameter values from the Bayesian analysis of Ref. [202]. Initial time is $\tau_0 = 0.2$ fm, and the EoS is the $s83s_{18}$ parametrisation from Ref. [202].

- In the case IP-Glasma initialization [77, 78], the calculated event-by-event fluctuating initial states [203] were further evolved [204] using the MUSIC code [205, 206, 207] constrained to boost-invariant expansion. We subsequently averaged the evaluated temperature profiles to obtain one average profile per centrality class. In these calculations, the switch from Yang-Mills to fluid-dynamical evolution took place at $\tau_{\rm switch} = 0.4$ fm, shear viscosity over entropy density ratio was constant $\eta/s = 0.12$, and the temperature-dependent bulk viscosity coefficient over entropy density ratio had its maximum value $\zeta/s = 0.13$. The equation of state was based on the HotQCD lattice results [208] as presented in Ref. [209].

- In the case of T$_{\rm R}$ENTo initialization [89], we create an ensemble of event-by-event fluctuating initial states, sort them into centrality classes, average, and evolve these average initial states. Unlike in other cases, we employ the version of the VISH2+1 code [210] described in Refs. [211, 212]. We run the code using the favored values of the Bayesian analysis of Ref. [212]; in particular, allow free streaming until $\tau = 1.16$ fm, the minimum value of the temperature-dependent η/s is 0.081, and the maximum value of the bulk viscosity coefficient ζ/s is 0.052. The EoS is the same HotQCD lattice results [208] based parametrization used in Refs. [211, 212].

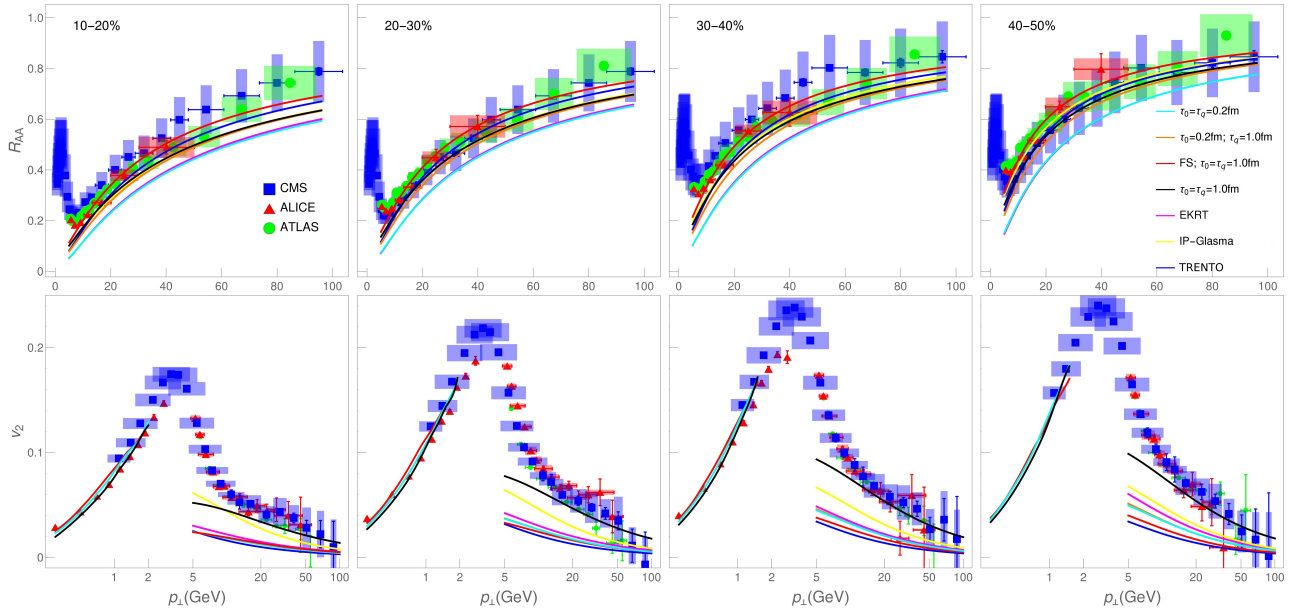

Figure A.1: Charged hadron DREENA-A R_{AA} (upper panels) and v_2 (lower panels) predictions, generated for various initializations and subsequent hydrodynamical evolutions, are compared with ALICE [144, 145], CMS [146, 147] and ATLAS [148, 149] data. Four columns, from left to right, correspond to 10–20%, 20–30%, 30–40% and 40–50% centralities at $\sqrt{s_{NN}} = 5.02$ Pb+Pb collisions at the LHC. The chromomagnetic to chromoelectric mass ratio is set to $\mu_M/\mu_E = 0.5$. Note that the $p_\perp$ scale in the upper (R_{AA}) row is regular, while in the lower (v_2), it is logarithmic.

We calculated high-$p_\perp$ R_{AA} and v_2 for all these profiles, and the results are shown in Figure A.1. We confirm that the only case in which our results simultaneously match both R_{AA} and v_2 experimental data is in the case when both the transverse expansion and the energy loss are delayed to $\tau_0 = 1.0\,\text{fm}$.

Appendix B

Direct proportionality of high-$p_\perp$ v_2 and $1 - R_{AA}$ for various centrality classes

In the second part of Chapter 4, Fig 4.4 shows the direct proportionality of v_2 and $1 - R_{AA}$ at high $p_\perp$ in the 40-50% centrality bin. We here demonstrate that this holds for other centrality classes as well – see Fig. B.1, which shows the direct proportionality of high-$p_\perp$ v_2 and $1 - R_{AA}$ for three different centrality classes (10-20%, 20-30%, 30-40%).

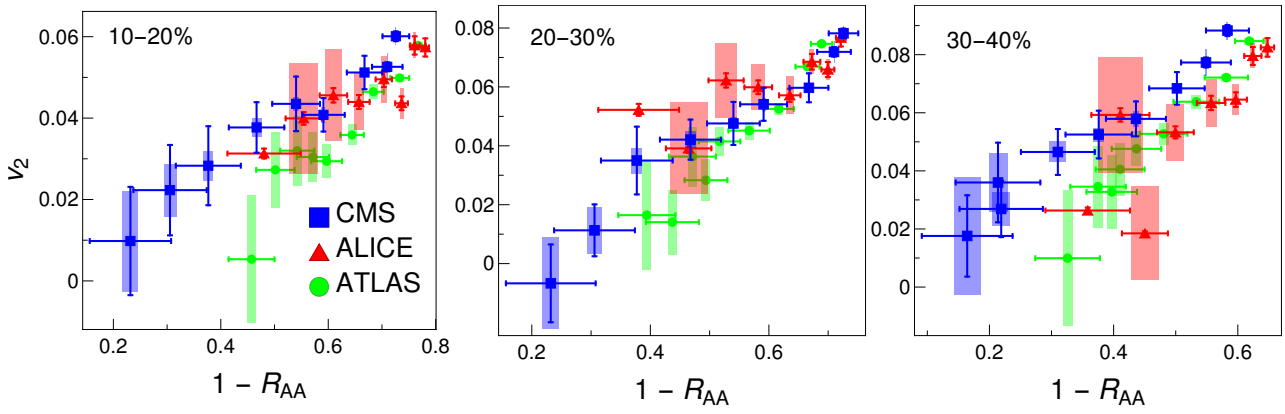

Figure B.1: Direct proportionality of high-$p_\perp$ v_2 and $1 - R_{AA}$, which suggests that their ratio is $p_\perp$-independent. The figure shows v_2 vs $1-R_{\rm AA}$ for $p_\perp > 10$ GeV data for charged hadrons from 5.02 TeV Pb+Pb ALICE [144, 145] (red triangles), CMS [146, 147] (blue squares) and ATLAS [148, 149] (green circles) experiments. The data is shown for the 10-20%, 20-30% and 30-40% centrality bins. Each collaboration's datapoints correspond to different values of $p_\perp$, with both v_2 and $1-R_{\rm AA}$ decreasing with increasing $p_\perp$.

Appendix C

Analytical expressions for dN_g/dx for higher orders in opacity

C.1 General form

The gluon radiation spectrum up to the 4^{th} order in opacity contains the following terms, which are here given in detail:

$$\begin{aligned}\left(\frac{dN_g}{dx}\right) &= \left(\frac{dN_g^{(1)}}{dx}\right)+\left(\frac{dN_g^{(2)}}{dx}\right)_1-\left(\frac{dN_g^{(2)}}{dx}\right)_2 \\ &+ \left(\frac{dN_g^{(3)}}{dx}\right)_1-\left(\frac{dN_g^{(3)}}{dx}\right)_2-\left(\frac{dN_g^{(3)}}{dx}\right)_3+\left(\frac{dN_g^{(3)}}{dx}\right)_4 \\ &+ \left(\frac{dN_g^{(4)}}{dx}\right)_1-\left(\frac{dN_g^{(4)}}{dx}\right)_2-\left(\frac{dN_g^{(4)}}{dx}\right)_3+\left(\frac{dN_g^{(4)}}{dx}\right)_4 \\ &- \left(\frac{dN_g^{(4)}}{dx}\right)_5+\left(\frac{dN_g^{(4)}}{dx}\right)_6+\left(\frac{dN_g^{(4)}}{dx}\right)_7-\left(\frac{dN_g^{(4)}}{dx}\right)_8 \end{aligned} \tag{C.1}$$

Numerical integrations with respect to the momentum $\mathbf{k}$ are performed over $0 < |\mathbf{k}| < 2Ex(1-x)$, and the ones with respect to momenta $\mathbf{q}_i$ are performed over $0 < |\mathbf{q}_i| < \sqrt{4ET}$ [236]. The integrations with respect to angles φ_i are performed over $0 < \varphi_i < 2\pi$. Under the constant T approximation used here, the expressions presented below can be analytically integrated over z_i, significantly simplifying subsequent numerical calculations (see Appendix B.2).

In the expressions below, the following equations hold for $i, j \in \{1, 2, 3, 4\}$:

$$\mathbf{k}\cdot\mathbf{q}_i = |\mathbf{k}||\mathbf{q}_i|\cos\varphi_i, \tag{C.2}$$

$$\mathbf{q}_i\cdot\mathbf{q}_j = |\mathbf{q}_i||\mathbf{q}_j|\cos(\varphi_i-\varphi_j). \tag{C.3}$$

The 1^{st} order in opacity term is given by:

$$\left(\frac{dN_g^{(1)}}{dx}\right) = \frac{4C_R}{\pi x}\int_0^L dz_1 \int \frac{d^2\mathbf{k}}{\pi}\int \frac{d^2\mathbf{q}_1}{\pi}\,\alpha_s(Q_k^2)\frac{1}{\lambda_{dyn}}\frac{\mu_E^2-\mu_M^2}{(\mathbf{q}_1^2+\mu_E^2)(\mathbf{q}_1^2+\mu_M^2)} \frac{\chi^2(\mathbf{q}_1\cdot(\mathbf{q}_1-\mathbf{k}))+(\mathbf{q}_1\cdot\mathbf{k})(\mathbf{k}-\mathbf{q}_1)^2}{(\chi^2+\mathbf{k}^2)(\chi^2+(\mathbf{k}-\mathbf{q}_1)^2)^2}\sin^2\left(\frac{\chi^2+(\mathbf{k}^2-\mathbf{q}_1)^2}{4xE}z_1\right). \tag{C.4}$$

After integration with respect to z_1, this expression reduces to the expression used to obtain dN_g/dx in the original DREENA-C framework [107].

The 2^{nd} order in opacity contains two terms, which are given by:

$$\left(\frac{dN_g^{(2)}}{dx}\right)_1 = \frac{4C_R}{\pi x}\int_0^L\int_{z_1}^L dz_1dz_2\int\frac{d^2\mathbf{k}}{\pi}\iint\frac{d^2\mathbf{q}_1}{\pi}\frac{d^2\mathbf{q}_2}{\pi} \alpha_s(Q_k^2)\frac{1}{\lambda_{dyn}^2}\frac{\mu_E^2-\mu_M^2}{(\mathbf{q}_1^2+\mu_E^2)(\mathbf{q}_1^2+\mu_M^2)}\frac{\mu_E^2-\mu_M^2}{(\mathbf{q}_2^2+\mu_E^2)(\mathbf{q}_2^2+\mu_M^2)} \frac{\chi^2(\mathbf{q}_2\cdot(\mathbf{q}_1+\mathbf{q}_2-\mathbf{k}))+(\mathbf{q}_2\cdot\mathbf{k})(\mathbf{k}-\mathbf{q}_2)^2+(\mathbf{k}\cdot\mathbf{q}_1)(\mathbf{q}_2\cdot(\mathbf{q}_2-2\mathbf{k}))+\mathbf{k}^2(\mathbf{q}_2\cdot\mathbf{q}_1)}{(\chi^2+\mathbf{k}^2)(\chi^2+(\mathbf{k}-\mathbf{q}_2)^2)(\chi^2+(\mathbf{k}-\mathbf{q}_1-\mathbf{q}_2)^2)} \sin\left(\frac{\chi^2+(\mathbf{k}-\mathbf{q}_1-\mathbf{q}_2)^2}{4xE}z_1\right)\sin\left(\frac{\chi^2+(\mathbf{k}-\mathbf{q}_1-\mathbf{q}_2)^2}{4xE}z_1+\frac{\chi^2+(\mathbf{k}-\mathbf{q}_2)^2}{2xE}z_2\right), \tag{C.5}$$

$$\left(\frac{dN_g^{(2)}}{dx}\right)_2 = \frac{4C_R}{\pi x}\int_0^L\int_{z_1}^L dz_1dz_2\int\frac{d^2\mathbf{k}}{\pi}\int\frac{d^2\mathbf{q}_2}{\pi}\alpha_s(Q_k^2)\frac{1}{\lambda_{dyn}^2}\frac{\mu_E^2-\mu_M^2}{(\mathbf{q}_2^2+\mu_E^2)(\mathbf{q}_2^2+\mu_M^2)} \frac{\chi^2(\mathbf{q}_2\cdot(\mathbf{q}_2-\mathbf{k}))+(\mathbf{q}_2\cdot\mathbf{k})(\mathbf{k}-\mathbf{q}_2)^2}{(\chi^2+\mathbf{k}^2)(\chi^2+(\mathbf{k}-\mathbf{q}_2)^2)^2}\sin\left(\frac{\chi^2+(\mathbf{k}-\mathbf{q}_2)^2}{4xE}z_1\right)\sin\left(\frac{\chi^2+(\mathbf{k}-\mathbf{q}_2)^2}{2xE}(\frac{z_1}{2}+z_2)\right). \tag{C.6}$$

The 3^{rd} order in opacity contains four terms, which are given by:

$$\left(\frac{dN_g^{(3)}}{dx}\right)_1 = \frac{4C_R}{\pi x}\int_0^L\int_{z_1}^L\int_{z_2}^L dz_1dz_2dz_3\int\frac{d^2\mathbf{k}}{\pi}\iiint\frac{d^2\mathbf{q}_1}{\pi}\frac{d^2\mathbf{q}_2}{\pi}\frac{d^2\mathbf{q}_3}{\pi} \alpha_s(Q_k^2)\frac{1}{\lambda_{dyn}^3}\frac{\mu_E^2-\mu_M^2}{(\mathbf{q}_1^2+\mu_E^2)(\mathbf{q}_1^2+\mu_M^2)}\frac{\mu_E^2-\mu_M^2}{(\mathbf{q}_2^2+\mu_E^2)(\mathbf{q}_2^2+\mu_M^2)}\frac{\mu_E^2-\mu_M^2}{(\mathbf{q}_3^2+\mu_E^2)(\mathbf{q}_3^2+\mu_M^2)} \frac{\chi^2(\mathbf{q}_3\cdot(\mathbf{q}_1+\mathbf{q}_2+\mathbf{q}_3-\mathbf{k}))+(\mathbf{q}_3\cdot\mathbf{k})(\mathbf{k}-\mathbf{q}_3)^2+(\mathbf{k}\cdot(\mathbf{q}_1+\mathbf{q}_2))(\mathbf{q}_3\cdot(\mathbf{q}_3-2\mathbf{k}))+\mathbf{k}^2(\mathbf{q}_3\cdot(\mathbf{q}_1+\mathbf{q}_2))}{(\chi^2+\mathbf{k}^2)(\chi^2+(\mathbf{k}-\mathbf{q}_3)^2)(\chi^2+(\mathbf{k}-\mathbf{q}_1-\mathbf{q}_2-\mathbf{q}_3)^2)} \sin\left(\frac{\chi^2+(\mathbf{k}-\mathbf{q}_1-\mathbf{q}_2-\mathbf{q}_3)^2}{4xE}z_1\right) \sin\left(\frac{\chi^2+(\mathbf{k}-\mathbf{q}_1-\mathbf{q}_2-\mathbf{q}_3)^2}{4xE}z_1+\frac{\chi^2+(\mathbf{k}-\mathbf{q}_2-\mathbf{q}_3)^2}{2xE}z_2+\frac{\chi^2+(\mathbf{k}-\mathbf{q}_3)^2}{2xE}z_3\right), \tag{C.7}$$

$$\left(\frac{dN_g^{(3)}}{dx}\right)_2 = \frac{4C_R}{\pi x}\int_0^L\int_{z_1}^L\int_{z_2}^L dz_1dz_2dz_3\int\frac{d^2\mathbf{k}}{\pi}\iint\frac{d^2\mathbf{q}_1}{\pi}\frac{d^2\mathbf{q}_3}{\pi} \alpha_s(Q_k^2)\frac{1}{\lambda_{dyn}^3}\frac{\mu_E^2-\mu_M^2}{(\mathbf{q}_1^2+\mu_E^2)(\mathbf{q}_1^2+\mu_M^2)}\frac{\mu_E^2-\mu_M^2}{(\mathbf{q}_3^2+\mu_E^2)(\mathbf{q}_3^2+\mu_M^2)} \frac{\chi^2(\mathbf{q}_3\cdot(\mathbf{q}_1+\mathbf{q}_3-\mathbf{k}))+(\mathbf{q}_3\cdot\mathbf{k})(\mathbf{k}-\mathbf{q}_3)^2+(\mathbf{k}\cdot\mathbf{q}_1)(\mathbf{q}_3\cdot(\mathbf{q}_3-2\mathbf{k}))+\mathbf{k}^2(\mathbf{q}_3\cdot\mathbf{q}_1)}{(\chi^2+\mathbf{k}^2)(\chi^2+(\mathbf{k}-\mathbf{q}_3)^2)(\chi^2+(\mathbf{k}-\mathbf{q}_1-\mathbf{q}_3)^2)} \sin\left(\frac{\chi^2+(\mathbf{k}-\mathbf{q}_1-\mathbf{q}_3)^2}{4xE}z_1\right)\sin\left(\frac{\chi^2+(\mathbf{k}-\mathbf{q}_1-\mathbf{q}_3)^2}{4xE}z_1+\frac{\chi^2+(\mathbf{k}-\mathbf{q}_3)^2}{2xE}(z_2+z_3)\right), \tag{C.8}$$

$$\left(\frac{dN_g^{(3)}}{dx}\right)_3 = \frac{4C_R}{\pi x}\int_0^L\int_{z_1}^L\int_{z_2}^L dz_1dz_2dz_3\int\frac{d^2\mathbf{k}}{\pi}\iint\frac{d^2\mathbf{q}_2}{\pi}\frac{d^2\mathbf{q}_3}{\pi} \alpha_s(Q_k^2)\frac{1}{\lambda_{dyn}^3}\frac{\mu_E^2-\mu_M^2}{(\mathbf{q}_2^2+\mu_E^2)(\mathbf{q}_2^2+\mu_M^2)}\frac{\mu_E^2-\mu_M^2}{(\mathbf{q}_3^2+\mu_E^2)(\mathbf{q}_3^2+\mu_M^2)} \frac{\chi^2(\mathbf{q}_3\cdot(\mathbf{q}_2+\mathbf{q}_3-\mathbf{k}))+(\mathbf{q}_3\cdot\mathbf{k})(\mathbf{k}-\mathbf{q}_3)^2+(\mathbf{k}\cdot\mathbf{q}_2)(\mathbf{q}_3\cdot(\mathbf{q}_3-2\mathbf{k}))+\mathbf{k}^2(\mathbf{q}_3\cdot\mathbf{q}_2)}{(\chi^2+\mathbf{k}^2)(\chi^2+(\mathbf{k}-\mathbf{q}_3)^2)(\chi^2+(\mathbf{k}-\mathbf{q}_2-\mathbf{q}_3)^2)} \sin\left(\frac{\chi^2+(\mathbf{k}-\mathbf{q}_2-\mathbf{q}_3)^2}{4xE}z_1\right)\sin\left(\frac{\chi^2+(\mathbf{k}-\mathbf{q}_2-\mathbf{q}_3)^2}{2xE}\left(\frac{z_1}{2}+z_2\right)+\frac{\chi^2+(\mathbf{k}-\mathbf{q}_3)^2}{2xE}z_3\right), \tag{C.9}$$

$$\left(\frac{dN_g^{(3)}}{dx}\right)_4 = \frac{4C_R}{\pi x}\int_0^L\int_{z_1}^L\int_{z_2}^L dz_1dz_2dz_3\int\frac{d^2\mathbf{k}}{\pi}\int\frac{d^2\mathbf{q}_3}{\pi} \alpha_s(Q_k^2)\frac{1}{\lambda_{dyn}^3}\frac{\mu_E^2-\mu_M^2}{(\mathbf{q}_3^2+\mu_E^2)(\mathbf{q}_3^2+\mu_M^2)}\frac{\chi^2(\mathbf{q}_3\cdot(\mathbf{q}_3-\mathbf{k}))+(\mathbf{q}_3\cdot\mathbf{k})(\mathbf{k}-\mathbf{q}_3)^2}{(\chi^2+\mathbf{k}^2)(\chi^2+(\mathbf{k}-\mathbf{q}_3)^2)^2} \sin\left(\frac{\chi^2+(\mathbf{k}-\mathbf{q}_3)^2}{4xE}z_1\right)\sin\left(\frac{\chi^2+(\mathbf{k}-\mathbf{q}_3)^2}{2xE}\left(\frac{z_1}{2}+z_2+z_3\right)\right). \tag{C.10}$$

The 4^{th} order in opacity is given by eight terms, which are given by:

$$\left(\frac{dN_g^{(4)}}{dx}\right)_1 = \frac{4C_R}{\pi x}\int_0^L\int_{z_1}^L\int_{z_2}^L\int_{z_3}^L dz_1dz_2dz_3dz_4\int\frac{d^2\mathbf{k}}{\pi}\iiint\frac{d^2\mathbf{q}_1}{\pi}\frac{d^2\mathbf{q}_2}{\pi}\frac{d^2\mathbf{q}_3}{\pi}\frac{d^2\mathbf{q}_4}{\pi} \alpha_s(Q_k^2)\frac{1}{\lambda_{dyn}^4}\frac{\mu_E^2-\mu_M^2}{(\mathbf{q}_1^2+\mu_E^2)(\mathbf{q}_1^2+\mu_M^2)}\frac{\mu_E^2-\mu_M^2}{(\mathbf{q}_2^2+\mu_E^2)(\mathbf{q}_2^2+\mu_M^2)}\frac{\mu_E^2-\mu_M^2}{(\mathbf{q}_3^2+\mu_E^2)(\mathbf{q}_3^2+\mu_M^2)}\frac{\mu_E^2-\mu_M^2}{(\mathbf{q}_4^2+\mu_E^2)(\mathbf{q}_4^2+\mu_M^2)} \frac{\chi^2(\mathbf{q}_4\cdot(\mathbf{q}_1+\mathbf{q}_2+\mathbf{q}_3+\mathbf{q}_4-\mathbf{k}))+(\mathbf{q}_4\cdot\mathbf{k})(\mathbf{k}-\mathbf{q}_4)^2+(\mathbf{k}\cdot(\mathbf{q}_1+\mathbf{q}_2+\mathbf{q}_3))(\mathbf{q}_4\cdot(\mathbf{q}_4-2\mathbf{k}))+\mathbf{k}^2(\mathbf{q}_4\cdot(\mathbf{q}_1+\mathbf{q}_2+\mathbf{q}_3))}{(\chi^2+\mathbf{k}^2)(\chi^2+(\mathbf{k}-\mathbf{q}_4)^2)(\chi^2+(\mathbf{k}-\mathbf{q}_1-\mathbf{q}_2-\mathbf{q}_3-\mathbf{q}_4)^2)} \sin\left(\frac{\chi^2+(\mathbf{k}-\mathbf{q}_1-\mathbf{q}_2-\mathbf{q}_3-\mathbf{q}_4)^2}{4xE}z_1+\frac{\chi^2+(\mathbf{k}-\mathbf{q}_2-\mathbf{q}_3-\mathbf{q}_4)^2}{2xE}z_2+\frac{\chi^2+(\mathbf{k}-\mathbf{q}_3-\mathbf{q}_4)^2}{2xE}z_3+\frac{\chi^2+(\mathbf{k}-\mathbf{q}_4)^2}{2xE}z_4\right) \sin\left(\frac{\chi^2+(\mathbf{k}-\mathbf{q}_1-\mathbf{q}_2-\mathbf{q}_3-\mathbf{q}_4)^2}{4xE}z_1\right), \tag{C.11}$$

$$\left(\frac{dN_g^{(4)}}{dx}\right)_2 = \frac{4C_R}{\pi x}\int_0^L\int_{z_1}^L\int_{z_2}^L\int_{z_3}^L dz_1dz_2dz_3dz_4\int\frac{d^2\mathbf{k}}{\pi}\iiint\frac{d^2\mathbf{q}_1}{\pi}\frac{d^2\mathbf{q}_2}{\pi}\frac{d^2\mathbf{q}_4}{\pi} \alpha_s(Q_k^2)\frac{1}{\lambda_{dyn}^4}\frac{\mu_E^2-\mu_M^2}{(\mathbf{q}_1^2+\mu_E^2)(\mathbf{q}_1^2+\mu_M^2)}\frac{\mu_E^2-\mu_M^2}{(\mathbf{q}_2^2+\mu_E^2)(\mathbf{q}_2^2+\mu_M^2)}\frac{\mu_E^2-\mu_M^2}{(\mathbf{q}_4^2+\mu_E^2)(\mathbf{q}_4^2+\mu_M^2)} \frac{\chi^2(\mathbf{q}_4\cdot(\mathbf{q}_1+\mathbf{q}_2+\mathbf{q}_4-\mathbf{k}))+(\mathbf{q}_4\cdot\mathbf{k})(\mathbf{k}-\mathbf{q}_4)^2+(\mathbf{k}\cdot(\mathbf{q}_1+\mathbf{q}_2))(\mathbf{q}_4\cdot(\mathbf{q}_4-2\mathbf{k}))+\mathbf{k}^2(\mathbf{q}_4\cdot(\mathbf{q}_1+\mathbf{q}_2))}{(\chi^2+\mathbf{k}^2)(\chi^2+(\mathbf{k}-\mathbf{q}_4)^2)(\chi^2+(\mathbf{k}-\mathbf{q}_1-\mathbf{q}_2-\mathbf{q}_4)^2)} \sin\left(\frac{\chi^2+(\mathbf{k}-\mathbf{q}_1-\mathbf{q}_2-\mathbf{q}_4)^2}{4xE}z_1+\frac{\chi^2+(\mathbf{k}-\mathbf{q}_2-\mathbf{q}_4)^2}{2xE}z_2+\frac{\chi^2+(\mathbf{k}-\mathbf{q}_4)^2}{2xE}(z_3+z_4)\right) \sin\left(\frac{\chi^2+(\mathbf{k}-\mathbf{q}_1-\mathbf{q}_2-\mathbf{q}_4)^2}{4xE}z_1\right), \tag{C.12}$$

$$\left(\frac{dN_g^{(4)}}{dx}\right)_3 = \frac{4C_R}{\pi x}\int_0^L\int_{z_1}^L\int_{z_2}^L\int_{z_3}^L dz_1dz_2dz_3dz_4\int\frac{d^2\mathbf{k}}{\pi}\iiint\frac{d^2\mathbf{q}_1}{\pi}\frac{d^2\mathbf{q}_3}{\pi}\frac{d^2\mathbf{q}_4}{\pi} \alpha_s(Q_k^2)\frac{1}{\lambda_{dyn}^4}\frac{\mu_E^2-\mu_M^2}{(\mathbf{q}_1^2+\mu_E^2)(\mathbf{q}_1^2+\mu_M^2)}\frac{\mu_E^2-\mu_M^2}{(\mathbf{q}_3^2+\mu_E^2)(\mathbf{q}_3^2+\mu_M^2)}\frac{\mu_E^2-\mu_M^2}{(\mathbf{q}_4^2+\mu_E^2)(\mathbf{q}_4^2+\mu_M^2)} \frac{\chi^2(\mathbf{q}_4\cdot(\mathbf{q}_1+\mathbf{q}_3+\mathbf{q}_4-\mathbf{k}))+(\mathbf{q}_4\cdot\mathbf{k})(\mathbf{k}-\mathbf{q}_4)^2+(\mathbf{k}\cdot(\mathbf{q}_1+\mathbf{q}_3))(\mathbf{q}_4\cdot(\mathbf{q}_4-2\mathbf{k}))+\mathbf{k}^2(\mathbf{q}_4\cdot(\mathbf{q}_1+\mathbf{q}_3))}{(\chi^2+\mathbf{k}^2)(\chi^2+(\mathbf{k}-\mathbf{q}_4)^2)(\chi^2+(\mathbf{k}-\mathbf{q}_1-\mathbf{q}_3-\mathbf{q}_4)^2)} \sin\left(\frac{\chi^2+(\mathbf{k}-\mathbf{q}_1-\mathbf{q}_3-\mathbf{q}_4)^2}{4xE}z_1+\frac{\chi^2+(\mathbf{k}-\mathbf{q}_3-\mathbf{q}_4)^2}{2xE}(z_2+z_3)+\frac{\chi^2+(\mathbf{k}-\mathbf{q}_4)^2}{2xE}z_4\right) \sin\left(\frac{\chi^2+(\mathbf{k}-\mathbf{q}_1-\mathbf{q}_3-\mathbf{q}_4)^2}{4xE}z_1\right), \tag{C.13}$$

$$\left(\frac{dN_g^{(4)}}{dx}\right)_4 = \frac{4C_R}{\pi x}\int_0^L\int_{z_1}^L\int_{z_2}^L\int_{z_3}^L dz_1dz_2dz_3dz_4\int\frac{d^2\mathbf{k}}{\pi}\iint\frac{d^2\mathbf{q}_1}{\pi}\frac{d^2\mathbf{q}_4}{\pi} \alpha_s(Q_k^2)\frac{1}{\lambda_{dyn}^4}\frac{\mu_E^2-\mu_M^2}{(\mathbf{q}_1^2+\mu_E^2)(\mathbf{q}_1^2+\mu_M^2)}\frac{\mu_E^2-\mu_M^2}{(\mathbf{q}_4^2+\mu_E^2)(\mathbf{q}_4^2+\mu_M^2)} \frac{\chi^2(\mathbf{q}_4\cdot(\mathbf{q}_1+\mathbf{q}_4-\mathbf{k}))+(\mathbf{q}_4\cdot\mathbf{k})(\mathbf{k}-\mathbf{q}_4)^2+(\mathbf{k}\cdot\mathbf{q}_1)(\mathbf{q}_4\cdot(\mathbf{q}_4-2\mathbf{k}))+\mathbf{k}^2(\mathbf{q}_4\cdot\mathbf{q}_1)}{(\chi^2+\mathbf{k}^2)(\chi^2+(\mathbf{k}-\mathbf{q}_4)^2)(\chi^2+(\mathbf{k}-\mathbf{q}_1-\mathbf{q}_4)^2)} \sin\left(\frac{\chi^2+(\mathbf{k}-\mathbf{q}_1-\mathbf{q}_4)^2}{4xE}z_1\right)\sin\left(\frac{\chi^2+(\mathbf{k}-\mathbf{q}_1-\mathbf{q}_4)^2}{4xE}z_1+\frac{\chi^2+(\mathbf{k}-\mathbf{q}_4)^2}{2xE}(z_2+z_3+z_4)\right), \tag{C.14}$$

$$\left(\frac{dN_g^{(4)}}{dx}\right)_5 = \frac{4C_R}{\pi x}\int_0^L\int_{z_1}^L\int_{z_2}^L\int_{z_3}^L dz_1dz_2dz_3dz_4\int\frac{d^2\mathbf{k}}{\pi}\iiint\frac{d^2\mathbf{q}_2}{\pi}\frac{d^2\mathbf{q}_3}{\pi}\frac{d^2\mathbf{q}_4}{\pi}$$
$$\alpha_s(Q_k^2)\frac{1}{\lambda_{dyn}^4}\frac{\mu_E^2-\mu_M^2}{(\mathbf{q}_2^2+\mu_E^2)(\mathbf{q}_2^2+\mu_M^2)}\frac{\mu_E^2-\mu_M^2}{(\mathbf{q}_3^2+\mu_E^2)(\mathbf{q}_3^2+\mu_M^2)}\frac{\mu_E^2-\mu_M^2}{(\mathbf{q}_4^2+\mu_E^2)(\mathbf{q}_4^2+\mu_M^2)}$$
$$\frac{\chi^2(\mathbf{q}_4\cdot(\mathbf{q}_2+\mathbf{q}_3+\mathbf{q}_4-\mathbf{k}))+(\mathbf{q}_4\cdot\mathbf{k})(\mathbf{k}-\mathbf{q}_4)^2+(\mathbf{k}\cdot(\mathbf{q}_2+\mathbf{q}_3))(\mathbf{q}_4\cdot(\mathbf{q}_4-2\mathbf{k}))+\mathbf{k}^2(\mathbf{q}_4\cdot(\mathbf{q}_2+\mathbf{q}_3))}{(\chi^2+\mathbf{k}^2)(\chi^2+(\mathbf{k}-\mathbf{q}_4)^2)(\chi^2+(\mathbf{k}-\mathbf{q}_2-\mathbf{q}_3-\mathbf{q}_4)^2)}$$
$$\sin\left(\frac{\chi^2+(\mathbf{k}-\mathbf{q}_2-\mathbf{q}_3-\mathbf{q}_4)^2}{2xE}(\frac{z_1}{2}+z_2)+\frac{\chi^2+(\mathbf{k}-\mathbf{q}_3-\mathbf{q}_4)^2}{2xE}z_3+\frac{\chi^2+(\mathbf{k}-\mathbf{q}_4)^2}{2xE}z_4\right)$$
$$\sin\left(\frac{\chi^2+(\mathbf{k}-\mathbf{q}_2-\mathbf{q}_3-\mathbf{q}_4)^2}{4xE}z_1\right), \tag{C.15}$$

$$\left(\frac{dN_g^{(4)}}{dx}\right)_6 = \frac{4C_R}{\pi x}\int_0^L\int_{z_1}^L\int_{z_2}^L\int_{z_3}^L dz_1dz_2dz_3dz_4\int\frac{d^2\mathbf{k}}{\pi}\iint\frac{d^2\mathbf{q}_2}{\pi}\frac{d^2\mathbf{q}_4}{\pi}$$
$$\alpha_s(Q_k^2)\frac{1}{\lambda_{dyn}^4}\frac{\mu_E^2-\mu_M^2}{(\mathbf{q}_2^2+\mu_E^2)(\mathbf{q}_2^2+\mu_M^2)}\frac{\mu_E^2-\mu_M^2}{(\mathbf{q}_4^2+\mu_E^2)(\mathbf{q}_4^2+\mu_M^2)}$$
$$\frac{\chi^2(\mathbf{q}_4\cdot(\mathbf{q}_2+\mathbf{q}_4-\mathbf{k}))+(\mathbf{q}_4\cdot\mathbf{k})(\mathbf{k}-\mathbf{q}_4)^2+(\mathbf{k}\cdot\mathbf{q}_2)(\mathbf{q}_4\cdot(\mathbf{q}_4-2\mathbf{k}))+\mathbf{k}^2(\mathbf{q}_4\cdot\mathbf{q}_2)}{(\chi^2+\mathbf{k}^2)(\chi^2+(\mathbf{k}-\mathbf{q}_4)^2)(\chi^2+(\mathbf{k}-\mathbf{q}_2-\mathbf{q}_4)^2)}$$
$$\sin\left(\frac{\chi^2+(\mathbf{k}-\mathbf{q}_2-\mathbf{q}_4)^2}{4xE}z_1\right)\sin\left(\frac{\chi^2+(\mathbf{k}-\mathbf{q}_2-\mathbf{q}_4)^2}{2xE}(\frac{z_1}{2}+z_2)+\frac{\chi^2+(\mathbf{k}-\mathbf{q}_4)^2}{2xE}(z_3+z_4)\right), \tag{C.16}$$

$$\left(\frac{dN_g^{(4)}}{dx}\right)_7 = \frac{4C_R}{\pi x}\int_0^L\int_{z_1}^L\int_{z_2}^L\int_{z_3}^L dz_1dz_2dz_3dz_4\int\frac{d^2\mathbf{k}}{\pi}\iint\frac{d^2\mathbf{q}_3}{\pi}\frac{d^2\mathbf{q}_4}{\pi}$$
$$\alpha_s(Q_k^2)\frac{1}{\lambda_{dyn}^4}\frac{\mu_E^2-\mu_M^2}{(\mathbf{q}_3^2+\mu_E^2)(\mathbf{q}_3^2+\mu_M^2)}\frac{\mu_E^2-\mu_M^2}{(\mathbf{q}_4^2+\mu_E^2)(\mathbf{q}_4^2+\mu_M^2)}$$
$$\frac{\chi^2(\mathbf{q}_4\cdot(\mathbf{q}_3+\mathbf{q}_4-\mathbf{k}))+(\mathbf{q}_4\cdot\mathbf{k})(\mathbf{k}-\mathbf{q}_4)^2+(\mathbf{k}\cdot\mathbf{q}_3)(\mathbf{q}_4\cdot(\mathbf{q}_4-2\mathbf{k}))+\mathbf{k}^2(\mathbf{q}_4\cdot\mathbf{q}_3)}{(\chi^2+\mathbf{k}^2)(\chi^2+(\mathbf{k}-\mathbf{q}_4)^2)(\chi^2+(\mathbf{k}-\mathbf{q}_3-\mathbf{q}_4)^2)}$$
$$\sin\left(\frac{\chi^2+(\mathbf{k}-\mathbf{q}_3-\mathbf{q}_4)^2}{4xE}z_1\right)\sin\left(\frac{\chi^2+(\mathbf{k}-\mathbf{q}_3-\mathbf{q}_4)^2}{2xE}(\frac{z_1}{2}+z_2+z_3)+\frac{\chi^2+(\mathbf{k}-\mathbf{q}_4)^2}{2xE}z_4\right), \tag{C.17}$$

$$\left(\frac{dN_g^{(4)}}{dx}\right)_8 = \frac{4C_R}{\pi x}\int_0^L\int_{z_1}^L\int_{z_2}^L\int_{z_3}^L dz_1dz_2dz_3dz_4\int\frac{d^2\mathbf{k}}{\pi}\int\frac{d^2\mathbf{q}_4}{\pi}$$
$$\alpha_s(Q_k^2)\frac{1}{\lambda_{dyn}^4}\frac{\mu_E^2-\mu_M^2}{(\mathbf{q}_4^2+\mu_E^2)(\mathbf{q}_4^2+\mu_M^2)}\frac{\chi^2(\mathbf{q}_4\cdot(\mathbf{q}_4-\mathbf{k}))+(\mathbf{q}_4\cdot\mathbf{k})(\mathbf{k}-\mathbf{q}_4)^2}{(\chi^2+\mathbf{k}^2)(\chi^2+(\mathbf{k}-\mathbf{q}_4)^2)^2}$$
$$\sin\left(\frac{\chi^2+(\mathbf{k}-\mathbf{q}_4)^2}{4xE}z_1\right)\sin\left(\frac{\chi^2+(\mathbf{k}-\mathbf{q}_4)^2}{2xE}(\frac{z_1}{2}+z_2+z_3+z_4)\right). \tag{C.18}$$

C.2 In a constant-temperature medium

Within the DREENA-C framework, under the assumption of constant medium temperature, we can explicitly perform analytical integrations for z_i, where $(i=1,2,3,4)$. $\omega_{(m\ldots n)}$ coefficients are defined in the Theoretical framework section. The expression for the 1^{st} order in opacity then became:

$$\left(\frac{dN_g^{(1)}}{dx}\right) = \frac{2C_R}{\pi x}\int\frac{d^2\mathbf{k}}{\pi}\int\frac{d^2\mathbf{q}_1}{\pi}\alpha_s(Q_k^2)\frac{L}{\lambda_{dyn}}\frac{\mu_E^2-\mu_M^2}{(\mathbf{q}_1^2+\mu_E^2)(\mathbf{q}_1^2+\mu_M^2)}$$
$$\frac{\chi^2(\mathbf{q}_1\cdot(\mathbf{q}_1-\mathbf{k}))+(\mathbf{q}_1\cdot\mathbf{k})(\mathbf{k}-\mathbf{q}_1)^2}{(\chi^2+\mathbf{k}^2)(\chi^2+(\mathbf{k}-\mathbf{q}_1)^2)^2}\left(1-\frac{\sin(L\omega_{(1)})}{L\omega_{(1)}}\right), \tag{C.19}$$

The expressions for higher orders in opacity became:

$$\left(\frac{dN_g^{(2)}}{dx}\right)_1 = \frac{2C_R}{\pi x}\int\frac{d^2\mathbf{k}}{\pi}\iint\frac{d^2\mathbf{q}_1}{\pi}\frac{d^2\mathbf{q}_2}{\pi}\,\alpha_s(Q_k^2)\frac{1}{\lambda_{dyn}^2}\frac{\mu_E^2-\mu_M^2}{(\mathbf{q}_1^2+\mu_E^2)(\mathbf{q}_1^2+\mu_M^2)}\frac{\mu_E^2-\mu_M^2}{(\mathbf{q}_2^2+\mu_E^2)(\mathbf{q}_2^2+\mu_M^2)}$$
$$\frac{\chi^2(\mathbf{q}_2\cdot(\mathbf{q}_1+\mathbf{q}_2-\mathbf{k}))+(\mathbf{q}_2\cdot\mathbf{k})(\mathbf{k}-\mathbf{q}_2)^2+(\mathbf{k}\cdot\mathbf{q}_1)(\mathbf{q}_2\cdot(\mathbf{q}_2-2\mathbf{k}))+\mathbf{k}^2(\mathbf{q}_2\cdot\mathbf{q}_1)}{(\chi^2+\mathbf{k}^2)(\chi^2+(\mathbf{k}-\mathbf{q}_2)^2)(\chi^2+(\mathbf{k}-\mathbf{q}_1-\mathbf{q}_2)^2)}$$
$$\frac{1}{\omega_{(2)}}\left(\frac{\omega_{(2)}\cos\big(L\big(\omega_{(2)}+\omega_{(12)}\big)\big)}{\big(\omega_{(2)}+\omega_{(12)}\big)\,\omega_{(12)}}+L\sin\big(L\omega_{(2)}\big)-\frac{\big(\omega_{(2)}-\omega_{(12)}\big)\cos\big(L\omega_{(2)}\big)}{\omega_{(2)}\omega_{(12)}}-\frac{\omega_{(12)}}{\omega_{(2)}\big(\omega_{(2)}+\omega_{(12)}\big)}\right), \tag{C.20}$$

$$\left(\frac{dN_g^{(2)}}{dx}\right)_2 = \frac{2C_R}{\pi x}\int\frac{d^2\mathbf{k}}{\pi}\int\frac{d^2\mathbf{q}_2}{\pi}\,\alpha_s(Q_k^2)\frac{1}{\lambda_{dyn}^2}\frac{\mu_E^2-\mu_M^2}{(\mathbf{q}_2^2+\mu_E^2)(\mathbf{q}_2^2+\mu_M^2)}$$
$$\frac{\chi^2(\mathbf{q}_2\cdot(\mathbf{q}_2-\mathbf{k}))+(\mathbf{q}_2\cdot\mathbf{k})(\mathbf{k}-\mathbf{q}_2)^2}{(\chi^2+\mathbf{k}^2)(\chi^2+(\mathbf{k}-\mathbf{q}_2)^2)^2}\frac{\sin\big(L\omega_{(2)}\big)\,\big(L\omega_{(2)}-\sin\big(L\omega_{(2)}\big)\big)}{\omega_{(2)}^2}, \tag{C.21}$$

$$\left(\frac{dN_g^{(3)}}{dx}\right)_1 = \frac{2C_R}{\pi x}\int\frac{d^2\mathbf{k}}{\pi}\iiint\frac{d^2\mathbf{q}_1}{\pi}\frac{d^2\mathbf{q}_2}{\pi}\frac{d^2\mathbf{q}_3}{\pi}$$
$$\alpha_s(Q_k^2)\frac{1}{\lambda_{dyn}^3}\frac{\mu_E^2-\mu_M^2}{(\mathbf{q}_1^2+\mu_E^2)(\mathbf{q}_1^2+\mu_M^2)}\frac{\mu_E^2-\mu_M^2}{(\mathbf{q}_2^2+\mu_E^2)(\mathbf{q}_2^2+\mu_M^2)}\frac{\mu_E^2-\mu_M^2}{(\mathbf{q}_3^2+\mu_E^2)(\mathbf{q}_3^2+\mu_M^2)}$$
$$\frac{\chi^2(\mathbf{q}_3\cdot(\mathbf{q}_1+\mathbf{q}_2+\mathbf{q}_3-\mathbf{k}))+(\mathbf{q}_3\cdot\mathbf{k})(\mathbf{k}-\mathbf{q}_3)^2+(\mathbf{k}\cdot(\mathbf{q}_1+\mathbf{q}_2))(\mathbf{q}_3\cdot(\mathbf{q}_3-2\mathbf{k}))+\mathbf{k}^2(\mathbf{q}_3\cdot(\mathbf{q}_1+\mathbf{q}_2))}{(\chi^2+\mathbf{k}^2)(\chi^2+(\mathbf{k}-\mathbf{q}_3)^2)(\chi^2+(\mathbf{k}-\mathbf{q}_1-\mathbf{q}_2-\mathbf{q}_3)^2)}$$
$$\left(\frac{\omega_{(3)}\omega_{(123)}+2\omega_{(23)}\omega_{(123)}-\omega_{(23)}^2-\omega_{(3)}\omega_{(23)}}{\omega_{(23)}^2(\omega_{(3)}+\omega_{(23)})^2\omega_{(123)}}\sin\big(L(\omega_{(3)}+\omega_{(23)})\big)-\frac{\omega_{(123)}\sin\big(L\omega_{(3)}\big)}{\omega_{(3)}\omega_{(23)}^2\,\big(\omega_{(23)}+\omega_{(123)}\big)}\right.$$
$$\left.+\frac{\sin\big(L\,\big(\omega_{(3)}+\omega_{(23)}+\omega_{(123)}\big)\big)}{\omega_{(123)}\,\big(\omega_{(23)}+\omega_{(123)}\big)\,\big(\omega_{(3)}+\omega_{(23)}+\omega_{(123)}\big)}-\frac{L\cos\big(L\,\big(\omega_{(3)}+\omega_{(23)}\big)\big)}{\omega_{(23)}\,\big(\omega_{(3)}+\omega_{(23)}\big)}\right), \tag{C.22}$$

$$\left(\frac{dN_g^{(3)}}{dx}\right)_2 = \frac{C_R}{\pi x}\int\frac{d^2\mathbf{k}}{\pi}\iint\frac{d^2\mathbf{q}_1}{\pi}\frac{d^2\mathbf{q}_3}{\pi}\alpha_s(Q_k^2)\frac{1}{\lambda_{dyn}^3}\frac{\mu_E^2-\mu_M^2}{(\mathbf{q}_1^2+\mu_E^2)(\mathbf{q}_1^2+\mu_M^2)}\frac{\mu_E^2-\mu_M^2}{(\mathbf{q}_3^2+\mu_E^2)(\mathbf{q}_3^2+\mu_M^2)}$$
$$\frac{\chi^2(\mathbf{q}_3\cdot(\mathbf{q}_1+\mathbf{q}_3-\mathbf{k}))+(\mathbf{q}_3\cdot\mathbf{k})(\mathbf{k}-\mathbf{q}_3)^2+(\mathbf{k}\cdot\mathbf{q}_1)(\mathbf{q}_3\cdot(\mathbf{q}_3-2\mathbf{k}))+\mathbf{k}^2(\mathbf{q}_3\cdot\mathbf{q}_1)}{(\chi^2+\mathbf{k}^2)(\chi^2+(\mathbf{k}-\mathbf{q}_3)^2)(\chi^2+(\mathbf{k}-\mathbf{q}_1-\mathbf{q}_3)^2)}$$
$$\left(\frac{\left(\frac{3\omega_{(13)}}{2}-\omega_{(3)}\right)\sin\big(2L\omega_{(3)}\big)}{\omega_{(3)}^3\omega_{(13)}}-\frac{2\omega_{(13)}\sin\big(L\omega_{(3)}\big)}{\omega_{(3)}^3\big(\omega_{(3)}+\omega_{(13)}\big)}+\frac{\sin\left(2L\left(\omega_{(3)}+\frac{\omega_{(13)}}{2}\right)\right)}{\left(\omega_{(3)}+\frac{\omega_{(13)}}{2}\right)\omega_{(13)}\,\big(\omega_{(3)}+\omega_{(13)}\big)}-\frac{L\cos\big(2L\omega_{(3)}\big)}{\omega_{(3)}^2}\right), \tag{C.23}$$

$$\left(\frac{dN_g^{(3)}}{dx}\right)_3 = \frac{2C_R}{\pi x}\int\frac{d^2\mathbf{k}}{\pi}\iint\frac{d^2\mathbf{q}_2}{\pi}\frac{d^2\mathbf{q}_3}{\pi}\alpha_s(Q_k^2)\frac{1}{\lambda_{dyn}^3}\frac{\mu_E^2-\mu_M^2}{(\mathbf{q}_2^2+\mu_E^2)(\mathbf{q}_2^2+\mu_M^2)}\frac{\mu_E^2-\mu_M^2}{(\mathbf{q}_3^2+\mu_E^2)(\mathbf{q}_3^2+\mu_M^2)}$$
$$\frac{\chi^2(\mathbf{q}_3\cdot(\mathbf{q}_2+\mathbf{q}_3-\mathbf{k}))+(\mathbf{q}_3\cdot\mathbf{k})(\mathbf{k}-\mathbf{q}_3)^2+(\mathbf{k}\cdot\mathbf{q}_2)(\mathbf{q}_3\cdot(\mathbf{q}_3-2\mathbf{k}))+\mathbf{k}^2(\mathbf{q}_3\cdot\mathbf{q}_2)}{(\chi^2+\mathbf{k}^2)(\chi^2+(\mathbf{k}-\mathbf{q}_3)^2)(\chi^2+(\mathbf{k}-\mathbf{q}_2-\mathbf{q}_3)^2)}$$
$$\left(\frac{\sin\left(2L\left(\frac{\omega_{(3)}}{2}+\omega_{(23)}\right)\right)}{4\omega_{(23)}^2\left(\frac{\omega_{(3)}}{2}+\omega_{(23)}\right)}-\frac{\sin\big(L\omega_{(3)}\big)}{2\omega_{(23)}^2\omega_{(3)}}+\frac{\frac{\sin\big(L\big(\omega_{(3)}+\omega_{(23)}\big)\big)}{\omega_{(3)}+\omega_{(23)}}-L\cos\big(L\,\big(\omega_{(3)}+\omega_{(23)}\big)\big)}{\omega_{(23)}\,\big(\omega_{(3)}+\omega_{(23)}\big)}\right), \tag{C.24}$$

$$\left(\frac{dN_g^{(3)}}{dx}\right)_4 = \frac{C_R}{\pi x}\int\frac{d^2\mathbf{k}}{\pi}\int\frac{d^2\mathbf{q}_3}{\pi}\alpha_s(Q_k^2)\frac{1}{\lambda_{dyn}^3}\frac{\mu_E^2-\mu_M^2}{(\mathbf{q}_3^2+\mu_E^2)(\mathbf{q}_3^2+\mu_M^2)}\frac{\chi^2(\mathbf{q}_3\cdot(\mathbf{q}_3-\mathbf{k}))+(\mathbf{q}_3\cdot\mathbf{k})(\mathbf{k}-\mathbf{q}_3)^2}{(\chi^2+\mathbf{k}^2)(\chi^2+(\mathbf{k}-\mathbf{q}_3)^2)^2}$$
$$\frac{1}{\omega_{(3)}^2}\left(-\frac{\sin\big(L\omega_{(3)}\big)}{\omega_{(3)}}+\frac{\sin\big(2L\omega_{(3)}\big)}{2\omega_{(3)}}+\frac{\sin\big(3L\omega_{(3)}\big)}{3\omega_{(3)}}-L\cos\big(2L\omega_{(3)}\big)\right), \tag{C.25}$$

$$\left(\frac{dN_g^{(4)}}{dx}\right)_1 = \frac{2C_R}{\pi x}\int\frac{d^2\mathbf{k}}{\pi}\iiint\frac{d^2\mathbf{q}_1}{\pi}\frac{d^2\mathbf{q}_2}{\pi}\frac{d^2\mathbf{q}_3}{\pi}\frac{d^2\mathbf{q}_4}{\pi}$$
$$\alpha_s(Q_k^2)\frac{1}{\lambda_{dyn}^4}\frac{\mu_E^2-\mu_M^2}{(\mathbf{q}_1^2+\mu_E^2)(\mathbf{q}_1^2+\mu_M^2)}\frac{\mu_E^2-\mu_M^2}{(\mathbf{q}_2^2+\mu_E^2)(\mathbf{q}_2^2+\mu_M^2)}\frac{\mu_E^2-\mu_M^2}{(\mathbf{q}_3^2+\mu_E^2)(\mathbf{q}_3^2+\mu_M^2)}\frac{\mu_E^2-\mu_M^2}{(\mathbf{q}_4^2+\mu_E^2)(\mathbf{q}_4^2+\mu_M^2)}$$
$$\frac{\chi^2(\mathbf{q}_4\cdot(\mathbf{q}_1+\mathbf{q}_2+\mathbf{q}_3+\mathbf{q}_4-\mathbf{k}))+(\mathbf{q}_4\cdot\mathbf{k})(\mathbf{k}-\mathbf{q}_4)^2+(\mathbf{k}\cdot(\mathbf{q}_1+\mathbf{q}_2+\mathbf{q}_3))(\mathbf{q}_4\cdot(\mathbf{q}_4-2\mathbf{k}))+\mathbf{k}^2(\mathbf{q}_4\cdot(\mathbf{q}_1+\mathbf{q}_2+\mathbf{q}_3))}{(\chi^2+\mathbf{k}^2)(\chi^2+(\mathbf{k}-\mathbf{q}_4)^2)(\chi^2+(\mathbf{k}-\mathbf{q}_1-\mathbf{q}_2-\mathbf{q}_3-\mathbf{q}_4)^2)}$$
$$\Bigg(-\frac{L\sin\left(L\left(\omega_{(4)}+\omega_{(34)}+\omega_{(234)}\right)\right)}{\omega_{(234)}\left(\omega_{(34)}+\omega_{(234)}\right)\left(\omega_{(4)}+\omega_{(34)}+\omega_{(234)}\right)}$$
$$-\frac{\cos\left(L\left(\omega_{(4)}+\omega_{(34)}+\omega_{(234)}+\omega_{(1234)}\right)\right)}{\omega_{(1234)}\left(\omega_{(234)}+\omega_{(1234)}\right)\left(\omega_{(34)}+\omega_{(234)}+\omega_{(1234)}\right)\left(\omega_{(4)}+\omega_{(34)}+\omega_{(234)}+\omega_{(1234)}\right)}$$
$$+\frac{F_{41}}{\omega_{(234)}^2\left(\omega_{(34)}+\omega_{(234)}\right)^2\left(\omega_{(4)}+\omega_{(34)}+\omega_{(234)}\right)^2\omega_{(1234)}}\cos\left(L(\omega_{(4)}+\omega_{(34)}+\omega_{(234)})\right)$$
$$+\frac{\omega_{(1234)}\cos\left(L\left(\omega_{(4)}+\omega_{(34)}\right)\right)}{\omega_{(34)}\left(\omega_{(4)}+\omega_{(34)}\right)\omega_{(234)}^2\left(\omega_{(234)}+\omega_{(1234)}\right)}-\frac{\omega_{(1234)}\cos\left(L\omega_{(4)}\right)}{\omega_{(4)}\omega_{(34)}\left(\omega_{(34)}+\omega_{(234)}\right)^2\left(\omega_{(34)}+\omega_{(234)}+\omega_{(1234)}\right)}$$
$$+\frac{\omega_{(1234)}}{\omega_{(4)}\left(\omega_{(4)}+\omega_{(34)}\right)\left(\omega_{(4)}+\omega_{(34)}+\omega_{(234)}\right)^2\left(\omega_{(4)}+\omega_{(34)}+\omega_{(234)}+\omega_{(1234)}\right)}\Bigg), \tag{C.26}$$

where $F_{41}=(\omega_{(34)}+\omega_{(234)})\left[(\omega_{(4)}+\omega_{(34)})(\omega_{(234)}-\omega_{(1234)})+\omega_{(234)}^2-3\omega_{(234)}\omega_{(1234)}\right]-\omega_{(4)}\omega_{(234)}\omega_{(1234)}$.

$$\left(\frac{dN_g^{(4)}}{dx}\right)_2 = \frac{C_R}{\pi x}\int\frac{d^2\mathbf{k}}{\pi}\iiint\frac{d^2\mathbf{q}_1}{\pi}\frac{d^2\mathbf{q}_2}{\pi}\frac{d^2\mathbf{q}_4}{\pi}$$
$$\alpha_s(Q_k^2)\frac{1}{\lambda_{dyn}^4}\frac{\mu_E^2-\mu_M^2}{(\mathbf{q}_1^2+\mu_E^2)(\mathbf{q}_1^2+\mu_M^2)}\frac{\mu_E^2-\mu_M^2}{(\mathbf{q}_2^2+\mu_E^2)(\mathbf{q}_2^2+\mu_M^2)}\frac{\mu_E^2-\mu_M^2}{(\mathbf{q}_4^2+\mu_E^2)(\mathbf{q}_4^2+\mu_M^2)}$$
$$\frac{\chi^2(\mathbf{q}_4\cdot(\mathbf{q}_1+\mathbf{q}_2+\mathbf{q}_4-\mathbf{k}))+(\mathbf{q}_4\cdot\mathbf{k})(\mathbf{k}-\mathbf{q}_4)^2+(\mathbf{k}\cdot(\mathbf{q}_1+\mathbf{q}_2))(\mathbf{q}_4\cdot(\mathbf{q}_4-2\mathbf{k}))+\mathbf{k}^2(\mathbf{q}_4\cdot(\mathbf{q}_1+\mathbf{q}_2))}{(\chi^2+\mathbf{k}^2)(\chi^2+(\mathbf{k}-\mathbf{q}_4)^2)(\chi^2+(\mathbf{k}-\mathbf{q}_1-\mathbf{q}_2-\mathbf{q}_4)^2)}$$
$$\Bigg(\frac{2\left(\omega_{(24)}\left(2\omega_{(4)}^2+3\omega_{(24)}\omega_{(4)}+\omega_{(24)}^2\right)-\left(2\omega_{(4)}^2+6\omega_{(24)}\omega_{(4)}+3\omega_{(24)}^2\right)\omega_{(124)}\right)\cos\left(L\left(2\omega_{(4)}+\omega_{(24)}\right)\right)}{\omega_{(24)}^2\left(\omega_{(4)}+\omega_{(24)}\right)^2\left(2\omega_{(4)}+\omega_{(24)}\right)^2\omega_{(124)}}$$
$$-\frac{2\cos\left(L\left(2\omega_{(4)}+\omega_{(24)}+\omega_{(124)}\right)\right)}{\omega_{(124)}\left(\omega_{(24)}+\omega_{(124)}\right)\left(\omega_{(4)}+\omega_{(24)}+\omega_{(124)}\right)\left(2\omega_{(4)}+\omega_{(24)}+\omega_{(124)}\right)}+\frac{\omega_{(124)}\cos\left(2L\omega_{(4)}\right)}{\omega_{(4)}^2\omega_{(24)}^2\left(\omega_{(24)}+\omega_{(124)}\right)}$$
$$-\frac{2L\sin\left(L\left(2\omega_{(4)}+\omega_{(24)}\right)\right)}{\omega_{(24)}\left(\omega_{(4)}+\omega_{(24)}\right)\left(2\omega_{(4)}+\omega_{(24)}\right)}-\frac{2\omega_{(124)}\cos\left(L\omega_{(4)}\right)}{\omega_{(4)}^2\left(\omega_{(4)}+\omega_{(24)}\right)^2\left(\omega_{(4)}+\omega_{(24)}+\omega_{(124)}\right)}$$
$$+\frac{\omega_{(124)}}{\omega_{(4)}^2\left(2\omega_{(4)}+\omega_{(24)}\right)^2\left(2\omega_{(4)}+\omega_{(24)}+\omega_{(124)}\right)}\Bigg), \tag{C.27}$$

$$\left(\frac{dN_g^{(4)}}{dx}\right)_3 = \frac{C_R}{2\pi x}\int\frac{d^2\mathbf{k}}{\pi}\iiint\frac{d^2\mathbf{q}_1}{\pi}\frac{d^2\mathbf{q}_3}{\pi}\frac{d^2\mathbf{q}_4}{\pi}$$
$$\alpha_s(Q_k^2)\frac{1}{\lambda_{dyn}^4}\frac{\mu_E^2-\mu_M^2}{(\mathbf{q}_1^2+\mu_E^2)(\mathbf{q}_1^2+\mu_M^2)}\frac{\mu_E^2-\mu_M^2}{(\mathbf{q}_3^2+\mu_E^2)(\mathbf{q}_3^2+\mu_M^2)}\frac{\mu_E^2-\mu_M^2}{(\mathbf{q}_4^2+\mu_E^2)(\mathbf{q}_4^2+\mu_M^2)}$$
$$\frac{\chi^2(\mathbf{q}_4\cdot(\mathbf{q}_1+\mathbf{q}_3+\mathbf{q}_4-\mathbf{k}))+(\mathbf{q}_4\cdot\mathbf{k})(\mathbf{k}-\mathbf{q}_4)^2+(\mathbf{k}\cdot(\mathbf{q}_1+\mathbf{q}_3))(\mathbf{q}_4\cdot(\mathbf{q}_4-2\mathbf{k}))+\mathbf{k}^2(\mathbf{q}_4\cdot(\mathbf{q}_1+\mathbf{q}_3))}{(\chi^2+\mathbf{k}^2)(\chi^2+(\mathbf{k}-\mathbf{q}_4)^2)(\chi^2+(\mathbf{k}-\mathbf{q}_1-\mathbf{q}_3-\mathbf{q}_4)^2)}$$
$$\Bigg(-\frac{2L\sin\left(L\left(\omega_{(4)}+2\omega_{(34)}\right)\right)}{\omega_{(34)}^2\left(\omega_{(4)}+2\omega_{(34)}\right)}-\frac{4\cos\left(L\left(\omega_{(4)}+2\omega_{(34)}+\omega_{(134)}\right)\right)}{\omega_{(134)}\left(\omega_{(34)}+\omega_{(134)}\right)\left(2\omega_{(34)}+\omega_{(134)}\right)\left(\omega_{(4)}+2\omega_{(34)}+\omega_{(134)}\right)}$$
$$+\frac{\left(2\omega_{(34)}\left(\omega_{(4)}+2\omega_{(34)}\right)-\left(3\omega_{(4)}+8\omega_{(34)}\right)\omega_{(134)}\right)\cos\left(L\left(\omega_{(4)}+2\omega_{(34)}\right)\right)}{\omega_{(34)}^3\left(\omega_{(4)}+2\omega_{(34)}\right)^2\omega_{(134)}}-\frac{\omega_{(134)}\cos\left(L\omega_{(4)}\right)}{\omega_{(4)}\omega_{(34)}^3(2\omega_{(34)}+\omega_{(134)})}$$
$$+\frac{4\omega_{(134)}}{\left(\omega_{(4)}+\omega_{(34)}\right)}\left(\frac{\cos\left(L\left(\omega_{(4)}+\omega_{(34)}\right)\right)}{\omega_{(34)}^3\left(\omega_{(34)}+\omega_{(134)}\right)}+\frac{1}{\omega_{(4)}\left(\omega_{(4)}+2\omega_{(34)}\right)^2\left(\omega_{(4)}+2\omega_{(34)}+\omega_{(134)}\right)}\right)\Bigg), \tag{C.28}$$

$$\left(\frac{dN_g^{(4)}}{dx}\right)_4 = \frac{C_R}{3\pi x}\int\frac{d^2\mathbf{k}}{\pi}\iint\frac{d^2\mathbf{q}_1}{\pi}\frac{d^2\mathbf{q}_4}{\pi}\alpha_s(Q_k^2)\frac{1}{\lambda_{dyn}^4}\frac{\mu_E^2-\mu_M^2}{(\mathbf{q}_1^2+\mu_E^2)(\mathbf{q}_1^2+\mu_M^2)}\frac{\mu_E^2-\mu_M^2}{(\mathbf{q}_4^2+\mu_E^2)(\mathbf{q}_4^2+\mu_M^2)}$$
$$\frac{\chi^2(\mathbf{q}_4\cdot(\mathbf{q}_1+\mathbf{q}_4-\mathbf{k}))+(\mathbf{q}_4\cdot\mathbf{k})(\mathbf{k}-\mathbf{q}_4)^2+(\mathbf{k}\cdot\mathbf{q}_1)(\mathbf{q}_4\cdot(\mathbf{q}_4-2\mathbf{k}))+\mathbf{k}^2(\mathbf{q}_4\cdot\mathbf{q}_1)}{(\chi^2+\mathbf{k}^2)(\chi^2+(\mathbf{k}-\mathbf{q}_4)^2)(\chi^2+(\mathbf{k}-\mathbf{q}_1-\mathbf{q}_4)^2)}$$
$$\frac{1}{\omega_{(4)}^3}\Bigg(-\frac{6\omega_{(4)}^3\cos\left(L\left(3\omega_{(4)}+\omega_{(14)}\right)\right)}{\omega_{(14)}\left(\omega_{(4)}+\omega_{(14)}\right)\left(2\omega_{(4)}+\omega_{(14)}\right)\left(3\omega_{(4)}+\omega_{(14)}\right)}+\left(\frac{1}{\omega_{(14)}}-\frac{11}{6\omega_{(4)}}\right)\cos(3L\omega_{(4)})$$
$$-L\sin\left(3L\omega_{(4)}\right)-\frac{3\omega_{(14)}\cos\left(L\omega_{(4)}\right)}{4\omega_{(4)}^2+2\omega_{(14)}\omega_{(4)}}+\frac{3\omega_{(14)}\cos\left(2L\omega_{(4)}\right)}{\left(\omega_{(4)}+\omega_{(14)}\right)\omega_{(4)}}+\frac{\omega_{(14)}}{9\omega_{(4)}^2+3\omega_{(14)}\omega_{(4)}}\Bigg), \tag{C.29}$$

$$\left(\frac{dN_g^{(4)}}{dx}\right)_5 = \frac{C_R}{\pi x}\int\frac{d^2\mathbf{k}}{\pi}\iiint\frac{d^2\mathbf{q}_2}{\pi}\frac{d^2\mathbf{q}_3}{\pi}\frac{d^2\mathbf{q}_4}{\pi}$$
$$\alpha_s(Q_k^2)\frac{1}{\lambda_{dyn}^4}\frac{\mu_E^2-\mu_M^2}{(\mathbf{q}_2^2+\mu_E^2)(\mathbf{q}_2^2+\mu_M^2)}\frac{\mu_E^2-\mu_M^2}{(\mathbf{q}_3^2+\mu_E^2)(\mathbf{q}_3^2+\mu_M^2)}\frac{\mu_E^2-\mu_M^2}{(\mathbf{q}_4^2+\mu_E^2)(\mathbf{q}_4^2+\mu_M^2)}$$
$$\frac{\chi^2(\mathbf{q}_4\cdot(\mathbf{q}_2+\mathbf{q}_3+\mathbf{q}_4-\mathbf{k}))+(\mathbf{q}_4\cdot\mathbf{k})(\mathbf{k}-\mathbf{q}_4)^2+(\mathbf{k}\cdot(\mathbf{q}_2+\mathbf{q}_3))(\mathbf{q}_4\cdot(\mathbf{q}_4-2\mathbf{k}))+\mathbf{k}^2(\mathbf{q}_4\cdot(\mathbf{q}_2+\mathbf{q}_3))}{(\chi^2+\mathbf{k}^2)(\chi^2+(\mathbf{k}-\mathbf{q}_4)^2)(\chi^2+(\mathbf{k}-\mathbf{q}_2-\mathbf{q}_3-\mathbf{q}_4)^2)}$$
$$\frac{1}{\omega_{(234)}^2}\Bigg(\frac{2\omega_{(234)}^3}{\omega_{(4)}\left(\omega_{(4)}+\omega_{(34)}\right)\left(\omega_{(4)}+\omega_{(34)}+\omega_{(234)}\right)^2\left(\omega_{(4)}+\omega_{(34)}+2\omega_{(234)}\right)}+\frac{\cos\left(L\left(\omega_{(4)}+\omega_{(34)}\right)\right)}{\omega_{(34)}\left(\omega_{(4)}+\omega_{(34)}\right)}$$
$$-\frac{2\omega_{(234)}^3\cos\left(L\omega_{(4)}\right)}{\omega_{(4)}\omega_{(34)}\left(\omega_{(34)}+\omega_{(234)}\right)^2\left(\omega_{(34)}+2\omega_{(234)}\right)}-\frac{2L\omega_{(234)}\sin(L(\omega_{(4)}+\omega_{(34)}+\omega_{(234)}))}{\left(\omega_{(34)}+\omega_{(234)}\right)\left(\omega_{(4)}+\omega_{(34)}+\omega_{(234)}\right)}$$
$$-\frac{\cos\left(L\left(\omega_{(4)}+\omega_{(34)}+2\omega_{(234)}\right)\right)}{\left(\omega_{(34)}+2\omega_{(234)}\right)\left(\omega_{(4)}+\omega_{(34)}+2\omega_{(234)}\right)}-\frac{2\omega_{(234)}(\omega_{(4)}+2\omega_{(34)}+2\omega_{(234)})\cos(L(\omega_{(4)}+\omega_{(34)}+\omega_{(234)}))}{\left(\omega_{(34)}+\omega_{(234)}\right)^2\left(\omega_{(4)}+\omega_{(34)}+\omega_{(234)}\right)^2}\Bigg), \tag{C.30}$$

$$\left(\frac{dN_g^{(4)}}{dx}\right)_6 = \frac{C_R}{\pi x}\int\frac{d^2\mathbf{k}}{\pi}\iint\frac{d^2\mathbf{q}_2}{\pi}\frac{d^2\mathbf{q}_4}{\pi}\alpha_s(Q_k^2)\frac{1}{\lambda_{dyn}^4}\frac{\mu_E^2-\mu_M^2}{(\mathbf{q}_2^2+\mu_E^2)(\mathbf{q}_2^2+\mu_M^2)}\frac{\mu_E^2-\mu_M^2}{(\mathbf{q}_4^2+\mu_E^2)(\mathbf{q}_4^2+\mu_M^2)}$$
$$\frac{\chi^2(\mathbf{q}_4\cdot(\mathbf{q}_2+\mathbf{q}_4-\mathbf{k}))+(\mathbf{q}_4\cdot\mathbf{k})(\mathbf{k}-\mathbf{q}_4)^2+(\mathbf{k}\cdot\mathbf{q}_2)(\mathbf{q}_4\cdot(\mathbf{q}_4-2\mathbf{k}))+\mathbf{k}^2(\mathbf{q}_4\cdot\mathbf{q}_2)}{(\chi^2+\mathbf{k}^2)(\chi^2+(\mathbf{k}-\mathbf{q}_4)^2)(\chi^2+(\mathbf{k}-\mathbf{q}_2-\mathbf{q}_4)^2)}$$
$$\Bigg(\frac{\omega_{(24)}}{8\omega_{(4)}^2\left(\omega_{(4)}+\frac{\omega_{(24)}}{2}\right)^2\left(\omega_{(4)}+\omega_{(24)}\right)}-\frac{L\sin\left(L\left(2\omega_{(4)}+\omega_{(24)}\right)\right)+\frac{\left(\frac{3\omega_{(4)}}{2}+\omega_{(24)}\right)\cos\left(2L\left(\omega_{(4)}+\frac{\omega_{(24)}}{2}\right)\right)}{\left(\omega_{(4)}+\frac{\omega_{(24)}}{2}\right)\left(\omega_{(4)}+\omega_{(24)}\right)}}{\left(\omega_{(4)}+\frac{\omega_{(24)}}{2}\right)\left(\omega_{(4)}+\omega_{(24)}\right)\omega_{(24)}}$$
$$+\frac{\left(\frac{\cos\left(2L\omega_{(4)}\right)}{2\omega_{(4)}}-\frac{\omega_{(4)}\cos\left(2L\left(\omega_{(4)}+\omega_{(24)}\right)\right)}{4\left(\frac{\omega_{(4)}}{2}+\omega_{(24)}\right)\left(\omega_{(4)}+\omega_{(24)}\right)}\right)}{\omega_{(4)}\omega_{(24)}^2}-\frac{\omega_{(24)}\cos\left(L\omega_{(4)}\right)}{\omega_{(4)}^2\left(\frac{\omega_{(4)}}{2}+\omega_{(24)}\right)\left(\omega_{(4)}+\omega_{(24)}\right)^2}\Bigg), \tag{C.31}$$

$$\left(\frac{dN_g^{(4)}}{dx}\right)_7 = \frac{C_R}{2\pi x}\int\frac{d^2\mathbf{k}}{\pi}\iint\frac{d^2\mathbf{q}_3}{\pi}\frac{d^2\mathbf{q}_4}{\pi}\alpha_s(Q_k^2)\frac{1}{\lambda_{dyn}^4}\frac{\mu_E^2-\mu_M^2}{(\mathbf{q}_3^2+\mu_E^2)(\mathbf{q}_3^2+\mu_M^2)}\frac{\mu_E^2-\mu_M^2}{(\mathbf{q}_4^2+\mu_E^2)(\mathbf{q}_4^2+\mu_M^2)}$$
$$\frac{\chi^2(\mathbf{q}_4\cdot(\mathbf{q}_3+\mathbf{q}_4-\mathbf{k}))+(\mathbf{q}_4\cdot\mathbf{k})(\mathbf{k}-\mathbf{q}_4)^2+(\mathbf{k}\cdot\mathbf{q}_3)(\mathbf{q}_4\cdot(\mathbf{q}_4-2\mathbf{k}))+\mathbf{k}^2(\mathbf{q}_4\cdot\mathbf{q}_3)}{(\chi^2+\mathbf{k}^2)(\chi^2+(\mathbf{k}-\mathbf{q}_4)^2)(\chi^2+(\mathbf{k}-\mathbf{q}_3-\mathbf{q}_4)^2)}$$
$$\frac{1}{\omega_{(34)}^2\left(\frac{\omega_{(4)}}{2}+\omega_{(34)}\right)}\Bigg(\frac{2\omega_{(34)}^3}{\omega_{(4)}\left(\omega_{(4)}+\omega_{(34)}\right)\left(\omega_{(4)}+2\omega_{(34)}\right)\left(\omega_{(4)}+3\omega_{(34)}\right)}-\frac{\left(\frac{\omega_{(4)}}{2}+2\omega_{(34)}\right)\cos\left(L\left(\omega_{(4)}+2\omega_{(34)}\right)\right)}{\left(\omega_{(4)}+2\omega_{(34)}\right)\omega_{(34)}}$$
$$-L\sin\left(L\left(\omega_{(4)}+2\omega_{(34)}\right)\right)-\frac{\left(\frac{\omega_{(4)}}{2}+\omega_{(34)}\right)\left(\frac{\cos\left(L\omega_{(4)}\right)}{\omega_{(4)}}-\frac{6\cos\left(L\left(\omega_{(4)}+\omega_{(34)}\right)\right)}{\omega_{(4)}+\omega_{(34)}}+\frac{2\cos\left(L\left(\omega_{(4)}+3\omega_{(34)}\right)\right)}{\omega_{(4)}+3\omega_{(34)}}\right)}{3\omega_{(34)}}\Bigg), \tag{C.32}$$

$$\left(\frac{dN_g^{(4)}}{dx}\right)_8 = \frac{C_R}{3\pi x}\int\frac{d^2\mathbf{k}}{\pi}\int\frac{d^2\mathbf{q}_4}{\pi}\alpha_s(Q_k^2)\frac{1}{\lambda_{dyn}^4}\frac{\mu_E^2-\mu_M^2}{(\mathbf{q}_4^2+\mu_E^2)(\mathbf{q}_4^2+\mu_M^2)}\frac{\chi^2\mathbf{q}_4\cdot(\mathbf{q}_4-\mathbf{k})+(\mathbf{q}_4\cdot\mathbf{k})(\mathbf{k}-\mathbf{q}_4)^2}{(\chi^2+\mathbf{k}^2)(\chi^2+(\mathbf{k}-\mathbf{q}_4)^2)^2}$$
$$\frac{1}{\omega_{(4)}^3}\left(\frac{1}{12\omega_{(4)}}-L\sin\left(3L\omega_{(4)}\right)-\frac{\cos\left(L\omega_{(4)}\right)}{2\omega_{(4)}}+\frac{3\cos\left(2L\omega_{(4)}\right)}{2\omega_{(4)}}-\frac{5\cos\left(3L\omega_{(4)}\right)}{6\omega_{(4)}}-\frac{\cos\left(4L\omega_{(4)}\right)}{4\omega_{(4)}}\right). \tag{C.33}$$

Appendix D

Higher orders in opacity results for dN_g/dx for $L = 3$ and $L = 1$

This section shows dN_g/dx as a function of x for medium lengths $L = 3\,\text{fm}$ and $L = 1\,\text{fm}$. Here, the figures are more conventional, with $\mu_M/\mu_E = 0.6$ and $\mu_M/\mu_E = 0.4$ cases separately shown.

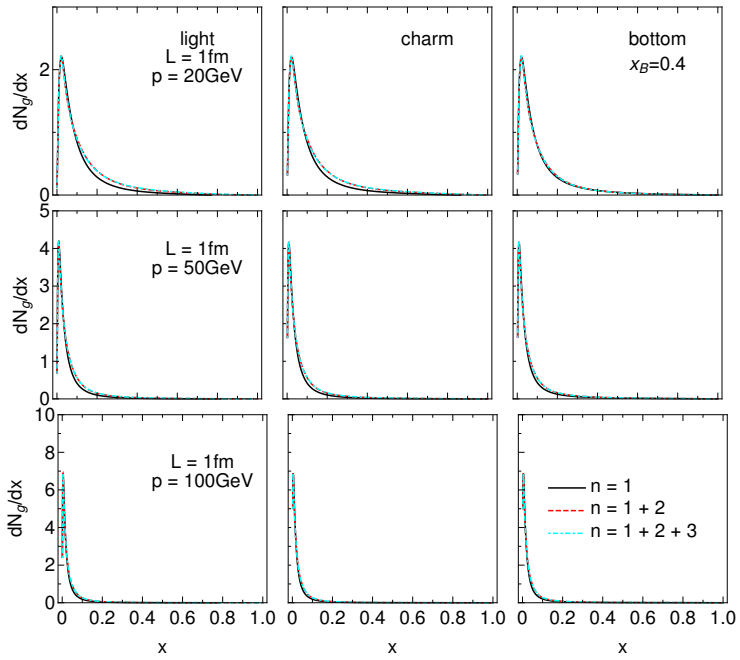

Figure D.1: Gluon radiation spectrum dN_g/dx as a function of x, for the medium length of $L = 1\,\text{fm}$ and various jet momenta. Different columns correspond to light, charm, and bottom quarks. Solid black curves show the 1^{st} order in opacity results, red dashed curves show the results up to the 2^{nd} order, while cyan dot-dashed curves up to the 3^{rd} order in opacity. The chromomagnetic and chromoelectric mass ratio is $\mu_M/\mu_E = 0.4$.

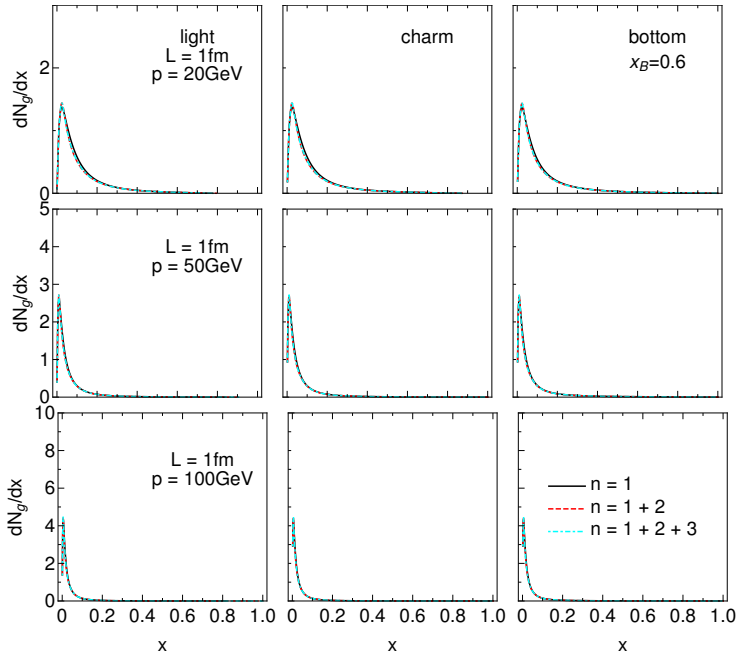

Figure D.2: Gluon radiation spectrum dN_g/dx as a function of x, for the medium length of $L = 1\,\text{fm}$ and various jet momenta. Different columns correspond to light, charm, and bottom quarks. Solid black curves show the 1$^{\text{st}}$ order in opacity results, red dashed curves show the results up to the 2$^{\text{nd}}$ order, while cyan dot-dashed curves up to the 3$^{\text{rd}}$ order in opacity. The chromomagnetic and chromoelectric mass ratio is $\mu_M/\mu_E = 0.6$.

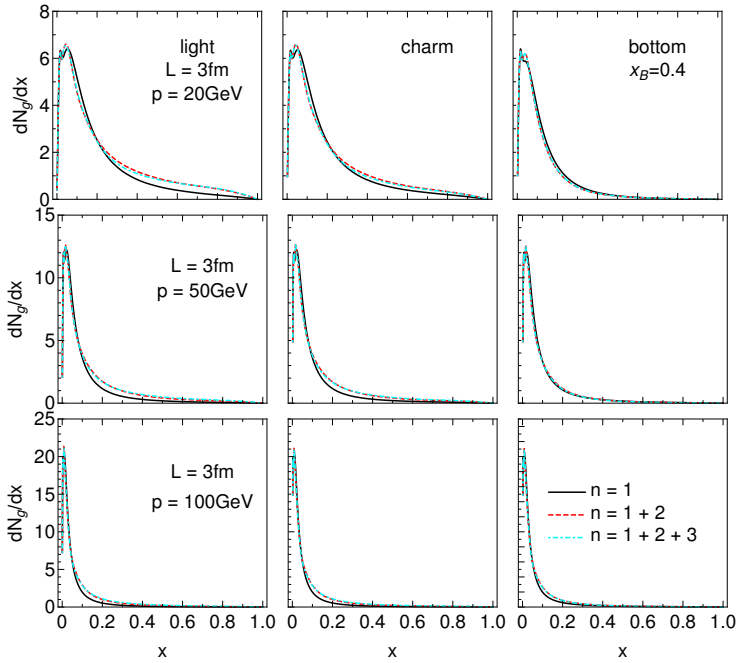

Figure D.3: Gluon radiation spectrum dN_g/dx as a function of x, for the medium length of $L = 3\,\text{fm}$ and various jet momenta. Different columns correspond to light, charm, and bottom quarks. Solid black curves show the 1$^{\text{st}}$ order in opacity results, red dashed curves show the results up to the 2$^{\text{nd}}$ order, while cyan dot-dashed curves up to the 3$^{\text{rd}}$ order in opacity. The chromomagnetic and chromoelectric mass ratio is $\mu_M/\mu_E = 0.4$.

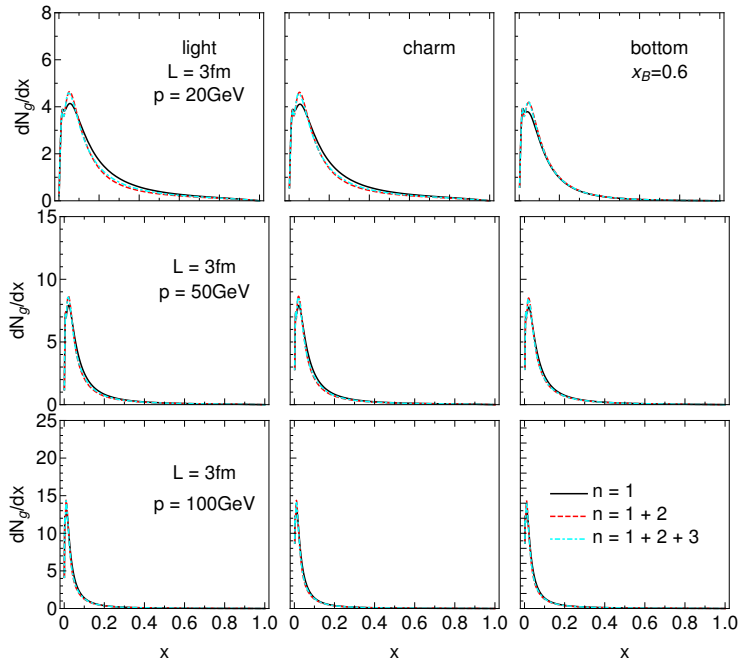

Figure D.4: Gluon radiation spectrum dN_g/dx as a function of x, for the medium length of $L = 3\,\mathrm{fm}$ and various jet momenta. Different columns correspond to light, charm, and bottom quarks. Solid black curves show the 1^{st} order in opacity results, red dashed curves show the results up to the 2^{nd} order, while cyan dot-dashed curves up to the 3^{rd} order in opacity. The chromomagnetic and chromoelectric mass ratio is $\mu_M/\mu_E = 0.6$.

Appendix E

v_2 results for higher orders in opacity

Figure E.1 shows the results for v_2 up to the 3^{rd} order in opacity, with only radiative energy loss taken into account, while Figure E.2 shows the results which include both radiative and collisional energy loss. Note that here the lower (upper) boundary of each band corresponds to the $\mu_M/\mu_E = 0.6$ ($\mu_M/\mu_E = 0.4$) case (opposite with respect to the R_{AA} results). We observe the same behavior as R_{AA}.

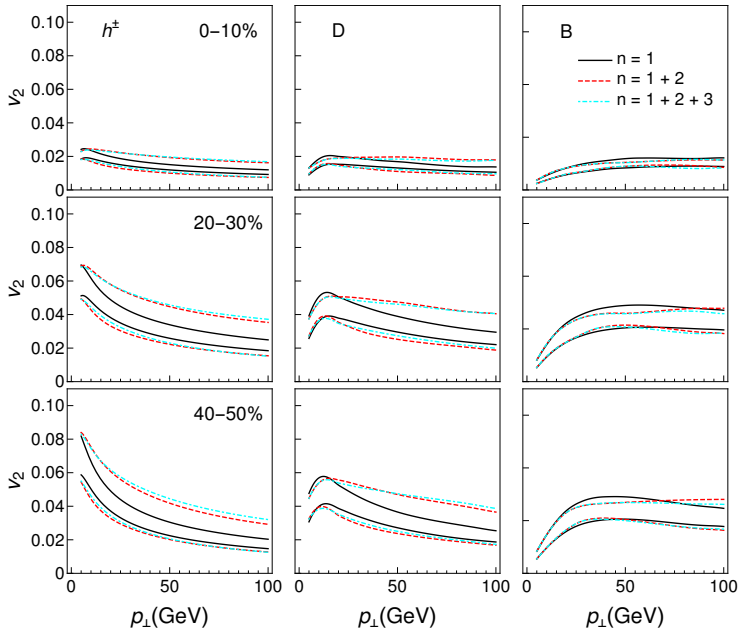

Figure E.1: v_2 results obtained within DREENA-C, with only radiative energy loss taken into account. The panel shows three centrality classes. Different columns correspond to charged hadrons, D, and B mesons, while different rows show different centrality classes. Solid black curves show the 1^{st} order in opacity results, red and dashed curves show the results up to the 2^{nd} order, while cyan and dot-dashed curves up to the 3^{rd} order in opacity. The lower (upper) boundary of each band corresponds to the $\mu_M/\mu_E = 0.6$ ($\mu_M/\mu_E = 0.4$) case.

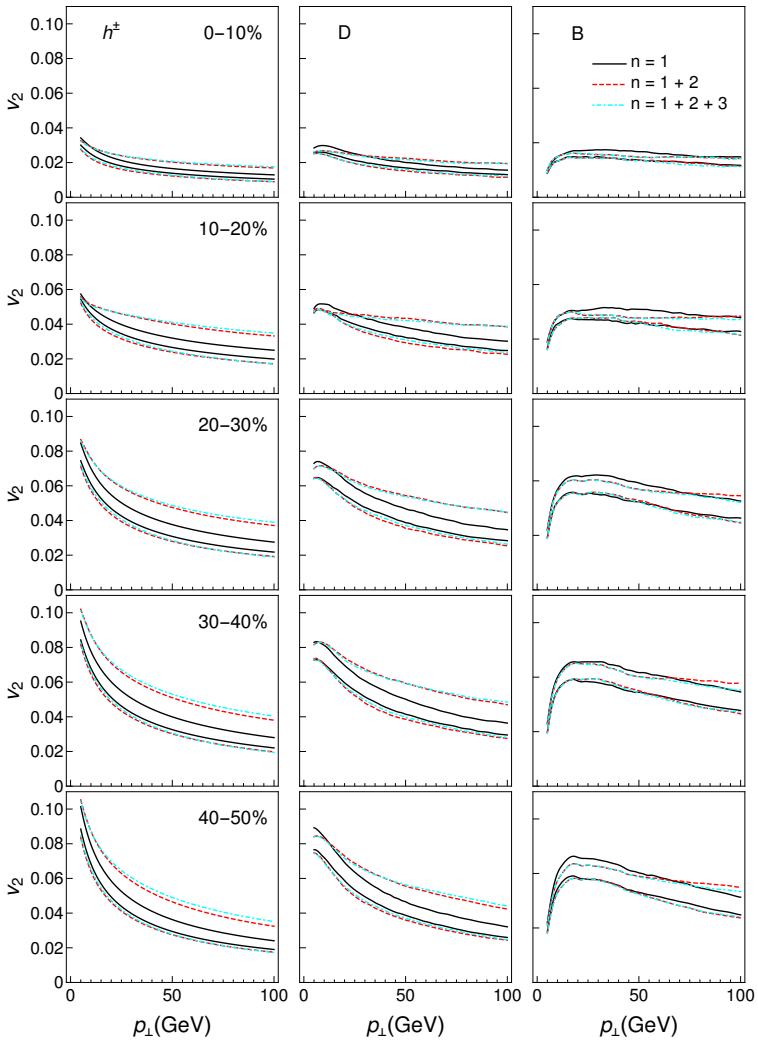

Figure E.2: v_2 results obtained within DREENA-C, with both radiative and collisional energy loss taken into account. The panel shows all centrality classes. Different columns correspond to charged hadrons, D, and B mesons, while different rows show different centrality classes. Solid black curves show the 1$^{\text{st}}$ order in opacity results, red and dashed curves show the results up to the 2$^{\text{nd}}$ order, while cyan and dot-dashed curves up to the 3$^{\text{rd}}$ order in opacity. The lower (upper) boundary of each band corresponds to the $\mu_M/\mu_E = 0.6$ ($\mu_M/\mu_E = 0.4$) case.

Appendix F

R_{AA} results for higher orders in opacity with full energy loss

In this Appendix, the results for R_{AA} generated by taking into account full energy loss in DREENA (that is, both radiative and collisional energy loss mechanisms). We observe the same behavior as in the case when only radiative energy loss is included, as expected.

The figure F.1 shows the R_{AA} results (with both radiative and collisional energy loss) for $\mu_M/\mu_E = 0.4$ and $\mu_M/\mu_E = 0.6$. The same conclusions hold as in the case when only radiative energy loss is included (Figure 5.4 in Chapter 5 and the corresponding discussion in Section 5.4).

The Figure F.2 shows the R_{AA} results (with both radiative and collisional energy loss) for $\mu_M/\mu_E = \frac{1}{\sqrt{3}}$. In this way, we test the effect of higher orders in opacity on the contribution of the electric potential in dynamical energy loss (see Equations 5.10 and 5.11 in Section 5.2 and the corresponding discussion), by replacing $v(\mathbf{q})$ by $v_L(\mathbf{q})$ in the DREENA framework. Surprisingly, we find it negligible, as shown in Fig. 5.5 and Fig. F.2. Thus, higher orders in opacity essentially do not influence the electric contribution in a dynamical QCD medium.

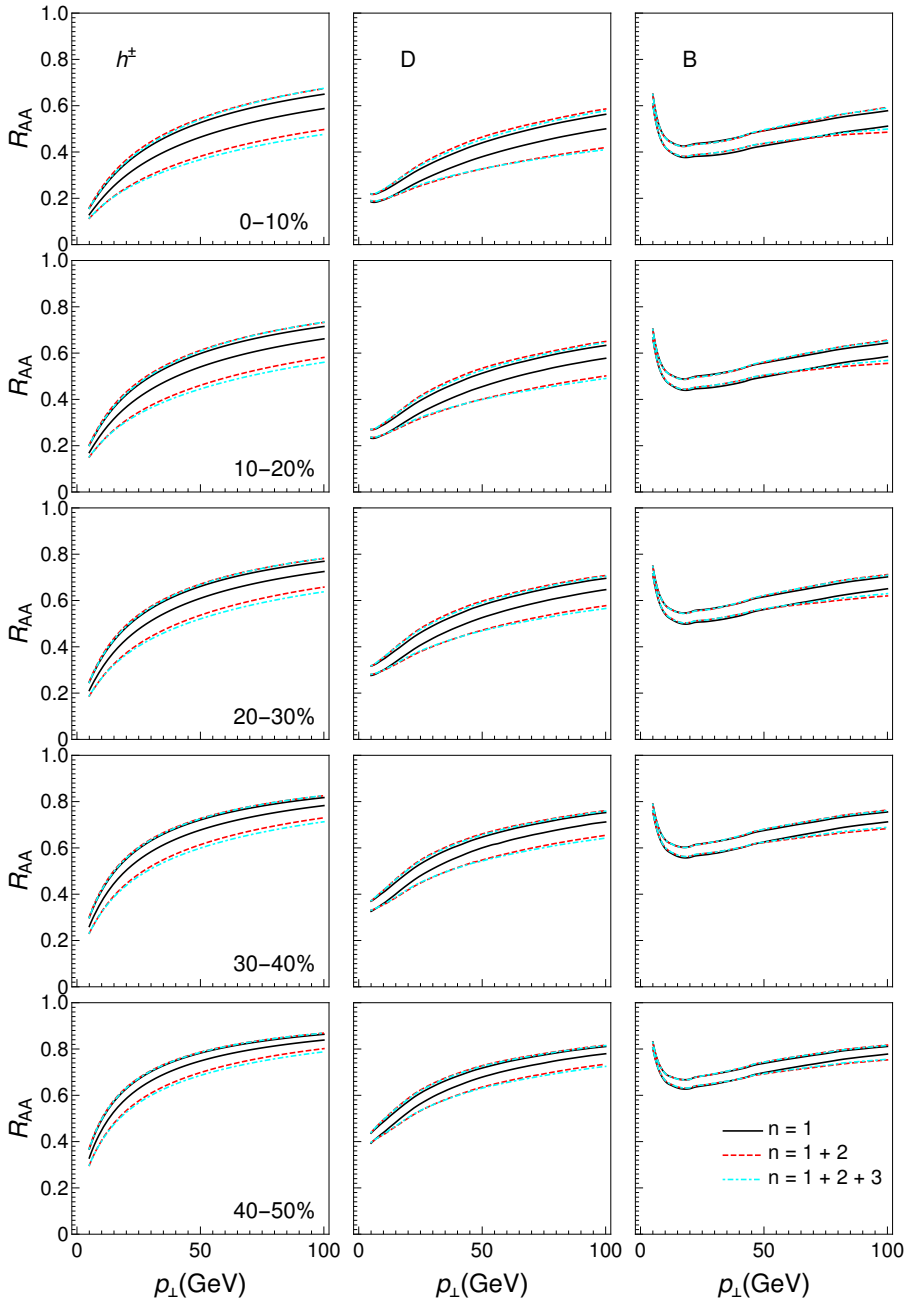

Figure F.1: R_{AA} results obtained within DREENA-C, with both radiative and collisional energy loss considered. The panel shows all centrality classes. Different columns correspond to charged hadrons, D, and B mesons, while different rows show different centrality classes. Solid black curves show the 1$^{\text{st}}$ order in opacity results, red and dashed curves show the results up to the 2$^{\text{nd}}$ order, while cyan and dot-dashed curves up to the 3$^{\text{rd}}$ order in opacity. The lower (upper) boundary of each band corresponds to the $\mu_M/\mu_E = 0.4$ ($\mu_M/\mu_E = 0.6$) case.

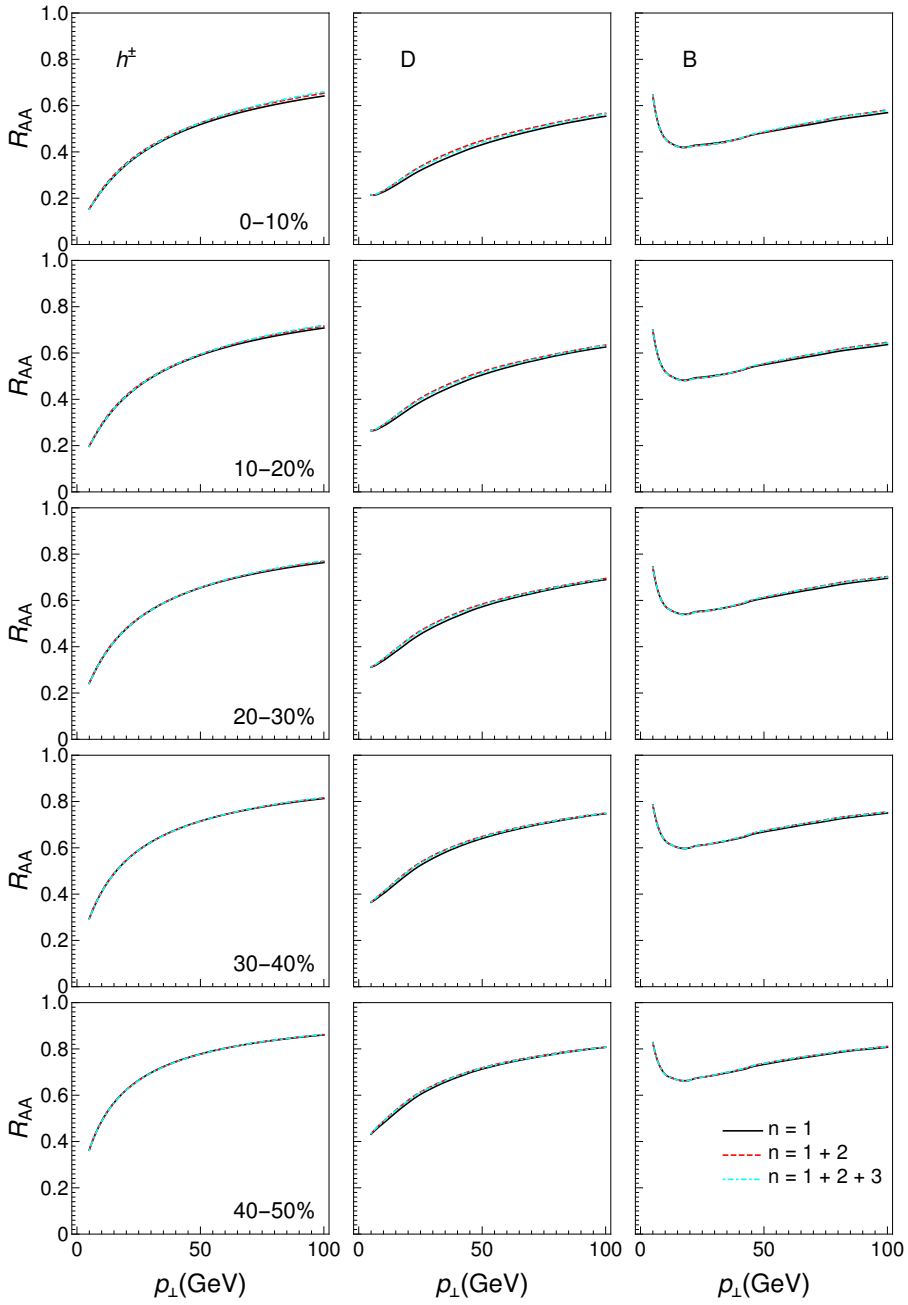

Figure F.2: R_{AA} results obtained within DREENA-C, with both radiative and collisional energy loss considered. The panel shows all centrality classes. Different columns correspond to charged hadrons, D, and B mesons, while different rows show different centrality classes. Solid black curves show the 1$^{\text{st}}$ order in opacity results, red and dashed curves show the results up to the 2$^{\text{nd}}$ order, while cyan and dot-dashed curves up to the 3$^{\text{rd}}$ order in opacity. The ratio of chromomagnetic and chromoelectric mass is fixed to $\mu_M/\mu_E = \frac{1}{\sqrt{3}}$.

Appendix G

Higher orders in opacity: full temperature-dependence panel

We here show the entire panel with R_{AA} results up to the 3^{rd} order in opacity for the D meson, in the temperature range 155–600MeV, which broadly covers the range of energies accessible at the LHC and RHIC. From Figure G.1, we see that the higher orders in opacity effects are largely independent of the temperature, and we do not expect the inclusion of full medium evolution to change our conclusions substantially.

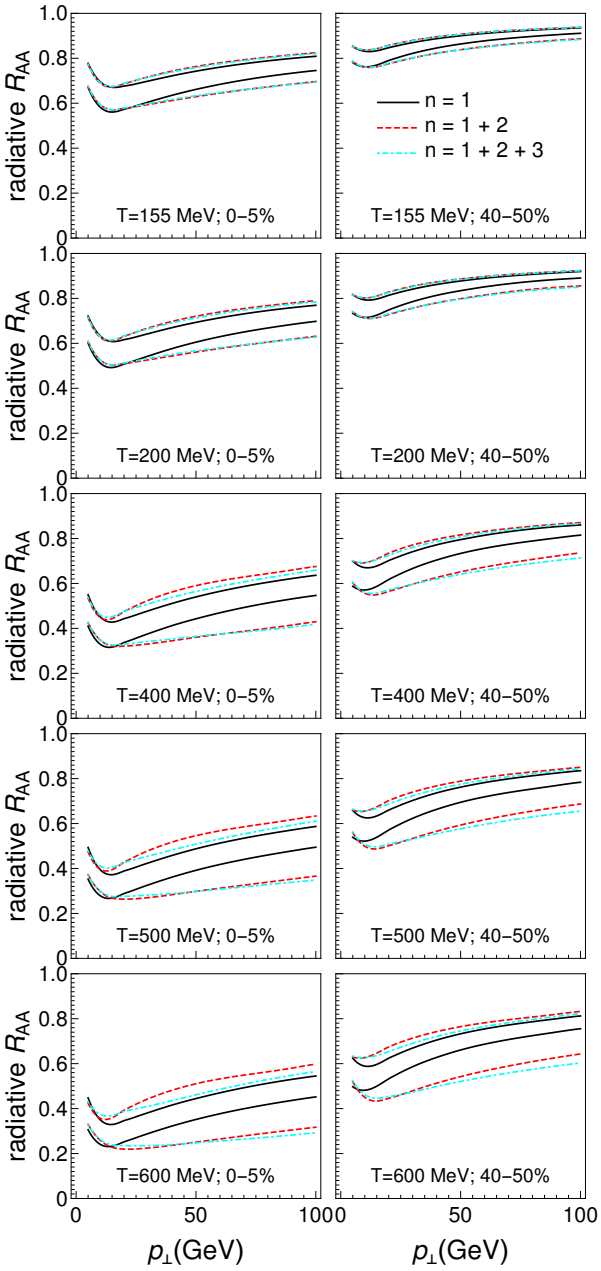

Figure G.1: Full panel representing the effects of higher orders in opacity for different medium temperatures. We show D meson radiative R_{AA} results obtained within DREENA-C for different temperature values. The left column corresponds to 0-5% centrality, while the right column corresponds to 40-50% centrality. The values of temperature are denoted on each plot. The solid black curves show the 1^{st} order in opacity results, and the dashed red curves show the results up to the 2^{nd} order in opacity, while the cyan dot-dashed curves show the results up to the 3^{rd} order in opacity. The lower (upper) boundary of each band corresponds to the $\mu_M/\mu_E = 0.4$ ($\mu_M/\mu_E = 0.6$) case.

Bibliography

[1] S. Stojku, J. Auvinen, M. Djordjevic, M. Djordjevic, P. Huovinen, Acta Phys. Pol. B Proc. Suppl. **16**, 1-A156 (2023)

[2] S. Stojku, J. Auvinen, M. Djordjevic, P. Huovinen, and M. Djordjevic, Physical Review C **105**, L021901 (2022)

[3] M. Djordjevic, S. Stojku, M. Djordjevic, and P. Huovinen, Phys. Rev. C **100**, 031901(R) (2019)

[4] S. Stojku, J. Auvinen, L. Zivkovic, P. Huovinen, M. Djordjevic, Physics Letters B **835**, 137501 (2022)

[5] S. Stojku, B. Ilic, I. Salom, M. Djordjevic, arXiv:2303.14527 [nucl-th] (under positive review in Physical Review C)

[6] E. V. Shuryak, Nucl. Phys. A **750**, 64 (2005); Rev. Mod. Phys. **89**, 035001 (2017).

[7] M. Gyulassy and L. McLerran, Nucl. Phys. A **750**, 30 (2005).

[8] B. Jacak and P. Steinberg, Phys. Today **63**, 39 (2010).

[9] B. Muller, J. Schukraft and B. Wyslouch, Ann. Rev. Nucl. Part. Sci. **62**, 361 (2012).

[10] W. Greiner, S. Schramm, E. Stein, *Quantum Chromodynamics*, Springer-Verlag (2002)

[11] R. M. Barnett, H. Mühry, H. R. Quinn, *The Charm of Strange Quarks: Mysteries and Revolutions of Particle Physics*, Springer-Verlag New York (2000).

[12] H. Kragh, *Quantum generations: A history of physics in the twentieth century*, Princeton, USA: Univ. Pr. 494 (1999).

[13] M. Gell-Mann, Phys. Lett. **8**, 214 (1964)

[14] V. E. Barnes et al., Phys. Rev. Lett. **12**, 204 (1964)

[15] G. Zweig, CERN Reports Nos. 8182/TH.401 and 8419/TH.412 (1964).

[16] O.W. Greenberg, Phys. Rev. Lett. **13**, 598 (1964).

[17] M.Y. Han and Y. Nambu, Phys. Rev. **139**, B1006 (1965).

[18] E.D. Bloom et al., Phys. Rev. Lett. **23**, 930 (1969)

[19] M. Breidenbach et al., Phys. Rev. Lett. **23**, 935 (1969).

[20] D. Griffiths, *Introduction to Elementary Particles*, WILEY-VCH Verlag, Weinheim (2008)

[21] M. Peskin, D. Schroeder, *An Introduction to Quantum Field Theory*, CRC Press (2018)

[22] J. I. Kapusta, *Finite-Temperature Field Theory* (Cambridge University Press, 1989).

[23] H. D. Politzer, Phys. Rev. Lett. **30**, 1346 (1973).

[24] H. D. Gross, and F. Wilczek, Phys. Rev. Lett. **30**, 1343 (1973).

[25] *Asymptotic Freedom and Quantum ChromoDynamics: the Key to the Understanding of the Strong Nuclear Forces*, Advanced information on the Nobel Prize in Physics, 5 October 2004

[26] G. Prosperi, M. Raciti and C. Simolo, Prog. Part. Nucl. Phys. **58**, 387–438. (2007)

[27] R. Field, *Applications of Perturbative QCD*, Perseus Books, Cambridge, MA, (1995)

[28] S. Bethke, Prog. Part. Nucl. Phys. **58**, 351 (2007)

[29] M. Thomson, *Modern Particle Physics*, Cambridge University Press (2013)

[30] https://www.claymath.org/wp-content/uploads/2022/06/yangmills.pdf

[31] Bornyakov, V. G. et al., Phys. Rev. D **70**, 054506 (2004).

[32] Suganuma, H., Takahashi, T. T., Okiharu, F. and Ichie, H., Nucl. Phys. B Proc. Suppl. **141**, 92–98 (2005).

[33] E. G. Ferreiro, Nuclear Physics A **982**, 127-133, (2019)

[34] G. Martinez, *Advances in Quark Gluon Plasma*, arXiv:1304.1452 [nucl-ex]

[35] F. Karsch , E. Laermann and A. Peikert, Nucl. Phys. B **605**, 579 (2001).

[36] D.R. Williams, *Sun Fact Sheet*, (23 February 2018) https://nssdc.gsfc.nasa.gov/planetary/factsheet/sunfact.html

[37] W. Florkowski, *Phenomenology of Ultra-relativistic Heavy-ion Collisions*, World-Scientific (2010)

[38] Braun-Munzinger P. and Dönigus B., Nucl. Phys. A **987**, 144–201 (2019).

[39] Boris Tomášik, *Phenomenology of heavy-ion collisions*, lectures at THOR School, Jahorina, Bosnia and Herzegovina (2020)

[40] H. Masui (for the STAR collaboration), talk given at SQM2008, Beijing, China (2008).

[41] G. Aad et al. (The ATLAS Collaboration), Physics Letters B **710**, Issue 3 (2012)

[42] R . P. Feynman, Phys. Rev. Lett. **23** (1969)

[43] J. Adam et al. (The ALICE Collaboration), Physics Letters B **772** (2017)

[44] J. Adam et al., Phys. Rev. C **94**, 034903 (2016)

[45] STAR Collaboration, J. Adams et al., Phys. Rev. C**70**, 054907 (2004)

[46] PHENIX Collaboration, S. Adler et al., Phys. Rev. C**71** (2005) 034908

[47] PHENIX Collaboration, K. Adcox et al., Phys. Rev. Lett. **87** (2001) 052301

[48] M. Miller, K. Reygers, S. J. Sanders, and P. Steinberg, Ann. Rev. Nucl. Part. Sci. **57**, 205 (2007).

[49] B. Abelev et al. (ALICE Collaboration) Phys. Rev. C **88**, 044909 (2013)

[50] U.A. Wiedemann, *Heavy-ion collisions – selected topics*, lecture notes for the 2007 European School of High-Energy Physics (2007)

[51] D. d'Enterria, J. Phys. G **34**, S53 (2007).

[52] PHENIX Collaboration, Nature Physics **15**, 214–220 (2019).

[53] M.J. Tannenbaum, J. Phys. Conf. Ser. **589**, 012019 (2015).

[54] J.Y. Ollitrault, Phys. Rev. D **46**, 229 (1992).

[55] S. Voloshin and Y. Zhang, Z. Phys. C **70**, 665 (1996).

[56] Raimond Snellings, New J. Phys. **13** 055008 (2011)

[57] Christiansen P, Tywoniuk K and Vislavicius V, Phys. Rev. C **89** 034912 (2014)

[58] H. Caines, Nucl. Phys. A **967**, 121–128 (2017).

[59] A. Bazavov, et al., Phys. Rev. D **90** (2014) 094503.

[60] M. G. Alford, A. Schmitt, K. Rajagopal, and T. Schäfer, Rev. Mod. Phys. **80**, 1455 (2008)

[61] A. Steidl, CRC-TR-2011, https://www.gsi.de/work/forschung/theorie/theory-new/hot-and-dense-qcd

[62] *Events recorded by ALICE from the first lead ion collisions in 2011*, (Dec. 13, 2013) https://cds.cern.ch/record/1400435.

[63] K. Aamodt et al., "The ALICE experiment at the CERN LHC", JINST **3**, S08002 (2008).

[64] K. Adcox et al. (PHENIX Collaboration), Phys. Rev. Lett. **88**, 022301 (2001)

[65] S. S. Adler et al. (PHENIX Collaboration), Phys. Rev. Lett. **91**, 072303 (2003)

[66] J. Adams et al. [STAR Collaboration], Phys. Rev. Lett. **92**, 062301 (2004)

[67] P. R. Sorensen, hadronization of the bulk partonic matter created in Au + Au collisions at arXiv:nucl-ex/0309003. Ph.D. thesis.

[68] J. Adams et al. [STAR Collaboration], Phys. Rev. Lett. **92**, 052302 (2004)

[69] C. Adler et al. [STAR Collaboration], Phys. Rev. C **66**, 034904 (2002)

[70] S. S. Adler et al. [PHENIX Collaboration], Phys. Rev. Lett. **91**, 182301 (2003)

[71] Wong C-Y. *Introduction to High-Energy Heavy-Ion Collisions*, Singapore: World Scientific. (1994)

[72] Roger D. Woods and David S. Saxon, Phys. Rev. **95**, 577 (1954)

[73] H. De Vries, C. W. De Jager, and C. De Vries, At. Data Nucl. Data Tables **36**, 495 (1987).

[74] I. Angeli, K.P. Marinova, Atomic Data and Nuclear Data Tables, **99** (2013)

[75] B. Alver, M. Baker, C. Loizides, and P. Steinberg, arXiv:0805.4411 [nucl-ex]

[76] Chauvin J., Bebrun D., Lounis A., Buenerd M. Phys. Rev. C. **83** (1983)

[77] B. Schenke, P. Tribedy, R. Venugopalan, Phys. Rev. Lett. **108** 252301 (2012)

[78] B. Schenke, P. Tribedy, R. Venugopalan, Phys. Rev. C **86**, 034908 (2012)

[79] L. McLerran, *The Color Glass Condensate and Small x Physics: 4 Lectures*, arXiv:0104285 [hep-ph]

[80] J. Breitweg et al. (ZEUS Collaboration), Eur. Phys. J. C 7, **609** (1999).

[81] A.D. Martin, W.J. Stirling, R.S. Thorne and G. Watt, Eur. Phys. J. C **63**, 189 (2009).

[82] E. Iancu, A. Leonidov, L. McLerran, arXiv:0202270 [hep-ph]

[83] E. Iancu, R. Venugopalan, in: R.C. Hwa, X.-N. Wang (Eds.), Quark-Gluon Plasma **3**, World Scientific, Singapore, 2004, pp. 249–363

[84] F. Gelis, E. Iancu, J. Jalilian-Marian, R. Venugopalan, Annu. Rev. Nucl. Part. Sci. **60** (2010) 463.

[85] T. Lappi, Int. J. Mod. Phys. E **20** (2011) 1

[86] K. J. Eskola, K. Kajantie, P. V. Ruuskanen and K. Tuominen, Nucl. Phys. B **570**, 379 (2000).

[87] R. Paatelainen, K. J. Eskola, H. Holopainen and K. Tuominen, Phys. Rev. C **87**, 044904 (2013).

[88] R. Paatelainen, K. J. Eskola, H. Niemi and K. Tuominen, Phys. Lett. B **731**, 126 (2014).

[89] J. S. Moreland, J. E. Bernhard and S. A. Bass, Phys. Rev. C **92**, 011901 (2015).

[90] T. Hirano, P. Huovinen, K. Murase and Y. Nara, Prog. Part. Nucl. Phys. **70**, 108 (2013).

[91] C. V. Johnson and P. Steinberg, Physics Today **63**, 29 (2010)

[92] P. Huovinen, *Hydrodynamical description of collective flow*, arXiv:0305064 [nucl-th]

[93] J. D. Bjorken, Physical review D **27**, 140 (1983).

[94] C. A. Salgado, *Lectures on high-energy heavy-ion collisions at the LHC*, arXiv:0907.1219 [hep-ph]

[95] D. H. Rischke, arXiv/9809044 [nucl-th]

[96] C. Gale, S. Jeon and B. Schenke, Int. J. Mod. Phys. A **28**, 1340011 (2013)

[97] C. Gale et al., Physical Review Letters **110**, 012302 (2013)

[98] P. K. Kovtun, D. T. Son, and A. O. Starinets, Physical Review Letters **94**, 111601 (2005)

[99] Cremonini, S., Gürsoy, U. Szepietowski, P. J. High Energ. Phys. 2012, 167 (2012).

[100] M. Prakash, M. Prakash, R. Venugopalan and G. Welke, Phys. Rept. **227** (1993) 321

[101] P.B. Arnold, G.D. Moore and L.G. Yaffe, JHEP **11** (2000) 001

[102] H. Song, S.A. Bass, U. Heinz, T. Hirano and C. Shen, Phys. Rev. C **83**, 054910 (2011)

[103] H.B. Meyer, Phys. Rev. D **76**, 101701 (2007)

[104] E. Molnar, H. Holopainen, P. Huovinen and H. Niemi, Phys. Rev. C **90**, 044904 (2014).

[105] M. Djordjevic, Phys. Rev. C **80**, 064909 (2009)

[106] M. Djordjevic, Phys. Rev. C **74** 064907 (2006)

[107] D. Zigic, I. Salom, J. Auvinen, M. Djordjevic and M. Djordjevic, J. Phys. G **46**, 085101 (2019).

[108] D. Zigic, I. Salom, J. Auvinen, M. Djordjevic and M. Djordjevic, Phys. Lett. B **791**, 236 (2019).

[109] D. Zigic, I. Salom, J. Auvinen, P. Huovinen and M. Djordjevic, Front. in Phys. **10**, 957019 (2022).

[110] M. Gyulassy, P. Lévai, and I. Vitev, Nucl. Phys. B **594**, 371 (2001).

[111] M. Gyulassy, P. Levai and I. Vitev, Nucl. Phys. A **661**, 637 (1999).

[112] M. Gyulassy, P. Levai and I. Vitev, Nucl. Phys. B **571**, 197 (2000).

[113] M. Gyulassy, P. Levai and I. Vitev, Phys. Rev. Lett. **85**, 5535 (2000).

[114] M. Gyulassy, P. Levai and I. Vitev, Phys. Lett. B **538**, 282 (2002).

[115] M. Djordjevic and M. Gyulassy, Nucl. Phys. A **733**, 265 (2004).

[116] S.S. Adler et al. (PHENIX Collaboration), Phys. Rev. Lett. **96**, 032301 (2006); Y. Akiba et al. (PHENIX Collaboration), Nucl. Phys. A **774**, 403 (2006).

[117] R. Baier, Y. Dokshitzer, A. Mueller, S. Peigne, and D. Schiff, Nucl.Phys.B **484**, 265 (1997).

[118] N. Armesto, C. A. Salgado, and U. A. Wiedemann, Phys. Rev. D **69**, 114003 (2004).

[119] X. N. Wang and X. f. Guo, Nucl. Phys. A **696**, 788-832 (2001).

[120] M. Le Bellac, *Thermal Field Theory*, Cambridge University Press (1996)

[121] M. Djordjevic and U. Heinz, Phys. Rev. Lett. **101**, 022302 (2008).

[122] M. Djordjevic and M. Gyulassy, Phys. Rev. C **68**, 034914 (2003).

[123] M. Djordjevic and M. Djordjevic, Phys. Lett. B **709**, 229 (2012).

[124] M. Djordjevic and M. Djordjevic, Phys. Lett. B **734**, 286 (2014).

[125] B. Blagojevic, M. Djordjevic and M. Djordjevic, Phys. Rev. C **99**, 024901 (2019).

[126] B. Blagojevic and M. Djordjevic, J. Phys. G **42**, 075105 (2015).

[127] E. Braaten and M. H. Thoma, Phys. Rev. D **44**, 1298 (1991); Phys. Rev. D **44**, 2625 (1991).

[128] S. Peigne, A. Peshier, Phys. Rev. D **77** (2008)

[129] Z. B. Kang, I. Vitev and H. Xing, Phys. Lett. B 718, 482 (2012), R. Sharma, I. Vitev and B.W. Zhang, Phys. Rev. C **80**, 054902 (2009).

[130] M. Gyulassy, P. Levai and I. Vitev, Phys. Lett. B **538**, 282 (2002).

[131] D. de Florian, R. Sassot and M. Stratmann, Phys. Rev. D **75**, 114010 (2007).

[132] M. Cacciari, P. Nason, JHEP 0309, 006 (2003), E. Braaten, K.-M. Cheung, S. Fleming and T. C. Yuan, Phys. Rev. D **51**, 4819 (1995).

[133] V. G. Kartvelishvili, A.K. Likhoded, V.A. Petrov, Phys. Lett. B **78**, 615 (1978).

[134] M. Djordjevic, *Dynamical energy loss as a tool for QGP tomography*, seminar given at the Faculty of Physics, University of Belgrade (2017)

[135] Adam J et al (ALICE Collaboration), Phys. Rev. Lett. **116** 222302 (2016).

[136] Adam J et al (ALICE Collaboration), Phys. Lett. B **754** 235 (2016)
Wilde M and (for the ALICE Collaboration), Nucl. Phys. A **904-905** 573c (2013)

[137] A. Dainese [ALICE Collaboration], Eur. Phys. J. C **33**, 495 (2004).

[138] S. Stojku, B. Ilic, M. Djordjevic, and M. Djordjevic, Physical Review C **103**, 024908 (2021)

[139] D. Zigic, J. Auvinen, I. Salom, M. Djordjevic, and P. Huovinen, Phys. Rev. C **106**, 044909 – Published 20 October 2022

[140] D. Zigic, B. Ilic, M. Djordjevic and M. Djordjevic, Phys. Rev. C **101**, 064909 (2020).

[141] S. A. Bass, J. E. Bernhard and J. S. Moreland, Nucl. Phys. A **967**, 67-73 (2017).

[142] N. Borghini, P. M. Dinh, and J.-Y. Ollitrault Phys. Rev. C **64**, 054901 (2001)

[143] P. Huovinen and P. Petreczky, Nucl. Phys. A **837**, 26-53 (2010).

[144] S. Acharya *et al.* [ALICE], JHEP **1811**, 013 (2018).

[145] S. Acharya *et al.* [ALICE], JHEP **1807**, 103 (2018).

[146] V. Khachatryan, *et al.* [CMS], JHEP **1704**, 039 (2017).

[147] A. M. Sirunyan, *et al.* [CMS], Phys. Lett. B **776**, 195 (2018).

[148] [ATLAS], ATLAS-CONF-2017-012.

[149] M. Aaboud, *et al.* [ATLAS], Eur. Phys. J. C **78**, 997 (2018).

[150] A. Peshier, arXiv:0601119 [hep-ph]

[151] O. Kaczmarek, F. Karsch, F. Zantow and P. Petreczky, Phys. Rev. D **70** (2004) 074505; O. Kaczmarek and F. Zantow, Phys. Rev. D **71** (2005) 114510.

[152] Yu. Maezawa *et al.* [WHOT-QCD Collaboration], Phys. Rev. D **81** 091501 (2010);

[153] A. Nakamura, T. Saito and S. Sakai, Phys. Rev. D **69**, 014506 (2004).

[154] A. Hart, M. Laine and O. Philipsen, Nucl. Phys. B **586**, 443 (2000).

[155] D. Bak, A. Karch, L. G. Yaffe, JHEP **0708**, 049 (2007).

[156] S. Acharya, *et al.* [ALICE], JHEP **10**, 174 (2018).

[157] S. Acharya, *et al.* [ALICE], Phys. Rev. Lett. **120**, 102301 (2018).

[158] A. M. Sirunyan, *et al.* [CMS], Phys. Rev. Lett. **120**, no. 20, 202301 (2018).

[159] A. M. Sirunyan, *et al.* [CMS], Eur. Phys. J. C **78**, 509 (2018).

[160] M. Djordjevic, J. Phys. G **32**, S333-S342 (2006); M. Djordjevic and M. Djordjevic, Phys. Rev. C **90**, 034910 (2014).

[161] C. Andres, N. Armesto, H. Niemi, R. Paatelainen and C. A. Salgado, Phys. Lett. B **803**, 135318 (2020).

[162] A. Bazavov, *et al.* [HotQCD Collaboration], Phys. Rev. D **90**, 094503 (2014).

[163] W. van der Schee, P. Romatschke and S. Pratt, Phys. Rev. Lett. **111**, 222302 (2013).

[164] J. Liu, C. Shen and U. Heinz, Phys. Rev. C **91**, 064906 (2015).

[165] B. Schenke, C. Shen and P. Tribedy, Phys. Lett. B **803**, 135322 (2020).

[166] T. Nunes da Silva, D. Chinellato, M. Hippert, W. Serenone, J. Takahashi, G. S. Denicol, M. Luzum and J. Noronha, arXiv:2006.02324 [nucl-th]

[167] P. F. Kolb, J. Sollfrank and U. W. Heinz, Phys. Rev. C **62**, 054909 (2000).

[168] M. P. Heller and M. Spalinski, Phys. Rev. Lett. **115**, 072501 (2015).

[169] Y. Akamatsu, Nucl. Phys. A **1005**, 122000 (2021).

[170] C. Shen and L. Yan, Nucl. Sci. Tech. **31**, no.12, 122.

[171] A. Kurkela, A. Mazeliauskas, J. F. Paquet, S. Schlichting and D. Teaney, Phys. Rev. Lett. **122**, 122302 (2019).

[172] A. Kurkela, A. Mazeliauskas, J. F. Paquet, S. Schlichting and D. Teaney, Phys. Rev. C **99**, 034910 (2019).

[173] C. Chattopadhyay and U. W. Heinz, Phys. Lett. B **801**, 135158 (2020).

[174] W. Broniowski, W. Florkowski, M. Chojnacki and A. Kisiel, Phys. Rev. C **80**, 034902 (2009).

[175] H. Niemi, K. J. Eskola and R. Paatelainen, Phys. Rev. C **93**, 024907 (2016).

[176] I. Vitev and M. Gyulassy, Phys. Rev. Lett. **89**, 252301 (2002)

[177] T. Renk, H. Holopainen, U. Heinz and C. Shen, Phys. Rev. C **83**, 014910 (2011).

[178] B. Betz and M. Gyulassy, JHEP **08**, 090 (2014) [erratum: JHEP **10**, 043 (2014)].

[179] C. Andres, N. Armesto, H. Niemi, R. Paatelainen and C. A. Salgado, Phys. Lett. B **803**, 135318 (2020).

[180] S. Shi, J. Liao and M. Gyulassy, Chin. Phys. C **43** (2019) no.4, 044101.

[181] S. Shi, J. Liao and M. Gyulassy, Chin. Phys. C **42** (2018) no.10, 104104

[182] K. M. Burke *et al.* [JET], Phys. Rev. C **90** (2014) no.1, 014909

[183] A. Kumar, A. Majumder and C. Shen, Phys. Rev. C **101** (2020) no.3, 034908.

[184] Y. He, T. Luo, X.-N. Wang, and Y. Zhu, Phys. Rev. C **91**, 054908 (2015), [Erratum: Phys. Rev. C **97**, 019902 (2018)].

[185] S. Cao, T. Luo, G.-Y. Qin, and X.-N. Wang, Phys. Rev. C **94**, 014909 (2016).

[186] J. Xu, A. Buzzatti and M. Gyulassy, JHEP **08** (2014), 063.

[187] W. Zhao, W. Ke, W. Chen, T. Luo and X. N. Wang, arXiv:2103.14657 [hep-ph]

[188] K. Werner, I. Karpenko, M. Bleicher, T. Pierog and S. Porteboeuf-Houssais, Phys. Rev. C **85** (2012), 064907.

[189] P. Huovinen, *Hydrodynamics of Heavy-Ion Collisions*, lectures at THOR School, Jahorina, Bosnia and Herzegovina (2020)

[190] L. Adamczyk *et al.* [STAR Collaboration], Phys. Rev. C **92**, no. 1, 014904 (2015).

[191] H. Niemi, G. S. Denicol, H. Holopainen and P. Huovinen, Phys. Rev. C **87**, no. 5, 054901 (2013).

[192] C. Loizides, J. Kamin, D. d'Enterria, Phys. Rev. C **97**, 054910 (2018).

[193] K. J. Eskola, H. Niemi, R. Paatelainen and K. Tuominen, Phys. Rev. C **97**, no. 3, 034911 (2018).

[194] J. E. Bernhard, J. S. Moreland, S. A. Bass, J. Liu and U. Heinz, Phys. Rev. C **94**, no. 2, 024907 (2016)

[195] T. Renk, Phys. Rev. C **85**, 044903 (2012).

[196] D. Molnar and D. Sun, Nucl. Phys. A **932**, 140 (2014); Nucl. Phys. A **910-911**, 486 (2013).

[197] M. Djordjevic, D. Zigic, M. Djordjevic, J. Auvinen, Phys. Rev. C **99**, 061902 (2019)

[198] M. Djordjevic and M. Djordjevic, Phys. Rev. C **92**, 024918 (2015).

[199] S. Afanasiev *et al.* [PHENIX Collaboration], Phys. Rev. C **80**, 054907 (2009).

[200] Z. Qiu and U. Heinz, Phys. Rev. C **84**, 024911 (2011)

[201] ALICE Collaboration, Physics Letters B, 137453 (2022)

[202] J. Auvinen, K. J. Eskola, P. Huovinen, H. Niemi, R. Paatelainen and P. Petreczky, Phys. Rev. C **102**, 044911 (2020).

[203] B. Schenke, C. Shen and P. Tribedy, Phys. Rev. C **102**, 044905 (2020).

[204] C. Shen, private communication (2020).

[205] B. Schenke, S. Jeon and C. Gale, Phys. Rev. C **82**, 014903 (2010).

[206] B. Schenke, S. Jeon and C. Gale, Phys. Rev. Lett. **106**, 042301 (2011).

[207] B. Schenke, S. Jeon and C. Gale, Phys. Rev. C **85**, 024901 (2012).

[208] A. Bazavov *et al.* [HotQCD], Phys. Rev. D **90**, 094503 (2014).

[209] J. S. Moreland and R. A. Soltz, Phys. Rev. C **93**, 044913 (2016).

[210] H. Song and U. W. Heinz, Phys. Rev. C **77**, 064901 (2008).

[211] J. E. Bernhard, arXiv:1804.06469 [nucl-th]

[212] J. E. Bernhard, J. S. Moreland and S. A. Bass, Nature Phys. **15**, no.11, 1113-1117 (2019).

[213] H. Li, F. Liu, G. l. Ma, X. N. Wang and Y. Zhu, Phys. Rev. Lett. **106**, 012301 (2011).

[214] A. V. Sadofyev, M. D. Sievert and I. Vitev, Phys. Rev. D **104**, 094044 (2021).

[215] L. Antiporda, J. Bahder, H. Rahman and M. D. Sievert, Phys. Rev. D **105**, 054025 (2022).

[216] J. Barata, A. V. Sadofyev and C. A. Salgado, Phys. Rev. D **105**, 114010 (2022).

[217] B. Abelev et al. (The ALICE Collaboration), Phys.Lett.B **720** (2013) 52-62, 2013.

[218] S. Acharya et al. (The ALICE Collaboration), JHEP **07** (2018) 103, 2018.

[219] S. Chatrchyan et al. (CMS Collaboration), Eur. Phys. J. C **72**, 1945 (2012).

[220] S. Chatrchyan et al. (CMS Collaboration), Phys. Rev. C **87**, 014902 (2013).

[221] G. Aad et al. (The ATLAS Collaboration), JHEP **09** (2015) 050, 2015.

[222] G. Aad et al. (The ATLAS Collaboration), Phys.Lett.B **707** (2012) 330-348, 2012.

[223] James, F.W. (1994). MINUIT Function Minimization and Error Analysis: Reference Manual Version 94.1.

[224] R. Brun and F. Rademakers, Nucl. Inst. & Meth. in Phys. Res. A **389**, 81-86 (1997).

[225] B. Zakharov, JETP Lett. **63**, 952 (1996); ibid **65**, 615 (1997).

[226] A. Majumder and M. Van Leeuwen, Prog. Part. Nucl. Phys. **66** (2011).

[227] P. Arnold, G. D. Moore and L. G. Yaffe, JHEP **11**, 057 (2001); JHEP **12**, 009 (2001).

[228] C. Andres, L. Apolinário and F. Dominguez, JHEP **07**, 114 (2020).

[229] C. Andres, F. Dominguez and M. Gonzalez Martinez, JHEP **03**, 102 (2021).

[230] Y. Mehtar-Tani, JHEP **07**, 057 (2019).

[231] Y. Mehtar-Tani and K. Tywoniuk, JHEP **06**, 187 (2020).

[232] M. D. Sievert and I. Vitev, Phys. Rev. D **98**, 094010 (2018).

[233] M. D. Sievert, I. Vitev and B. Yoon, Phys. Lett. B **795**, 502 (2019).

[234] S. Wicks, arXiv:0804.4704 [nucl-th]

[235] S. Borsányi, Z. Fodor, S. D. Katz, A. Pásztor, K. K. Szabó and C. Török, JHEP **04** (2015), 138

[236] M. Djordjevic, M. Gyulassy, and S. Wicks, Phys. Rev. Lett. **94**, 112301 (2005)

Biography of the author

Stefan Stojku was born on 15 April 1994 in Pančevo, where he attended gymnasium "Uroš Predić". In 2012, he enrolled in BSc studies of Theoretical and Experimental Physics at the Faculty of Physics, University of Belgrade, graduating in 2018 with a GPA of 9.82/10.00. During his studies, from June to September 2016, he participated in CERN's Summer Student Programme, working in CERN's Theory Department within the Lattice Gauge Theory Group. In October 2018, he enrolled in the MSc studies at the Faculty of Physics, University of Belgrade, completing them in July 2019 (GPA: 9.67/10.00), when he defended his MSc thesis. The research for his MSc thesis was conducted under the supervision of Dr. Magdalena Djordjević and was later published as a journal article in Physical Review C.

In October 2019, he commenced his Ph.D. studies at the Faculty of Physics in the field of relativistic heavy-ion collisions and quark-gluon plasma. His supervisor was Dr. Magdalena Djordjević. The research for his thesis was completed at the Institute of Physics, University of Belgrade, where Stefan Stojku has been employed since October 2018 on the project funded by the European Research Council, grant ERC-2016-CoG:725741 ("A novel Quark-Gluon Plasma tomography tool: from jet quenching to exploring the extreme medium properties").

During his Ph.D. studies, Stefan Stojku co-authored five research papers in the field of high-energy physics and one article in quantitative biology. He presented his results at numerous conferences and workshops through contributed talks and posters. In 2022, he won the award for the best poster presentation at the 29th International Conference on Ultrarelativistic Nucleus-Nucleus Collisions *Quark Matter 2022*, held on April 4-10th in Kraków, Poland.

He is proficient in Serbian (native/bilingual proficiency), English (native/bilingual proficiency), Romanian (native/bilingual proficiency), and German (limited working proficiency) language.

Journal articles:

1. Stefan Stojku, Bojana Ilic, Igor Salom, Magdalena Djordjevic, *Importance of higher orders in opacity in QGP tomography*, arXiv:2303.14527 [nucl-th] (under positive review in Physical Review C)

2. Stefan Stojku, Jussi Auvinen, Lidija Zivkovic, Pasi Huovinen, Magdalena Djordjevic, *Jet-perceived anisotropy revealed through high-$p_\perp$ data*, Physics Letters B **835**, 137501 (2022)

3. Stefan Stojku, Jussi Auvinen, Marko Djordjevic, Pasi Huovinen, and Magdalena Djordjevic, *Early evolution constrained by high-$p_\perp$ quark-gluon plasma tomography*, Physical

Review C **105**, L021901 (2022)

4. Stefan Stojku, Bojana Ilic, Marko Djordjevic, and Magdalena Djordjevic, *Extracting the temperature dependence in high-$p_\perp$ particle energy loss*, Physical Review C **103**, 024908 (2021)

5. Magdalena Djordjevic, Marko Djordjevic, Bojana Ilic, Stefan Stojku, Igor Salom, *Understanding Infection Progression under Strong Control Measures through Universal COVID-19 Growth Signatures.* Global Challenges 2021, 5, 2000101

6. Magdalena Djordjevic, Stefan Stojku, Marko Djordjevic, and Pasi Huovinen, *Shape of the quark gluon plasma droplet reflected in the high- $p_\perp$ data*, Phys. Rev. C **100**, 031901(R) (2019)

Conference proceedings:

1. Stefan Stojku, Jussi Auvinen, Marko Djordjevic, Magdalena Djordjevic, Pasi Huovinen, *Initial Time τ_0 Constrained by High-$p_\perp$ Data*, Acta Phys. Pol. B Proc. Suppl. **16**, 1-A156 (2023)

2. Magdalena Djordjevic, Stefan Stojku, Dusan Zigic, Bojana Ilic, Jussi Auvinen, Igor Salom, Marko Djordjevic and Pasi Huovinen, *From high-$p_\perp$ theory and data to inferring anisotropy of Quark-Gluon Plasma*, Nucl. Phys. A **1005**, 121900 (2021)

This dissertation is based on journal articles 1, 2, 3, 6; as well as the first conference proceedings from the lists above.

Изјава о ауторству

Име и презиме аутора – **Стефан Стојку**

Број индекса – **8002/2019**

Изјављујем

да је докторска дисертација под насловом

Properties of Quark-Gluon Plasma Inferred from High-$p_\perp$ Data

(Одређивање особина кварк-глуонске плазме помоћу високоенергијских честица)

- резултат сопственог истраживачког рада;
- да дисертација у целини ни у деловима није била предложена за стицање друге дипломе према студијским програмима других високошколских установа;
- да су резултати коректно наведени и
- да нисам кршио ауторска права и користио интелектуалну својину других лица.

У Београду, 2023 **Потпис аутора**

_____

Изјава о истоветности штампане и електронске верзије докторског рада

Име и презиме аутора – **Стефан Стојку**

Број индекса – **8002/2019**

Студијски програм – Физика високих енергија и нуклеарна физика

Наслов рада – **Properties of Quark-Gluon Plasma Inferred from High-$p_\perp$ Data**

(Одређивање особина кварк-глуонске плазме помоћу високоенергијских честица)

Ментор – **др Магдалена Ђорђевић**

Изјављујем да је штампана верзија мог докторског рада истоветна електронској верзији коју сам предао ради похрањивања у **Дигиталном репозиторијуму Универзитета у Београду**.

Дозвољавам да се објаве моји лични подаци везани за добијање академског назива доктора наука, као што су име и презиме, година и место рођења и датум одбране рада.

Ови лични подаци могу се објавити на мрежним страницама дигиталне библиотеке, у електронском каталогу и у публикацијама Универзитета у Београду.

У Београду, 2023 **Потпис аутора**

_____

Изјава о коришћењу

Овлашћујем Универзитетску библиотеку „Светозар Марковић“ да у Дигитални репозиторијум Универзитета у Београду унесе моју докторску дисертацију под насловом:

Properties of Quark-Gluon Plasma Inferred from High-$p_\perp$ Data

(Одређивање особина кварк-глуонске плазме помоћу високоенергијских честица)

која је моје ауторско дело.

Дисертацију са свим прилозима предао сам у електронском формату погодном за трајно архивирање.

Моју докторску дисертацију похрањену у Дигиталном репозиторијуму Универзитета у Београду и доступну у отвореном приступу могу да користе сви који поштују одредбе садржане у одабраном типу лиценце Креативне заједнице (Creative Commons) за коју сам се одлучио.

1. Ауторство (CC BY)
2. Ауторство – некомерцијално (CC BY-NC)
3. Ауторство – некомерцијално – без прерада (CC BY-NC-ND)
4. **Ауторство – некомерцијално – делити под истим условима (CC BY-NC-SA)**
5. Ауторство – без прерада (CC BY-ND)
6. Ауторство – делити под истим условима (CC BY-SA)

(Молимо да заокружите само једну од шест понуђених лиценци.
Кратак опис лиценци је саставни део ове изјаве).

У Београду, 2023 **Потпис аутора**

_____

1. **Ауторство.** Дозвољавате умножавање, дистрибуцију и јавно саопштавање дела, и прераде, ако се наведе име аутора на начин одређен од стране аутора или даваоца лиценце, чак и у комерцијалне сврхе. Ово је најслободнија од свих лиценци.

2. **Ауторство – некомерцијално.** Дозвољавате умножавање, дистрибуцију и јавно саопштавање дела, и прераде, ако се наведе име аутора на начин одређен од стране аутора или даваоца лиценце. Ова лиценца не дозвољава комерцијалну употребу дела.

3. **Ауторство – некомерцијално – без прерада.** Дозвољавате умножавање, дистрибуцију и јавно саопштавање дела, без промена, преобликовања или употребе дела у свом делу, ако се наведе име аутора на начин одређен од стране аутора или даваоца лиценце. Ова лиценца не дозвољава комерцијалну употребу дела. У односу на све остале лиценце, овом лиценцом се ограничава највећи обим права коришћења дела.

4. **Ауторство – некомерцијално – делити под истим условима.** Дозвољавате умножавање, дистрибуцију и јавно саопштавање дела, и прераде, ако се наведе име аутора на начин одређен од стране аутора или даваоца лиценце и ако се прерада дистрибуира под истом или сличном лиценцом. Ова лиценца не дозвољава комерцијалну употребу дела и прерада.

5. **Ауторство – без прерада.** Дозвољавате умножавање, дистрибуцију и јавно саопштавање дела, без промена, преобликовања или употребе дела у свом делу, ако се наведе име аутора на начин одређен од стране аутора или даваоца лиценце. Ова лиценца дозвољава комерцијалну употребу дела.

6. **Ауторство – делити под истим условима.** Дозвољавате умножавање, дистрибуцију и јавно саопштавање дела, и прераде, ако се наведе име аутора на начин одређен од стране аутора или даваоца лиценце и ако се прерада дистрибуира под истом или сличном лиценцом. Ова лиценца дозвољава комерцијалну употребу дела и прерада. Слична је софтверским лиценцама, односно лиценцама отвореног кода.